THE DEFORMATION CHARACTERISTICS OF DEOXIDATION PRODUCTS IN HOT ROLLED STEEL.

A thesis submitted in application
for the degree of:
DOCTOR OF PHILOSOPHY
in
THE UNIVERSITY OF ASTON IN BIRMINGHAM
by
GRAHAM WARDLE

Department of Metallurgy and Materials,
The University of Aston in Birmingham,
Gosta Green, Birmingham. B4 7ET.

January, 1979.

THE DEFORMATION CHARACTERISTICS OF DEOXIDATION PRODUCTS IN HOT ROLLED STEEL.

GRAHAM WARDLE.

THESIS : DOCTOR OF PHILOSOPHY - JANUARY 1979.

SUMMARY

The deoxidation of steel at 1600°C. was achieved by the use of Mn-Si-Al alloys. Steels containing silicate inclusions of various compositions were deformed by rolling, and the deformation of these inclusions was studied with reference to various parameters.

Electron-probe micro analysis revealed that the 'as cast' inclusion compositions varied with respect to inclusion size.

The 'Relative Plasticity indices' of deformed inclusions have been measured and related to inclusion size, composition, matrix strain and the temperature of deformation. In addition attention has been focussed upon the measurement of 'relative plasticity' values obtained from other orthogonal planes.

It was shown that inclusions less than approximately 2 µm in diameter did not deform under any of the imposed deformation conditions. The size of deformed inclusions was represented by the use of the square root of the product of their major and minor axes.

Inclusions rolled at the lower temperatures behaved in a 'brittle' or 'rigid' manner. There was a rapid transition from brittle to deformable behaviour over a narrow temperature range. This transition temperature was often shown to be well below any solidus/liquidus temperature encountered within the oxide system under study.

It was found that the value of 'relative plasticity index' was lowered as the degree of matrix deformation was increased. An explanation in part has been proposed on the basis of a change in strain rate during a multi-pass rolling programme.

The variation in plasticity index values measured on the various orthogonal planes has been attributed to non-plane strain deformation. Equations have been derived to relate measurements to the plane strain condition.

(INCLUSIONS : DEFORMATION : PLASTICITY-INDEX : SIZE : COMPOSITION).

TO : VAL and RUSSELL .

VOL. I.

CONTENTS

VOLUME I

Page

SECTION 1 INTRODUCTION

SECTION 2 LITERATURE REVIEW

page

SECTION 3 EXPERIMENTAL PROCEDURE

SECTION 4 EXPERIMENTAL RESULTS

VOLUME II

SECTION 5 DISCUSSION OF RESULTS

page

SECTION 6.

1.1 Introduction.

Commercially produced steels contain non-metallic inclusions, and unless expensive techniques are used to remove these inclusions steels should be regarded as composite materials containing low volume fractions of non-metallics. The presence of these inclusions may, or may not affect the applications to which the steels are put into service.

The types of inclusion produced by steelmaking processes and the behaviour of these inclusions during processing are controlled by the type of deoxidation process employed. Excluding exogenous and re-oxidation products the main groups of inclusions encountered are the oxides and sulphides which result directly from the steelmaking practice.

During hot working processes, inclusions present within the steel may remain rigid, crack, shatter and disperse in a brittle manner, or deform with plastic or fluid characteristics.

If inclusions do not deform microcracks may form at the inclusion/matrix interface. This type of defect may have serious consequences if the steel is in a fatigue situation in service. Non-deformable inclusions may also have deleterious effects in the steel strip industries where they may cause surface blemishes, or act as preferential corrosion sites. Inclusions which are brittle during processing may again form internal crack defects, and it is well known that this type of defect causes problems within the wire drawing and tube making industries.

Inclusions which deform in a fluid manner form large planar defects in hot rolled strip, and may lead to serious defects when strip steel is welded i.e. lamellar defects. Deformable inclusions almost certainly produce some degree of mechanical anisotropy in the final product, although internal microcracks may be avoided.

A knowledge of the behaviour of the type of inclusion present may enable the harmful aspects of inclusions present to be overcome to some acceptable degree.

In general it has been established that non-metallic inclusions influence such mechanical properties as, fatigue impact and fracture toughness, and a large amount of work has been aimed at assessing these effects. However, a knowledge of how to process steels containing different types of inclusions may alleviate some of the problems they cause at present.

1.2 Present work.

From the previous section, it is clear that an understanding of the ways in which inclusion phases deform during processing may enable inclusion types to be tailored to processing needs, and reduce harmful effects in certain areas of steels application.

There have been numerous investigations into the origins and formation of non-metallic inclusions, and their effect upon mechanical properties in the cast and processed material. However, until recently less attention had been paid to the more specific aspects of inclusion deformation and the factors governing the deformation process.

The aim of the present work was to investigate the deformation characteristics of inclusions resulting from Mn - Si and Mn - Si - Al deoxidation. In addition specific fields of study were to provide information on the variation of 'inclusion relative plasticity' with respect to the following parameters

(i) Inclusion composition
(ii) Inclusion size
(iii) Temperature of deformation
(iv) Degree of matrix strain

During the course of investigation further information concerning the non-homogeneous deformation of the steel matrix was established. In addition the value of relative plasticity measured on the other orthogonal planes was studied.

It had initially been intended that mechanical testing of the final product be incorporated into the work, and related to the various parameters studied. This unfortunately was not accomplished in the time available.

LITERATURE REVIEW

2.1. Deoxidation

Steelmaking processes involve the removal of large quantities of dissolved impurities from the melt. The majority of these impurities are removed by oxidation reactions promoted by the use of oxidising slags or gases. As the concentration of oxidisable impurities is reduced there is an increase in the activity of oxygen in the melt and a large quantity of oxygen is present in solution. The oxygen solubility in the liquid steel is dependent upon temperature and residual elements present after the oxidation period is completed.

The variation in oxygen solubility with temperature has been studied quantitatively (1.2.3.) and solubility data for the Fe-O system is summarised in figure 2.1. Oxygen solubility at 1600°C. is approximately 0.23%wt (4.) and at the monotectic temperature of 1530°C., 0.16%wt. (5. 6. 7.) . However, the solubility of oxygen in liquid steel is always lower than in pure iron-oxygen melts, but is usually of the order 0.1%wt, (8.) although the actual value is dependent mainly upon the carbon content of the liquid steel. Oxygen solubility in the solid state is very much lower than in the liquid, and solubility measurements have produced diverse results in the range 0.003-0.009wt% as detailed by Lindon (9.).

If a steel melt was to be cast without deoxidation

2·1·1

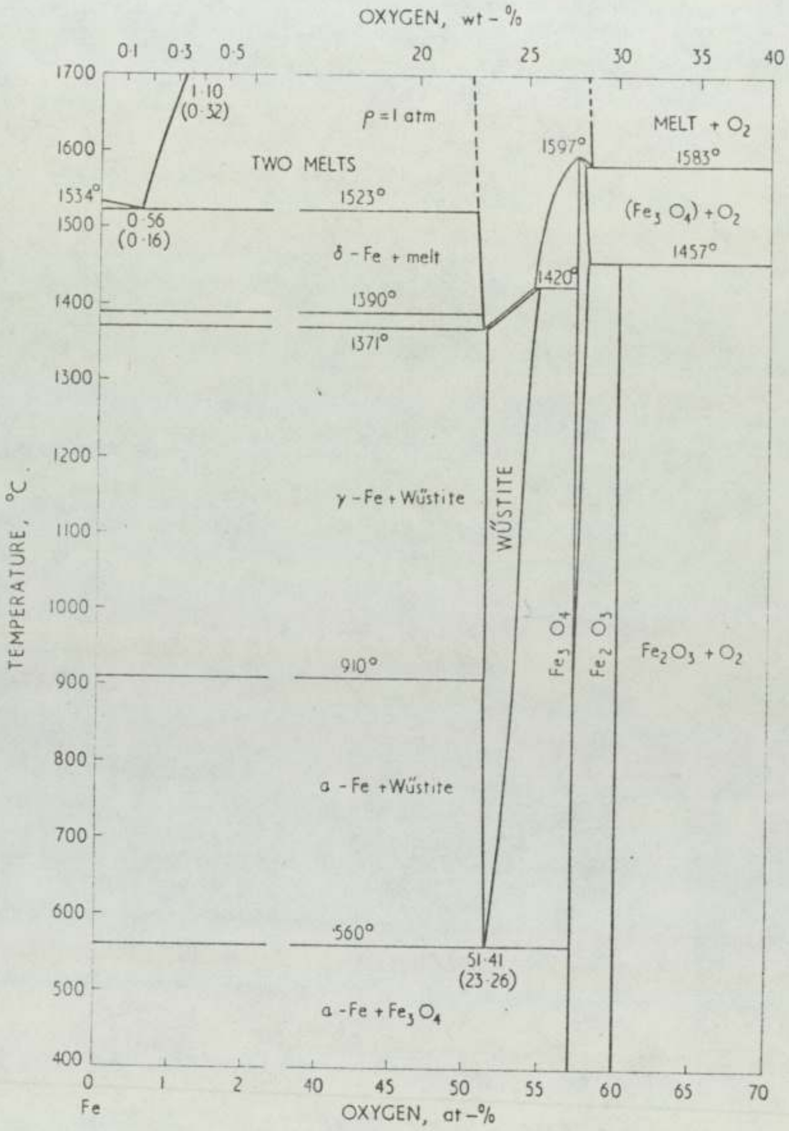

74 The iron–oxygen system, constitution diagram (*from M. Hansen "Constitution of binary alloys", 1958, McGraw-Hill*) treatment a carbon-oxygen reaction would take place during the cooling and solidification of an ingot. The ensuing carbon monoxide effervescence would result in a highly porous steel. Control of the carbon-oxygen reaction in the production of rimming steels enables low carbon ingots to be produced where the rimming action compensates for volume contraction during solidification. The oxygen required for a controlled rimming action is relatively high and residual oxygen reacts with the residual manganese and silicon present to form non-metallic inclusions. A large proportion of these inclusions become trapped in the ingot. Kiessling (10.) has suggested that one tonne of carbon steel contains approximately 10^{12}-10^{13} oxide inclusions, 80-90% of all inclusions resulting from deoxidation directly (11.). By controlling the amount of dissolved oxygen present by deoxidation practice and solidification techniques rimming, balanced, semi-killed and capped steels may be produced.

The extensive segregation of impurities in rimming steels however, limits their use in many engineering applications. High quality steels requiring uniformity of properties and composition are required to be fully deoxidised (i.e. fully killed). This reduces the activity of oxygen to a level less than that required for carbon monoxide evolution.

The removal of dissolved oxygen by the use of the carbon-oxygen reaction has the advantage of excluding solid oxide precipitates within the liquid steel, an advantage utilised in various vacuum degassing techniques. Such techniques are not widely used because of economic factors, and there is the likelihood of introducing exogenous inclusions into the metal due to the reduction of refactory linings under vacuum conditions (12.).

2.1.1. Deoxidation processes.

Commercial deoxidation processes are aimed at reducing the oxygen activity by the controlled addition of elements having a high affinity for oxygen, and which are soluble in the steel. It is usual to prevent the formation of iron oxide as a product of deoxidation, since the presence of FeO leads to hot shortness during subsequent mechanical processing. It is essential therefore to choose a deoxidant whose oxide is thermodynamically more stable than iron oxide (figure 2.1.2). Deoxidation practice in the steelmaking industry is very varied, and is dependent upon the type and requirements of the steel to be produced. It is however, usual to split the deoxidation treatment into three parts.

Initially the weaker deoxidants such as ferromanganese are added to the steel bath prior to and during tapping. Stronger deoxidants such as ferrosilicon and ferroaluminium are added during the tapping process. Finally aluminium (when required) is added to the ingot mould in top poured ingots, or to the trumpet in the case of bottom poured ingots.

Variations to this basic theme include the use of

2•1•2

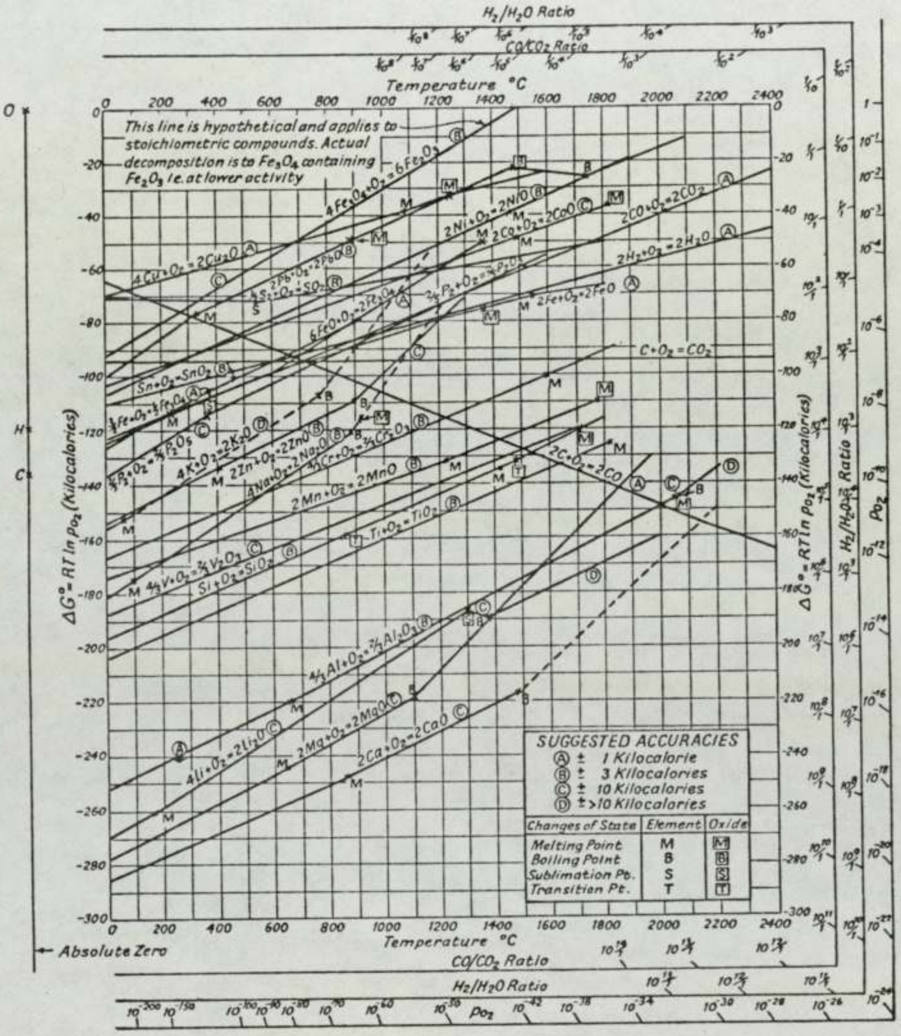

Fig. 15. The standard free energy of formation of metallurgically important oxides as a function of temperature (from Darken and Gurry [32]).

silicomanganese and calcium silicide additions. Other deoxidants such as titanium are used for specific qualities of steel, and modifying agents such as 'mischmetal' are used as required for sulphide shape control.

2.1.2. Inclusion classifications.

Inclusions which form as a result of a deoxidation reaction may be split into two categories, namely primary and secondary deoxidation products. Primary products are those formed in the melt as the direct result of a deoxidant addition. Secondary products are those resulting from the action of elements in the liquid and solid state as the melt cools, and result in a decrease in oxygen solubility. It is usual to find both primary and secondary products in cast steels, although the primary products have a greater time to escape to the surface before solidification is complete.

Inclusions may also be classified in terms of their origin (10,13,14) i.e. Indigenous and Exogenous. Indigenous inclusions are principally oxides and sulphides arising from the primary and secondary deoxidation processes outlined above. Exogenous inclusions are not however formed by deoxidation reactions, but result from the entrapment of 'foreign material' such as slag and refactory particles.

Exogenous inclusions are usually distinguishable from indigenous types; the former being generally larger, complex in structure, irregular in shape and of sporadic occurrence. However, Pickering (15.) and Morgan et al (16.) have observed indigenous precipitation upon exogenous nuclei. Although such factors complicate simple classifications outlined above, the classification provides a basis for the discussion of inclusion origins.

2.1.2.1. Inclusion origins.

Material charged to the steelmaking furnace contains oxidisable elements, carbon escapes from the system as carbon monoxide but the other elements such as aluminium silicon and manganese remain as insoluble oxides. These oxides are normally fluxed and taken up by the slag. During the casting and teeming processes exogenous inclusions may be picked up, in addition to the indigenous inclusions formed by later alloying additions.

The addition of deoxidants and alloying additions in industrial practice results in some degree of slag/metal admixing prior to and during tapping. Pickering (15.) had in fact found evidence that the simultaneous tapping of slag and metal results in the elimination of numerous persistent small inclusions normally encountered.

Reoxidation of the melt during the tapping and teeming processes always complicates the issue in industrial situations, and inclusion products formed as a result (17.) must be considered.

2.1.3. Deoxidation thermodynamics.

2.1.3.1. Deoxidation equilibria.

There have been numerous studies concerned with deoxidation equilibria and the thermodynamics of deoxidation, and much of this data has previously been reviewed (4, 9, 18-20). However, the majority of the data available is for the elements in their standard states 'i.e. pure substances' and simple binary and ternary systems. The validity of such data pertinent to the experimental work in hand is questionable because of the short time between deoxidising and casting ($<$ 30 seconds) and the rapid solidification ($<$ 30 seconds)[21] utilised in this present work. The data available (20, 22, 23) has however, been used in part as the basis of deoxidant alloy calculation.

2.1.3.2. Manganese deoxidation.

From free energy-temperature diagrams (figure 2.1.2.) manganese is seen as one of the weaker deoxidants used in practice. The influence of manganese as a deoxidant has been based upon the reaction

$$FeO_{(L)} + \underline{Mn} \longrightarrow MnO_{(L)} + \underline{Fe}_{(L)}$$

where $\underline{Mn}$ indicates manganese dissolved in liquid iron.

In a literature review Bell (4) concluded that MnO and FeO were completely miscible in the liquid state. However, it was pointed out that only a range of MnO-FeO compositions were liquid at steelmaking temperatures, thus showing the disadvantage of manganese as a deoxidant (figure 2. 1 3.).

In pure Fe-Mn-O melts FeO-MnO mixtures behave as approximately ideal solutions (4.) and the equilibrium constant approximates to

$$K'_{MnO} = \frac{a_{MnO}}{\underline{Mn}\% \ \underline{O}\%}$$

Values of the Mn-O equilibrium constant published and summarised by Bodsworth (20.) are found to be very similar.

2.1.3.3. Silicon deoxidation.

Silicon deoxidation has been based upon the silicon-oxygen equilibria for the reaction,

$$\underline{Si} + 2\underline{O} \longrightarrow SiO_2$$

It was proposed (24.) that the activity coefficient of oxygen was reduced by silicon, the activity coefficient increasing with increasing concentration. From their experiments Gocken and Chipman (24.) found that for pure Fe-Si-O melts containing less than 2wt% Si that the change in silicon activity coefficient (f_{Si}) with oxygen concentration was almost exactly balanced by the change in the oxide activity coeffecient squared i.e. (f_O^2). Since the product (f_{Si}) (f_O^2) was approximately constant the equilibrium constant approximated to:

2 • 1 • 3

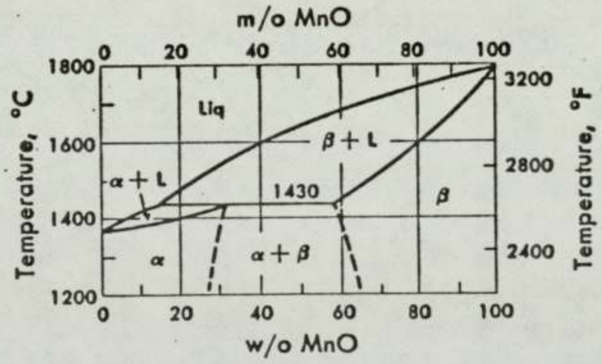
m/o MnO
0
20
40
60
80
100
1800
1600
1400
1200
Temperature, °C
3200
2800
2400
Temperature, °F
Liq
β + L
α + L
1430
β
α
α + β
0
20
40
60
80
100
w/o MnO

$$K'_{Si-O} = \frac{a_{SiO_2}}{\underline{Si}\% . \underline{O}^2\%}$$

Although silica stability is greater than that of manganese oxide, the principal difference between silicon and manganese deoxidation lies in the acidic nature of SiO_2 compared with the basic nature of a_{MnO} (20.). This is underlined by the observations that a_{MnO} increases and a_{SiO_2} decreases as slag basicity is increased. It has also been shown (20.) that the silica reaction is more markedly temperature dependent. As a result the additional deoxidation arising from the displacement of MnO equilibria during cooling to the solidification temperature, is less extensive than for silica.

At low levels of silicon content the equilibrium product is not solid silica (9.) but consists of a FeO - SiO_2 mixture.

2.1.3.4. Manganese - silicon deoxidation.

Manganese and silicon are the most common deoxidants added to steel in the furnace and/or ladle. Although deoxidation by silicon is more effective than by manganese (25.) (figure 2. 1.2.) simultaneous addition gives a much lower level of residual oxygen in solution. This fact was shown by Korber and Oelsen (26.) for liquid iron - slag systems.

Hilty and Crafts (27.) examined manganese - silicon deoxidation in alumina crucibles under an argon atmosphere and observed that oxygen equilibrium decreased with increasing manganese content. Bell (4.) concluded in his literature review that manganese increased the deoxidising power of silicon. Later he showed the effect of manganese on the silicon-oxygen equilibrium in liquid iron (28.), graphically illustrated in figure 2.1.4 . Walsh and Ramachandran (29.) explained the low oxygen values obtained by Hilty and Crafts by the fact that the deoxidation product was a manganese silicate having a silica activity (a_{SiO_2}) less than unity.

In later work Turkdogan (25.30.) calculated the manganese-silicon deoxidation equilibrium data for the reaction

$$2MnO + \underline{Si}_{\%} \longrightarrow 2\underline{Mn}_{\%} + SiO_2$$

for which K_{Si-Mn} is given by

$$K_{Si-Mn} = \frac{[\%Mn]^2}{[\%Si]} \cdot \frac{a_{SiO_2}}{a^2_{MnO}}$$

Where a_{SiO_2} and a_{MnO} are the Raoultian activities of oxides in the molten manganese oxide-silica deoxidation product. Turkdogan (25.) also showed that above a critical (%Si)/(%Mn)^2 ratio for a given temperature solid silica will form, illustrated in figure 2.1.5.

2.1.3.5. Aluminium deoxidation

Aluminium deoxidation has been reviewed and studied by many workers (9, 27, 31-35.) and values of aluminium

2.1.4

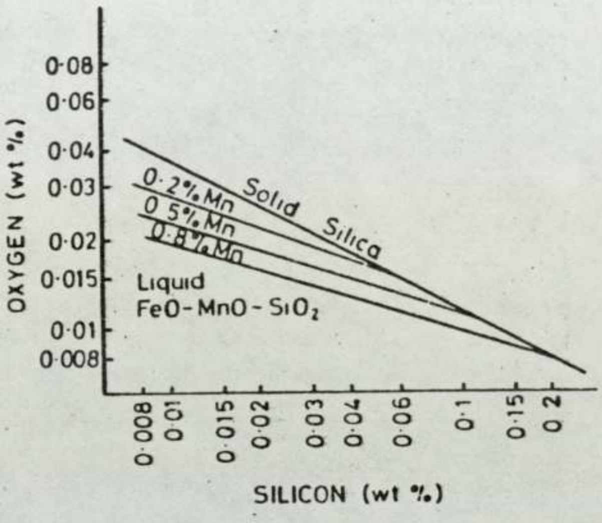
OXYGEN (wt %)
0·08
0·06
0·04
0·03
0·02
0·015
0·01
0·008
Solid Silica
0·2% Mn
0·5% Mn
0·8% Mn
Liquid
FeO-MnO-SiO₂
0·008
0·01
0·015
0·02
0·03
0·04
0·06
0·1
0·15
0·2
SILICON (wt %)

2.1.5

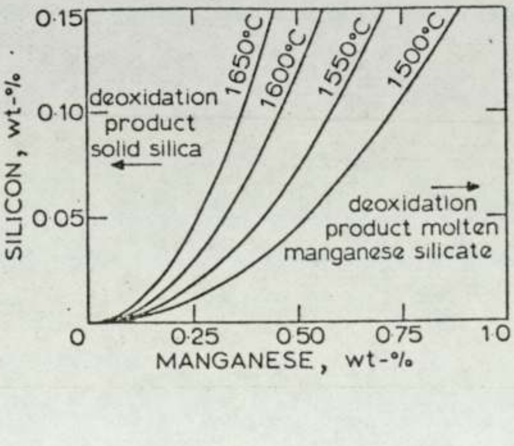
SILICON, wt-%
0·15
0·10
0·05
0
1650°C
1600°C
1550°C
1500°C
deoxidation product solid silica
deoxidation product molten manganese silicate
0·25
0·50
0·75
1·0
MANGANESE, wt-%

equilibrium constant have been determined in the range 10^{-9} to 10^{-14} at 1600°C. Although alumina is a very stable oxide Lindon (9.) has pointed out many experimental problems encountered in the determination of K_{Al-O} . Although alumina is the expected product of aluminium deoxidation, the spinel hercynite ($FeO.Al_2O_3$) is formed when the residual aluminium in the iron is not in excess of the residual oxygen content.

Differences in true and apparent equilibrium constant are thought possibly to be due to a slow rate of approach to equilibrium. Lindon and Billington (36.) have shown that Mn-O and Si-O reactions are considerably more rapid than the Al-O reaction. On the basis that the simultaneous addition of manganese and aluminium resulted in a close approach to equilibrium, it suggested that manganese displaced an Fe-Al-O film which normally retarded dissolution. If a liquid product forms in which oxide activities are less than unity then true equilibrium should be at lower residual levels of aluminium and oxygen. The work of McLean (37.) led to experimental confirmation to this suggestion

2.1.3.6. Manganese -silicon - aluminium deoxidation.

The influence of aluminium containing manganese - silicon deoxidants has not yet been fully examined in critical detail. However, Lindon (9.) pointed out that it would be expected that the presence of alumina in the deoxidation products would lead to a decrease in manganese oxide and silica activities. He has also pointed out that a manganese alumina silicate slag would equilibrate with a lower oxygen level for a given Mn:Si ratio. There is at present however only limited data available for the $MnO-SiO_2-Al_2O_3$ system (38.39) with respect to oxide activities. (figure 2.1.6. & 2.1.7.)

2.1.4. Kinetics of the deoxidation process.

Although the ability of elements to act as successful deoxidants is dependent upon the thermodynamics of metal/oxide systems, reaction kinetics are important in any real system.

Early studies on deoxidation reaction kinetics involving the formation, growth and separation of inclusions was carried out by Plockinger and Wahlster (40.41.). They showed that a rapid decrease in dissolved oxygen was associated with the formation of deoxidation products. In addition there was a delayed and slower decrease in total oxygen corresponding to the elimination of the deoxidation products. As a progressive understanding of deoxidation kinetics grew (42.) the process was divided into the categories of:

(i) Deoxidation solution.
(ii) Nucleation of deoxidation products.
(iii) Growth of nuclei.
(iv) Elimination of the inclusions.

Waudby (43) has pointed out that in practical situations these stages are not separable but overlap

2•1•6

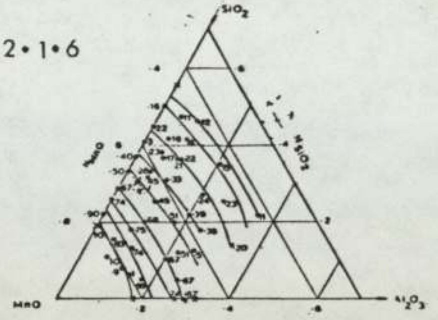
SiO$_2$
N$_{MnO}$
N$_{SiO_2}$
MnO
Al$_2$O$_3$
·2
·4
·6

2•1•7

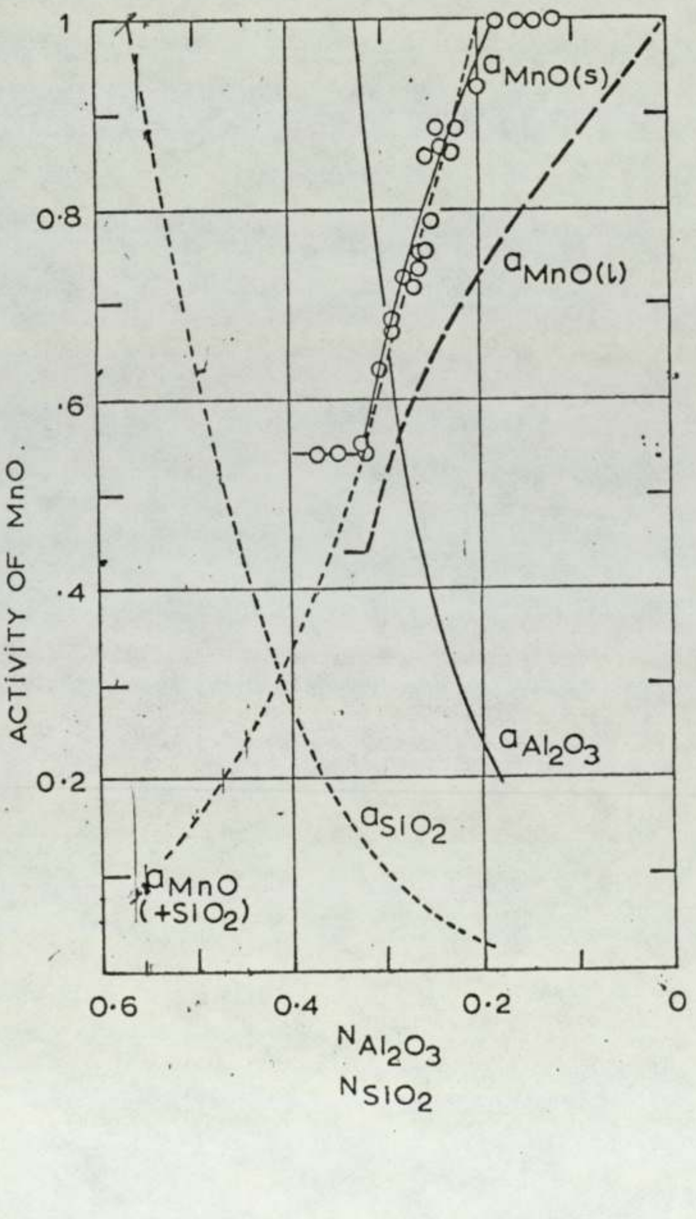
1
0·8
·6
·4
0·2
ACTIVITY OF MnO
a$_{MnO(s)}$
a$_{MnO(l)}$
a$_{Al_2O_3}$
a$_{SiO_2}$
a$_{MnO}$ (+SiO$_2$)
0·6
0·4
0·2
0
N$_{Al_2O_3}$
N$_{SiO_2}$

and are complicated by factors such as reoxidation and processing variables.

2.1.4.1. Deoxidant solution.

Levin(44.) showed that the presence of a deoxidising element, even below its equilibrium content caused the precipitation of oxides through progressive solution. The significance of the solution stage upon subsequent deoxidation has been reviewed (43.) on the basis of observations.

Heterogeneity of the alloying addition is observed both on the macro and micro scale, although it is observed to a greater extent in the latter.

Olette et al (45.) showed for aluminium deoxidation that the method of introducing the addition influenced the kinetics of the process. It was explained that a slower decrease in dissolved oxygen observed with a solid addition was due to delayed solution and homogenisation. This delay they attributed to a layer of fine alumina particles on the deoxidant surface thereby retarding solution. This observation was in agreement with Chipman's (46.) earlier proposal of a stabilising film at the interface of regions rich in oxygen. Grethan and Philippe (42.) showed that a galaxite ($MnO.Al_2O_3$) film was observed with the addition of Fe-Al-Mn alloys to a Fe-O melt.

The above examples are considered as evidence for the non instantaneous solution and distribution of a deoxidant (43.). Although this may augment the complexities of the deoxidation process, steelmaking practice may minimise the effect.

2.1.4.2. Nucleation of deoxidation products.

Since the basis of the deoxidation process is to form a new phase in the liquid iron, nucleation must occur either by homogenous or hetrogeneous modes. Homogeneous nucleation takes place without the need for an impurity nucleation site (and as such has been the subject of theoretical analyses (47.)), whereas hetrogeneous nucleation requires the provision of a substrate.

Turpin and Elliot(48.) applied the theory of homogeneous nucleation to oxide inclusions in steel, and the critical supersaturation to promote nucleation was expressed in free energy terms.

i.e.

$$\Delta G_{c\text{-}[hom]} = -RT \ln \left[\frac{K'}{K}\right]$$

where K is the equilibrium solubility product and K′ is the solubility product for the actual components in supersaturated solution. The value ($\frac{K'}{K}$) is termed the supersaturation ratio.

Early investigations on liquid iron-oxygen melts by Bogdandy et al (49.50) used pure aluminium and ferro-aluminium alloys added to the top surface of the melts. Their work showed that alumina rich and alumina deficient bands were established, iron oxide being formed in the aluminium deficient zones. The presence of hercynite ($FeO.Al_2O_3$) was infrequently observed. Bogdandy also calculated that a nucleus diameter was of the order of one molecule. This indicated that inhibition to nucleation referred to chemical reaction, and that the rate controlling stage was the formation of a discrete alumina particle. An increase in the aluminium content gave rise to a slower rate of growth of the alumina layers.

Using a similar technique, Woehlbier and Rengstorff (51.) used a Fe-10% Al alloy as the deoxidant. They reported that at 1600°C nucleation difficulties were encountered in the diffusion zones eventhough there was a high aluminium concentration present. In a subsequent experiment using a less pure iron containing 0.07% oxygen instead of a pure iron melt containing 0.16% oxygen they found the melt to be partially deoxidised. They concluded that a high degree of supersaturation was required for the nucleation of alumina, but a lower degree of supersaturation is sufficient to cause the precipitation of alumina on small heterogeneous nuclei without the formation of hercynite. Further work by the authors involved the stirring of aluminium in the upper zone of the melt. Homogeneous nucleation resulted at the point of addition and the resultant inclusions were carried down into the undeoxidised portion of the melt where they reacted with the residual oxygen to form hercynite.

Sigworth and Elliot (52.) reviewed the nucleation of oxides in iron-silicon-oxygen alloys. They concluded that investigations of the nucleation process were limited by experimental techniques and the lack of accurate interfacial energy data. In their own experimental work they found that although the supersaturation ratio required for homogeneous nucleation of silica was high, nucleation could occur readily when ferrosilicon was added. These conditions could also be achieved even in the presence of particles suitable for hetrogeneous nucleation if supersaturation could be provided rapidly.

2.1.4.2.1. Complex deoxidation.

In deoxidation with more than one deoxidant there is competition between different possible precipitatable phases (54.55). In the deoxidation of iron-oxygen melts (containing various levels of manganese) and using aluminium as the deoxidant it was observed (55.) that primary deoxidation products changed composition during the course of their formation. Initially the inclusions were very low in alumina, consisting mainly of iron and manganese oxides. After a few seconds the aluminium content had approached that of the spinel (FeMn)$O.Al_2O_3$. At the temperature employed of 1630°C these particles were fluid and coalesced readily giving inclusions of uniform composition. However, as time progressed the inclusions developed two regions of varying composition, the centre of approximately spinel composition and the outer layers of alumina.

An increase in aluminium addition was found to give an increase in the alumina content of the mixed oxides. Providing that the inclusions were liquid, composition homogenisation would occur. However, as the alumina content increased to that of the spinel composition solidification of the inclusions occurred.

From the evidence available Plockinger postulated that mixed oxides nucleated homogeneously. However, Frohberg and Potschke (56.) and Forster (57.) suggested that nucleation theory was contradicted if mixed oxides nucleated first. They were of the opinion that the phase for which the system was able to supply the energy for nucleation would be precipitated first. Alumina would nucleate first and the iron manganese oxides would be heterogeneously precipitated upon the alumina nuclei. Forster (57.), using zirconium instead of aluminium observed that shortly after deoxidation inclusions consisted of a zirconia core surrounded by mangano-wustite. These results suggested that zirconia was the first product to nucleate, and had not dissolved into the heterogeneously precipitated (FeMn)O.

There have been suggestions (54.) that in the case of aluminium deoxidation $FeO.Al_2O_3$ may form the nucleus, this being attributed to a decrease in interfacial energy of the melt/nucleus caused by chemical reaction between the two phases. In addition nuclei composition was considered to be determined by the soluble oxygen prior to deoxidation (figure 2.1. 8.).

2 • 1 • 8

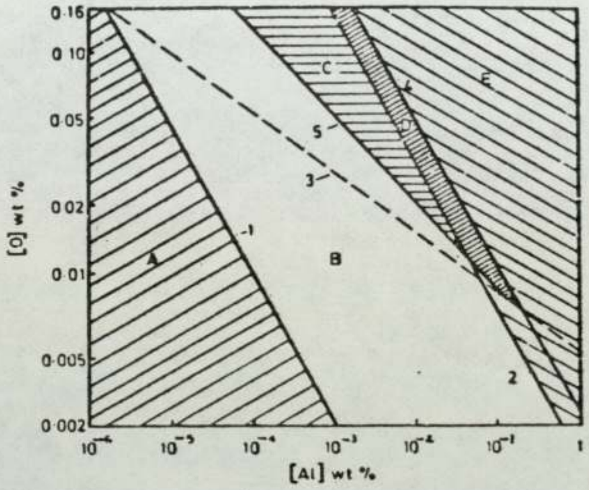
0.16
0.10
0.05
0.02
0.01
0.005
0.002
[O] wt %
10^{-6}
10^{-5}
10^{-4}
10^{-3}
10^{-2}
10^{-1}
1
[Al] wt %
A
B
C
E
1
2
3
4
5

2 • 1 • 9

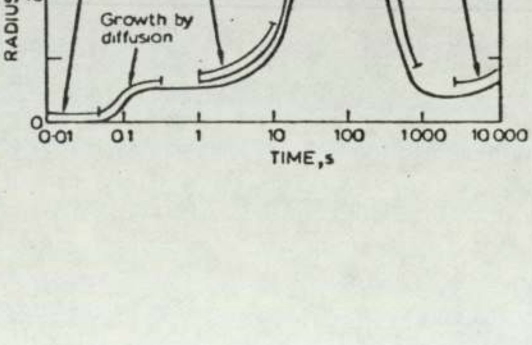
30
20
10
0
RADIUS OF PARTICLE, μ
0.01
0.1
1
10
100
1000
10 000
TIME, s
Nucleation
Growth by diffusion
Gradient collisions
Stokes collisions
Elimination of large particles
Coalescence by diffusion

In the case of aluminium - silicon simultaneous deoxidation, nucleation theory would predict the initial formation of alumina onto which silica would precipitate, (43.) a condition confirmed experimentally by Fröhberg and Pötschke (58.). On a commercial scale the introduction of foreign nuclei to promote hetrogeneous nucleation, and the addition of a high manganese containing deoxidant (to reduce the interfacial tension of the melt/oxide), have been advocated (59.) to increase the efficiency of deoxidation. The addition of a weak deoxidiser decreases supersaturation and promotes the formation of larger inclusions when a strong deoxidiser is added later. If the degree of local supersaturation in a melt is high a large number of small nuclei are formed, and if low only a few nuclei are formed, but these will grow. In order to attain low levels of local supersaturation, powdered deoxidants and low alloy concentrations in the ferro alloys may be used (43.).

2.1.4.3. Growth of nuclei.

A critical examination of the mechanisms of deoxidation product growth was made by Lindborg and Torssell (60.) who concluded the following:

(i) Precipitation and diffusional growth is completed within seconds and results in a narrow size distribution of about 2 μm radius.

(ii) Further growth to sizes 20 - 40 μm is due to collisions

(iii) Particles floated up in agreement with Stokes law

(iv) Separation of inclusions tends to take place in three stages for high inclusion concentrations. Namely an incubation period forming large inclusions, a period of rapid separation and finally a slow approach to equilibrium.

Their results are illustrated graphically in figure 2.1.9.

Turkdogan (61.) has shown using a theoretical analysis that the growth of oxide inclusions as they rise in the melt is influenced by the number of nuclei initially produced by deoxidation (fig. 2.1.10.). The larger the initial number of nuclei, the slower the rate of elimination. Turpin and Elliott (48.) also predicted that a strong deoxidant results in a large number of small inclusions because of the high degree of supersaturation. Weaker deoxidants resulted in fewer stable nuclei which grew into large products therefore aiding inclusion separation. In Turkdogans model when the number of initial particles (Z) was greater than $10^5 cm^{-3}$ inclusion growth was all but complete within 30 seconds. However for values less than $10^5 cm^{-3}$ the particles grew throughout their ascent to the surface. It was further pointed out that there was a critical number of nuclei to result in equilibrium oxygen values in steel. Above and below this value the oxygen was above the equilibrium level (fig. 2.1.11.)

Turkdogan has suggested that complexities of the nucleation, growth and flotation of inclusions may be due to variables which cannot be accounted for in a model system.

Gas evolution during deoxidation results in an increased

2.1.10

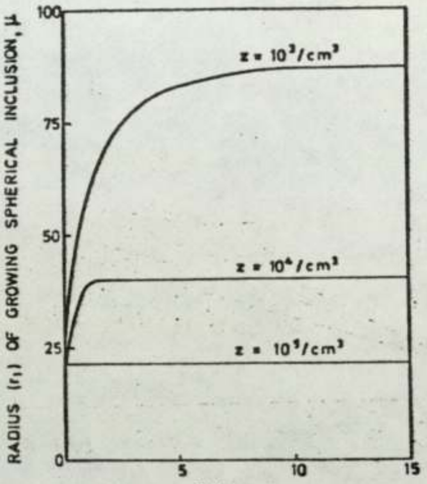

2.1.11

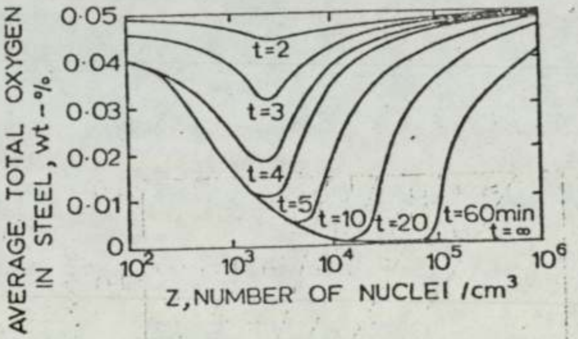

Calculated data on average total oxygen content of steel as functions of number of nuclei/cm^3 in stagnant liquid steel (even distribution is assumed) and holding time after deoxidizer additions - $[\%O]_0=0{\cdot}05$, $[\%O]_i=0$ and depth of liquid steel $l_0=2$ m (from ref. 25) rate of inclusion removal, due to the adhesion of gas bubbles onto deoxidation products aiding buoyancy. (A phenomenom made use of in the argon rinsing process (62.) although the surface properties of the inclusions will influence particle adhesion.)

Slag droplets may be occluded in the steel (16. 63.). These may react with deoxidant additions, or remove a large number of nuclei and growing inclusions, thereby prematurely ending deoxidation reactions.

Sluggish homogenisation of the added deoxidants (as outlined earlier), temperature drop in the ladle, convection currents and inclusion coagulation may all lead to complicating effects.

2.1.4.4. Elimination of inclusions.

The major objectives in deoxidation practice are seen to be to reduce the number of primary and secondary deoxidation products present in the ingot by reducing the oxygen level in the melt to a minimum. Secondly to eliminate the inclusions present in the melt so that they do not have an injuious effect upon the mechanical properties of the product. Although the thermodynamics and kinetics of the process play a major role in the first objective, inclusion elimination is governed principally by the physical properties of the inclusion and melt.

Early studies on inclusion elimination had been based upon Stokes law.

$$V = \frac{g D^2 \Delta\rho}{18\eta}$$

where V = rising velocity

D = inclusion diameter

g = gravitational constant

η = steel viscosity

$\Delta\rho$ = density difference between the oxide and the steel

This indicated the importance of inclusion size and density differences, and effective deoxidation had been based on these criteria (9.).

Early work by Herty and co-workers (64. 65.) showed the importance of size and composition on inclusion removal. They showed that the cleanest steel produced by manganese-silicon deoxidation occurred when the ratio of manganese to silicon was between 4 and 7, corresponding to the largest sizes of inclusions formed. The product composition was found to be in the low liquidus range of the MnO - FeO - SiO_2 diagram (fig 2.1. 12). at 35 - 45%SiO_2 45 - 55%MnO and approximately 10%FeO. This observation led to the conclusion that low melting point inclusions were advantageous. Their high level of fluidity allowed them to coalesce, thus increasing the particle size and improving buoyancy. This led to a more efficient elimination of particles from the melt.

Turkdogan (61.) showed that small inclusions did not readily float from a melt when a large number of nuclei were present. He suggested that the small inclusions attained a constant velocity within a short time due to the speed of the diffusion controlled reaction. This was contrasted with a small number of inclusions nuclei growing as they ascended the melt.

2 •1 • 12

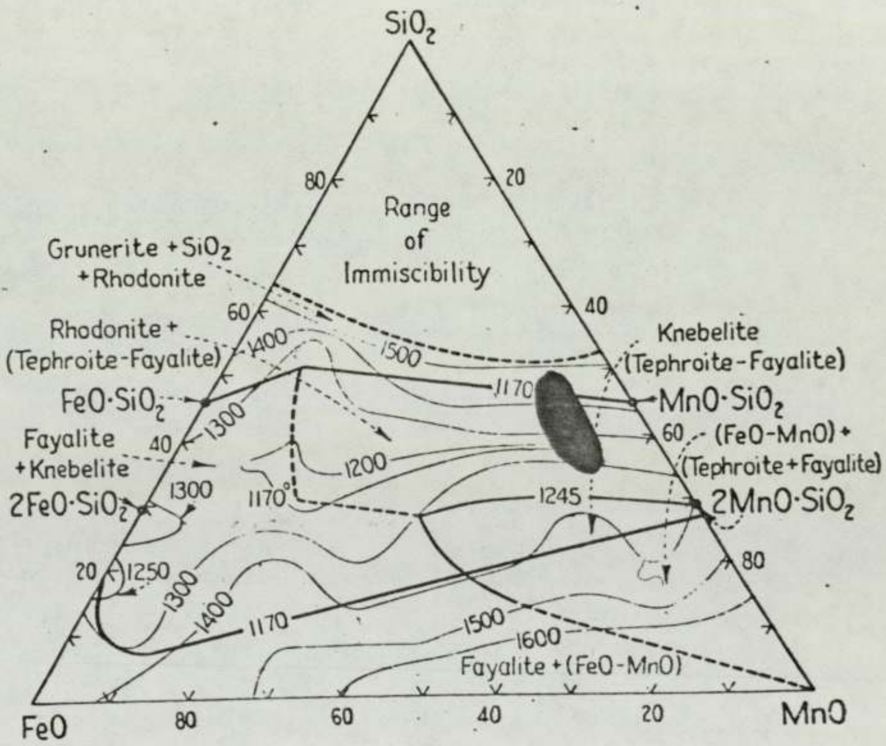
SiO$_2$
Range of Immiscibility
Grunerite + SiO$_2$ + Rhodonite
Rhodonite + (Tephroite-Fayalite)
FeO·SiO$_2$
Fayalite + Knebelite
2FeO·SiO$_2$
Knebelite (Tephroite-Fayalite)
MnO·SiO$_2$
(FeO-MnO) + (Tephroite + Fayalite)
2MnO·SiO$_2$
Fayalite + (FeO-MnO)
1500
1400
1170
1300
1200
1170
1300
1245
1250
1300
1400
1170
1500
1600
80
60
40
20
20
40
60
80
FeO
80
60
40
20
MnO

Later work by numerous workers (66,68) however, led to the conclusion that inclusion elimination was not governed by a simple law of hydrodynamics such as Stokes Law. Lindon and Billington (36.) examined the separation of inclusions within the $MnO-SiO_2-Al_2O_3$ system. They found that separation rate of the products increased with increasing Mn:Si and Al:Si ratios of the deoxidants used. Where low removal rates were observed silica rich inclusions were found to be present, coalescence of such inclusions being delayed due to the higher viscosity of silica rich products. They also found that fluid manganese aluminosilicates separated slower than anticipated by Stokes law. This was attributed to a low interfacial energy between melt and product.

Lindon and Billington (69.) also studied deoxidation by Ca-Si-Al and Mg-Si-Al alloys and compared their results with those for the Mn-Si-Al system (36.). They concluded that product separation rates increased as a result of increasing the melt/oxide interfacial energy, a confirmation of Plockinger and Wahlster's earlier work (70.) supporting the influence of surface properties upon inclusion removal. The work of Kozakevitch and Ollette (71.) has further demonstrated the importance of surface phenomenon upon inclusion coalescence and capture at the slag/metal interface.

In the review of Waudby(43.) he considered that an inclusion approaching the surface of the liquid metal may

(i) Remain just below the surface without escaping in which case the inclusion may be re-entrained into the metal by descending currents (the inclusion thoroughly wetted by the metal)

(ii) Escape and float on the melt surface (no wetting of the inclusion)

Waudby has also pointed out that inclusion emergence will occur if a reduction in surface free energy occurs.

$$\Delta G_s = \gamma_o - \gamma_m - \gamma_{om}$$

where γ is the surface energy, and the subscripts O, M and OM refer to the oxide, metal and oxide/metal respectively. Under practical steelmaking conditions ΔG_s is normally negative and thus promoting emergence. It must also be added that surface active impurity elements such as sulphur influence surface energy values, as does the oxygen content of the melt (fig.2.1.12)

Work (71) has also indicated that γ_{om} is dependent upon elements present in the iron as has been shown for alumina (table 2.1.1.).

In theory it is possible to calculate γ_{om} if γ_o and γ_m, and the contact angle (Θ) relating liquid metal on solid oxide can be measured from the equilibrium of surface forces.

i.e. $$\gamma_{om} = \gamma_o - \gamma_m \cos\Theta$$

However, in practice the measurement of contact angles is difficult and erroneous as had been pointed out by Segal (72). Contact angles have been determined by Kozakevitch and Olette (71) for several systems (table 2·1·2).

Effect of Sulfur on the Surface Tension of Liquid Iron at 1570°C (2858°F).

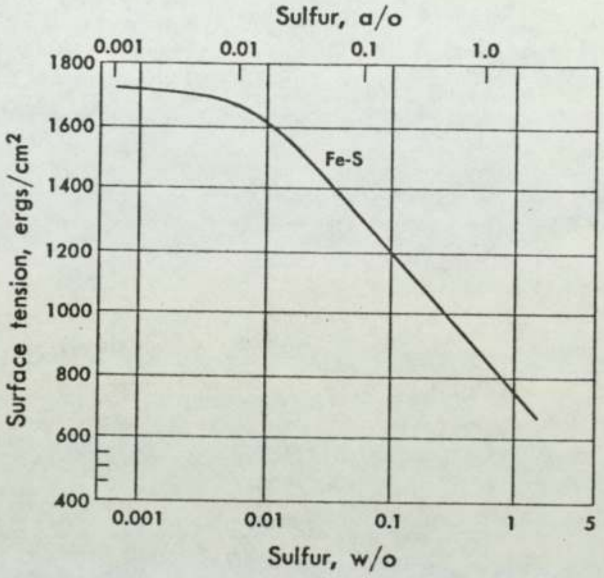

(i)

2.1.12 (a)

Effect of Oxygen on the Surface Tension of Liquid Iron at 1550°C (2822°F).

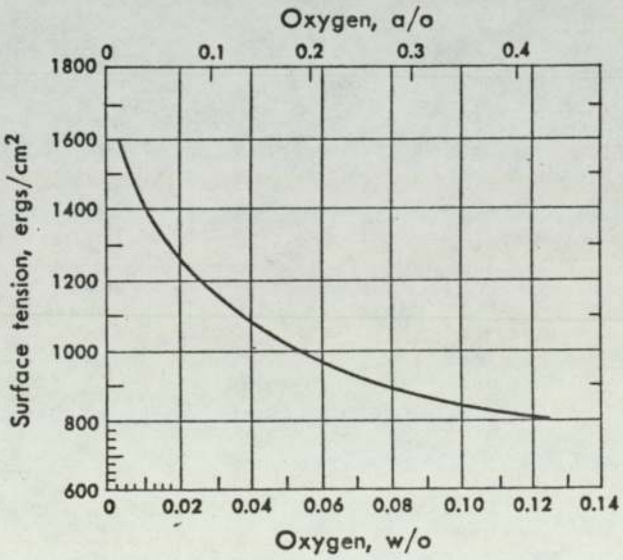

(ii)

Table 2.1.1. Values of $\Delta G = \gamma_s - \gamma_m = \gamma_m (\cos\theta - 1)$ obtained at 1600°C for Alumina (After Kozakevitch and Olette)

Melt Composition	$\theta°$	γ_m J/m^2 (erg/cm^2)	ΔG J/m^2 (erg/cm^2)	Estimates	
				γ_s J/m^2 (erg/cm^2)	γ_{sm} J/m^2 (erg/cm^2)
Pure iron	140	1.8 (1800)	-3.179 (-3179)	0.9 (900)	2.279 (2279)
Iron containing 4% C	133	1.73 (1730)	-2.91 (-2910)	0.9 (900)	2.08 (2080)
Iron containing 0.02% S	140	1.39 (1390)	-2.455 (-2455)	0.9 (900)	1.965 (1965)
Iron containing 0.07% O	80	1.1 (1100)	-0.909 (-909)	0.9 (900)	0.709 (709)

Table 2.1.2

Contact Angles (After Kozakevitch and Olette)

Solid oxide	Liquid metal	Gas	Contact angle θ°
Al_2O_3	Fe	Ar	141
Al_2O_3	Fe-4.5%C	Ar	133
Al_2O_3	Fe-5.1%Si	Ar	126
Al_2O_3	Fe-12.2%Mn	Ar	103
Al_2O_3	Fe	He	128
Al_2O_3	Fe-3.4%C	He	112
Al_2O_3	Fe-3.9%C	He	104
SiO_2	Fe	N_2	115
CaO	Fe	N_2	132
TiO_2	Fe	Vacuum	72
TiO_2	Fe	H_2	84
Cr_2O_3	Fe	Ar	88

Values of Θ greater than 90° indicate possible agglomeration whereas for Θ less than 90° its unlikely. However, for agglomeration of particles it is necessary that the two inclusion surfaces meet (promoted by turbulence). In the case where $\Theta > 90^\circ$ the liquid surrounding the point of contact will withdraw from the area, thus lowering the overall surface free energy.

A theoretical hydrodynamic approach (73) to deoxidation has shown the importance of melt turbulence in forming larger particles by coalescence and collision. It was pointed out that the rate of deoxidation increased as the amount of turbulence increased, and the separation of products was faster in stirred melts (an observation also made by Grevillius) (74.). Larger particles were found to be less affected by turbulence. It was also found that flow in the regions of the furnace wall may play an important role in inclusion removal, particularly in the case of small laboratory experiments.

Work by Ohkubo et al (75.76) provided a model to explain effects associated with turbulence and furnace lining on separation rate which had earlier been reported by Fischer and Wahlster (77.). Their experiments made in a high frequency furnace showed that oxide content of the steel could be expressed as

$$C_t = C_o e^{-kt}$$

where C_t = concentration of inclusions at a time t

C_o = maximum concentration when $t = o$

k = rate constant which is dependent upon the surface area to volume ratio of the melt.

This work however, does appear to assume that segregation of products by flotation, according to Stokes law is eliminated (9.). They proposed that inclusion removal in an agitated bath was by reaction between the particle and crucible material or perhaps by particle/ slag reaction in industrial situations.

In non turbulent quiescent bath conditions, Kawawa et al (78.) showed experimentally that an inclusion concentration - time relationship may be represented by

$$n = n_o e^{-A\gamma}$$

where n is the number of inclusions having a radius greater than γ. n_o and A are constants which may be determined experimentally. γ is an expression relating to the constants in Stokes law, the depth of the melt and time.

This relationship was for the situation where growth by coalescence did not occur. Lindon (9.) pointed out that coalescence would be expected to result in a smaller total number of inclusions (n_o). Also the number of large inclusions would increase leading to an increase in the slope of the $\ln n$ versus γ relationship. This increase $\frac{d \ln n}{d\gamma}$ was in fact observed by Lindon as time and, hence coalescence increased.

2.1.5. Formation of glassy and partially glassy deoxidation products.

The formation of glassy and partially glassy deoxidation products has been shown to be commonplace for many inclusion compositions in various oxide systems. Kiessling and Lange (79.) have indicated commonly observed inclusions of a glassy nature in the $MnO-SiO_2-Al_2O_3$ system used in the present work. It is therefore of interest to briefly review the underlying principles behind the formation of glassy type inclusions by reference to the formation of glasses in general. For a fuller account of glasses and glass formation reference is made to Seward (80.) and Rawson (81.).

The definition of a glass is that of a non-crystalline solid formed by cooling from a molten mass i.e. a macroscopically hard (rigid) amorphous substance. Since a glass has been regarded as a supercooled liquid it has been commonplace to use a viscosity criterion for solidity (82.). At temperatures below which the viscosity is greater than $10^{14.6}$ Poise (an arbitrary criterion) a glass is regarded as being metastable with respect to crystallisation.

Commercial glasses and some slag compositions have viscosities of the order 10^3 Poise at their liquidus temperatures (83.) indicating that kinetic factors are unfavourable for the formation of stable compounds. Information concerning the viscosity of glasses and slags may be plotted on phase diagrams. In binary systems an isoviscosity curve may be drawn for a specific viscosity (e.g. $10^{14.6}$ Poise) as illustrated in figure 2.1. 13, or in the case of ternary systems isoviscosity contours may be shown at temperatures of interest (figure 2.1. 14.).

2·1·13

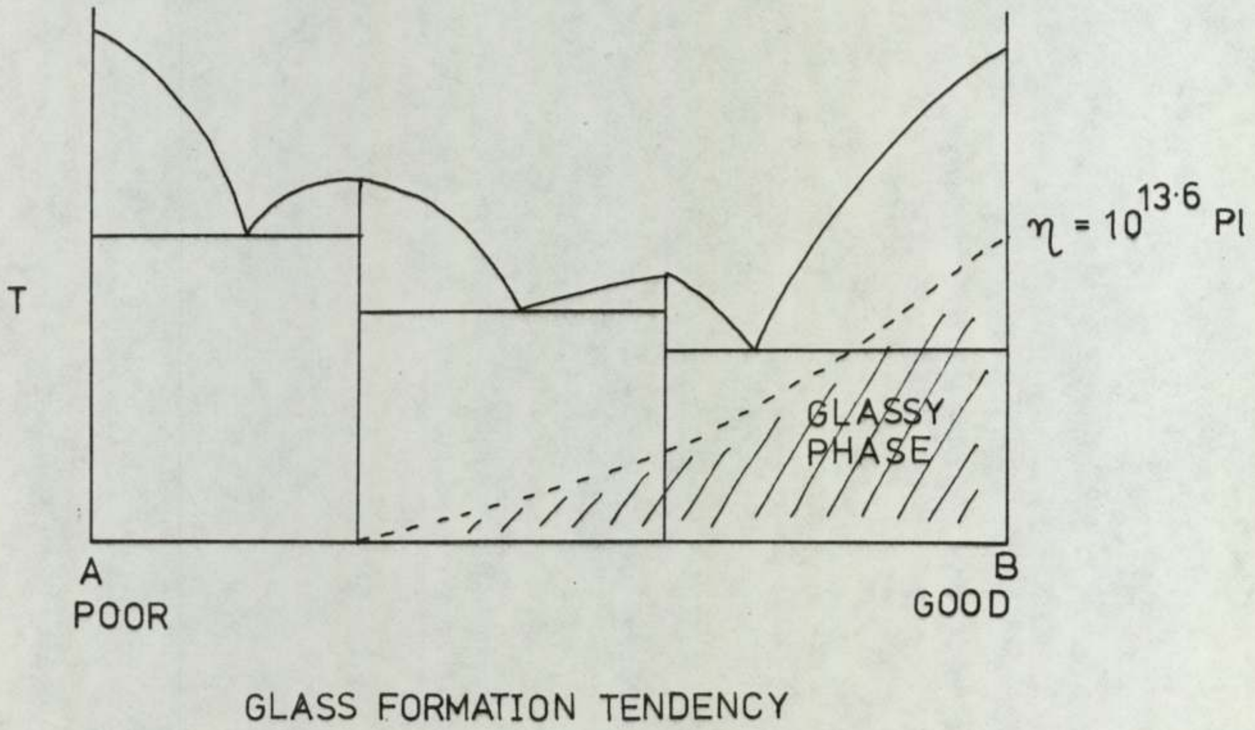
T
$\eta = 10^{13\cdot6}$ Pl
GLASSY PHASE
A
POOR
B
GOOD
GLASS FORMATION TENDENCY

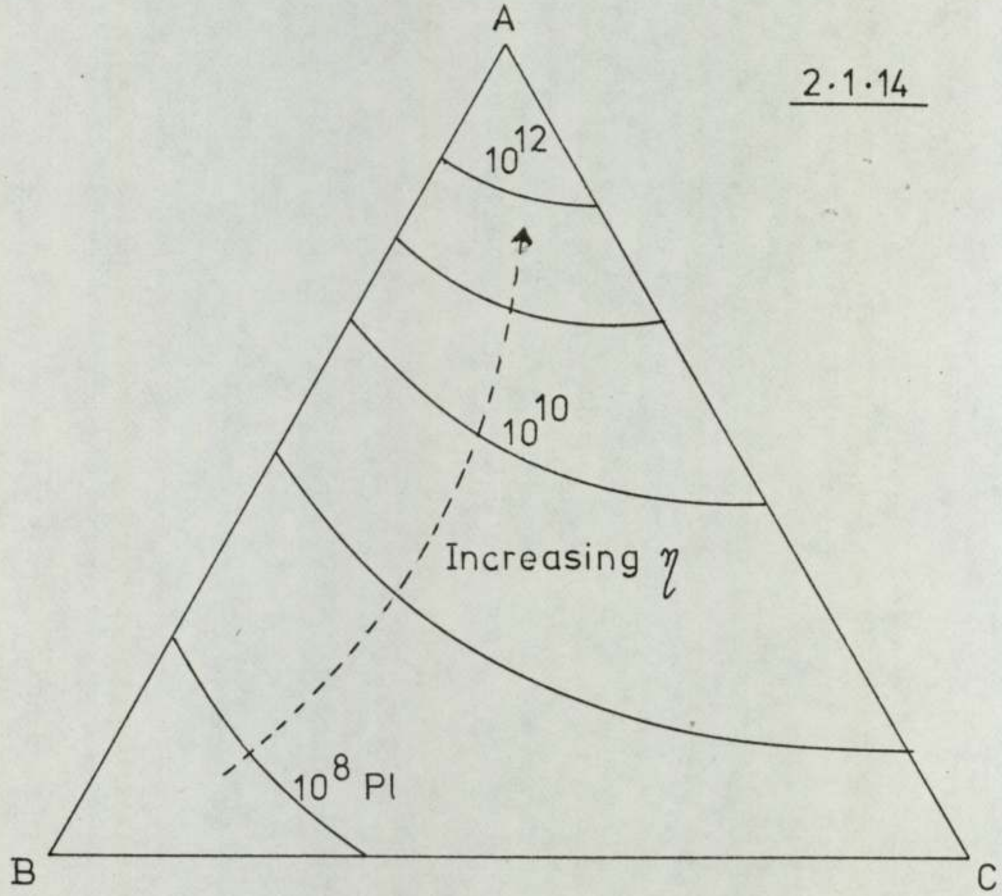

2.1.14

2.1.5.1. Phase separation and liquid immiscibility.

In some binary and multicomponent systems two liquid phases of different composition may exist in metastable equilibrium i.e. liquid immiscibility. The process by which the two phases separate from one homogeneous liquid is termed phase separation.

Liquid immiscibility is shown in some simple binary oxide systems e.g. ($MnO-SiO_2$), ($FeO-SiO_2$), ($Cr_2O_3-SiO_2$). As these liquids cool one or more glassy phases form. The silica rich phase usually forms a glass whereas the other phase(s) often crystallise.

It is possible in some systems (80.) that liquid immiscibility gaps occur below the liquidus but above the glass transition temperature, these gaps being known as metastable miscibility gaps. Glasses in these systems have often been found to consist of two submicroscopic phases (80.). On cooling through the miscibility gap the supercooled liquid separates until crystallisation occurs, or if the viscosity is sufficiently high another glass phase separates i.e. a solid is produced consisting of two glass phases.

Phase separation has been known to prevent good glass formation where it would be expected. This has been observed for the $SiO_2-Al_2O_3$ system (84.) where a $SiO_2-15\%Al_2O_3$ composition would be expected to form a good glass. However, it has been reported that phase separation may result in a dispersion of silica rich glass, and an alumina rich glass which easily crystallises.

Phase separation may be promoted by the presence of hetrogeneous catalysts e.g. sulphur.(80)

2.1.5.2. Volume - temperature relationships.

It has been well estabilished that glassy inclusions are often crystallised as a result of heat treatment and deformation processes (35,79). The crystallisation process involves a volume change, which is described by Rawson (81.) with reference to the volume-temperature diagram of Jones (85.) (figure 2.1.15). If the cooling rate of the liquid is slow and nuclei are present in the melt, crystallisation takes place and a volume change occurs i.e. line abcd, crystallisation taking place at T_f . However, rapid cooling rates give rise to supercooled liquids, and at the glass transition temperature a marked change in the volume-temperature curve takes place. Volume contraction follows the line of which is parallel to the line cd.

If the glass is reheated to a temperature T just below the transition temperature and held for a period of time volume contraction takes place reaching point g which is a continuation of the line abe. Above Tg however no volume contraction time dependence has been observed (81.).

2.1.5.3. Nucleation and growth of crystals in a glass.

With regard to nucleation and growth Rawson referred readers to a series of papers by Turnbull and Cohen (86-88).

2.1.15.

Glass - Volume V Temperature relationship.

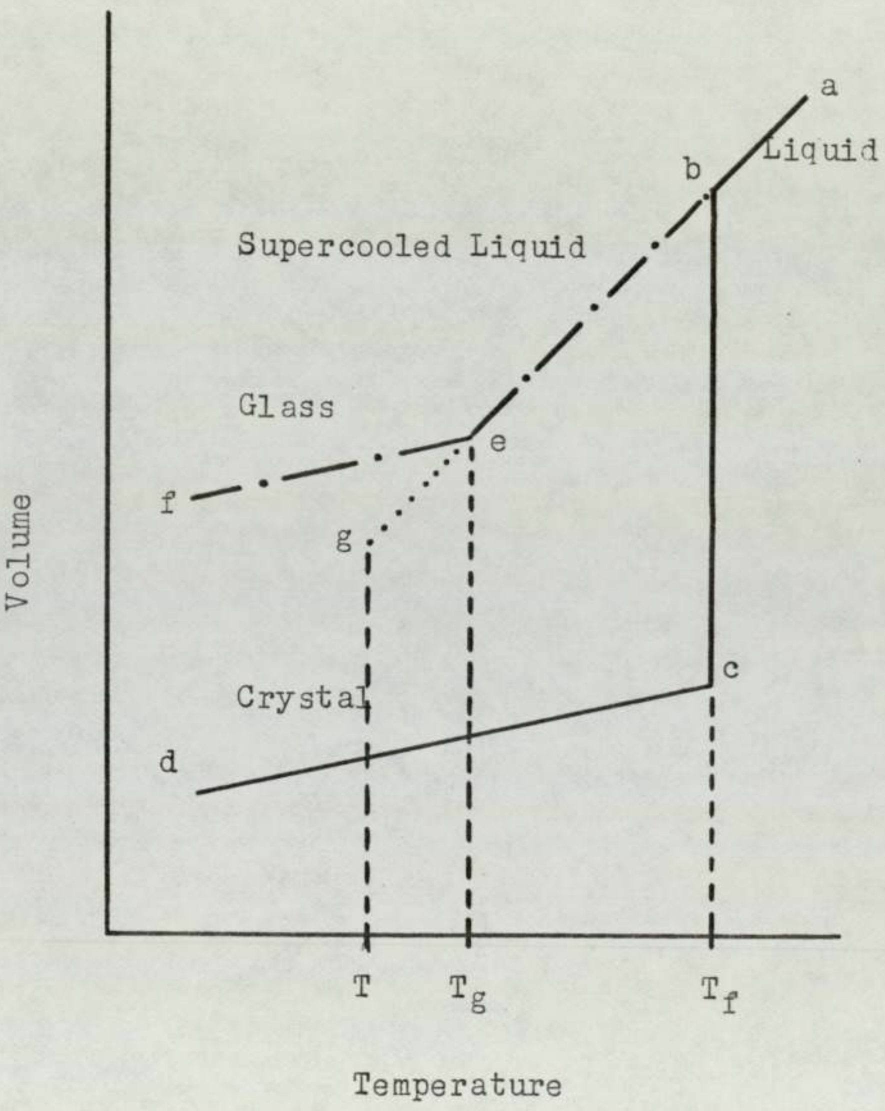

which discuss the thermodynamics of the process. However, a qualitative representation of nucleation and growth with respect to temperature is shown in figure 2.1.16. (after Macmillan (89)).

Isothermal devitrification curves for some glasses have been shown to follow a sigmoidal type of curve (81.) represented by the expression

$$V_t = V_o(1 - e^{-kt^n})$$

Where V_o is the volume of crystal phase when t=0 and n is an exponent between 1 and 4. k is a coefficient dependent upon nucleation frequency and crystallisation velocity,

However, the author has not been aware of similar work in respect of glass devitrification in the regions of the $MnO-SiO_2-Al_2O_3$ system of interest in this present study.

2.1.6. Constitution of non-metallic inclusions in steel.

The use of deoxidising elements, and the presence of oxyphillic elements in steel manufacture required the broad classification of inclusions previously given (section 2.1.2.). However, it is also important for the metallurgist to be aware of the constitution and morphology of the inclusion phases he is investigating. The following is a brief review of some of the inclusion phases encountered when working with the $(MnFe)O-Al_2O_3-SiO_2$ system. For a more detailed review reference is made to

2.1.16.

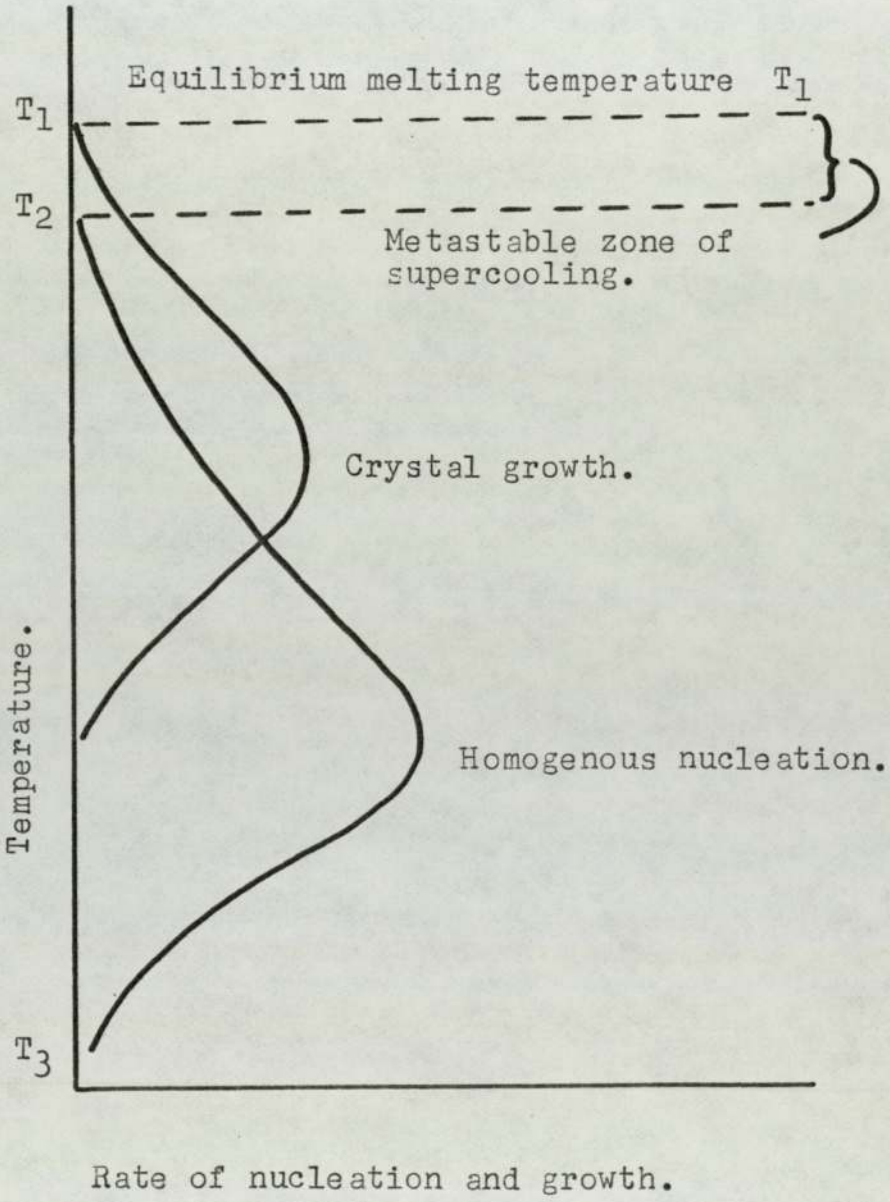
Equilibrium melting temperature T_1
T_1
T_2
Metastable zone of supercooling.
Crystal growth.
Homogenous nucleation.
Temperature.
T_3
Rate of nucleation and growth.

the reviews of Pickering (90.) and Kiessling and Lange (79.91.). The physical properties of oxides are summarised in table 2.1.3. which is compiled from reference (79.).

I. Alumina Al_2O_3 —

Alumina is the most common elemental oxide found in commercial steelmaking and it is usually in the form of corundum (α-Al_2O_3). When formed as a result of deoxidisation it is generally observed as globular clusters or dendrites and because of its high melting point it is in its primary crystallisation mode (90.). The appearance of either dendritic or globular morphologies is dependent upon the degree of alumina supersaturation and the free oxygen content of the melt. At high supersaturation the presence of a few nuclei gives rise to dendritic growth and forms a skeletal network which has been observed by numerous workers (35. 90.92). With low supersaturation and high oxygen contents globular clusters are encountered. This morphology is achieved via a proposed mixed oxide route in which liquid (FeMnAl) oxides are nucleated in preference to Al_2O_3 (90.). The Al in the melt subsequently reduces the (FeMn)O and thus retaining the original spherical inclusion character.

II. Silica SiO_2 —

Several modifications of silica are known (91.) namely quartz, tridymite and cristobalite. Pure silica is very rarely found in steels and is usually associated

Table 2.1. 3 Physical properties of phases encountered in the (MnFe)O-SiO_2-Al_2O_3 system

Name	Chemical Formulae	M.pt (°C)	hardness (Kp/mm^2)	density (Mg/m^3)
Cor~~r~~undum	Al_2O_3	2050	3000-4500	3.96
Cristobalite	SiO_2	1723	C 1600	2.23-2.38
Tridymite	SiO_2	1670	"	2.26-2.30
Quartz	SiO_2	1760	"	2.52-2.65
Manganosite	MnO	1850	400	5.37
Wustite	FeO	1370		5.76
Galaxite	$MnO.Al_2O_3$	1560▽	1500-1700	4.23
Hercynite	$FeO.Al_2O_3$	1780		4.05
Mullite	$3Al_2O_3.2SiO_2$	1850	1500	3.16
Rhodonite	$MnO.SiO_2$	1291■	750	3.72
Tephroite.	$2MnO.SiO_2$	1345	950	4.04
Fayalite	$2FeO.SiO_2$	1205▼		4.32
Spessartite	$3MnO.Al_2O_3.2SiO_2$	1195	1000-1100	4.80
Iron Sulphide	FeS	1190		4.77
Manganese sulphide	MnS	1610		3.99

▽ disintegrates

■ forms liquid + tridymite

▼ incongruent melting point

(taken from Kiessling & Lange. ISI Pub. vol. I andII) with mixed oxide phases, which form glasses. Quartz has been infrequently observed as dark regular plates in polished sections (91.), usually resulting from exogeneous sources (90.). Tridymite however has been observed in exogeneous (91.) and in highly siliceous deoxidation products (90.) in which it appears as thin dark plates or laths in microsection.

Cristobalite has often been reported (91.) as rosettes or dendrites in glassy or semi-crystallised silicate matrices viewed in microsection. It has, however, been reported (93.) that these phases are not crystalline but are nearly pure glassy silica resulting from liquid immiscibility.

III. Iron - Manganese oxides (FeMn)O.

Iron oxide (Wustite) and manganese oxide form a continuous series of solid solutions and hence are treated as one inclusion type. They precipitate from oxygen rich melts as liquid globules within the miscibility gap of the Fe-Mn-O system (figure 2.1.17.). They may form as large primary deoxidation products, or as a fine dispersion of secondary products. Although the occurrence of (FeMn)O precipitates is as single phase spherical globules, pure MnO occurs as a translucent idiomorphic or dendritic phase, (94.) because of its high melting point of 1850°C. The (FeMn) oxides have been reported as being two phase in character (94.) although this was attributed to the cooling cycle of the

2·1·17

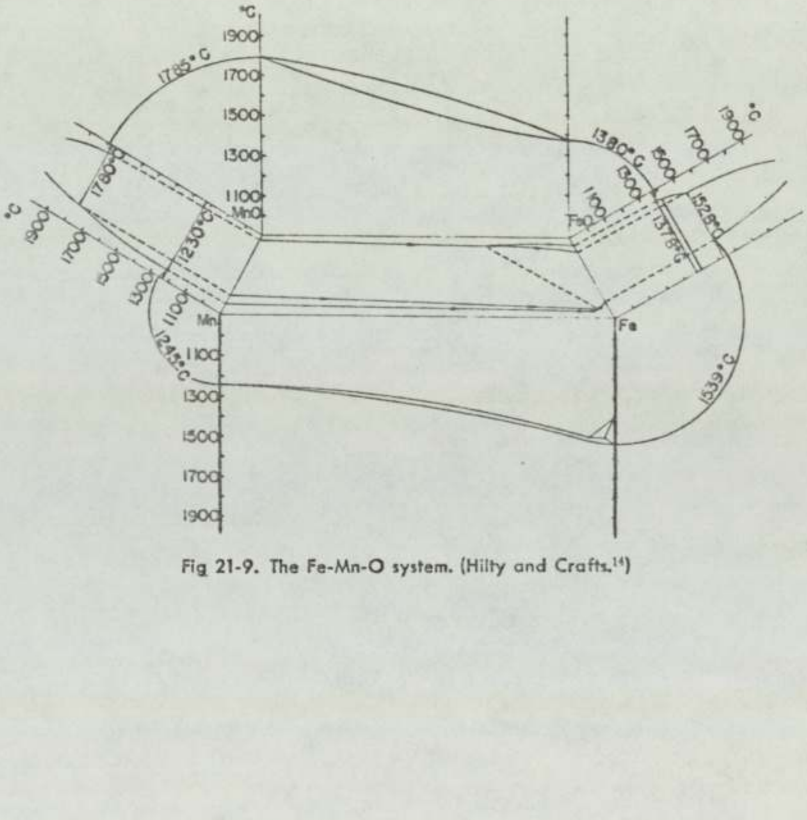

Fig 21-9. The Fe-Mn-O system. (Hilty and Crafts.[14])

steel. Fisher and Fleischer (95.) stated that (FeMn)O inclusions often were not in equilibrium with the steel and are FeO rich when precipitated but increase in Mn content if the cooling time is long. Kiessling and Lange (91.) have also stated that their composition may change upon heat treatment.

IV. Silicates.

Although silicates are often highly complex in commercial steelmaking this brief review is confined to the system (FeMn)O - SiO_2 - Al_2O_3.

(i) (FeMn)O - SiO_2

Iron manganese silicate inclusions commonly found in silicon deoxidised steels are glassy and/or crystalline. Depending upon the oxygen content, amount of silicon addition and cooling rate a number of phases or mixtures of phases are possible within the MnO-FeO-SiO_2 system (figure 2.1.12).

High silicon levels promote fayalite or tephroite whereas low levels promote mangowüstite (FeMn)O inclusions. Rhodonite (MnO.SiO_2) rarely occurs and Grunerite (FeOSiO_2) has not been found to occur (90.) in commercial practice.

In cases of fast cooling the tendency is to form glassy type inclusions, however, heat treatment and hot working may promote precipitation and crystallisation (91.). High silicon levels however promote glass stability, and liquid immiscibility often leads to the formation of duplex glasses (35.).

(ii) $(FeMn)O - SiO_2 - Al_2O_3$

In the majority of cases of inclusions in the $(FeMn)O - SiO_2 - Al_2O_3$ system it is usual to find precipitates within manganese alumino silicate glasses rather than the phases existing in isolation. It is normal to find the manganese rich phase due to the greater stability of MnO relative to FeO. However, it is usual to find some iron present within the inclusions. (91).

The appearance of precipitates within inclusions observed on microsection (described by Kiessling and Lange (91)) are summarised below.

Galaxite : Grey phase irregular in shape, sometimes of clover leaf appearance.

Mullite : Usually found as rhombic or rhombohedral crystals often with a glassy residue at their centres. Mullite may also be found as a very fine grained precipitate.

Rhodonite : This is one of the most common phases present in inclusions. Single phase rhodonite inclusions (sometimes glassy and spherical) are often mistaken for pure silica. At high silicon contents silica often precipitates resulting in a more or less crystallised rhodonite matrix. In multiphase inclusions rhodonite often forms bright laths which form a dense structure if near the composition of rhodonite.

Tephroite : Tephroite has a solubility for up to 15% Al_2O_3 and has a range of composition 65 - 73 at %MnO. It often forms banded structures in multiphase inclusions. Tephroite and spessartite are often confused since they have similar crystallisation patterns.

Spessartite : This forms feather like branched sections usually observed in hot worked or slow cooled steels. It does appear to have variable composition i.e. MnO (31 - 49wt%) SiO_2 (30-47%), Al_2O_3 (13 - 24%)

V . Spinels.

Spinels are fairly common phases observed in steels. They all have the $RO.B_2O_3$ double oxide structures which show extended homogeneity ranges (91.). Within the Fe-Mn-Al-Si-O system the spinels hercynite ($FeO.Al_2O_3$) and Galaxite ($MnO.Al_2O_3$) are often seen as small spherical clusters (90.), Although they are usually found as precipitates within siliceous inclusions Hercynite is very rarely found in manganese containing steels where Galaxite is promoted, although MnO is substituted in part by FeO.

Kiessling and Lange (91.) who extensively reviewed data on inclusions of the MnO - SiO_2 - Al_2O_3 system (figure 2.1.18) concluded that the mean compositions of MnO - SiO_2- Al_2O_3 inclusions were situated within the

2.1.18

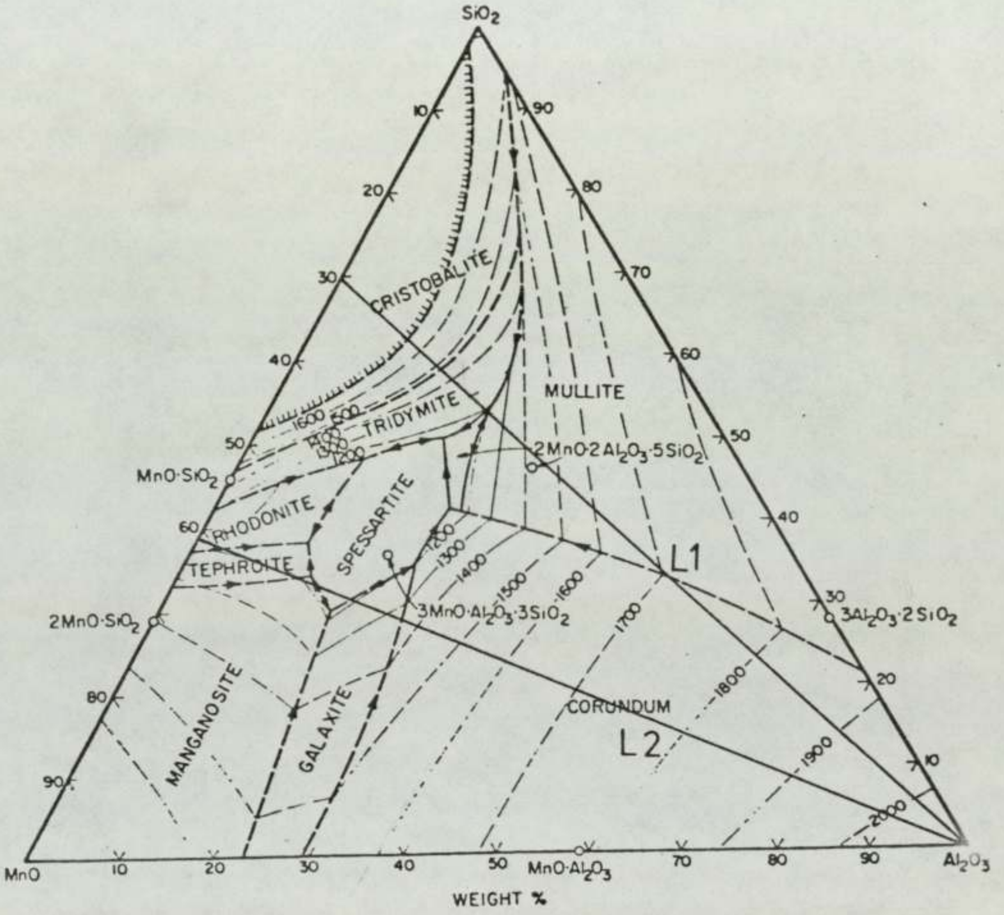
SiO₂
10
20
30
40
50
60
80
90
90
80
70
60
50
40
30
20
10
MnO
10
20
30
40
50
MnO·Al₂O₃
70
80
90
Al₂O₃
WEIGHT %
CRISTOBALITE
TRIDYMITE
MULLITE
RHODONITE
TEPHROITE
SPESSARTITE
MANGANOSITE
GALAXITE
CORUNDUM
MnO·SiO₂
2MnO·SiO₂
2MnO·2Al₂O₃·5SiO₂
3MnO·Al₂O₃·3SiO₂
3Al₂O₃·2SiO₂
L1
L2
1600
1500
1400
1300
1200
1200
1300
1400
1500
1600
1700
1800
1900
2000

regions shown by the lines of L1 and L2 in figure 2.1.18 .

VI . Sulphides.

Although in the course of this work the level of sulphur was approximately 0.005 wt% compared with about 0.015% in commercial practice, a very brief review of sulphides is worth including.

Sulphur is soluble in liquid iron and steel, but in the solid state its solubility is very low. In a pure Fe - S melt precipitates of FeS form either as primary dendrites, or as a eutectic with iron (Eutectic Temp 988°C). In the presence of oxygen the eutectic is lowered to about 940°C (i.e. FeO - FeS eutectic). The presence of these low melting point phases at grain boundaries gives rise to the phenomenon of hot shortness.

In order to avoid the formation of FeS, manganese is added which increases the melting point of the eutectics (FeO-MnO-MnS-FeS) above the normal hot working temperatures due to the greater stability of MnS compared to FeS. The form of MnS in cast steels is however dependent upon the degree of deoxidation of the melt. These morphologies were classified by Simms and Dahle (96.) as types I, II and III.

Type I.

In steel melts containing greater than 0.02wt% of dissolved oxygen a globular morphology is observed with a wide size distribution. Duplex inclusions often observed (97.) with oxygen compounds, and the duplex MnS - silicate may vary in appearance depending upon the S:O ratio. Type I morphologies are often found in rimmed steels (97.), where silicon is the main deoxidant.

Type II.

In steel melts in which the dissolved oxygen content is less than 0.01wt% the sulphide has a fan like dendritic structure (often termed grain boundary sulphide). This consists of interconnected rods in a skeletal structure in primary grain boundaries. This type of morphology is found in aluminium deoxidised steels without an excess of aluminium.

Type III.

As with type II inclusions type III require low oxygen contents, however other elements are also necessary (97.). Carbon appears to promote the type III (90.) morphology as does silicon aluminium and phosphorus (97.). Type III is irregular in shape and randomly distributed in the steel, often similar to type I in appearance. Type III is frequently encountered in steels deoxidised with excess aluminium, and forms monophase inclusions.

Other sulphide phases.

Because of the f.c.c. structure of MnS, Mn may be replaced by other soluble elements. These and many other sulphide phases have been reviewed by Pickering (90.) and Kiessling and Lange (91.), but it is not proposed to review them because they are not relevant to the present work.

INCLUSION DEFORMATION

2.2.1. Introduction.

In all working operations there is material flow, the direction of which is dependent upon the working process. Thus, in the case of a material containing a dispersed second phase the matrix dictates the movements of the second phase in the direction of matrix flow. The magnitude and state of stresses and strains present during deformation will influence the behaviour of the second phase particles, although the physical properties of the particles and the interdependence of particle/matrix properties govern their exact behaviour.

In the case of non metallic inclusions in steels being worked they may behave in a non deformable, brittle, plastic or fluid manner. In the case of the brittle plastic and fluid inclusions there is a tendency for them to string out in the directions of imposed flow whether they remain intact or disseminated. In the case of plastic and fluid inclusions their degree of deformation may be related to the deformation of the matrix, which is not possible in the case of brittle inclusions. Hence there is the possibility of relating the plasticity of an inclusion to that of the matrix in which it is embedded.

2.2.2.

Concept of a plasticity index.

From experimental work prior to 1950 it was known that the deformation of non metallic inclusions was influenced by their shape, size, number and distribution within the steel. Although quantitative work had been performed on the deformation of second phases in the non-ferrous field, (98.) it was not until the work Scheil and Schnell (99.) that any real quantitative work was performed on the deformation of inclusions within steel.

Their work involved the deformation of inclusions within cylindrical steel specimens deformed in a press. They observed the deformation of inclusions in microsections parallel to the direction of upsetting. Assuming that the as cast spherical inclusions deformed into oblate spheroids, which in microsection would be observed as ellipses, they measured the aspect ratio of such deformed inclusions as a measure of inclusion strain. As a measure of matrix deformation they used the diameter to thickness ratio of the deformed specimen.

The later work of Pickering (100.) was concerned with the measurement of inclusion deformation in rolled bars. Inclusion strain was measured from microsections parallel to the rolling direction. As with Scheil and Schnell, Pickering used the inclusion aspect ratios as a measure of inclusion strain. These aspect ratios were compared to the reduction in cross sectional area of the original ingot which was given by:

$$\left(\frac{a}{b}\right)_{\text{steel}} = \left(\frac{A_o}{A_f}\right)^{3/2}$$

where A_o and A_f are the original and final cross sectional area respectively.

The comparison of inclusion aspect ratio with the a/b ratio of the steel indicated that for a value greater than unity the inclusion was more deformable than the steel, less than unity the inclusion was less deformable than the steel.

Following the approach of Pickering, Malkiewicz and Rudnik (101.) defined a deformability index ν which related the true strain of an inclusion (ε_i) to the matrix true strain (ε_m)

i.e.

$$\nu = \frac{\varepsilon_i}{\varepsilon_m}$$

They showed that for bar rolling the deformability index could be represented by

$$\nu = \frac{2}{3}\frac{\ln\lambda}{\ln H}$$

where λ is the inclusion aspect ratio, and H is the initial to final cross sectional area of the bar.

They used $\ln\lambda$ when measuring deformability index in order to obtain a Gaussian (normal) distribution which aided statistical analysis, rather than λ which gave rise to skew distributions.

In later work Maunder and Charles[92] used a modification of the formula used by Malkiewicz and Rudnik in order to take account of the deformation in strip rolling. Their modified formula which has been used by other workers (35. 102. 103.) relates plasticity index to plane strain conditions.

i.e.

$$\nu = \frac{1}{2}\cdot\frac{\ln\lambda}{\ln H}$$

However, matrix strain had not been measured in the same way in all experimental work. Maunder and Charles defined (H) as the ratio of cross sectional area, whereas Ekerot (102) used (H) to signify the ratio of initial to final height in plane strain compression. Although these values will be the same in the treatment of idealised plane strain, in practice problems may arise due to the non homogeneous deformation of the matrix. Recently Robinson (35) has introduced the use of a 'true relative plasticity index' term based upon the observations that plasticity index decreases as the matrix strain increases. (i.e. inclusion strain is not linearly proportional to matrix strain).

Considering a schematic inclusion versus matrix strain diagram e.g. figure 2.2.1. , Robinson defined the plasticity indices as:

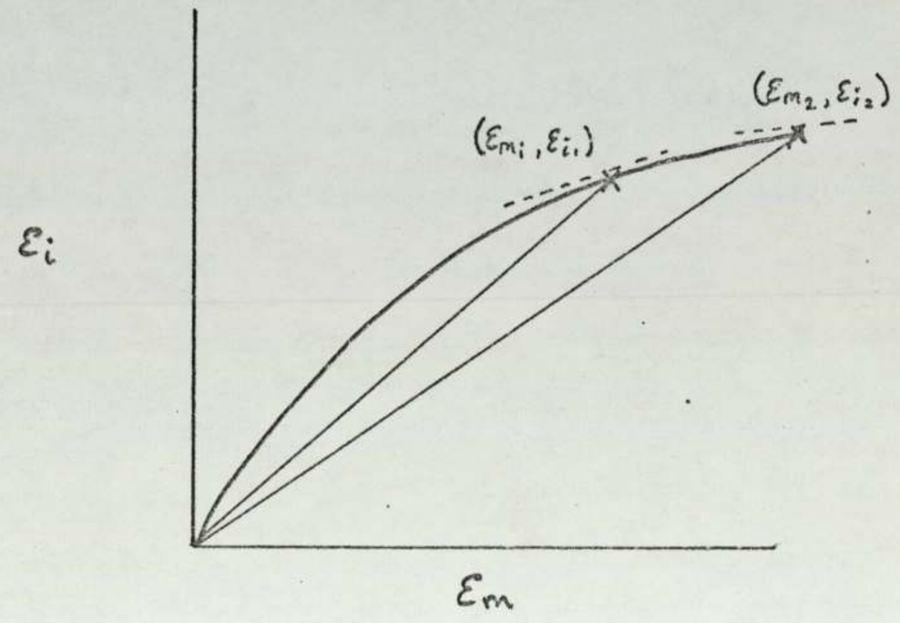

Apparent relative plasticity index (ν_A) (normally referred to as the inclusion plasticity index)

ν_A is the gradient of the chord from the origin to the point ($\varepsilon m, \varepsilon i$) at any value of εm

i.e.

$$\nu_A = \left| \varepsilon_i / \varepsilon_m \right|_{\varepsilon_m}$$

From figure 2.2.1 it is clear that even if an inclusion ceases to deform it still has an apparent relative plasticity.

True relative plasticity index (ν_T)

Robinson has also defined the tangent to the inclusion - matrix strain curve at any given point as the true relative plasticity index ν_T, which will have a value of zero when the inclusions cease to deform .

$$\nu_T = \left| \frac{d\varepsilon_i}{d\varepsilon_m} \right|_{\varepsilon_m}$$

He also pointed out that unless the relative plasticity indices are qualified by the matrix strain at measurement, the resultant indices are of little use. Schematically the variation of inclusion relative plasticity indices with matrix strain are shown in figure 2.2.2.

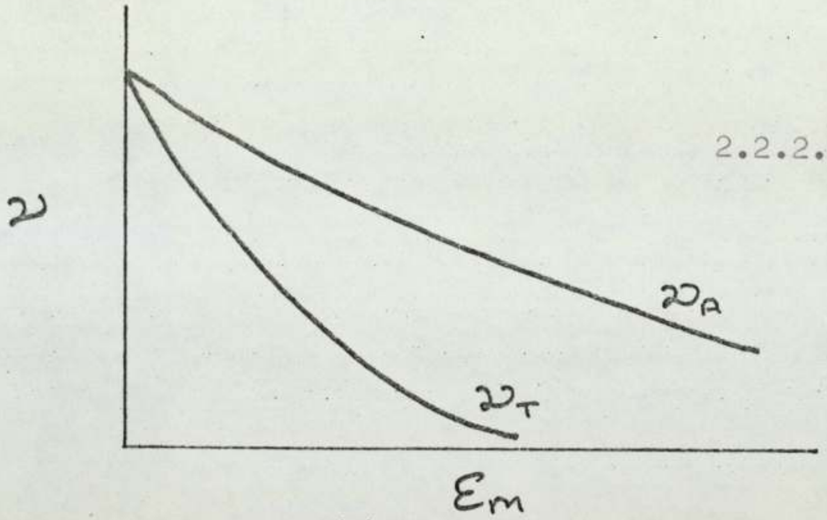

2.2.2.

which indicates that ν_T decreases w. r. t. ε_m at a greater rate than ν_A. He further emphasised that as

$\varepsilon_m \Rightarrow 0 \quad \nu_T \Rightarrow \nu_A$, and at the ordinate axis when

$\varepsilon_m = 0 \quad \nu_T = \nu_A$,

i.e.

$$\left| \frac{\varepsilon_i}{\varepsilon_m} \right|_{\varepsilon_m = 0} = \left| \frac{d\varepsilon_i}{d\varepsilon_m} \right|_{\varepsilon_m = 0}$$

Robinson suggested that the value of ν at $\varepsilon_m = 0$ was the INTRINSIC VALUE OF RELATIVE PLASTICITY (ν_i) INDEX which should be employed when comparing the relative plasticities of different types of inclusions.

2.2.3.
Measurement of inclusion plasticity.

The determination of inclusion relative plasticity index is dependent upon the measurement of inclusion strain and the confidence which may be placed on the results obtained is dependent upon the accuracy of measurement. The approach to inclusion measurement is either to measure a few inclusions accurately or to measure a large number of inclusions with less accuracy.

The traditional method of measuring inclusion strain is by the measurement of individual inclusion aspect ratios. This method, although simple and reasonably accurate, has the disadvantages of being tedious, time consuming and subject to operator bias unless random selection techniques are used. (104.) It does, however, have the advantages that inclusions with slight deviation from the plane of measurement can still be measured, also the operator has the ability to observe whether inclusions are brittle, plastic, fluid or contain precipitates.

The alternative to manual counting and measurement techniques is to use quantitative television microscopes in which the electronic image is analysed by computer circuitry. Instruments using this principle such as the Metals Research 'Quantimet' have been used for inclusion assessment (105) and the basic modes of operation have been reviewed by Baker (106). Automatic quantitative image analysing techniques have difficulty in measuring the traditional inclusion aspect ratios, and it has led to the use of the concept of projected length in the assessment of inclusion strain.

Baker and Charles (107) have shown that inclusion true strain may be quantified using the concept of projected length by the expression

$$\varepsilon_i = \ln\left(\frac{P}{P_o}\right)$$

where P_o and P are the projected lengths per unit aréa for the 'as cast' and deformed condition respectively.

The plasticity index has therefore been represented by:

$$\nu = \frac{\log P - \log P_o}{\log H}$$

Although the aspect ratio is not measured, it may be obtained from the square of the ratio of deformed and 'as cast' projected lengths (108) i.e.

$$\lambda = \left(\frac{P}{P_o}\right)^2$$

The validity of inclusion plasticity by this technique is dependent upon there being a constant volume fraction of inclusions. Although this is not the case this error can be corrected for by area (and hence) volume measurement (107).

Gladman (108) has shown that projected length may be measured without the need for electronic systems. Assuming a random distribution of monosized spheres, the projected inclusion length per unit area is numerically equal to the number of inclusions per unit length intersected by a line perpendicular to the plane of projection. The use of such a technique is, however, suspect due to the assumption of uniform sizes particles.

2.2.4 Factors influencing the inclusion plasticity index.

Early investigations into the deformation behaviour of non-metallic inclusions was were carried out by Scheil and Schnell, who reported that manganese sulphide inclusions had the ability to deform as much as the steel matrix during the forging process.

Observations on oxide, and sulphide inclusions, deformed over a range of temperatures indicated that there was a difference in the deformation behaviour for the two types of inclusions. Typical results/relationships are indicated in figure 2.2.3 .

The studies of Malkiewicz and Rudnik (101.) concentrated on steels (deoxidised by manganese-silicon and ferrosilicon plus ferromanganese) which were subsequently hot rolled. They observed that the deformation behaviour of the non-metallic inclusions was influenced by such parameters as: Rolling temperature Composition, Inclusion size and the degree of matrix deformation.

The effects of these parameters may be observed with reference to figures 2.2.3 & 2.2.4.

Van Vlack (104), in his investigations of inclusion behaviour during the rolling of resulphurised steels, also reported that inclusion shape and size were factors which must be taken into account when considering inclusion deformability. He also added that the length, to width ratio of MnS inclusions was an important guide to the machinability of such steels.

2.2.3.

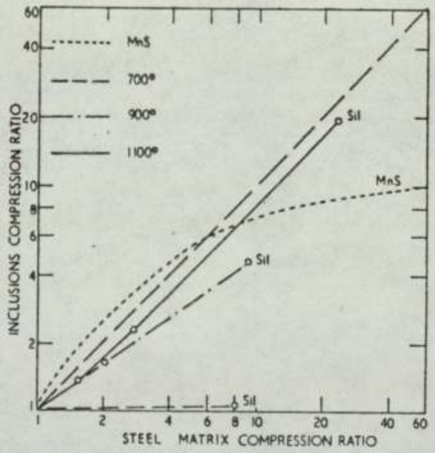

The oxide inclusions (Fe–Mn–silicates with unknown composition) are undeformed at lower compression temperatures, but their deformation behaviour becomes more similar to that of the steel with increasing temperature, independently of the compression ratio for the steel phase. The sulphide inclusions (MnS) deform in a manner similar to the steel matrix at all temperatures for lower compression ratios, but for compression ratios higher than about 6 the sulphide inclusions deform less than the steel matrix. This difference increases with increasing compression ratio for the steel and should be compared with the results from rolling. Fig. 212. From ref.214

210 Compression ratios for oxide and sulphide inclusions v. compression ratio for the steel matrix at different temperatures

2.24

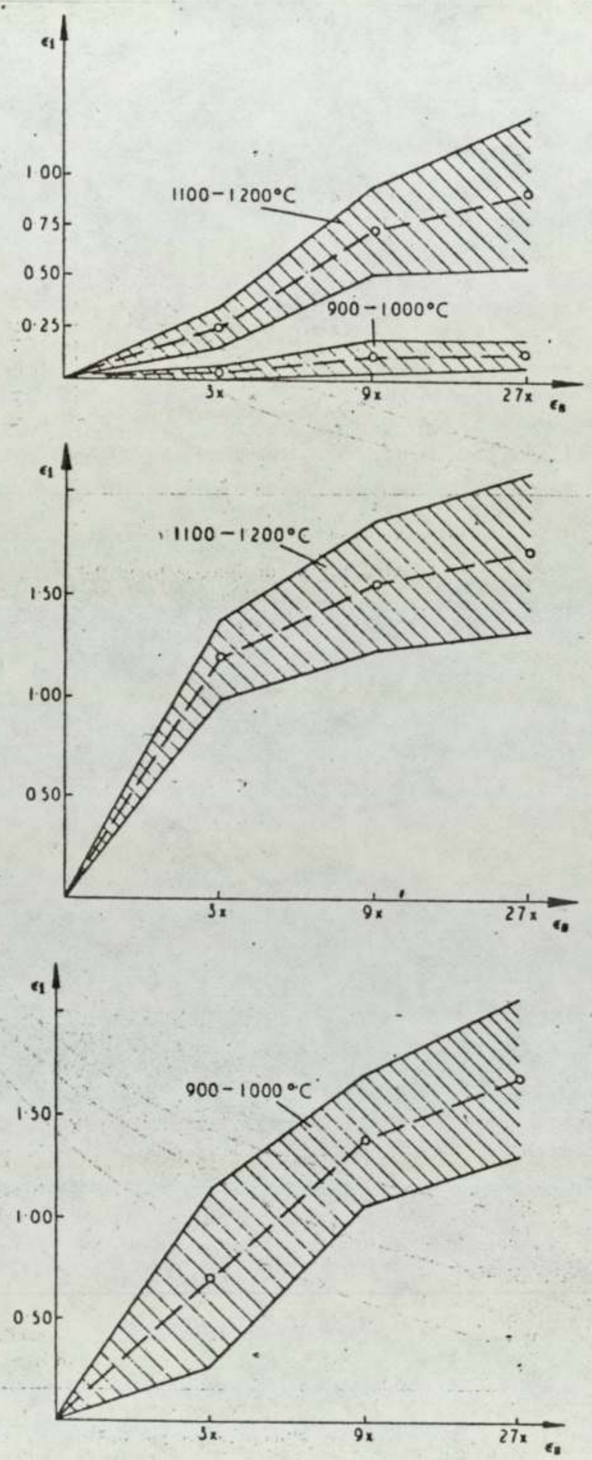

a ingot no.1 *b, c* ingot no.2
Inclusion deformation v. *steel deformation*

(a) Fe - Si Deoxidised

(b,c) Mn - Si Deoxidised

The work of Pickering (100) showed that siliceous inclusions deformed during rolling at high temperatures, but at lower temperatures they had the tendency to fracture with little or no deformation. Maunder and Charles (92.) showed that there was a sharp transition in the behaviour of silicate inclusions, from brittle to fluid, over a narrow range of temperature. They also reported that not only was deformation behaviour dependent upon size and composition, but also upon whether or not the matrix was austenitic or ferritic at the rolling temperature.

Later work by Gove and Charles (109.), and other workers (110.–114) has shown that the relative flow stresses of inclusion and matrix phases are an important factor to consider with respect to inclusion deformation.

From the above survey it is apparent that numerous factors influence the behaviour of non-metallic inclusions during hot working, and these are considered in more detail below.

2.2.4.1. The influence of inclusion and matrix strengths.

The influence of inclusion and matrix strengths upon inclusion plasticity have been well reported. However, there are various relationships reported between inclusion plasticity and the ratio of inclusion to matrix strengths.

Early work by Unkle (98.) in the non ferrous field showed the importance of relative flow stresses. In his work on the behaviour of two phase alloys during cold rolling, Unkle reported that the deformation of a second phase particle could result to a limited extent even if the ratio of inclusions to matrix flow stresses was as high as six.

Warrick and Van Vlack (110.) have also investigated the influence of relative strengths upon the degree of deformation of second phase particles during extrusion. Using ionic solids (i.e. KCl, NaCl, NaF and Lif) embedded in face centred cubic matrices (i.e. Pb, Al, Ag, Cu and '65 - 35 brass') they established a length to width ratio for the inclusions for various ratios of matrix and inclusion hardness. (fig.2.2.5.).

Zeisloft and Hosford (112.) investigated the relationship between inclusion and matrix strains using cylindrical rods in rectangular blocks, and spheres in cylinders. The matrix phase they used was Woods metal or lead. The inclusion phases were however of various materials which gave them the possibility of investigating second phase deformation at various matrix - inclusion strength ratios.

Their results obtained from compressive plane strain testing indicated, as with other workers, that the amount of inclusion deformation relative to that of the matrix (i.e. the plasticity index) decreased as the ratio of inclusion to matrix strength increased. Taking measurements of plasticity index from the linear regions of the inclusion strain/matrix strain curves they found that a maximum

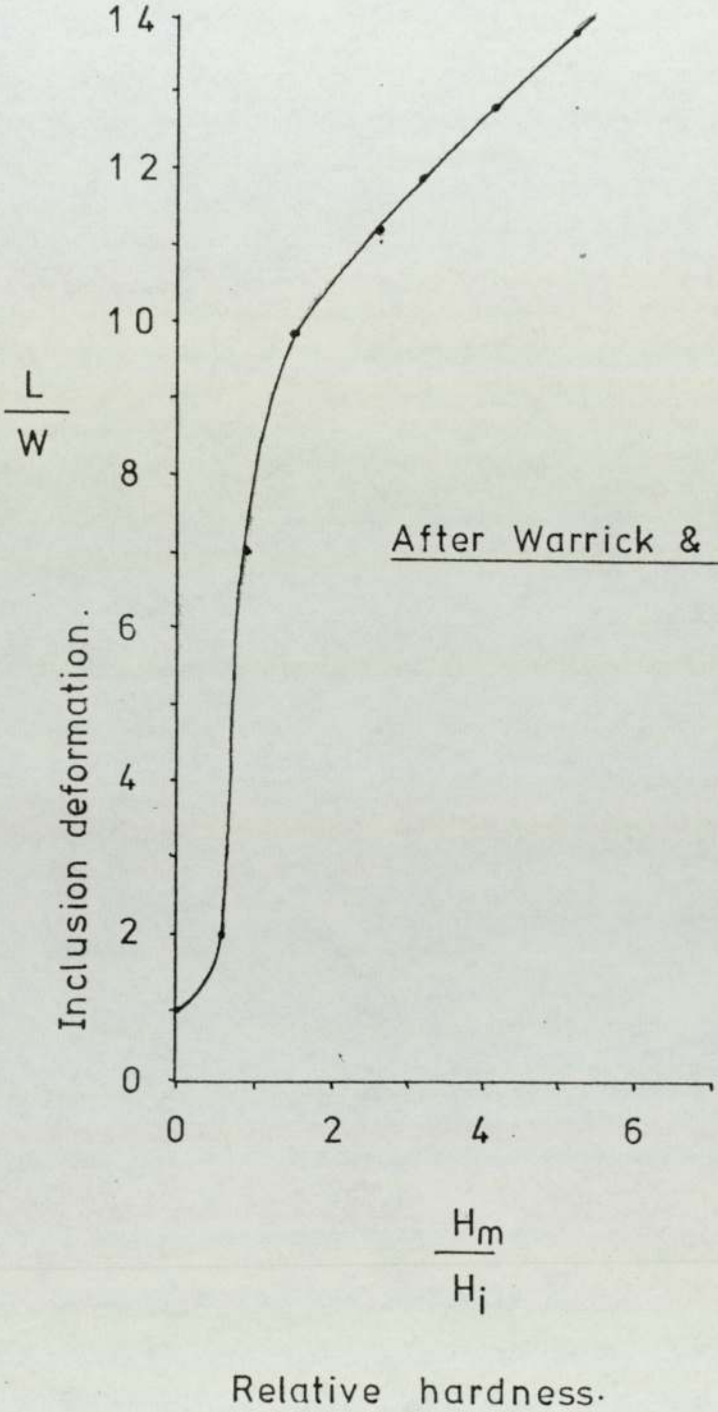

After Warrick & Van Vlack.

2·2·5

value of plasticity index approximately equal to 2.9 occurred when the ratio of inclusion to matrix strength tended towards zero. In addition they observed that there was very little deformation of the inclusion phase if this value of relative strength was greater than 2.0 - 2.5 (fig.2.2.6.). The most rapid change in the value of plasticity index was observed at a relative strength value in the region of unity, a phenomenon encountered by other workers.

One of the problems encountered in observing plasticity indices at various strength ratios, is in fact the measurement of the flow stress of the materials concerned. However, the work of Gove and Charles (109.) has overcome this problem, and the development of a high temperature microhardness tester by Gove (115.) has enabled the matrix and inclusion hardness to be measured in situ at the temperatures employed in the deformation process.

Experimental work performed on both model and actual inclusion/matrix systems has indicated that an approximately linear relationship exists between inclusion plasticity index and the inclusion to matrix hardness ratio (fig 2.2.7.). The relationship that Gove and Charles propose is that:

$$\nu = 2 - \left(\frac{H_i}{H_m}\right) \qquad 0 \leqq \nu \leqq 2$$

where ν is the plasticity index, and H_i and H_m are the hardness of the inclusion and matrix respectively.

The work of these authors, as with the work of Zeisloft and Hosford, uses the values of plasticity index derived from the initial linear region of the inclusion/

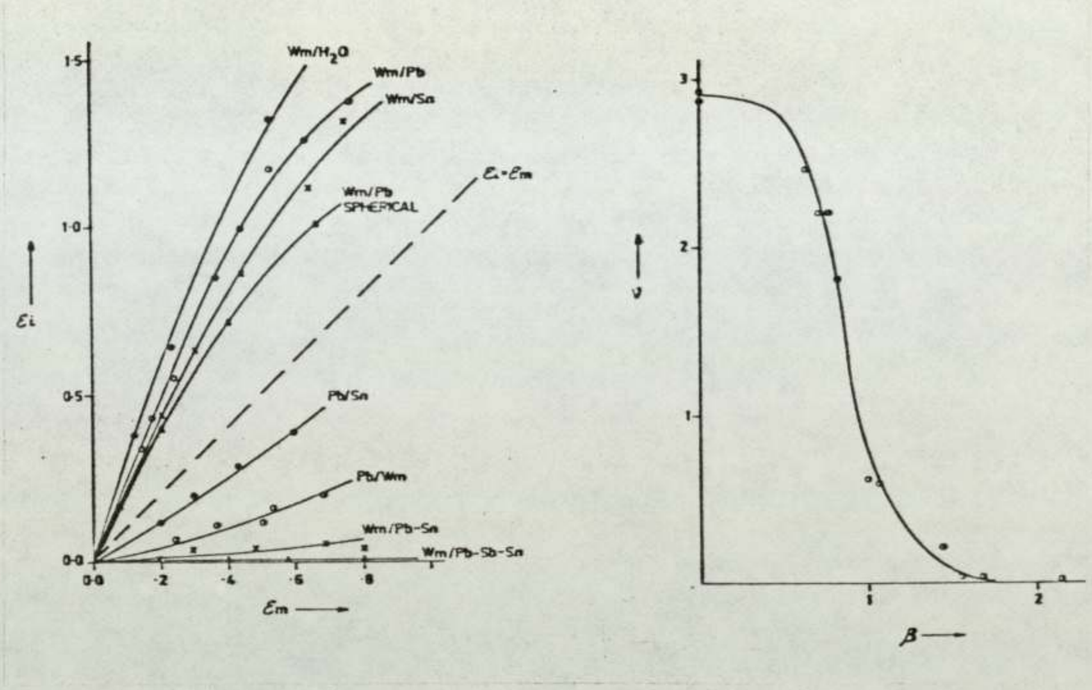

a 2 • 2 • 6 b

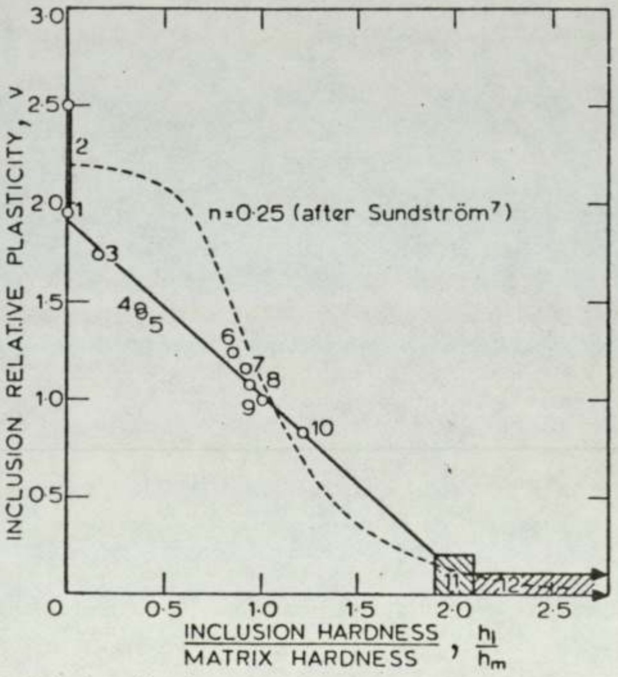

Relationship between relative plasticity and the ratio of inclusion to matrix hardness

2 • 2 • 7

matrix strain curves. The values of plasticity index are thus those at implied zero deformation, and therefore alleviate some of the problems arising due to the change in index with the degree of deformation. i.e. ν_i (intrinsic).

A theoretical approach to the changes in the values of inclusion to matrix strain with respect to different flow stress ratios has been given by Sundstrom (113). Basing his analysis on the earlier work of McClintock (114) Sundstrom analysed the plastic deformation of an elliptical inclusion, contained within an infinite plate stressed at infinity. Both the matrix and inclusion strain hardened at the same rate. In addition he also assumed that the flow stresses of both phases were related to the work hardening exponent (n) by the relationship:

$$\sigma = \sigma_0 \varepsilon^n$$

where ε is the true strain and σ_0 is the value of flow stress at zero deformation.

Providing small strains were involved Sundstrom's analysis reduced to:

$$\nu = \frac{\varepsilon_i}{\varepsilon_m} = \frac{2 \sinh (1-n)}{\left[2 + (\beta^{1/n} - 1)\right] (1-n)}$$

where β is the value of inclusion to matrix flow stress.

Assuming a value of n=0.25 (which is in the range 0.1-0.25 typical for the hot working of steel (116)) the maximum value of plasticity index was approximately 2.2 at a value of β =0 and tending towards zero for values of β greater than 2. In fact the shape of the curve at n=0.25 is in good agreement, and shows the basic features of that determined by Zeisloft and Hosford (112.) (fig 2.2.8).

The sharp change in plasticity index when the value of flow stress ratios is in the region of unity is again observed.

McClintock (117.) has analysed a comparable situation in which the deformation pattern of a longitudinal inclusion under the influence of longitudinal shear, (fig 2.2.9) is observed for various values of inclusion to matrix shear yield stress ratios (k_i/k_m) From his analysis he has shown that an inclusion slightly softer or harder than the matrix has pronounced effect upon the flow field, this effect being shown diagramatically in figure 2.2.10 .

A composite illustration of the variation in plasticity index with the ratio of strengths is shown, for the work of Warwick and Van Vlack (110), Sundstrom (113), and Zeisloft and Hosford, in figure 2.2.11, after Robinson (35), who has replotted the results of Warwick and Van Vlack interms of relative plasticity and relative strength.

A significant feature of the results of Warwick and Van Vlack is the lower values of plasticity index obtained in comparison to the work of Sundstrom and Zeisloft and Hosford. This may in fact be due to the results of Warwick and Van Vlack referring to a 75% (reduction area) deformation, whereas Sundstrom and Zeisloft and Hosford infer a deformation tending to zero.

Referring back to the work of Gove and Charles (109),

2 • 2 • 8

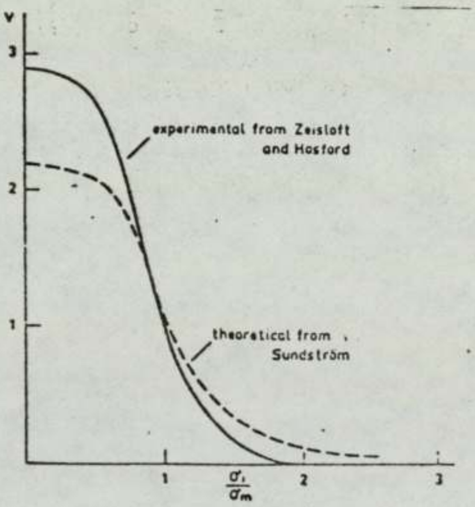
V
3
2
1
experimental from Zeisloft and Hosford
theoretical from Sundström
1
$\frac{\sigma_1}{\sigma_m}$
2
3

2 • 2 • 9

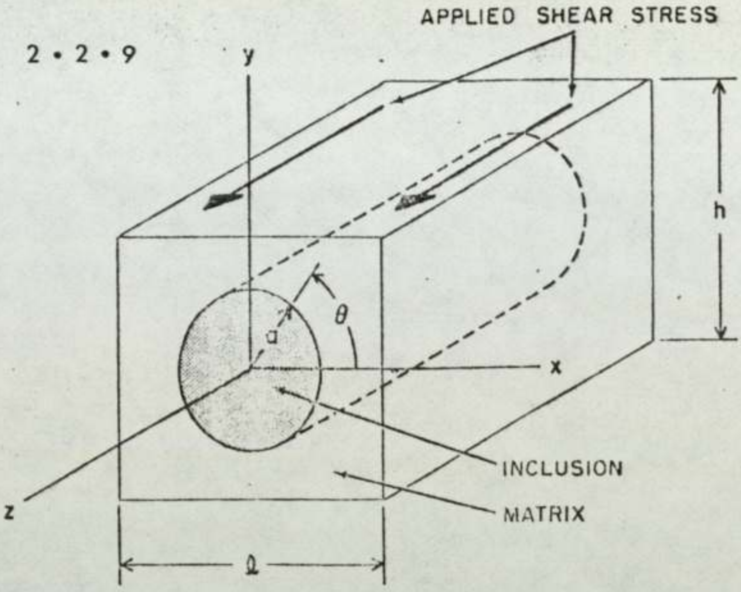

Fig. 1. An inclusion under longitudinal shear

2 • 2 • 10

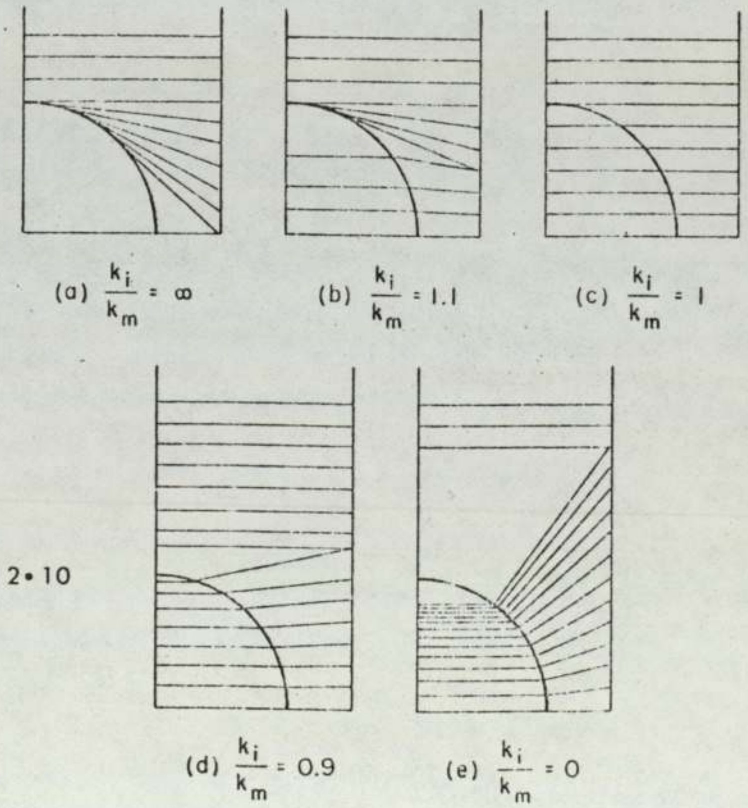
(a) $\frac{k_i}{k_m} = \infty$ (b) $\frac{k_i}{k_m} = 1.1$ (c) $\frac{k_i}{k_m} = 1$

(d) $\frac{k_i}{k_m} = 0.9$ (e) $\frac{k_i}{k_m} = 0$

Fig. 3. Flow fields for inclusions of various yield strengths

2 • 2 • 11

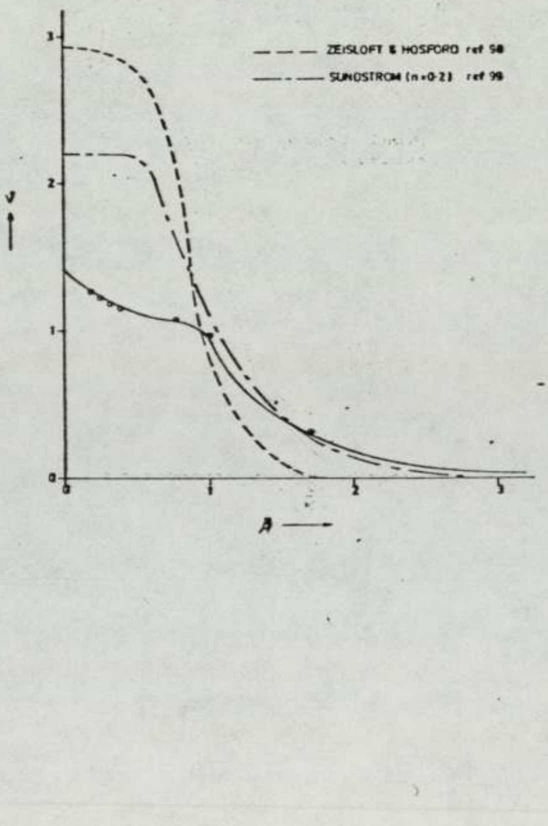

the distinct difference in the plasticity - relative strength relationship, has been attributed to the fact that an analysis similar to Sundstrom's refers to both matrix and inclusion strain hardening to the same extent. However, this is an oversimplification of any actual mechanism, and it is thought that a work hardening phenomenon may account for such deviations.

As can be seen from the work already cited there is some disagreement as to what the shape of the plasticity - relative strength curve should be. Applying the relationship of inclusion - matrix stress and strains to a very simplified case i.e. where the work done (per unit volume (V)) by the matrix equals the work done by the inclusion, then

$$\frac{\sigma_i \varepsilon_i}{V} = \frac{\sigma_m \varepsilon_m}{V}$$

i.e.

$$\nu = \frac{\varepsilon_i}{\varepsilon_m} = \frac{\sigma_m}{\sigma_i}$$

Viz a relationship (figure 2.2.12) exists between ν and (σ_i/σ_m) which may be looked at in comparison to the theory, and the practical results already examined.

Robinson (35.) in his literature review has referred to the work of Gay (118.) who analysed the behaviour of sperical and elliptical particles, deformed by pure and simple shear inside a 'Newtonian fluid' matrix. The

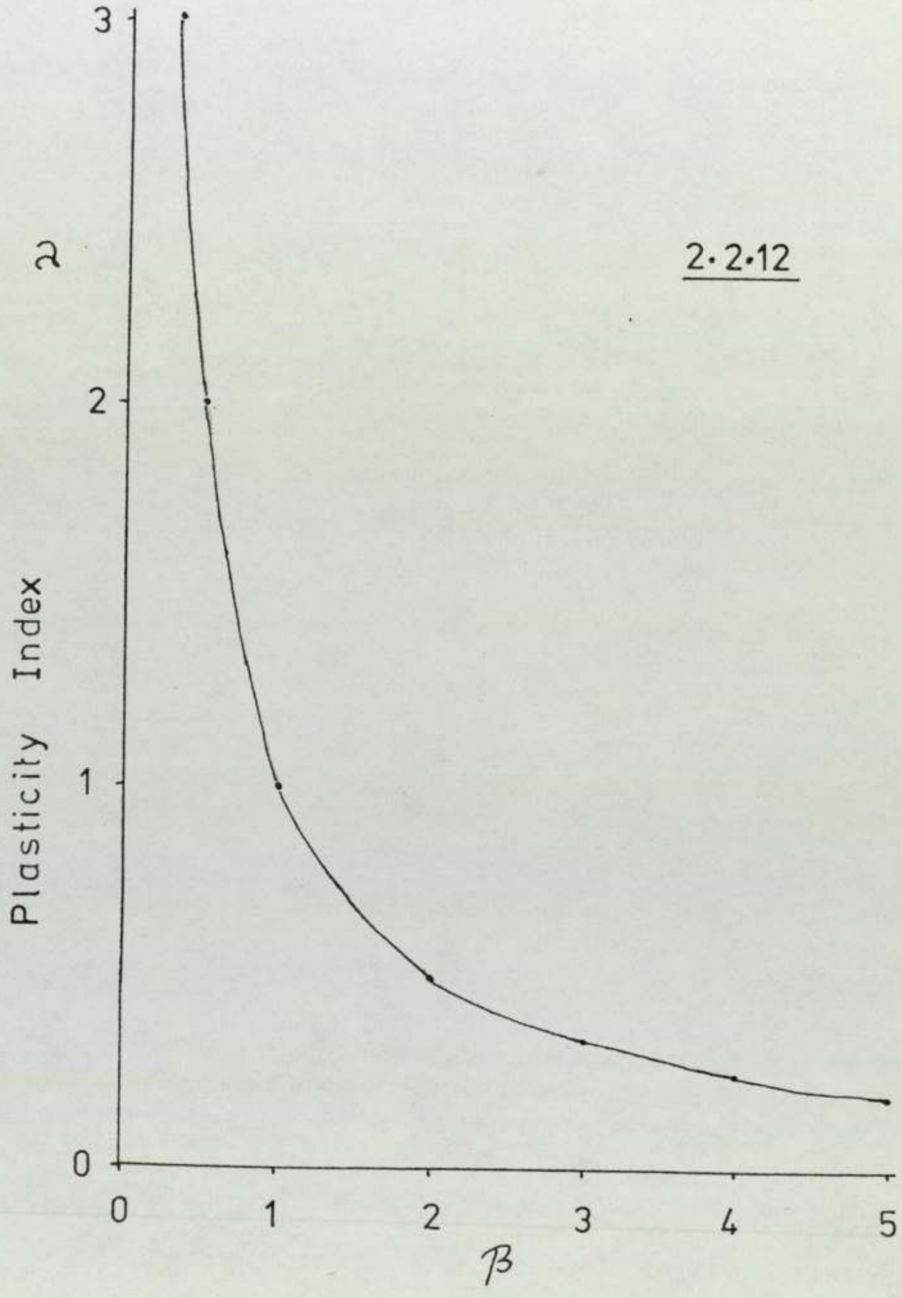

2·2·12

Inclusion : Matrix flow stress ratio

deformation of such bodies was then related to the relative viscosities of particles and matrix.

Assuming that the relative viscosities of the particle to matrix was comparable to their relative strengths Robinson converted the parameters used by Gay to those normally encountered in working on inclusion deformation. Assuming that the initial inclusion strain prior to deformation was zero Robinson obtained the relationship

$$\nu = \frac{\varepsilon_i}{\varepsilon_m} = \frac{5}{2\beta + 3}$$

This relationship is plotted (figure2.2.13) using the very simple case of $\nu = 1/\beta$ in comparison.

It may be seen that a similarity exists with the simple relationship at values of $\beta > 1.0$. However, it is obvious that a discrepancy exists for values $\beta < 1.0$.

Figure 2.2.14 has been produced as a composite diagram (excluding the work of Warwick and Van Vlack) showing the range of values of ν which may be expected in work concerning the deformation of inclusions.

From the work cited it is clear that the areas of greatest discrepancy in values of ν exist at values of relative strength $>$ or $<$ unit flow stress (or hardness) ratio.

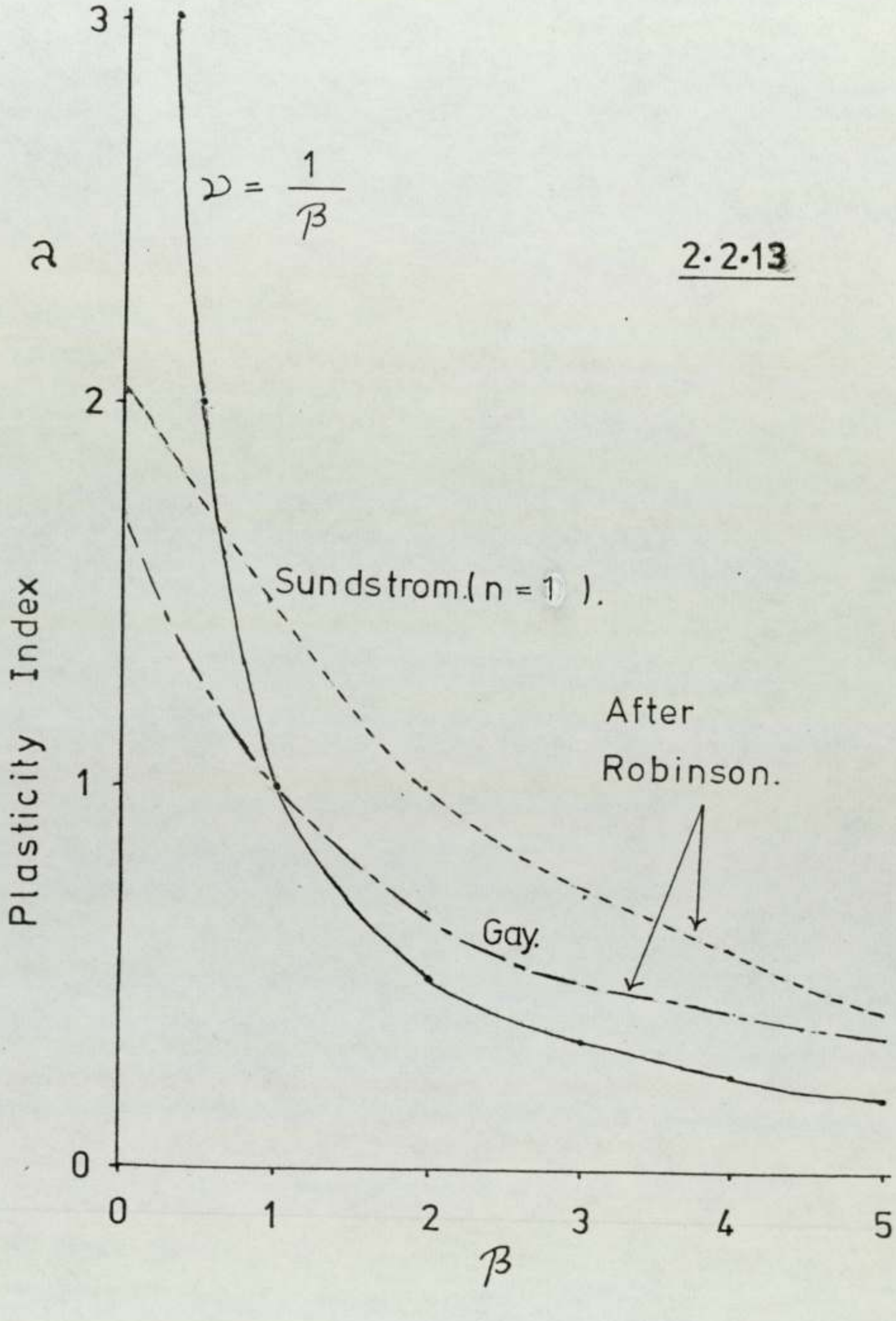

Inclusion : Matrix flow stress ratio

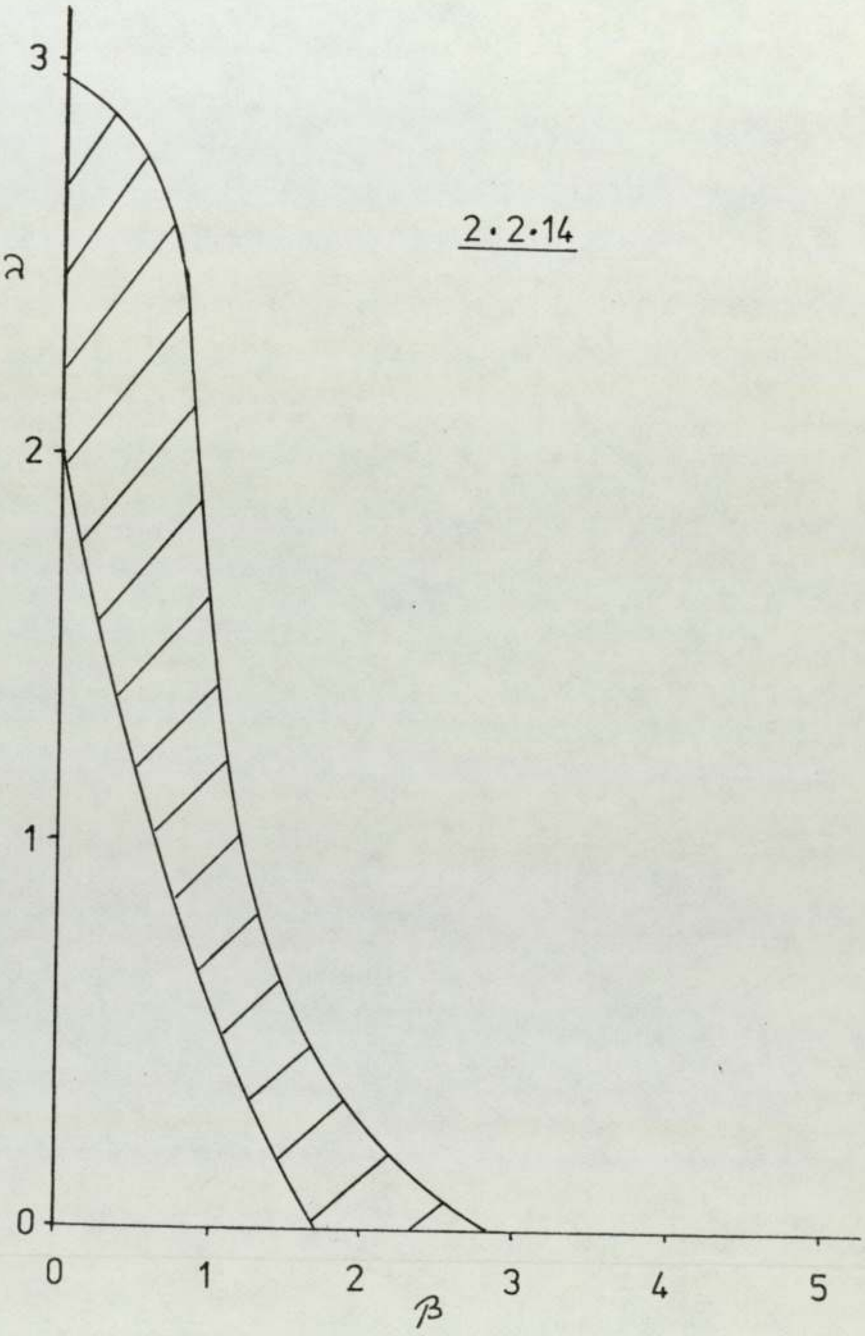

2·2·14

Consideration of relative strength values (β) $>$ 1.0

As mentioned earlier Unkle (98) had observed some deformation of the second phase when the hardness ratio (i.e. β) had been as high as 6. In comparison the work of Gove and Charles and Zeisloft and Hosford (109, 112) had shown that there was very little evidence to suggest that inclusion deformation occurred at inclusion to matrix strength ratios greater than 2.0.

In the discussion of Unkle's paper (98) it had been suggested that the matrix flow around a second phase particle would be influenced by the adhesive bonding between the matrix and the second phase. At low relative strengths the adhesion would be relatively unimportant since the second phase particle has the potential to deform greater than the matrix. However, at high relative strengths the matrix/second phase adhesion would play a significant role.

If the adhesion was poor, once the stress at the interface exceeded the adhesive stress (i.e. the matrix/second phase bond) the matrix would be able to slide over the interface. Hence, the second phase would not be induced to deform to the same degree as would be the case if there was a high degree of adhesion.

The recent work of Ashok (119) was concerned with the influence of adhesive strength upon the deformation of second phase particles. Ashok found that adhesion was a necessary criterion for deformation when the relative strengths (β) exceeded a value of 2. Experimentally he also showed, using copper rods in a copper matrix, that if there was an unbonded second phase of the same material, then this second phase particle could have a relative plasticity index of less than the value of unity which would be expected.

Ashok's results are summarised by figs 2.2.5 and are compared to the results of Unkle (which have been replotted in conventional terms by Robinson), and the work of other authors already cited. Ashok's results for bonded inclusions show a fair degree of similarity with those of Unkle, and to the mathematical model of Gay (118) and the simple relationship

$$\nu = 1/\beta$$

which assumes a bonded system.

The results of Zeisloft and Hosford,. Gove and Charles, and Warwick and Van Vlack, (where the inclusions are weakly bonded to the matrix) show much less deformation of the second phase, and show a similarity with the curve given by Ashok for unbonded second phases. figure. 2,2.15b,

Consideration of relative strength values (β) $<$ 1.0

As may be seen from figure 2.2.15b there seems to be a great amount of uncertainty regarding the value of plasticity index at values of $\beta < 1.0$. This uncertainty cannot be attributable to interface bonding, since the tendency is for the second phase to deform greater than the matrix. The bulk of evidence suggests that the

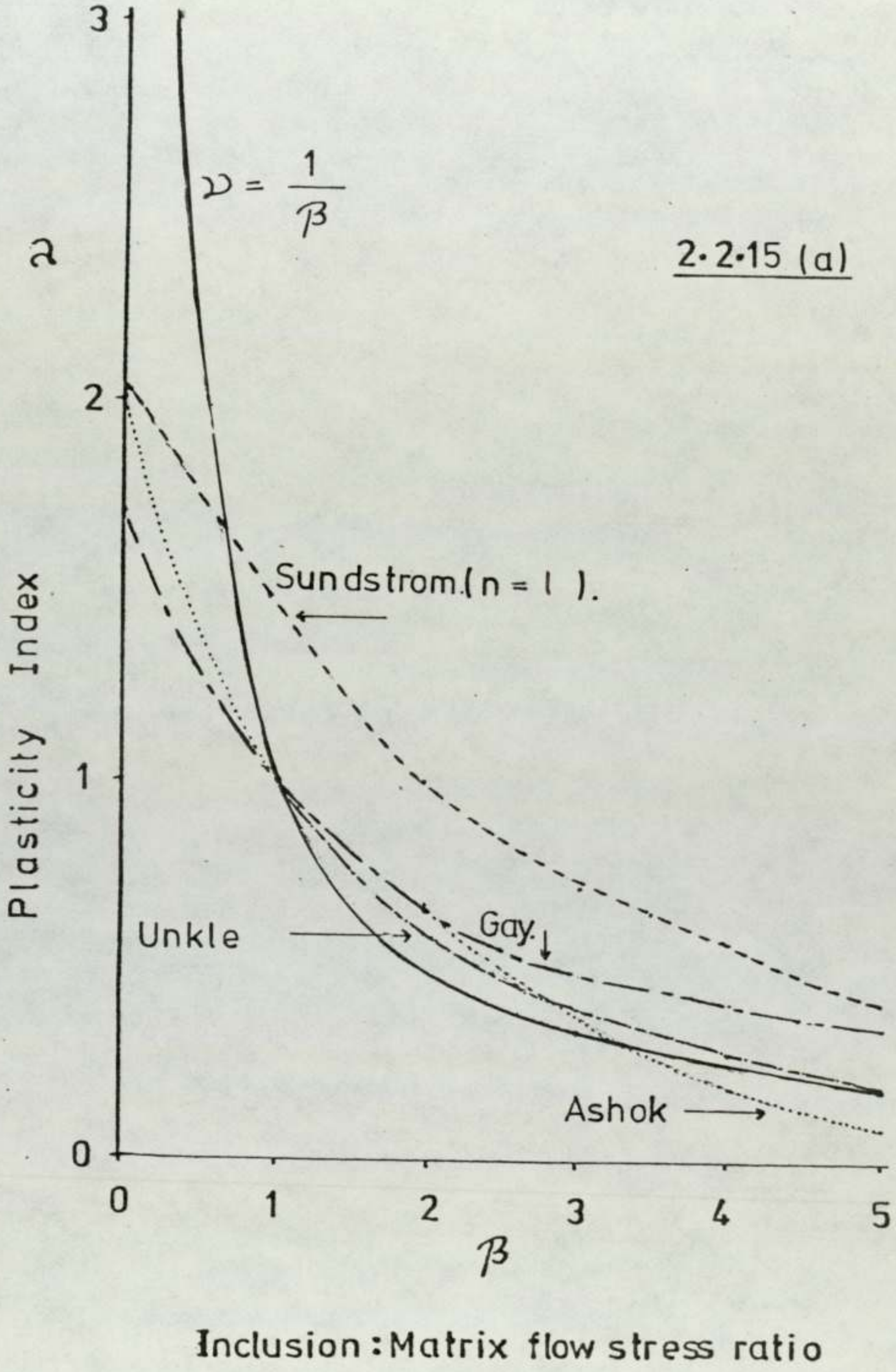
3
2
1
0
ν
Plasticity Index
$\nu = \frac{1}{\beta}$
Sundstrom.(n = 1).
Unkle
Gay.
Ashok
0
1
2
3
4
5
β
Inclusion : Matrix flow stress ratio

2·2·15 (a)

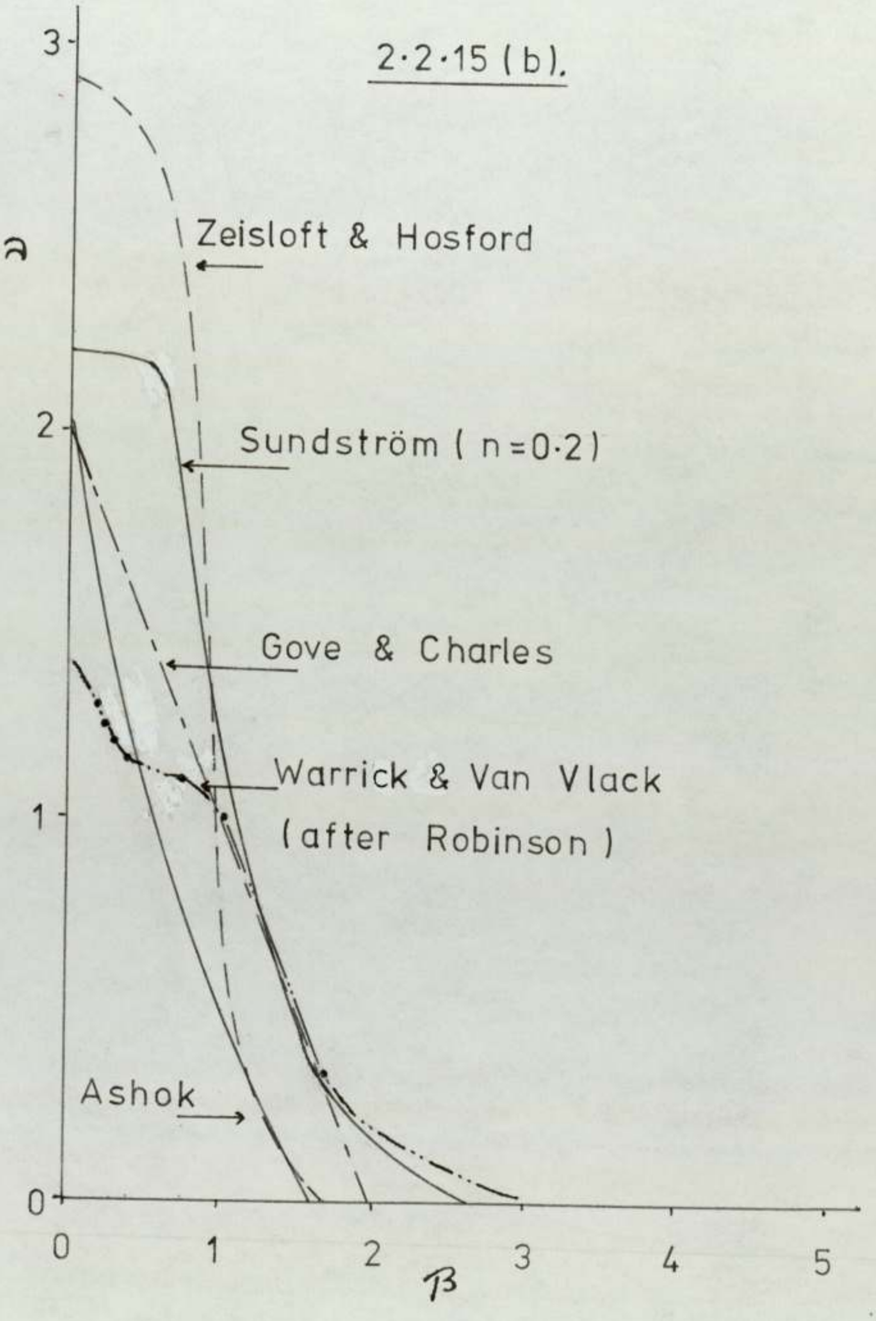

2·2·15 (b).

Zeisloft & Hosford
Sundström (n=0·2)
Gove & Charles
Warrick & Van Vlack
(after Robinson)
Ashok
α
β
0
1
2
3
0
1
2
3
4
5

maximum value of plasticity index (i.e. when $\varepsilon_m = 0$) is within the range 1.7 (118) to 3.5 (35.) and most investigators suggest that a value in the region 2.0 - 2.3 is to be expected. Experimentally, problems have occurred in the measurement of plasticity at low values of ε_m, notable in model inclusion/matrix systems e.g. water in plasticine, whereby the second phase inevitably leaks away during the deformation process.

The theoretical work of Rice and Tracy (120.) may be considered applicable to the maximum value of plasticity index obtainable at values of $\varepsilon_m \Rightarrow 0$. Their analysis predicts that in the absence of hydrostatic pressure a void of constant volume will elongate twice as fast as any region distant from the void. However, the work concerning the plasticity of inclusions has not quantified the effects of hydrostatic pressure, although the hydrostatic pressure may be expected to be influenced by the mode of deformation and the geometries of specimens and work faces.

Cavitation at inclusion/matrix interfaces.

The degree to which an inclusion will deform is governed in part by the relative strengths of inclusion and matrix, which determines its plasticity index. The plasticity of an inclusion phase, due to it being highly deformable or non-deformable, may lead to discontinuities between the inclusion and the steel.

Rudnik (121) who investigated discontinuities due to hot rolling, observed the following; and concluded that

$0.5 < \nu \leq 1.0$	No discontinuities
$0.03 < \nu < 0.3$	Fishtail cracking
$\nu \rightarrow 0.00$	Conical caps and hot tears frequently observed.

Gove and Charles (109) also noted the occurrence of cracks and voids adjacent to inclusions of low deformability Long narrow cracks were found in the direction of rolling frequently at one side but often on both sides. They also noted that the crack length approximated to the product of the original inclusion diameter and the rolling reduction, (H). (H = ratio of initial to final thickness of the rolled material.) It was also evident that these cracks welded up to some degree as the matrix was strained beyond a value of H = 3. This value of H = 3 corresponded to the maximum observed defects, which in turn correlated with the maximum density change in steel with respect to its reduction H (fig 2.2.16)

The importance of the formation of voids at inclusion /matrix interfaces is considered in more detail in section 2.3.

2.2.4.3

Degree of deformation

Numerous workers investigating inclusion behaviour in steels, and other second phase systems have observed the phenomenon that inclusion (or second phase) strain relative to matrix strain varies as the amount of strain increases. Robinson (35) has stated that from a logical

2 • 2 • 16

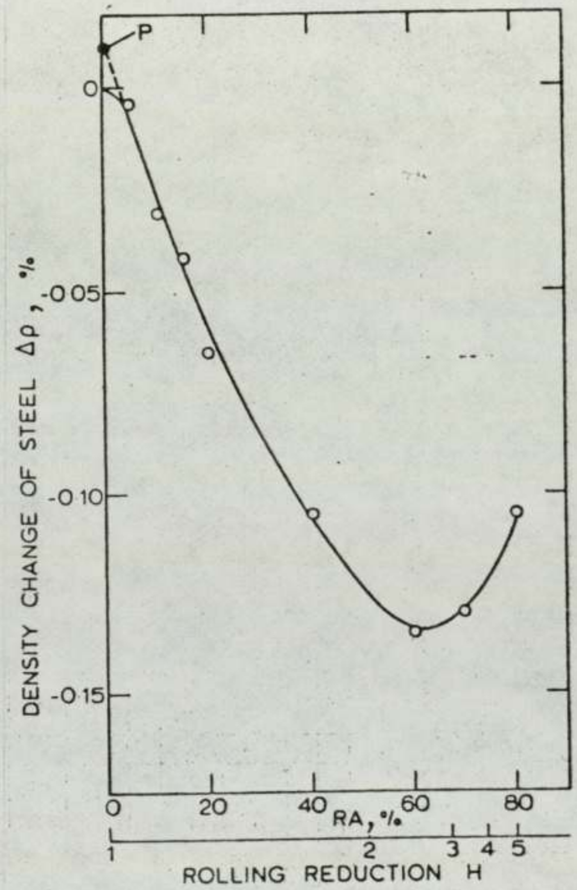

Density change of 0·2%C steel with reduction

point of view, it may be expected that, assuming interfacial bonding is strong, an inclusion inherently less plastic than the matrix should show an increasing rate of strain. Conversely, an inclusion which is initially more plastic than the matrix should show a decreasing rate of deformation with increasing matrix strain. Robinson has referred to the work of Smith (122.) who stated that an elongated inclusion will be constrained to deform at the same rate as its surroundings, irrespective of its viscosity relative to that of the matrix.

However, investigations have indicated that the relative plasticity index (ν) decreases as matrix strain increases (35. 103. 109.). Pickering (100.) proposed that the inclusions (FeO and MnS) work hardened rapidly and became less susceptible to deformation as the degree of matrix deformation increased. However, it is generally regarded that the work hardening of inclusions is not significant under the conditions of hot rolling.
As an alternative Pickering had suggested that the progressively more streamlined shape of the deformed inclusions would offer less resistance to the flow of the matrix and thus reduce interfacial shear forces. However, this argument can only apply to situations where inclusions are weakly bonded to the matrix. In the case of FeO and MnS this bonding is weak and as such may be a contributary factor in the reduction of plasticity index with strain.

Charles (123.) has summarised several reasons why a decrease in plasticity index should occur with progressive deformation viz.

i. Relative work hardening rate.

If the work hardening rate was greater for the inclusion phase (123.) then there is an increase in the relative (inclusion to matrix) flow stresses, and the observed plasticity will progressively decrease.

ii. Matrix constraint

If the potential relative plasticity of an inclusion is less than unity then the matrix adjacent to the inclusion will become constrained by friction at the interface. This constraint then impedes the flow of matrix around the inclusion, and thus impairs the progressive deformation of the inclusion.

iii. Localised work hardening of the matrix.

If the inclusion phase is softer than the matrix, then the adjacent matrix may work harden to a greater extent than observed at any distance from the inclusion. Hence, the inclusion becomes surrounded by a work hardened area of material thus impairing deformation. Charles showed evidence to support this case, via microhardness measurements around an artificial inclusion (i.e. copper) deformed in an iron matrix at 600°C. This increased hardness around the inclusion is only slight, and this effect may be minimised at the higher rolling temperatures (35.).

Baker and Charles (107.) suggested that reduction in plasticity may in part be due to the creation of new interface. They calculated that upon rolling to a X2 reduction an inclusion 7 μm in diameter the creation of new interface would take approximately 1% of the total deformation energy. However, 10% of the total deformation energy would be taken up at a X32 reduction.

More recently Ashok(119.) has based his argument of reduced plasticity with increased strain upon the stress concentration decreasing as the inclusion goes from a sphere to an ellipsoid. He proposed that the equation of Gove and Charles i.e.

$$\nu = 2 - \frac{H_i}{H_m}$$

be slightly modified to introduce the aspect ratio of the inclusion (λ)

Viz

$$\nu = 1 + \left(\frac{1}{\lambda}\right)^m - \left(\frac{H_i}{H_m}\right)$$

From this data he obtained an empirical value of $m = 0.1$. He also added that it was evident that the deformation of second phases was dependent upon the strength of the interface bond.

2.2.4.4.

Inclusion size

Many workers (35, 103, 124.) have reported a variation in inclusion plasticity with size. The work of Uchyiyama and Sumita (124) showed that for inclusions of the (FeMn)O type small inclusions deformed less than the large ones. Pickering (100.), and Malkiewicz and Rudnik (101) were of the same opinion, and in addition it was found that the smaller inclusions only tended to deform at low temperatures and large reductions i.e. when the forces acting upon them were large.

The work of Baker and Charles (107.) does predict however, a size dependence, such that as the inclusion size is reduced the amount of energy available for deformation is reduced. Reduced plasticity is predicted as a result of the greater surface area to volume ratio of smaller inclusions. However, their work suggests that reduction in plasticity should only occur at very small inclusion sizes (i.e. $< 0.1\ \mu m$) at large reductions. They do however, add that practical observations are complicated by variations in composition with size.

Recent work by Segal and Charles (125.) showed that for type III MnS inclusions less than 5 μm in diameter deformation was size dependent (figure2.2.17). The smaller inclusions were observed to be less deformed thus showing the type of behaviour predicted by Baker and Charles.

Robinson (35.) using a model system of globules of perspex cement and carbon tetrachloride, (with a

2•2•17

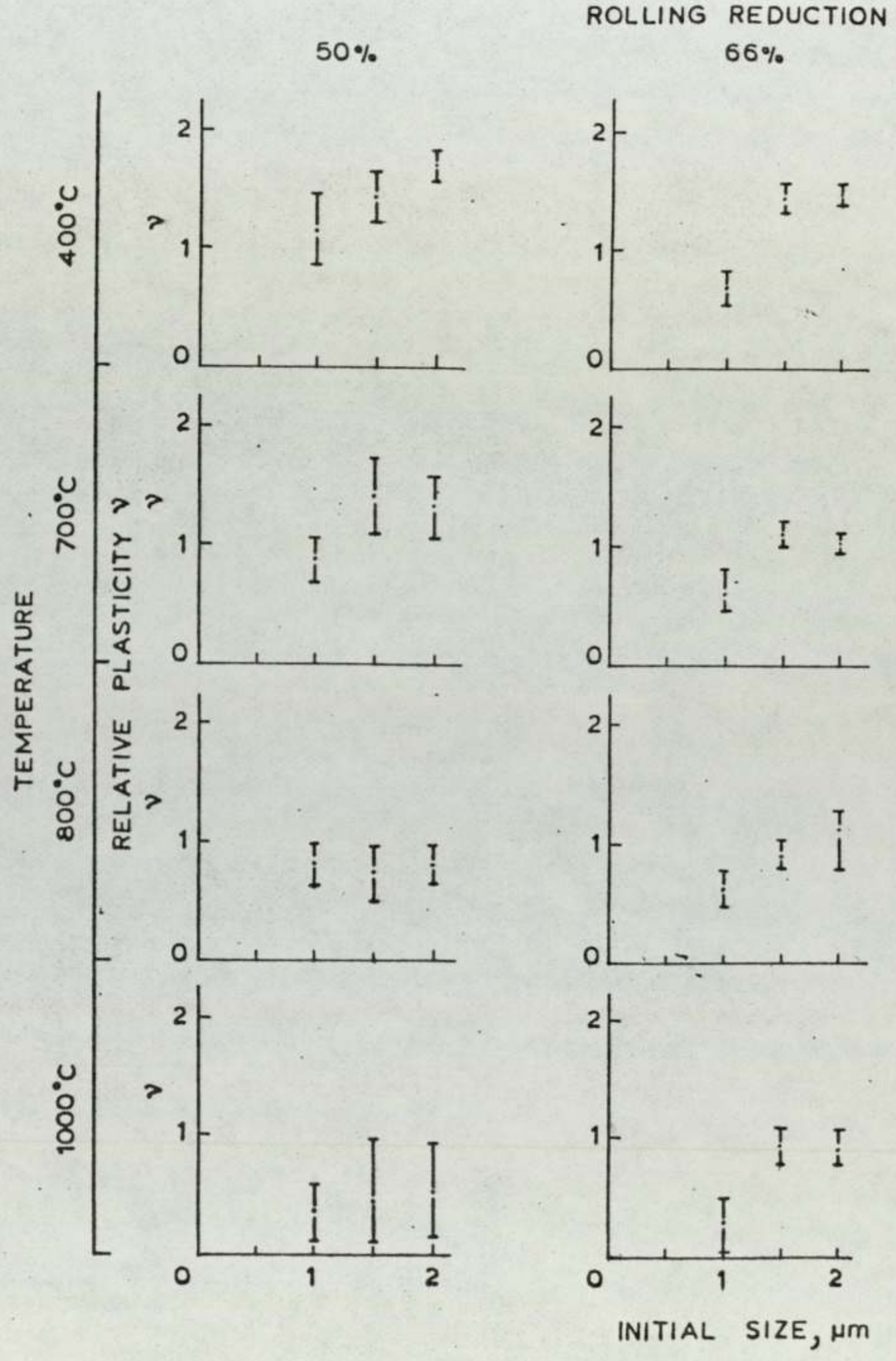
ROLLING REDUCTION
50%
66%
TEMPERATURE
400°C
700°C
800°C
1000°C
RELATIVE PLASTICITY ν
ν
0
1
2
INITIAL SIZE, μm

density matched to that of the sodium silicate medium) demonstrated as inclusion plasticity size relationship. Simulating the deformation of inclusions within a shear gradient, produced by the rotation of concentric perspex cylinders, he showed the basic features of inclusion deformation. The globules were observed to elongate into ellipses similar to the shapes of deformed inclusions found in steels. The noticeable feature though was that the larger inclusions deformed to a greater extent than the smaller ones.

2.2.4.5.

Temperature of deformation.

It has been well established for many years that the flow (yield) stresses of materials are dependent upon temperature. It has also been shown earlier that the deformation of 2nd phases within a 2 phase structure is dependent upon the 2nd phase/matrix flow stresses. Hence the way in which the flow stresses of the phases change with respect to temperature influences the value of plasticity index.

The resistance to deformation of low carbon steels is decreased as the temperature is increased. Over the normal hot rolling temperatures of 900 - 1300°C this variation is approximately linear (fig. 2.2.18 from the results of Larke (126.)). The work of Kiessling (127) and of Gove and Charles (109) using hot hardness measurements has shown the variation in hardness with temperature for pure iron, steels and of various inclusion

2.2.18

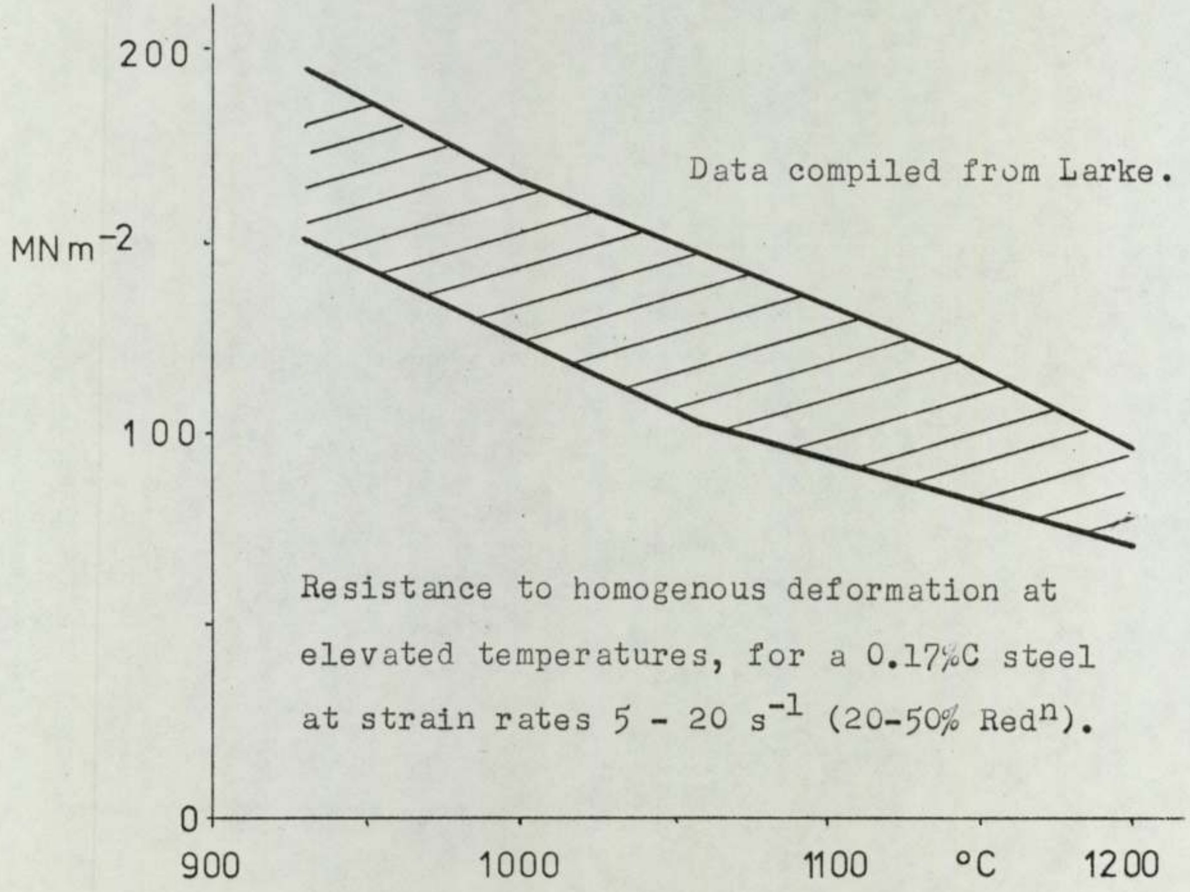

Data compiled from Larke.

Resistance to homogenous deformation at elevated temperatures, for a 0.17%C steel at strain rates 5 - 20 s^{-1} (20-50% Red^{n}).

2.2.19

(a)

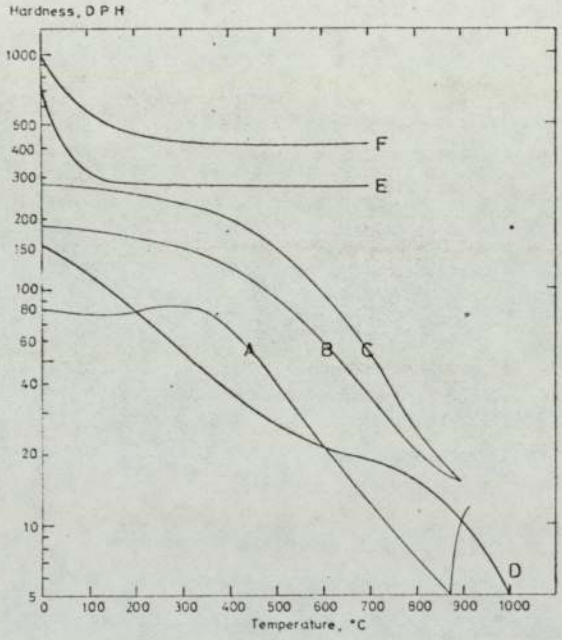

Fig. 19. Hot-hardness values for MnS, MnO·SiO_2 (rhodonite) and 2 MnO·SiO_2 (tephroite) as compared with iron and steel. From refs. [20, 21].

A Iron of high purity
B 1040 steel, 0.37–0.44 % C, 0.60–0.90 % Mn
C 1080 steel, 0.75–0.88 % C, 0.60–0.90 % Mn
D Single crystals of MnS
E MnO·SiO_2, rhodonite, polycrystalline sample
F 2MnO·SiO_2, tephroite, polycrystalline sample.

After Kiessling

2.2.19.

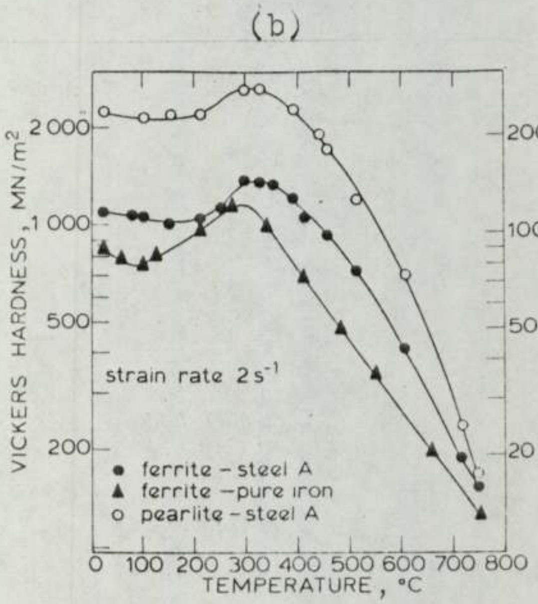

1 Hardness of ferrite and pearlite in a 0·2%C steel, and of ferrite in a nominally pure iron

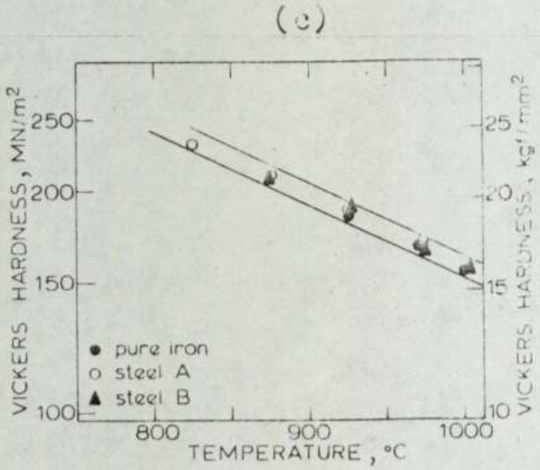

2 Hardness of austenite

After Gove & Charles

2.2.19

(d)

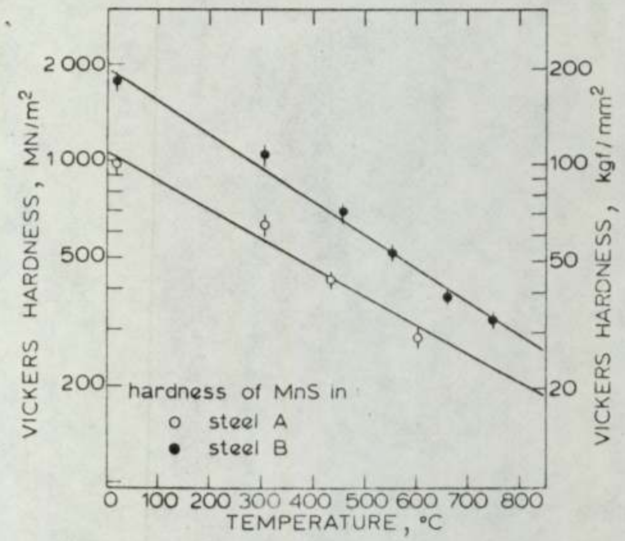

4 Hardness of Type I manganese sulphide inclusions

After Gove & Charles.

(e)

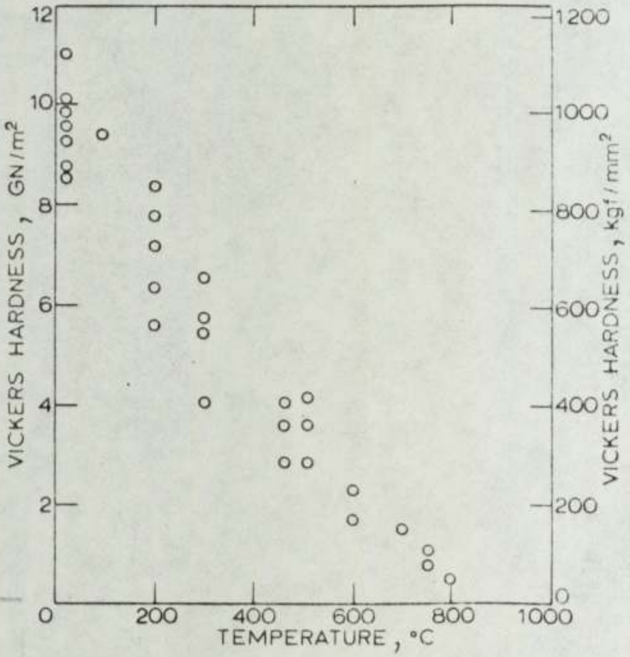

Hardness of various silicate inclusions

phases (figs 2.2.19).

Since in this work the inclusion phases being investigated are silicates, the focus of attention will be upon silicates. For information on the variation of plasticity index with temperature for MnS and other phases the reader is referred to the review of Robinson (35.).

The early work of Pickering (100) and Maunder and Charles (92.) had shown that silicates exhibited vastly different behaviour dependent upon the temperature of working. Pickering found that ~~at~~ working at low temperatures siliceous inclusions either behaved rigidly or in a brittle manner (especially if they were of a duplex crystalline nature). At higher working temperatures there was however a rapid transition to plastic - plastic /fluid behaviour. Maunder and Charles (92.) produced a schematic illustration of the behaviour of silicates (fig 2.2.20).

Most siliceous inclusions which are glassy in nature show an abrupt change in viscosity over a narrow temperature interval, the variation in viscosity following an Arrhenius relationship with temperature(83.).
i.e.

$$\eta = A e^{Q/RT}$$

Typical curves of viscosity versus temperature are shown in figures 2.2.21/22 .

Crystalline phases do not however show any abrupt changes in flow stress until their melting point is neared.[35]

2·2·20

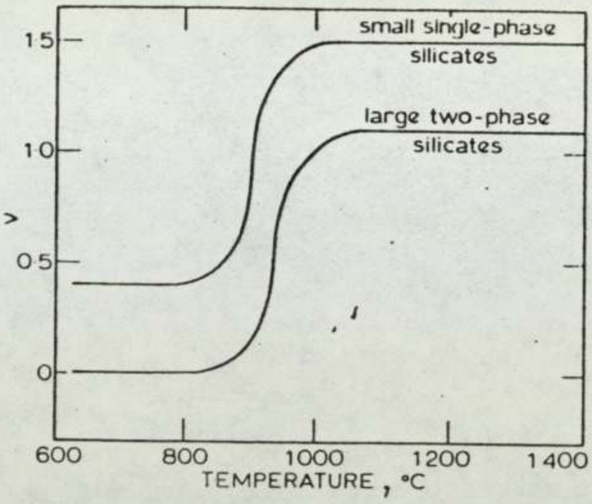

Relative plasticity of silicate inclusions

2·2·23

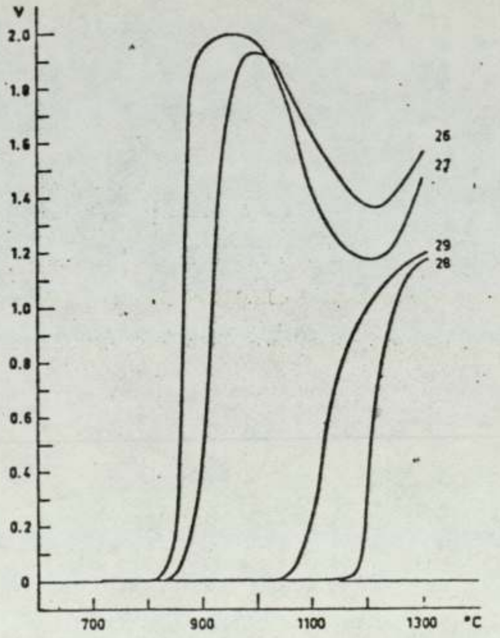

2.2.21

(a)

Viscosities of Long-Molecule and Short-Molecule Slags.

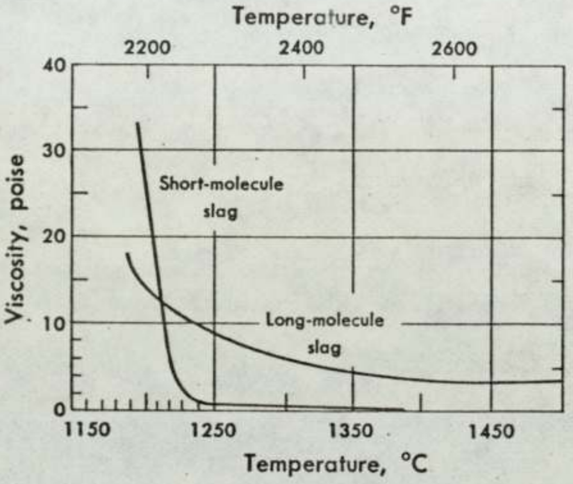

After Elliott et al

(b)

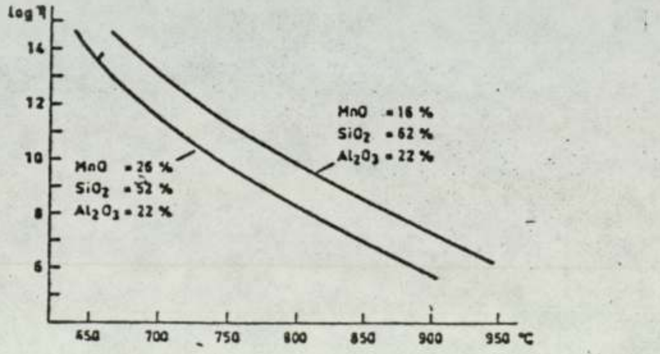

Typical curves of viscosity vs. temperature for silicate glass

After Ekerot

2.2.22.

Relation of Viscosity (η) and Temperature for SiO_2, Showing the Arrhenius Relationship.

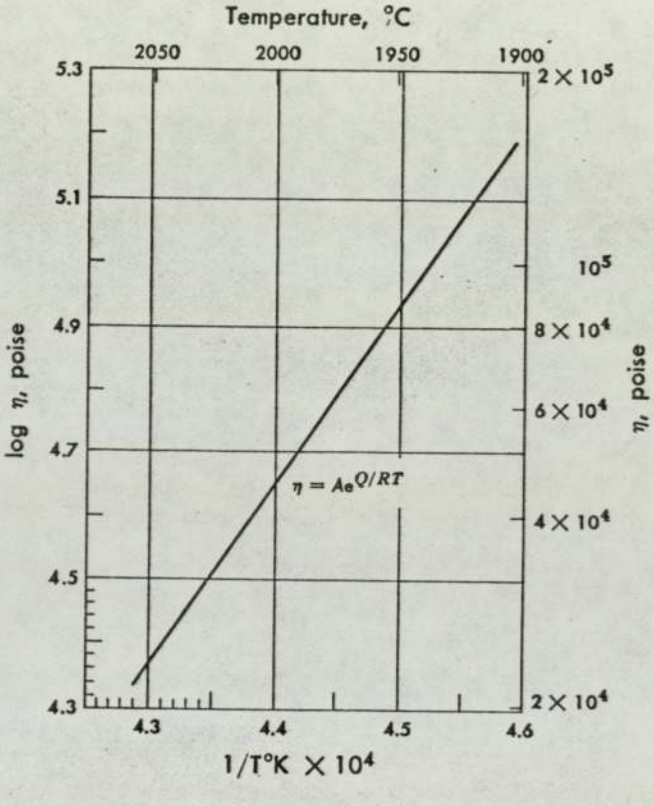

After Elliott et al

The work of Ekerot (102) on glassy silicates showed this rapid change in plasticity index over a narrow range of temperature, typically 25°C. He also developed a theory to explain this phenomenon. Assuming that an amorphous glassy phase behaved as a Newtonian fluid, then a change in viscosity could be related to a change in apparent flow stress.

i.e.

$$\sigma_A = \eta \dot{\varepsilon}$$

where σ_A is the apparent flow stress, η the viscosity and $\dot{\varepsilon}$ the strain rate.

In his discussion Ekerot pointed out that if the viscosity data of various inclusion phases was known, non-deformable/deformable transition temperatures could be estimated. He further pointed out that if the flow stress ratios could be derived using viscosity data, then plasticity indices could be determined using an analysis of or similar to that of Sundstrom (113.).

More recently however, Robinson (35.) has indicated that an error exists in Ekerot's calculation of critical viscosity. In addition Robinson stated that the form of the viscosity equation used by Ekerot was mathematically incorrect, though at zero strain (i.e. initial deformation) the equation would reduce to a similar form

i.e.

$$\sigma_A = 4\eta \dot{\varepsilon}$$

Using this latter form Robinson showed that the critical viscosity occurred at a temperature corresponding to one somewhat above the glass softening point. Using a more rigorous derivation he has shown that values of critical viscosity occur in the region of the glass softening temperature.

The work of Ekerot, Shirawa (129.) and Robinson has indicated that the softening temperatures of glassy and crystalline silicates are inherently different. From their work it would seem that the transition from rigid to plastic/fluid behaviour approximates to the solidus temperature in crystalline silicates. However, the transition temperature of glassy silicates is in the region 100 - 300 + °C below the solidus temperature.

At temperatures in excess of the transition temperature Pickering (100.) found that the relative plasticity index remained at a constant value. Ekerot (102) and Robinson (35) have however found that the value of plasticity may increase, decrease or remain constant above this temperature.

Whereas silicate inclusions show an increase in plasticity index with temperature, it is interesting to note that the inclusion phases which are plastic at lower temperatures (e.g. FeO and MnS) show a decrease in plasticity index as temperature is increased. A phenomenon attributed to the softening rate of the matrix exceeding that of the inclusion phase.

2.2.4.6.
Strain rate

One of the factors relating to inclusion deformation which appears to have been overlooked by many workers is strain rate during deformation. Strain rate is known to vary with specimen size (126.) and it is also known to be inhomogeneous within bulk material (129.).

It is well known that the deformation of steel at high temperatures is sensitive to strain rate, and for example deformation by rolling the mean rate of deformation for the matrix may be given by

$$\dot{\varepsilon} = f \cdot \sqrt{\frac{2}{D(h_1 - h_2)}} \cdot \ln\left(\frac{h_1}{h_2}\right)$$

(assuming sticking friction)

f = peripheral roll speed

D = roll diameter.

h_1 = entry height.

h_2 = exit height.

If it is assumed that inclusions are also influenced by strain rate (102.) then the strain rate, or change in strain rate may influence the deformation behaviour of inclusions, especially if there is a marked difference in sensitivity to strain rate between the matrix and the inclusions. It must also be recognised that strain rate affects temperature rises within the deforming material. For example an increase in strain rate may cause an inclusion to become more fluid than expected as a result of a higher temperature of deformation being attained.

The effect of strain rate should be taken into account when comparing the data of different workers. A 50% reduction in height may be a chosen criterion for investigating inclusion deformation. However, 50% deformation may be achieved in any number of incremental deformations and therefore numerous rates of straining.

For argument it may be considered that if a matrix strain hardens at a greater rate than the inclusion then the inclusion/matrix flow stress may decrease and thus lead to increased inclusion plasticity. Conversely if the inclusion strain hardens to a greater extent, a decrease in inclusion plasticity would be expected.

At present the author is not aware of any research into the effects of strain rate upon inclusion plasticity other than that of Robinson (35.) whose results apparently showed that inclusions are slightly more deformable at the higher strain rate of 0.6 cf 0.3 (figure 2.2.24).

2.2.24

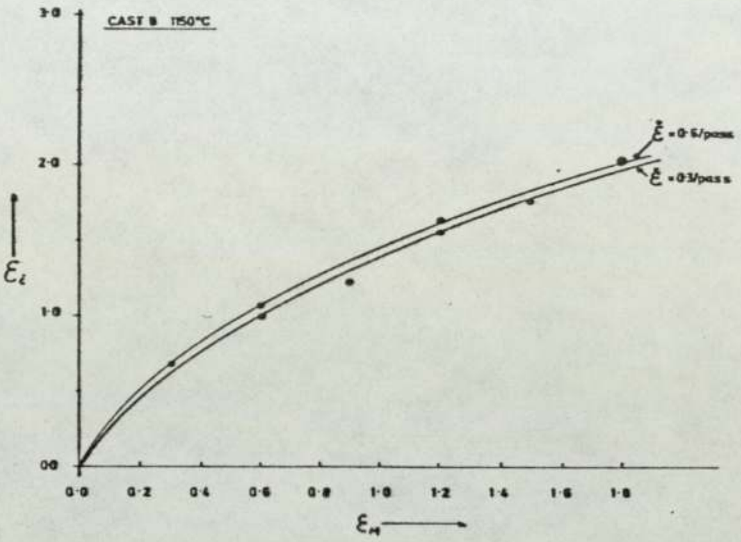
CAST B 1150°C
3·0
2·0
1·0
0·0
ε_i
$\dot{\varepsilon}$ = 0·6/pass
$\dot{\varepsilon}$ = 0·3/pass
0·0
0·2
0·4
0·6
0·8
1·0
1·2
1·4
1·6
1·8
ε_m

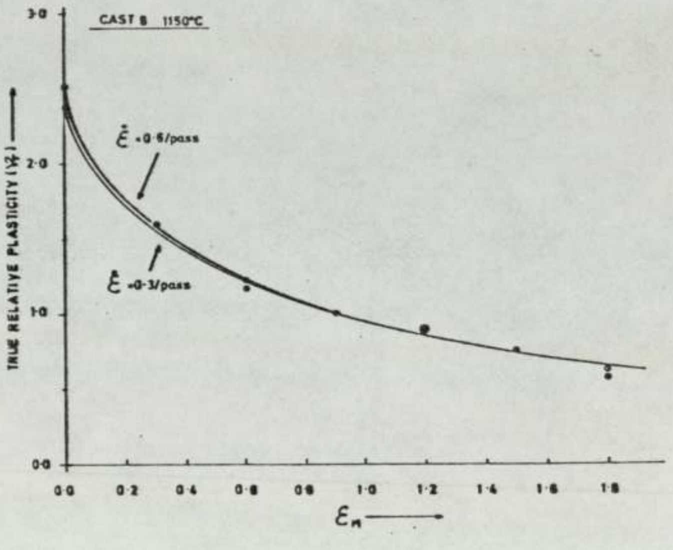
CAST B 1150°C
3·0
2·0
1·0
0·0
TRUE RELATIVE PLASTICITY (1/ε_i)
$\dot{\varepsilon}$ = 0·6/pass
$\dot{\varepsilon}$ = 0·3/pass
0·0
0·2
0·4
0·6
0·8
1·0
1·2
1·4
1·6
1·8
ε_m

2.3. The influence of inclusions on steel properties.

The presence of non-metallic inclusions with steels has been long recognised as a contributary factor to poor mechanical properties. Whether in the as cast or worked conditions it has been known that inclusions influence such properties as strength (130.), ductility (117.), and toughness (131.), as well as fatigue (132.) and impact properties (133.). Inclusions may be found detrimental in areas where mechanical properties are relatively unimportant. They may impair surface quality (134.), or act as preferential corrosion sites (135.).

Although inclusions are regarded essentially as being detrimental to steel properties, they may be beneficial in the area of steel machinability where they may enhance the machining process (136.).

2.3.1. Influence upon strength ductility and toughness.

The influence of non-metallic inclusions on the fracture process has been confined mainly to their role in the ductile failure mode. However, in high strength steels, and steels of low ductility it must be recognised that inclusions effectively act as notches if they are above the critical defect size (137.). Considering the case of fracture in ductile materials, the process may be split into four stages:

(i) The concentration of stress at the second phase particle, leading to localised deformation.

(ii) The initiation of voids around the stress concentrations.

(iii) The growth of voids from their nucleation sites.

(iv) Finally failure due to void coalescence.

However, the general observations of the fracture process are known to be influenced by variables which may act on one or more of the stages. Factors which have been observed to cause changes in behaviour include; size, shape and orientation of second phase; interparticle spacing and volume fraction, as well as the physical characteristics of the particle and particle/matrix bond.

2.3.1.1. General theoretical considerations.

The early work of Goodier (138.) showed that for a spherical inclusion in an elastic matrix stress concentration was related to Poisson's ratio. He showed that the maximum stress concentration was approximately twice the applied stress. Eshelby (139.) later derived that the strain around an inclusion was uniform when both the matrix and inclusion were elastic. However, in metal systems containing non deformable inclusion Ashby (140.) studied the build up of stresses by dislocation movements, as a result of constraint produced by the inclusion. These stresses would eventually exceed the yield stress and localised plastic deformation would result.

Once stresses build up around a particle, then, providing they are sufficiently high, void initiation will take place. This may take place by decohesion of the metal/particle interface (141.) or by cracking of the second phase particle (142.), a situation which seems to be governed by the strength of the bond between particle and matrix.

However, void nucleation has been found dependent also upon the shape and orientation of the particles (143.).

The voids once nucleated must then grow under the influence of the applied stress mode. Void growth models are considered to be of two types (144.):-

(i) Voids may be considered to expand in a visco elastic medium under action of tensile and transverse stresses, viz the model of McClintock (145).

(ii) The second model allows voids to grow only in the tensile direction and to approach each other by lateral contraction (146, 147.).

Ashby (140.) showed that cavities grew in the direction of the tensile stress, and that crack volume increased linearly with strain. However, Hellen (148.) has pointed out that void growth is linear for a plastic material but is non-linear for a work hardening material. Another observation of voids and void growth by Rogers (149.), and Palmer & Smith (150.), has been that voids tend to be concentrated in bands of pronounced plastic deformation. This may have been due to the growth of void nuclei only in these regions.

These voids will then grow until they are of sufficient size that localised regions between voids will yield and coalescence occurs until final failure. There is evidence (151.) which shows that the larger voids are present around the largest particles. However, the ratio of void size to inclusion size appears to remain constant.

2.3.1.2. Factors influencing the fracture process.

2.3.1.2.1. Inclusion size.

Early attempts at mathematical models for void initiation were carried out by Gurland and his co-workers (141. 142. 152.). Using a stored energy criterion analysis they showed that there was a particle size dependence for void formation, and that the larger particles formed voids first. Tanaka (153.) et al employing the solutions of Eshelby (139.) also showed that there was a size relationship where the larger particles would cavitate first.

Their analysis was based upon a rigid sperical inclusion in a plastically deformed matrix under uniaxial tensile stress. They showed that the critical strain to cavitation was given by

$$\begin{aligned}\varepsilon_{CRIT} &= \beta\left(\frac{1}{d}\right)^{1/2} &&: \alpha < 1 \\ &= \beta\left(\frac{1}{\alpha d}\right)^{1/2} &&: \alpha \geq 1\end{aligned}$$

α was the ratio of inclusion/matrix Young's moduli and β was a function which embraces stored elastic energy. They also calculated a stress criterion which was size independent. Diagrammatically their results are shown in figure 2.3.1.

The prediction that voids are nucleated at larger particles first is also held by other workers (153. – 155.), where the critical strain has again been found inversely proportional to the square root of the particle size.

2 .3.1.

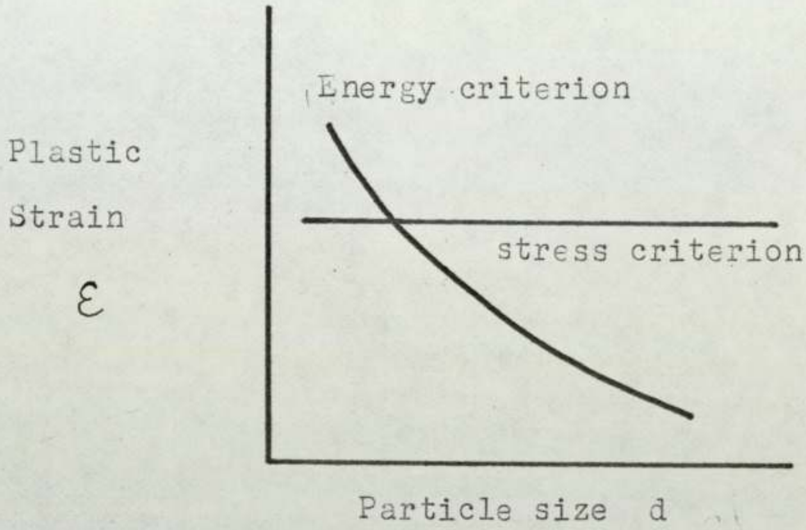
Energy criterion
Plastic
Strain
ε
stress criterion
Particle size d

2 .3.2.

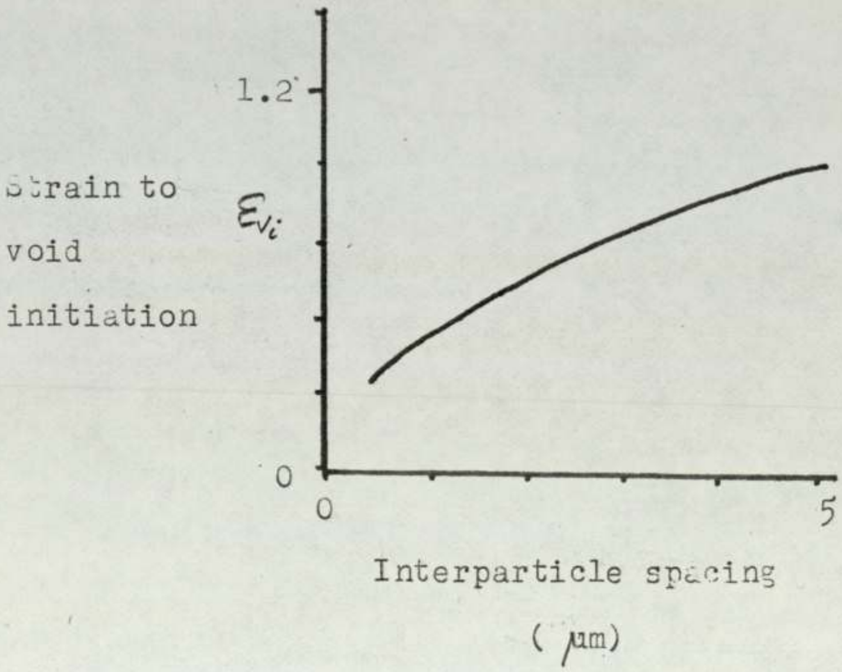
1.2
Strain to
void
initiation
ε_{v_i}
0
0
5
Interparticle spacing
(μm)

In contrast however, the work of Brown and Stobbs(156.) using an energy criterion predicted only a weak dependence upon particle size. Their work which took into account plastic relaxation of the matrix resulted in the prediction of cavitation at the small particles first viz

$$\varepsilon_p \propto r^{1/4}$$

where r is the particle radius.

Palmer and Smith (150.) have suggested that larger particles act as better sinks for embrittling impurities, and Cox and Low (157.) have suggested a statistical basis for size dependence. They considered that since the majority of second phase particles are brittle they should have cracks associated with them, and cavitation should occur at lower strains for the larger particles.

The recent experimental work of Klevebring (158.) et al and Baker (159.) which is relevant to the research topic under study, has shown that under hot deformation by forging (158.) and rolling (159.), it is the inclusions which are greater than approximately 3 μm in size which show voids. The inclusions present in the steels were silicates and manganese sulphides respectively. However, the work of Roesch (160.) using alumina particles has not shown any relationship between size and cavitation, but these were sintered specimens which may have suffered interface reactions.

2.3.1.2.2. Interparticle spacing and volume fraction.

Numerous workers (133, 142, 160.—163.) have investigated the influence of various types of inclusion phases of different interparticle spacings and volume fractions on the ductile fracture of irons and steels.

For a monosized uniformly distributed second phase the interparticle spacing is related to both volume and size of particle (144.)

i.e. $$d = r_o\left(\sqrt{\frac{2\pi}{3V_f}} - \sqrt{\frac{8}{3}}\right)$$

where r_o is the void (particle) radius and V_f the volume fraction. Although for a polydispersed system it can only be regarded as a rough guide, it does enable a summary under one category.

Inoue and Kinshita (164.) investigated the effect of particle size and interparticle spacing on the ductile fracture of spheroidised carbides and concluded that the strain to void initiation increased as the interparticle spacing increased. (fig. 2.3.2). At the same conference Brown and Embury (147.) reported that the strain to final fracture was proportional to volume and interparticle spacing. Edelson and Baldwin (163.) in studying the effect of second phase particles on the mechanical properties of alloys concluded that ductility was dependent upon volume fraction and interdependent of particle size. This view, based upon their own results and those of other workers (165. 166.) showed that as the volume fraction increased there was a non linear decay in the total strain to fracture.

Pickering (151.) in his work on austenitic steels observed that the maximum uniform strain and total ductility decreased with increased volume fraction, although the total ductility was influenced the most. He found that the relationships for sulphides and oxides were similar to those for Nb(CN) and Ti(CN) inclusions, and that the relationships were similar to that obtained by other workers. figures 2.3.3. & 2.3.4.

Baker (159.) considered the example that since inclusion spacing is proportional to size it might be expected that small inclusions would be more detrimental than the larger ones. In his experimental work (on two steels containing deformed inclusions with similar aspect ratios, but different matrix properties) he observed that the steel containing the smaller inclusions was of lower toughness.

Kinoshita et al (167.) have observed that ductility decreases with an increase in the number of fine inclusions less than 5 μm in diameter, which is to be expected (159.). The work of Gladman (168.) has also shown that as the volume fraction of sulphides in a C - Mn steel increases then at high strain rates in tensile tests the work hardening rate is reduced.

Argon et al (169.) have recently pointed out that for volume fractions less than 0.01 i.e. (1%), plastic zones of particles do not interact and they behave as isolated particles. Although this implies that in practice inclusions behave as isolated particles, if gross segreation exists localised areas may be present where inclusion stress/strain interact.

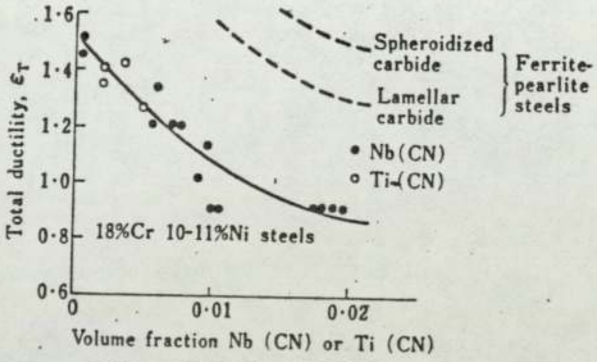

Effect of Nb(CN) and Ti(CN) on total ductility.

(a)

2.3.3.

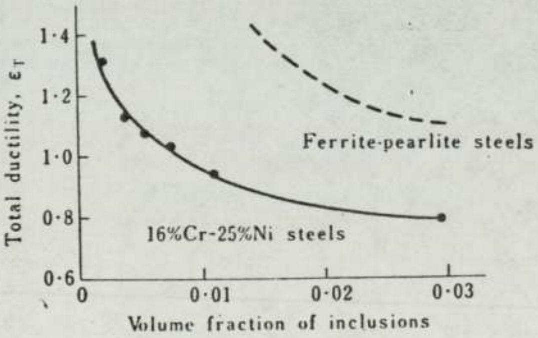

Effect of inclusions on total ductility.

(b)

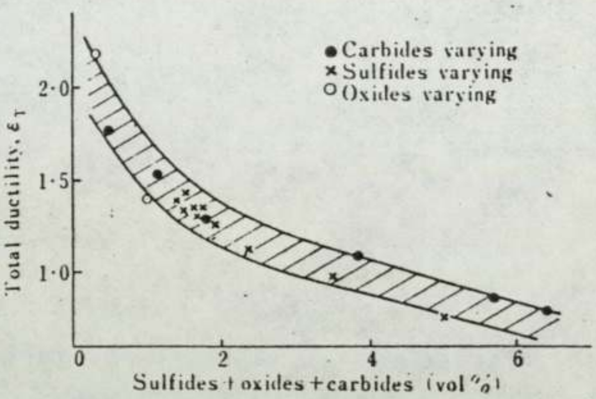

Effect of second-phase particles on ε_T.

(a)

2.3.4.

(b)

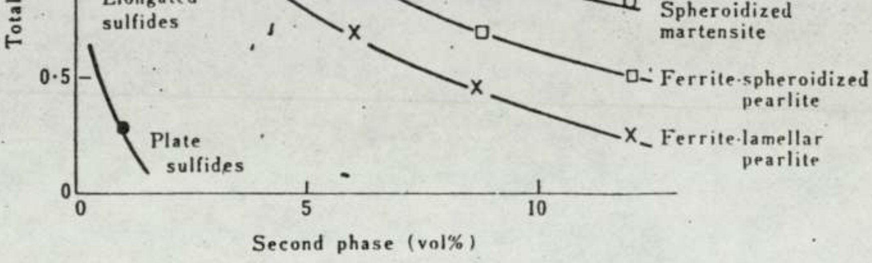

2.3.1.2.3. Inclusion morphology.

In the case of as cast structures, specimens are normally isotropic with regard to fracture. Deformation of the as cast structure during hot rolling or other working operations may result in the deformation of the inclusion phase and lead to anisotropy in the fracture of steels.

In semi killed steels the inclusion products are likely to be type I globular sulphides and oxides which will deform into ellipsoids of dimensions dependent upon the mode of deformation. If, however, these inclusions do not deform voids may be nucleated and grow in the direction of deformation (107.). In this case the fracture process becomes essentially the growth and coalescence of voids.

In fully killed steels it is likely that skeletal structures of Al_2O_3 and type II MnS will be present. These will be reorientated into the working direction and will produce anisotropic defects.

The presence of spinel type inclusions which are generally less than 25 μm have little influence[170.] upon the mechanical performance of steels, unless they are present in steels used for critical applications. The agglomeration of spinels by surface tension effects or by the presence of a low melting point silicate is much more likely to cause serious problems.

Pickering (151.) has commented that the behaviour of oxides and sulphides is qualitatively similar. However, the mechanism is considered to be different. Oxides crack readily, whereas sulphides are decoherent, and Pickering has presented expressions which represent the cracking and decohesion mechanisms in terms of particle spacing, volume fraction, morphology and strain.

In work using elongated, and plate like sulphides Pickering observed that an increase in volume fraction caused an increase in void volume for any given tensile strain. In addition a decrease in the length to width ratio of the inclusions with respect to the tensile axis increased void growth rates with increasing strain. He also observed that void coalescence would occur earlier than expected in theory. This phenomenon be attributed to the theory assuming uniform particle spacing, whereas in practice local segregation will exist. Also the banding of inclusions may give distinct planes of weakness (144.). Gladman et al (171.) attribute the detrimental influence of transverse inclusions to the fact that once a void is formed, strain is highly concentrated at the ends of the void where a small radius of curvature is encountered. Using 'crack opening displacement' toughness tests Baker and Charles (172.) have shown the influence of morphology upon COD values 2.3.5a - 2.3.8

2.3.1.3.4. Deformation.

Considering materials which have undergone deformation, inclusions may lead to the development of planar defects (strip rolling). Vogels & Bruening (173.) and Dahl et al (174.) investigated the differences in longitudinal and transverse mechanical properties in commercially rolled steels, which arose as a result of the deformation of inclusions. Their findings were that transverse properties were inferior.

2 • 3 • 5

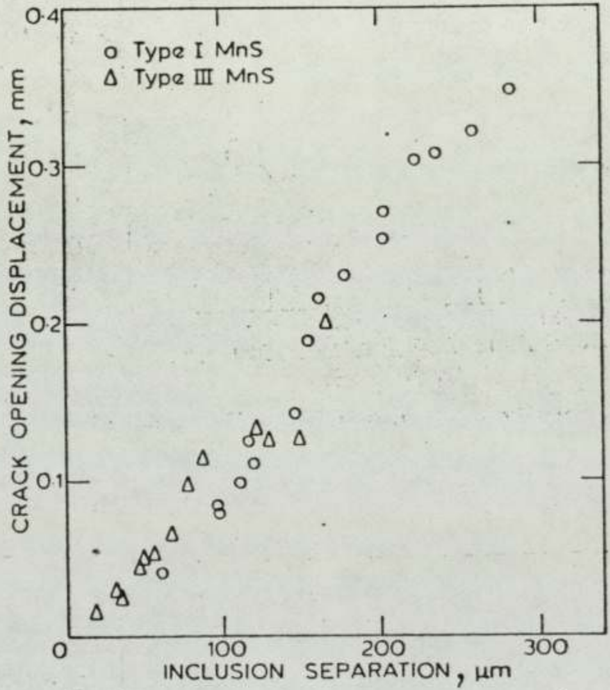

Relationship between short-transverse toughness and inclusion separation in direction of fracture

2 • 3 • 6

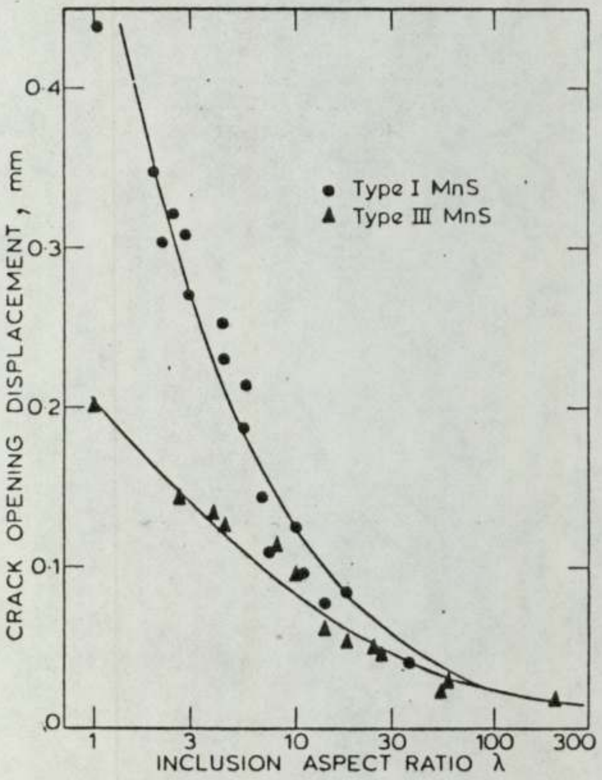

Effect of inclusion aspect ratio on short-transverse toughness

2 • 3 • 7

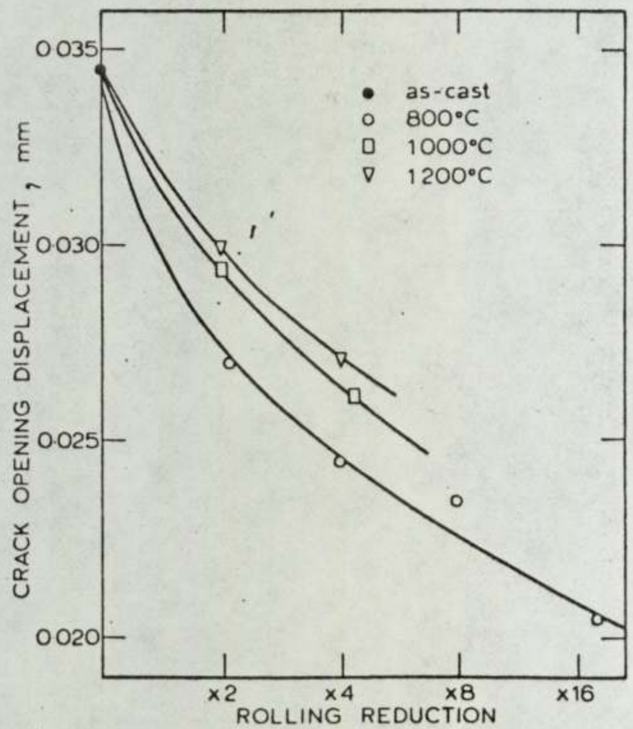

Effect of rolling temperature and reduction on short-transverse toughness of steel containing Type II MnS

2 • 3 • 8

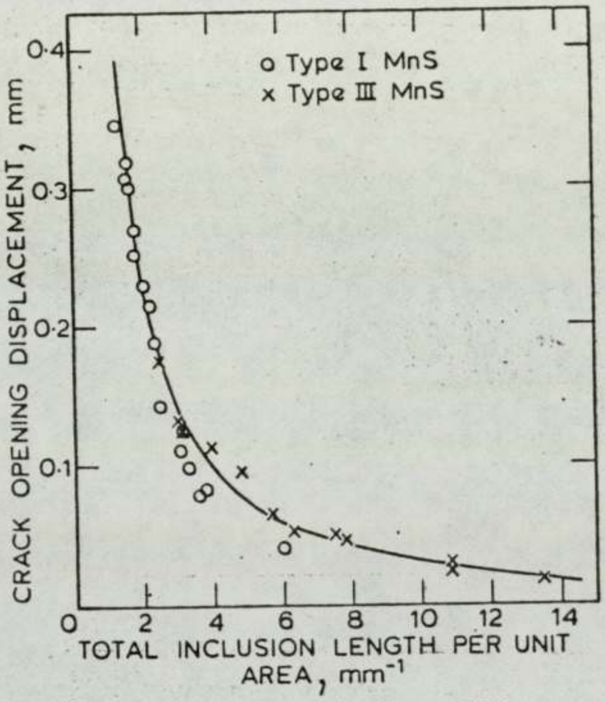

Influence of inclusion projection on COD

The importance of inclusion deformation on the mechanical properties of steels was shown by the use of shape control elements (175. — 177.), which prevented inclusions deforming, and anisotropy was also seen to be reduced by the spheroidisation of deformed inclusions (174). Also it was noted that broken up stringers had less effect than those that remained intact.

Investigation of short transverse direction properties had received little attention prior to the last decade since it was unusual to put this direction under direct stress in engineering applications. However, with the advent of fabricated structures in which the short transverse direction became stressed it was important to investigate the effect of inclusions on short transverse properties. Work carried out has shown that the most marked deterioration was in toughness (159. 178.-180.) and this is accentuated as inclusion deformation is increased (159.). Baker et al (181.) have shown that the C.O.D. (crack opening displacement) in the short transverse direction is influenced by inclusion aspect ratio (figure 2.3.6) and by rolling reduction (figure 2.3.7).

The majority of studies of short transverse properties has been hampered by the lack of material in that direction. Baker et al (172.) have found that the silver soldering of extension pieces onto this type of section provides an adequate method for C.O.D. testing. They found that the silver solder joint did not influence the plastic flow zones associated with the notch.

From numerous investigations it has been observed that the toughness of rolled material decreases on going from longitudinal through transverse directions.

Farrow (182.) and Trigwell (183.) working on the present system under study have shown that the tensile properties of materials tested in the longitudinal, transverse and intermediate directions were not significantly different. Very little difference in strength and ductility was observed whether the inclusions had deformed or not at various rolling temperatures. They did however emphasise that investigations were hampered by the use of small test pieces.

Inclusion orientation has been observed to give a more pronounced effect in (C.O.D.) toughness tests than for uniaxial tensile tests. It has been shown by Smith and Knott (184.) that for free cutting steel the crack opening displacement in the longitudinal direction is approximately three times that of the transverse direction.

2.3.1.2.5. Matrix particle bond.

The strength of the matrix/particle bond should be expected to influence the fracture process on the basis of void initiation around a second phase particle. The analysis of Gurland and Plateau (141.) infers rupture at the matrix/particle interface in an elastic situation. In metals however plastic deformation proceeds to rupture and dislocation movements lead to stress concentrations at the interface (140.).

Most common silicates, Al_2O_3 and MnS are weakly bonded to the matrix (144.) and the strain to void initiation is approximately zero. Although it is not clear whether stresses produced around voids are significant with respect to initiation strains, they may influence whether or not an inclusion fractures or decoheses. If the stress at the inclusion is greater than the interfacial strength decohesion would be expected. However, if this interface bond is strong stress relief may occur by fracture of the particle (e.g. carbides (142.)).

In the case of non metallic inclusions where weak bonds exist (144.) decohesion of the interface has been observed with both deformed and non deformed inclusions (159.). In the case of MnS because of its differential thermal contraction properties relative to steel (185.), it may be regarded as effectively sited in holes. Hence, there is no strain required to initiate bond decohesion.

The work of Easterling et al (186. 187.) has indicated that void nucleation is related to the matrix/particle bond, and they have suggested that the steel composition influences the strength of this bond (187.), which may account for observations of inclusion decohesion and cracking. However, the work of Easterling was concerned with sintered powders and in those materials such effects may be masked or over-emphasised to some degree.

2.3.1.3. Lamellar tearing.

Lamellar tearing may be regarded as a specific case of fracture in the short transverse direction, and is associated with the welding of fabricated structures. The tear is the result of planar like defects which effectively reduce the cross sectional area and therefore reduce the amount of strain required to initiate a void.

Lamellar tearing is known to occur under T, and fillet welds (188.) where tensile strains are in evidence in the short transverse sections. They may also arise from weld shrinkage augmented by restraint in large structures (180.).

Baker (159.) and Watkinson et al (180.) have shown that short transverse toughness is impaired by inclusion strain, separation and volume fraction etc. figures 2.2.5-2.2.8 . Both workers used the C.O.D. test as a measure of toughness, but Watkinson et al also investigated the reduction in area of short transverse tensile test pieces, by friction welding extensions onto the short transverse sections (figure2.3.9).

2.3.2. Impact resistance.

It is well known that an increase in volume fraction of inclusions leads to a decrease in impact shelf energy▼(151. 174, 189, 190.), and Kinoshita et al (167) have observed that impact values are decreased with increase in the number of fine inclusions (less than 5 μm).

However, the influence on impact transition temperature is less convincing, and Dahl (174) and Roesch (189.) indicate very little effect, whereas Pickering (151.) has indicated that there is some work which does show an effect. In his review Pickering has observed that low volume fractions of sulphides caused the transition temperature to rise, whereas at higher volume fractions the transition temperature was lowered (particularly noticeable in the longitudinal test direction, figure 2.3.12)

Anisotropy is observed to influence the impact behaviour

▼(Figures 2.3.10&2.311)

2.3.9.

Method of extraction of short transverse tensile specimen.

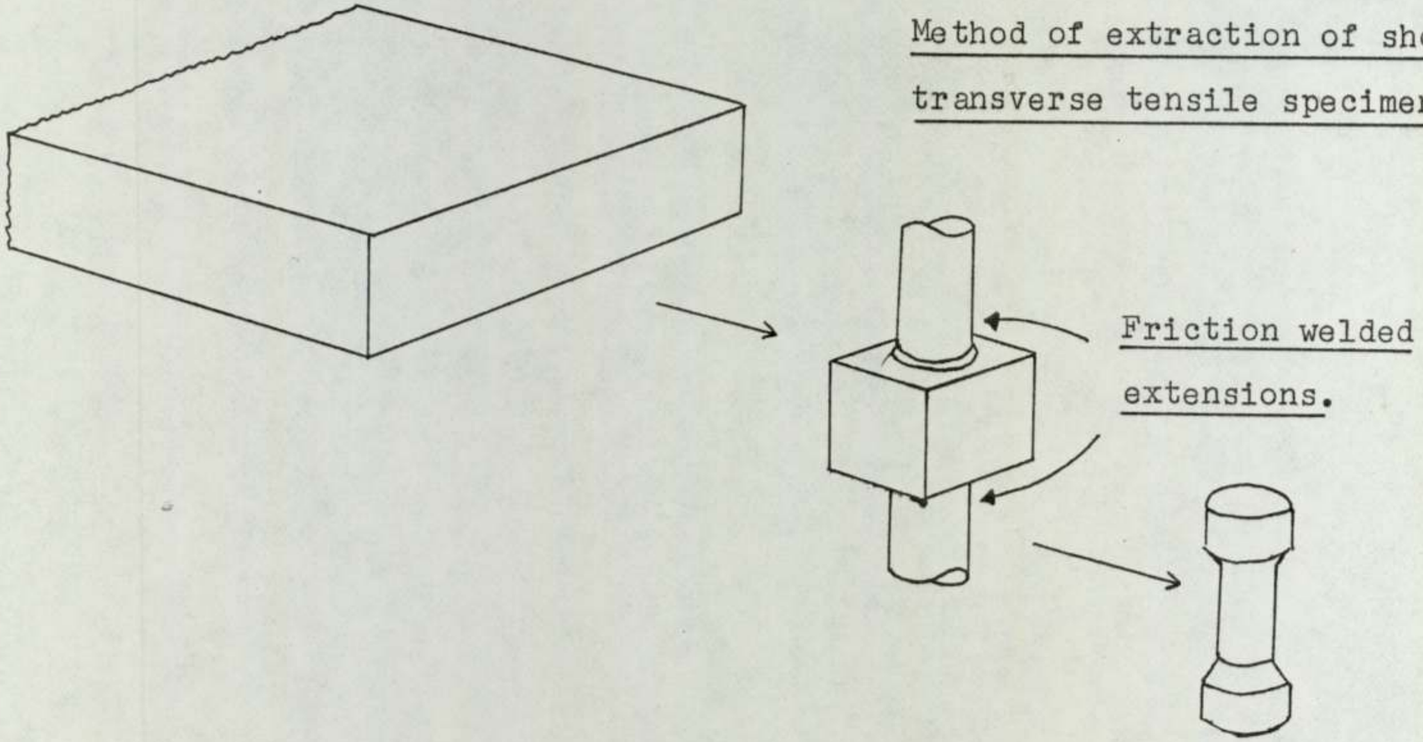

2• 3 •10

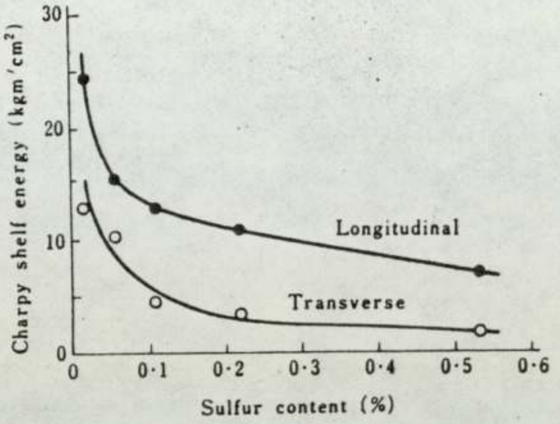

Effect of sulfur content on Charpy shelf energy.

2 • 3 • 11

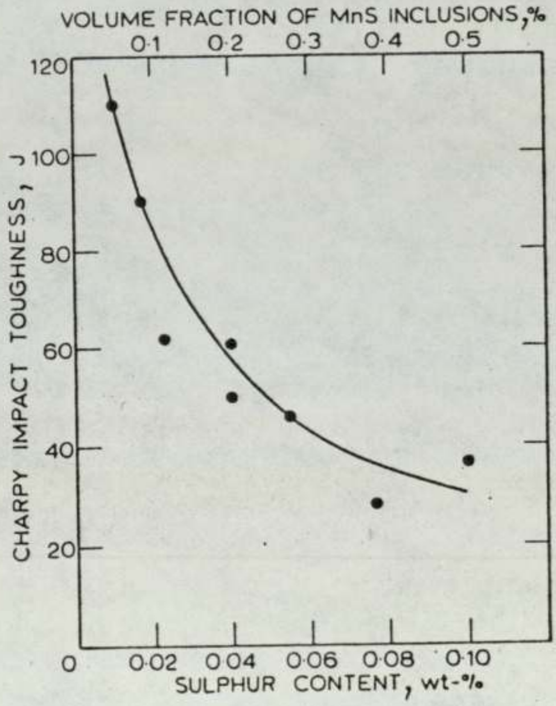

4

Effect of inclusion volume fraction on transverse impact toughness

2 • 3 •1 2

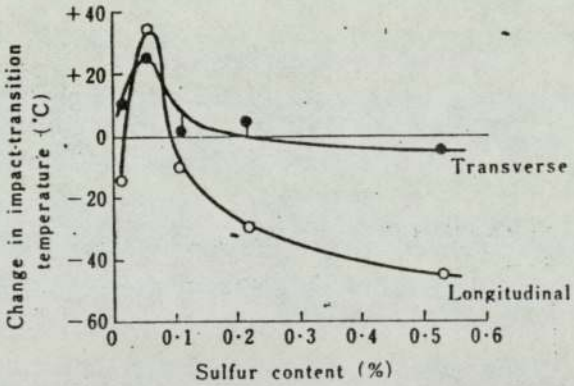

Effect of sulfur content on impact-transition temperature.

of steels (151.) and deformable sulphide and oxide inclusions give rise to anisotropy of impact values. The planar form of inclusions in rolled material is considered to be analogous (191.) to a composite of thin lamellar plates, and should promote transition from cleavage to fibrous fracture at lower temperatures due to a relaxation in triaxiallity of stress (192.). Walker and Barr (192.) have shown that the transverse upper shelf energy is reduced by the presence of lamellar inclusions (fig 2.3.13).

Pickering (151.) has commented that at low volume fractions inclusions act as crack nucleation sites which have the effect of increasing the impact transition temperature. At higher levels of volume fraction although the number of nucleation sites is increased, crack propagation is impeded by the greater number of obstacles, therefore decreasing the transition temperature. Elongated inclusions are the most effective obstacles to crack propagation, and this was considered an analogous situation to the work of Embury (191.) who had observed similar effects with mild steel laminates.

2.3.3. Fatigue.

One of the principal features of non metallic inclusions has been their action as stress concentrations in fatigue situations. Fatigue properties have been related to inclusion content, size and composition (193 - 195). Inclusion deformation characteristics have also been shown to influence fatigue. In rolled alloy steels brittle and non deformable inclusions were found most detrimental to fatigue properties (196.). Andrews in a recent review (197)

2.3.13

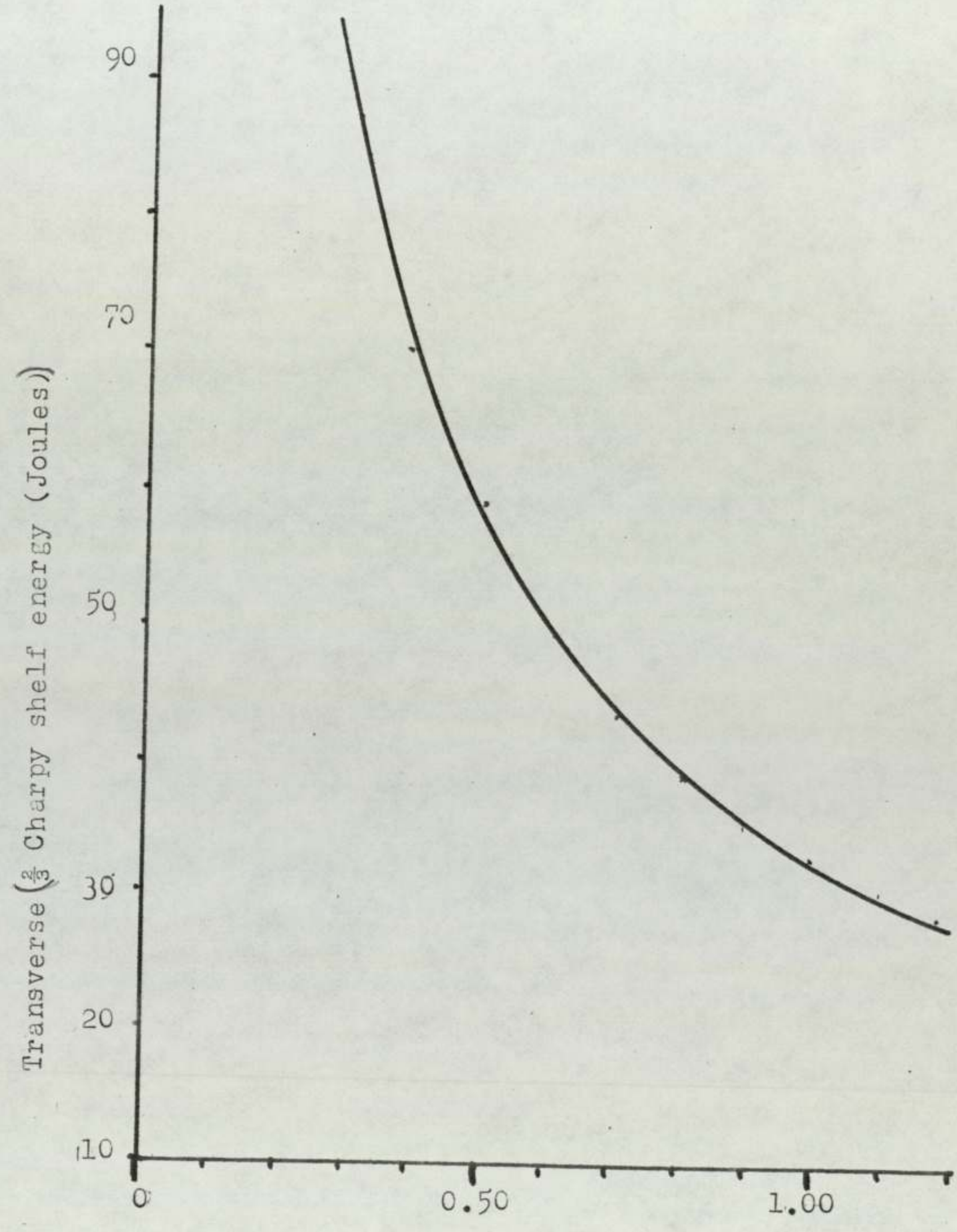
90
70
50
30
20
10
0
0.50
1.00
Transverse (⅔ Charpy shelf energy (Joules))
Total projected length (mm/mm^2)

has summarised diagramatically the influence of inclusions upon fatigue properties (figures 2.3.14).

Brookesbank and Andrews (198.) have used and commented upon photoelastic analogue techniques as a means of representing stress fields around inclusions. The authors consider that there is some confidence in the method, on the basis that observed stress fields agree closely with those calculated for the plane stress situation. They have also shown that pairs or clusters of inclusions provide a more hazardous condition than single inclusions of the same size.

Andrews (197.) in his review stated that Tessellated stresses arise around inclusions and second phase particles because of differential thermal contractions of matrix and particle, and were of the form

$$\phi\left[(\alpha_m - \alpha_i)\Delta T\right]$$

where α_m and α_i are the thermal expansion coefficients of the matrix and inclusion respectively. ΔT is the temperature change (negative) and ϕ is a compliance factor dependent upon elatic moduli, size, shape and inclusion distribution.

The influence of expansion characteristics upon stress and void forming potentials is shown in figure (2.3.15)

From this figure it may be seen that MnS is not a stress raiser, but a potential void former. It may be possible that the presence of sulphide shells around oxide inclusions (as observed by Trigwell (183)) effectively reduce the stress raising potential of an inclusion

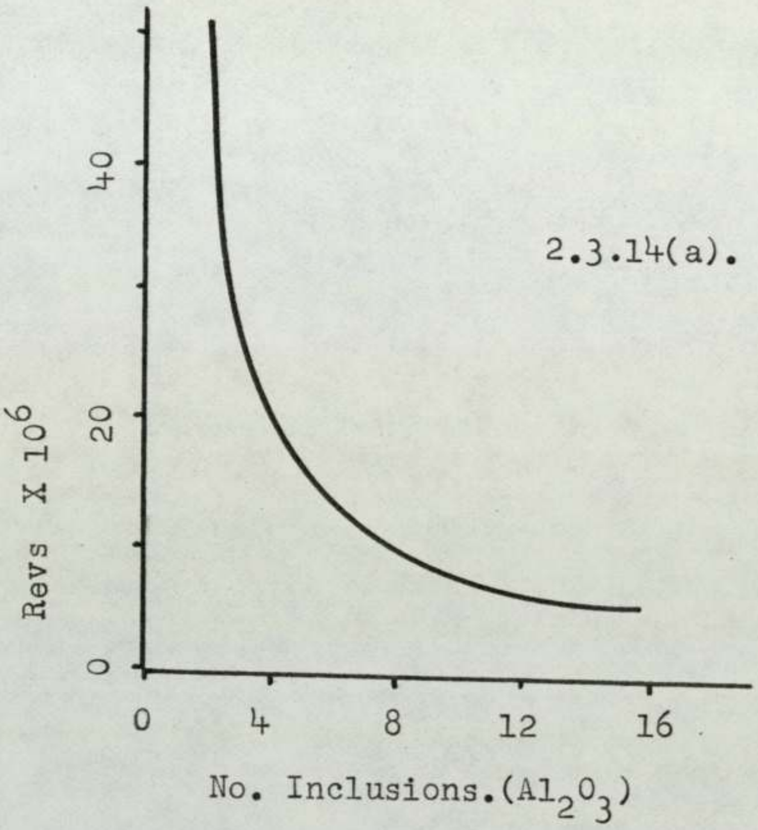

2.3.14(a).

Revs X 10^6
0
20
40
0
4
8
12
16
No. Inclusions.(Al_2O_3)

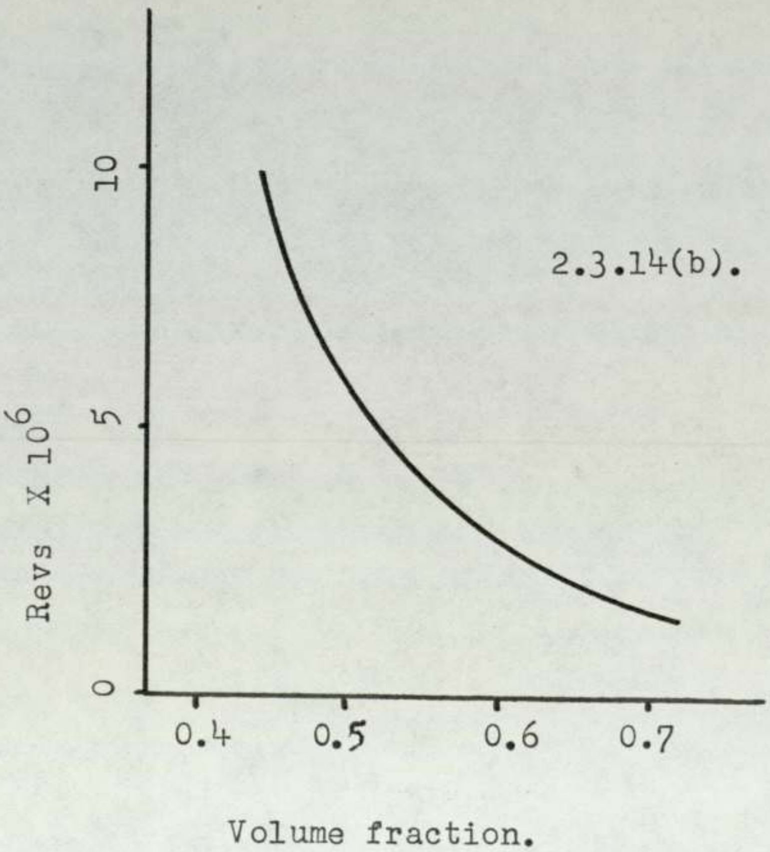

2.3.14(b).

Revs X 10^6
0
5
10
0.4
0.5
0.6
0.7
Volume fraction.

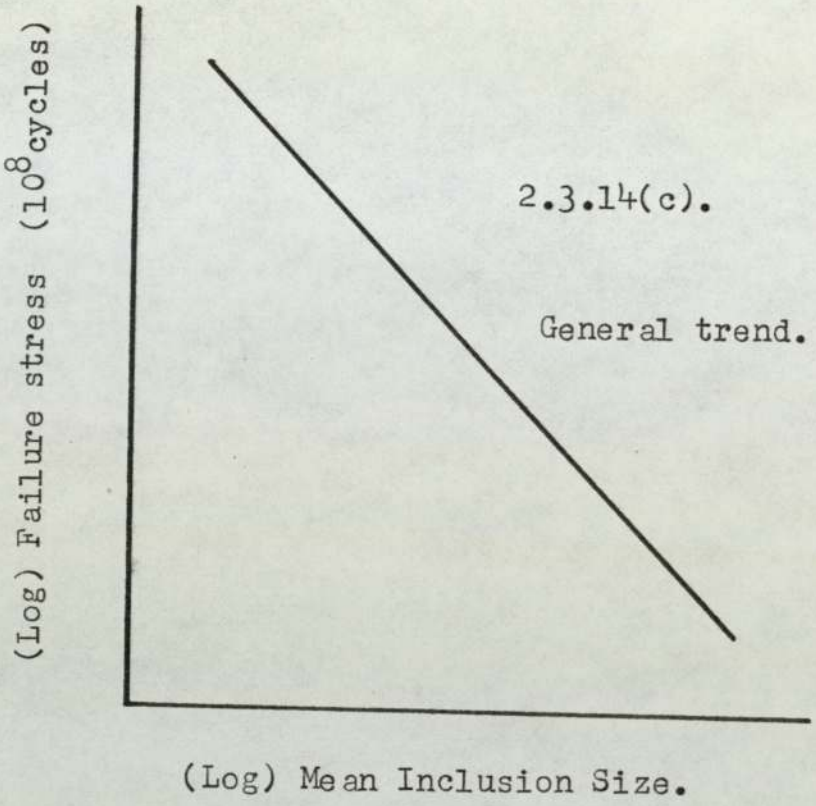
(Log) Failure stress (10^8cycles)
General trend.
(Log) Mean Inclusion Size.

2.3.14(c).

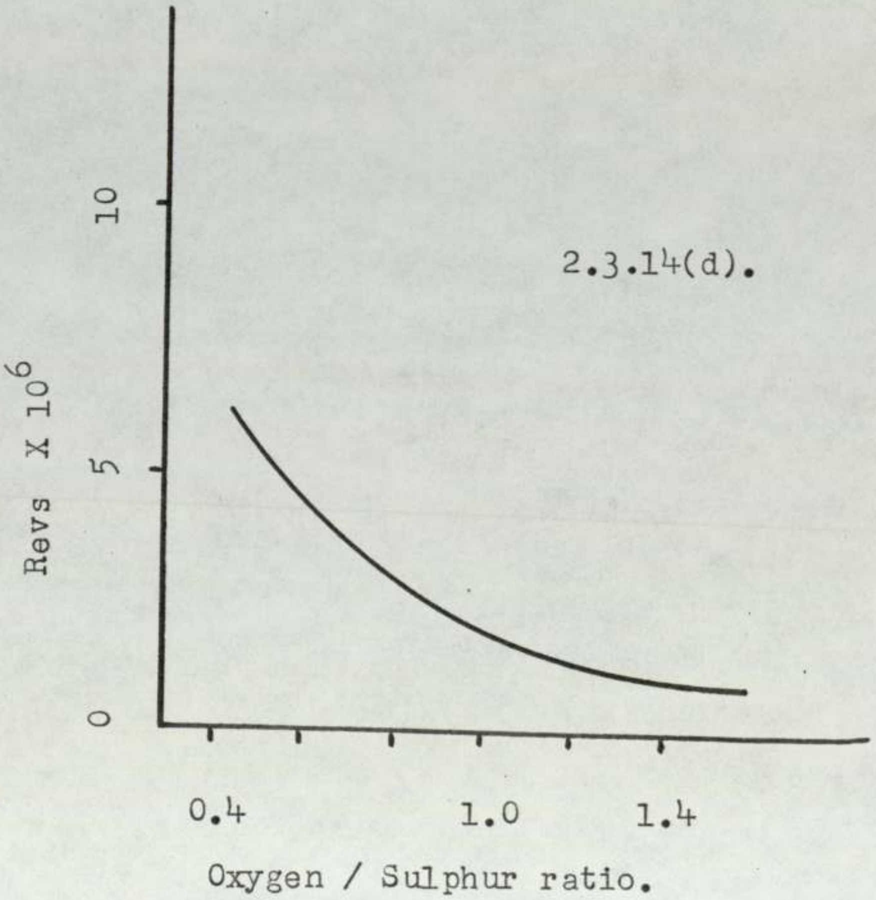
Revs X 10^6
10
5
0
0.4
1.0
1.4
Oxygen / Sulphur ratio.

2.3.14(d).

2 • 3 • 15

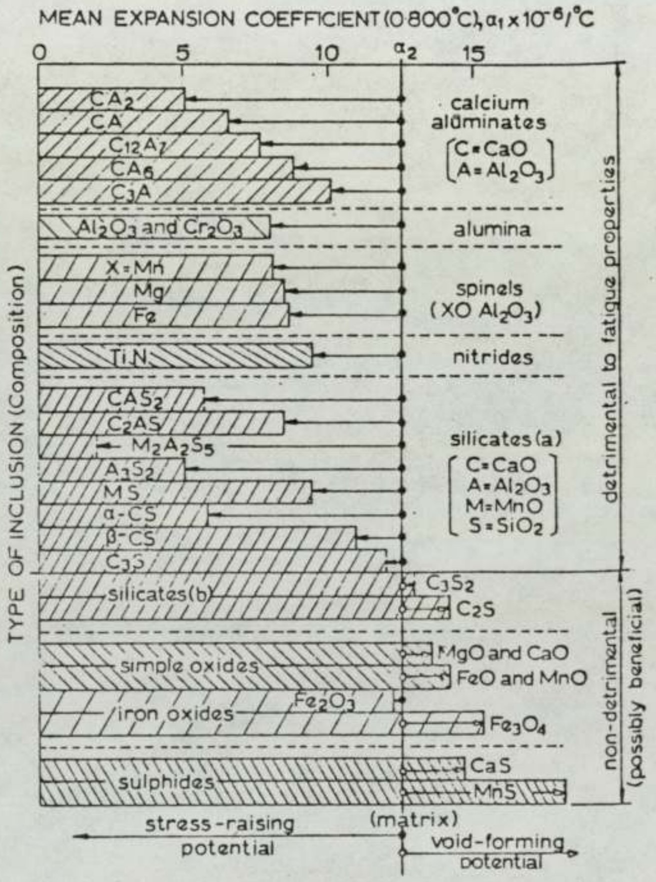

Stress-raising properties of inclusions in 1%C–Cr bearing steels

or alleviate some of the stress by localised plastic deformation in the shell.

In considering the influence of non-metallic inclusions upon fatigue properties the matrix properties should be considered. In high strength steels such as the 1%C 1.5%Cr bearing steels (196.) which have a small critical. defect size and little ability to blunt cracks the presence of inclusions is critical In lower strength steels the critical defect size is larger and crack propagation is less rapid and the presence of inclusions is less dramatic. This critical defect size may be given

$$d = k(k_f)^3$$

where d = inclusion diameter

k = constant

K_f is the ratio $\frac{N_f \text{ (without inclusion present)}}{N_f \text{ (with inclusion present)}}$

and N_f is the N° of cycles to failure. It has ~~though~~ been found that the preferential nucleation of voids occurs at inclusions irrespective of matrix strength.

Fatigue properties of steels are subject to the influences of inclusion distribution with respect to the presence of inclusions at the surface of a component causing premature failure. Surface inclusions may be contributing factors leading to the wide distribution of fatigue test results.

Kiessling (10.) has suggested that the high plasticity of MnS restrains it from acting as a crack nucleation site and therefore does not influence fatigue properties. He also indicated that inclusions with high plasticity indices would be able to absorb some of the stresses developed at the inclusion/matrix interface during fatigue cycling. In the light of the work of Andrews (197.) however, the less injurious nature of MnS may be attributed to its contractional characteristics.

2.3.4. Machinability.

It has been recognised (199.) that the presence and properties of non-metallic inclusions influence the machinability of steels. Where the presence of non-metallic inclusions is beneficial, economic savings may be made.

Inclusions if they are to be of benefit should initiate crack formation and embrittle swarf by their action as stress concentraters. Although inclusions are encouraged to participate in the increase in shear of the metal flow zone, they should not disrupt metal flow and/or impair the working characteristics of the tool, or abrade the work face In addition they should ideally act as diffusion barriers at the rake face of the tool at the interface temperature.

How well inclusions conform to the above specifications is governed by numerous factors.

2.3.4.1. Inclusion type and morphology.

It is generally recognised that exogenous particles are detrimental to machinability, primarily due to their being of a refactory nature. In addition it has been reported (199.) that the globular type MnS is preferred to types II and III MnS morpholgy.

2.3.4.2. Compostion and deformability of inclusions.

Manganese sulphide has been an important acceptable inclusion phase because of its highly deformable nature over a wide range of working temperatures. However, the presence of duplex MnO. MnS type inclusions, lowers the inclusion deformability.

Oxide inclusions are normally avoided because of their high softening/melting temperatures. However, Trent (200) and Opitz & Konig (201.) have shown that under certain cutting conditions deoxidation products may act in a similar manner to MnS. They have pointed out that some inclusion compositions in the $MnO-SiO_2-Al_2O_3$ and $CaO-SiO_2-Al_2O_3$ systems deform in the steel 'flow zone' at temperatures of 1000°C. Keane (199.) has indicated that with high strength steels, where the cutting temperatures are high, and the deformability of MnS is low, the use of low melting point (easily deformable) oxides may be advocated.

2.3.4.3. Volume fraction.

It is well known that the machinability of steels is improved by an increased sulphur (therefore increased MnS) levels. The use of higher levels of MnS in free cutting steels led to economic savings in areas of the engineering industry where extensive machining was necessary. However, the influence of an increased volume fraction of MnS above approximately 1% has little beneficial effect (199.).

2.3.4.4. Size and shape.

It is usually the case that 'machining steels' contain MnS as slightly elongated ellipsoids. Although this is usually due to the high temperatures employed in rolling free cutting steels, globular type I inclusions are preferred (202). In order that the inclusions should be beneficial they must deform in the flow zone. However, elongated inclusions show lower levels of deformability once they have been deformed (202), also their orientation to the flow zone makes them less effective.

With regard to inclusion size, the larger inclusions are deemed beneficial. Marston and Murray (203) concluded that the beneficial effect of inclusion size was observed with inclusions greater than 10 μm diameter. It has been shown by Charles and his co-workers (109. 125) that below 5 μm diameter the deformability (plasticity index) of MnS inclusions is impaired.

2.3.5. Influence of inclusions on other properties.

Work by Morinaga et al (204.) has shown that the volume fraction of deformed inclusions influences Erichsen and Torsion test results on sheet material. The Erichsen value at failure was found to decrease with increase in %S (i.e. increased vol. fractionsof MnS), and the degree of cracking in a torsion test increased with increased volume fraction. They did point out that the main influence upon failure was the presence of the larger sulphide inclusions. (2.3.16)

Jones et al (205.) have also cited evidence which indicates that the bend formability of steel is reduced by the increase in inclusion volume fraction.

2 • 3 • 16

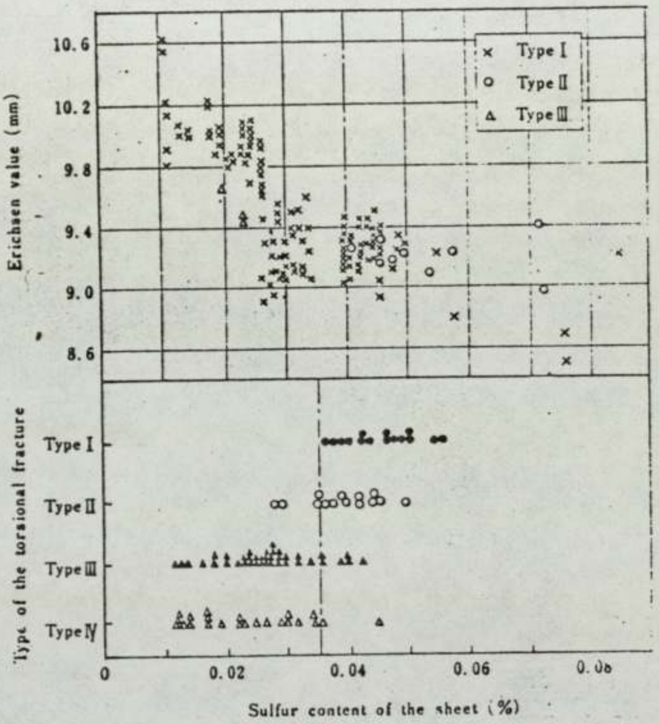

Correlation between the Erichsen value, the type of tortional fracture and the sulphur content

EXPERIMENTAL PROCEDURE.

3.1. Melting and casting procedures.

3.1.1. Selection of experimental conditions.

The experimental melting and casting programme was designed to keep a close control on the production of the various inclusion compositions. The conditions were chosen to provide maximum freedom from external influences and to limit the number of variables which could possibly result from this stage in the experimental programme.

3.1.1.1. Melt material.

The choice of a suitable melt material was based upon two criteria, namely:-

(i) A high oxygen concentration.

(ii) A very low level of sulphur.

The former condition was imposed in order that a high concentration of oxide inclusions could be obtained from the addition of a suitable deoxidant(s). In order for there to be a high free oxygen content in the melt, the presence of oxyphillic elements had to be avoided.

The other condition to be met, was that of limiting the content of sulphur. It is well known (97.) that the presence of oxide/sulphide constituents in deoxidation products influences the latter's character and behaviour in deformation processes.

The material used which fulfilled these requirements was electrolytic iron and the composition of which is given in table 3.1.

Table 3.1.

C	S	P	Si	Mn	Al	O	Fe
0.01	0.01	0.01	0.01	0.01	0.005	0.065	Balance

3.1.1.2. Crucible material.

The governing factor concerning the choice of a suitable crucible material was that it should not react with the melt and/or solutes present. Recrystallized alumina crucibles were chosen, since at the residual oxygen levels aimed for (approx. 0.005wt%) the equilibrium aluminium concentration with that oxygen is approx. 10^{-4} wt%. At this low level it was expected that there would be little reaction between melt and crucible even when there was no aluminium present in the melt.

The oxygen content of the melt was kept as low as possible in the early stages prior to deoxidation. This was essential because the presence of greater than 0.045% oxygen in an iron melt contained within an alumina crucible, may lead to a melt - crucible reaction. Hercynite has been shown to be produced as a result of such a reaction in this system (206.)

3.1.2. Experimental equipment.

3.1.2.1. Melting furnaces.

The two furnaces used in the production of the deoxidant alloys, and in the melting of the electrolytic iron were both linked to the same high frequency melting unit. The melting unit contained a motor alternator set to supply a high frequency current at 8.5kHz. The maximum rating of the unit was 15kW and power factor correction was by switching in appropriate capacitance as required.

A schematic vertical section of the iron melting unit is shown in figure 3.1. The only basic difference between this and the unit used in the production of the deoxidant alloys was that the capacity of the deoxidant unit was 80% smaller. In both cases the susceptors were machined from electrode graphite, the machining ensuring that there was a close tolerance fit when the crucibles were in place. This prevented excessive wear due to circulating gases .

Temperature measurement was by means of two platinum/ platinum - 13% rhodium thermocouples connected to a twin pen recorder. One thermocouple was fitted into the base of the susceptor, thus enabling the susceptor temperature to be monitored during the melting period. The second thermocouple was used for immersion in the molten melt. This second thermocouple was protected by a silica sheath, and access to the melt was via the sampling hole in the susceptor lid.

FURNACE ASSEMBLY

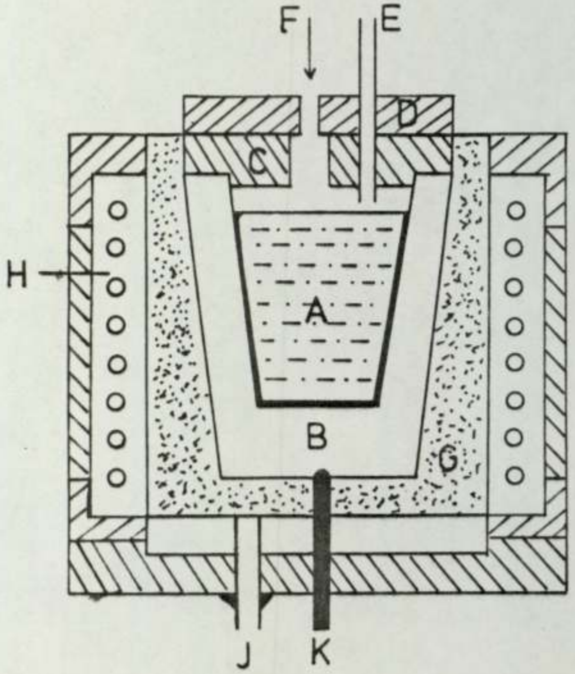

A : IRON MELT IN ALUMINA CRUCIBLE.

B : GRAPHITE SUSCEPTOR

C : SUSCEPTOR LID

D : GRAPHITE COVER

E : ARGON INLET TUBE

F : SAMPLING HOLE

G : FURNACE LINING

H : WATER COOLED INDUCTION COIL

J : EARTH LEAKAGE SPIDER

K : THERMOCOUPLE SHEATH

Fig. 3·1

3.1.2.2. Furnace atmospheres.

It was considered necessary to prevent oxidation of both deoxidant alloys and the iron melts. Any such oxidation would cause the calculated deoxidant addition to be erroneous in respect of its deoxidising capacity, and result in inclusion compositions different to those expected.

The exposed surface of the melt was therefore protected by a non oxidising atmosphere. The iron melts were protected by argon flowing at a controlled rate of 2.5 litres per minute. The deoxidant alloys however were melted under a hydrogen atmosphere, but cooled under argon. The hydrogen flow rate was 2.5 litres per minute, and the argon flow rate was 10.0 litres per minute.

3.1.3. Selection of deoxidant compositions.

The choice of deoxidant alloy compositions was primarily based upon the products of Mn - Si and Mn - Si - Al deoxidation with liquidus temperatures below 1300°C. This ensured that the products were liquid at the maximum rolling temperature of 1300°C. Figure 3.2. shows the liquidus surface for the MnO - SiO_2 - Al_2O_3 system at 1300°C.

The deoxidant additions required to give the desired products were calculated assuming specific initial and final oxygen levels, 100% utilisation of the deoxidant elements and appropriate solute equilibrium data at 1600°C. A detailed calculation of a typical deoxidant alloy is shown in Appendix 3.1 . This illustrates the idealised way in

Fig 3.2

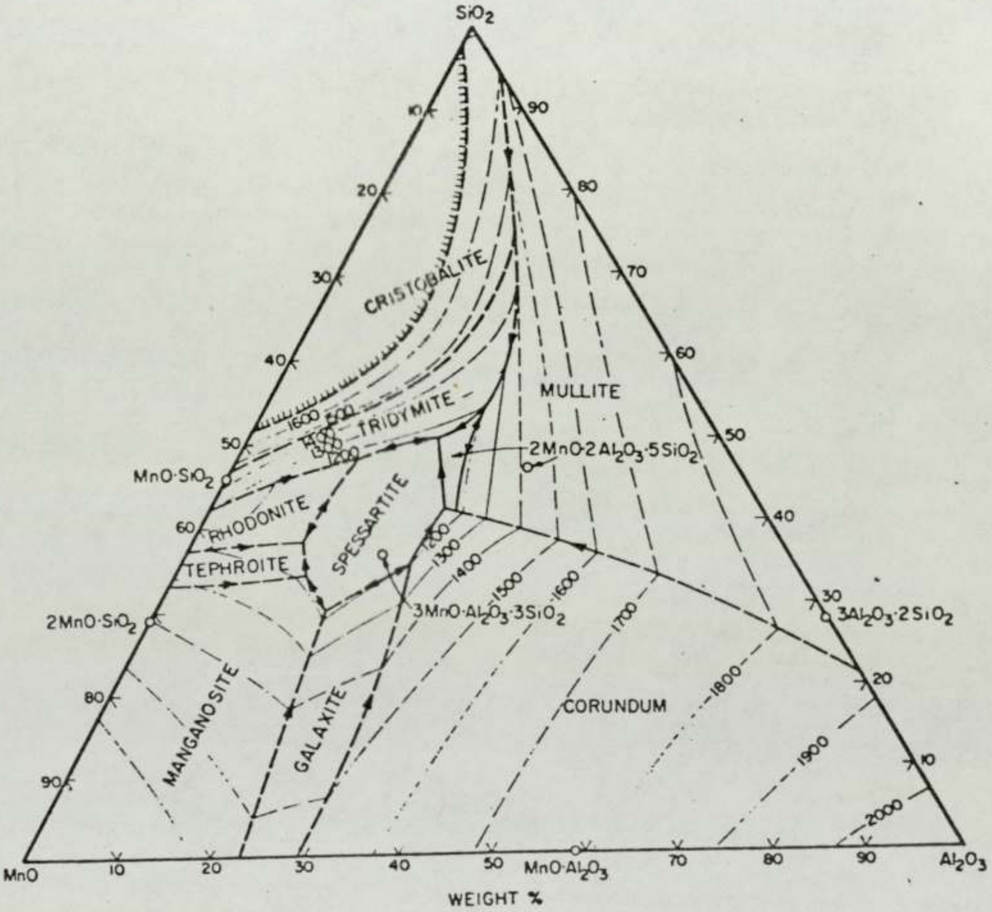

Liquidus temperatures for the SiO$_2$-MnO-Al$_2$O$_3$ system.

which oxygen in the melt is distributed between the manganese silicon and aluminium present in the deoxidant. The total deoxidant addition was computed from the individual stoichiometric and equilibrium additions for the various elements present in the alloy. Appendix 3.2 summarises these values for each of the deoxidants used.

3.1.4 Preparation of deoxidant alloys.

The correct proportions of electrolytic manganese flakes and granular silicon were intermixed and transferred to an alumina crucible. The constituents were then melted under a hydrogen atmosphere. When molten the susceptor lid was removed and the super pure aluminium (when required) stirred in, and the lid refitted. The hydrogen atmosphere was then displaced by argon, and the ingot allowed to cool under the argon blanket.

The resultant ingots approximately 200 gms in weight were removed from their crucibles and their surfaces ground and wire brushed to remove any adherent oxide films. They were then crushed and ground to particle sizes less than 500 µm. The powders so produced were considered to be more homogeneous than the alloys in lump form, which in many instances had a coarse needle like structure, observed when the ingots were fractured.

3.1.5. Experimental melts.

3.1.5.1. Iron - oxygen alloys (melting procedure).

1.5kg of Japanese electrolytic iron was weighed out and the majority of the charge transferred to a clean alumina crucible. This was then placed in the graphite susceptor. The susceptor lid and cover were set in place and the argon flow (2.5 litres per minute) turned on at an initial power input to the furnace of 5kW. The susceptor temperature was continuously recorded. When a temperature of 1600°C was reached the power input was increased to 12 - 13kw. Once the charge was observed to be molten the susceptor lid and cover were removed and the balance of the charge added, replacing the lid and cover after the addition. When the charge was again observed to be molten, the power input was reduced to approximately 9kW. Using the immersion thermocouple in conjunction with the susceptor thermocouple the power was adjusted to give a stabilized melt temperature of 1600°C.

At this temperature a sample of the iron - oxygen melt was taken, prior to the addition of a precalculated quantity of iron oxide (Fe_2O_3) to bring the oxygen content of the melt up to approximately 0.09 - 0.10 wt%. Appendix 3.3 gives details of the addition. After a period of approximately 5 minutes a second melt sample was taken to determine the oxygen content of the melt at the time of deoxidation. At this stage the susceptor lid and cover were removed and a predetermined amount of powdered deoxidant was stirred into the melt. As soon as the deoxidant had dissolved, the molten charge was immediately suction cast into a silica tube, and the furnace switched off.

3.1.5.2. Sampling and deoxidation procedure.

Sampling of the melt was performed by drawing off approximately 10gms of metal into a 3mm bore silica tube. The partial vacuum required was obtained by the use of a hand aspirator. The silica tube was inserted into the melt via the sampling hole in the lid, and withdrawn 1 - 2cm from the bottom of the crucible before taking the sample. By this method samples were always taken from a similar plane in the melt.

Deoxidant additions were made by plunging the shim steel cartridge containing the deoxidant below the melt surface. The deoxidant was stirred into the melt for between 5 and 15 seconds prior to instantaneous casting.

3.1.5.3. Casting technique.

The technique of suction casting was hoped to ensure a uniform dispersion of deoxidation products throughout the as cast bar , and to prevent any reoxidation of the products during casting. The suction casting apparatus consisted of a nominally 24mm internal bore silica tube 350 - 1000mm long attached via pressure tubing to a vacuum pump. The partial vacuum employed was 200mm.Hg, which ensured that a bar of material approximately 300mm long was produced. A small amount of metal however always remained in the crucible which was later removed. A vacuum less than 200mm.Hg. resulted in a lower yield of cast bar, but a value much above 200mm resulted in the production of a tube.

3.1.5.4. Sectioning of cast bars.

The sectioning of the as cast bars is schematically shown in figure 3.3. for an ideal situation. Samples taken for hot rolling were hopefully in the region of 80mm in length, although this was dependant upon the material yield. Samples taken for as cast metallography and microprobe analysis were transverse sections. These sections had a maximum thickness of 10mm in order that they would fit into the specimen stage of the microprobe analyser.

3.1.6. Development of programme.

Two short experimental series were made, one which involved the addition of alloying elements to the melt, and the second in which extra aluminium was added to the powdered deoxidant.

In the first series which used alloy DA12 as the deoxidant the variation in experimental procedure with respect to the alloying additions was:-

Melt Code	Alloy addition	Comments
NI50A12	50% Ni	Added as Ni pellets in the charge material
NIA12	1%Ni	Added as Ni pellets in the charge material
CRA12	1% Cr	Added as powdered ($< 500\ \mu m$) ferrochromium in a shim steel cartridge immediately after deoxidation and stirred

Idealised sectioning of 'as cast' material.

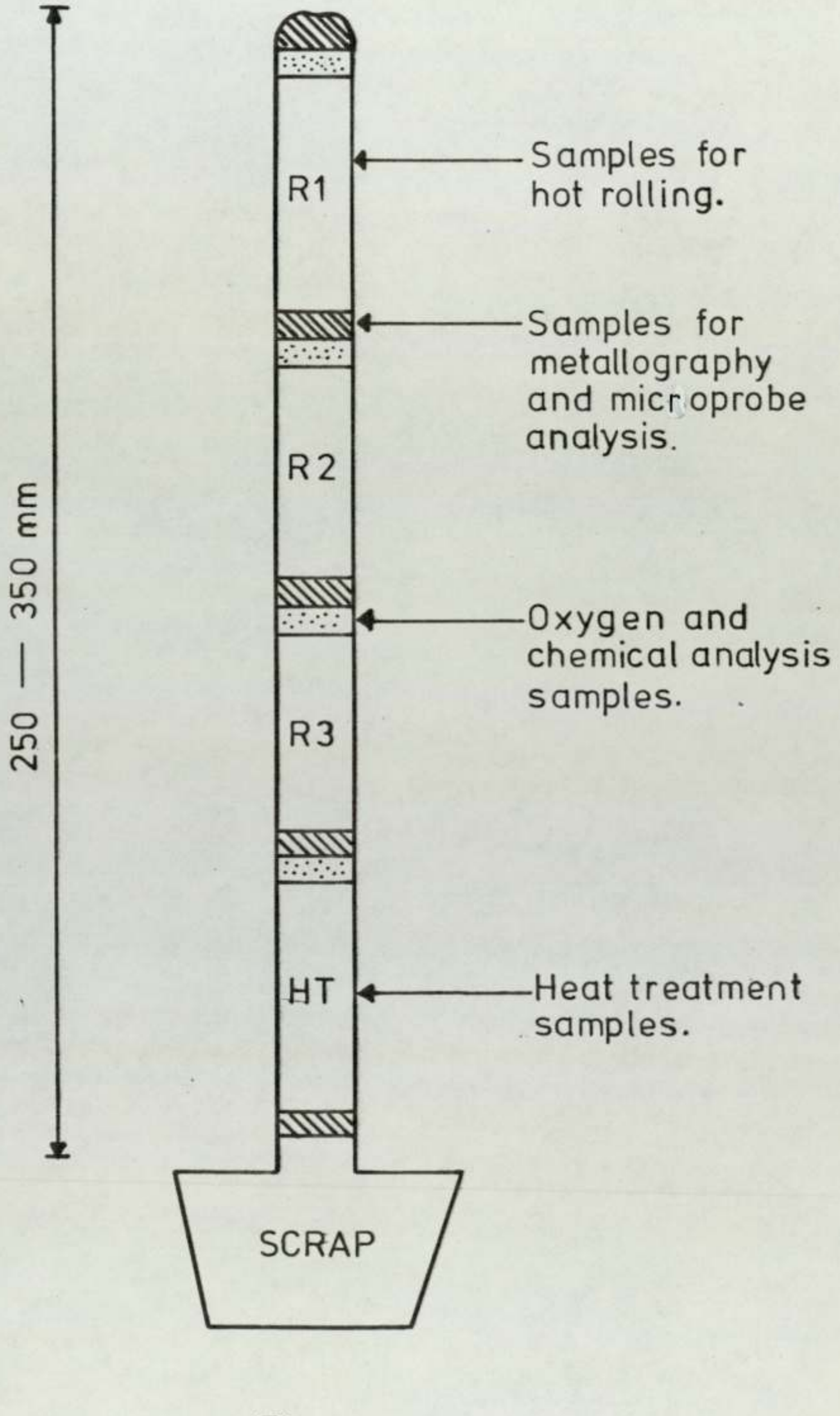

Fig. 3·3

Melt code	Alloy addition	Comments
		into the melt prior to casting.
VAl2	1% V	Added as ferrovanadium as for melt CrAl2

In addition a melt using deoxidant alloy DAl4 had 0.2% carbon (in the form of powdered graphite) added via a shim steel cartridge directly after deoxidation. (Coded Al4C). However, a large proportion of this was lost by ignition and apparent melt effervescemce.

In the second second series of experiments, deoxidant DAl4 was used with extra aluminium admixed with the powdered deoxidant. In order to observe the influence of aluminium on product composition for a given deoxidant, extra additions of 0.022% and 0.044% **Al** were made. These melts were coded Al7 and Al8 respectively.

3.2. Rolling prodedures.

3.2.1. Selection of experimental conditions.

3.2.1.1. Sample reductions.

The as cast material was rolled at 20% reduction in height per pass. (True strain of 0.22). Thus ten passes were required to obtain a nominal 90% total reduction (table 3.2.). However the first 20% reduction was usually performed in two 10% passes. A rolling schedule was derived by test rolling 25mm diameter mild steel (EN3) bars, and experimental material at various rolling temperatures. Thus the mill was calibrated, and appropriate mill settings

HOT ROLLING PROGRAMME

NOMINAL THICKNESS h (mm) Entry	pass No.	Exit	TOTAL REDN. $\%R_h$	TOTAL (ε_m) TRUE STRAIN $\ln {}^{h_o}/_h$
25.00	1	20.00	20.00	0.2231
20.00	2	16.00	36.00	0.4462
16.00	3	12.80	48.80	0.6693
12.80	4	10.24	59.04	0.8924
10.24	5	8.19	67.24	1.1155
8.19	6	6.55	73.80	1.3386
6.55	7	5.24	79.04	1.5617
5.24	8	4.19	83.24	1.7848
4.19	9	3.36	86.56	2.0079
3.36	10	2.68	89.28	2.2310

20% Rd^n/pass i.e. ε_m/pass = 0.2231

Table 3.2

were derived for each strain increment.

3.2.1.2. Rolling Temperatures.

The range of temperatures employed during the investigations was 600°C - 1300°C, the relevant temperatures used were determined by the type and composition of inclusion under investigation. In order to ensure that the material was rolled at the required temperature a series of calibration experiments were performed to determine the temperature drop from the furnace to the rolls. Samples of material of various thickness and at various temperatures were withdrawn from the furnace. The fall in temperature 3 seconds after removal from the furnace was measured at the centre of the bar/strip by means of a platinum/platinum - 13% rhodium thermocouple. The results have been plotted in figure 3.4.

Actual transfer times were observed to vary between two and five seconds depending on the stage of reduction.

When working at 1000°C and below, the soaking temperature was 10°C higher than the rolling temperature, up to 50% total reduction in height, after which the excess temperature was 20°C until the strip was 5mm thick. At temperatures of 1100°C and above the excess temperature employed was 20°C up to 50% reduction. Beyond 50% reduction excess temperatures of 30°C, 40°C and 50°C were employed at 1100°C, 1200°C and 1300°C respectively until the strip was 5mm thick. When the material was less than 5mm thick approximate temperatures for soaking were estimated from figure 3.4.

No allowance was made for the cooling effects of the

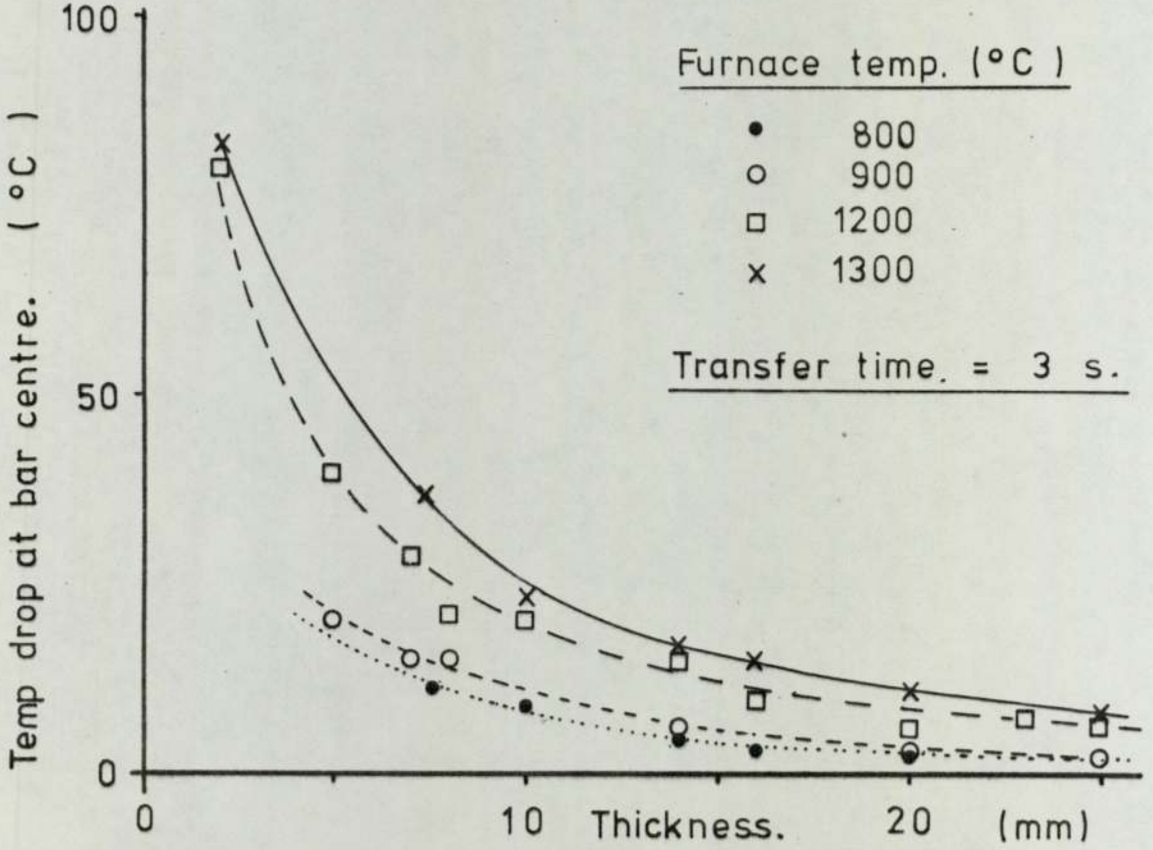
Furnace temp. (°C)
● 800
○ 900
□ 1200
× 1300
Transfer time = 3 s.
Temp drop at bar centre. (°C)
100
50
0
0
10
Thickness.
20
(mm)

Fig. 3·4

rolls due to the complex nature of heat flow. The use of complex heat flow equations and numerous assumptions, would have led to a result subject to large errors. Simple calculations show that the contact time of the rolls with a given element in the material is of the order 0.05 seconds. In addition there is an insulating effect of an oxide scale layer and also heat derived from working the material.

Deformation heating effect is increased as the thickness of the material decreases due to the increased rate of deformation. Asante (103.) has shown that the temperature rise is in the range 5° - 10°C for a 10% reduction in height.

3.2.2. Experimental equipment.

3.2.1.1. Rolling mill.

Rolling was carried out using a 2 high 'Robertson' mill, with 0.203m diameter rolls and a peripheral roll speed of 0.42Ms^{-1} (i.e. 40 R.P.M.). Sheet asbestos insulation was used at the roll feed in order to minimise heat loss.

3.2.2.2. Furnaces.

Two furnaces were used for preheating and reheating material between passes. Both furnaces were electrically heated, and had the facility for partially controlled atmospheres of $90\%N_2 - 10\%H_2$ to limit oxidation. The larger furnace ($\sim 0.6\text{m}^2$ hearth) had a maximum operating temperature of 1050°C, and the smaller ($\sim 0.1\text{m}^2$hearth) 1400°C. The smaller furnace used an Inconel support to prevent the sticking of samples to refactories, caused by refactory - iron oxide fusion at high temperatures.

Both furnaces had automatic temperature control but during heating and reheating the 'hot zone' temperature was monitored using Pt/Pt-13%Rh thermocouples. The maximum number of samples in the furnaces at any given time were 3 in the larger and 2 in the smaller.

3.2.3. Sectioning of rolled samples.

Sectioning of the rolled material was normally parallel to the rolling direction and perpendicular to the plane of rolling. (i.e. the (XY) plane in figure 3 .5.)
Sections were occasionally taken on the (XZ) and (YZ) planes (figure 3.5.). During this sectioning care is needed to ensure that the cutting does not deviate from the section plane, particularly important on the (XZ) plane otherwise inclusion aspect ratios are not true values. In addition it was essential that material was not taken from the ends of the rolled strip, because of the non representative metal flow. (Illustrated in figure 3.5.). For (XY) samples taken for 'probe' analysis the maximum allowable depth in the Z direction was 10mm.

3.2.4. Plasticine model system.

In order to obtain the homogeneous patternof deformation of the steel matrix in these experiments, a plasticine model system was used. Hopefully the deformation of a plasticine composite at room temperature was indicative of the deformation of a hot rolled steel sample.

Numerous pieces of unused plasticine were rolled to a

Fig. 3.5 : Sectioning of rolled samples.

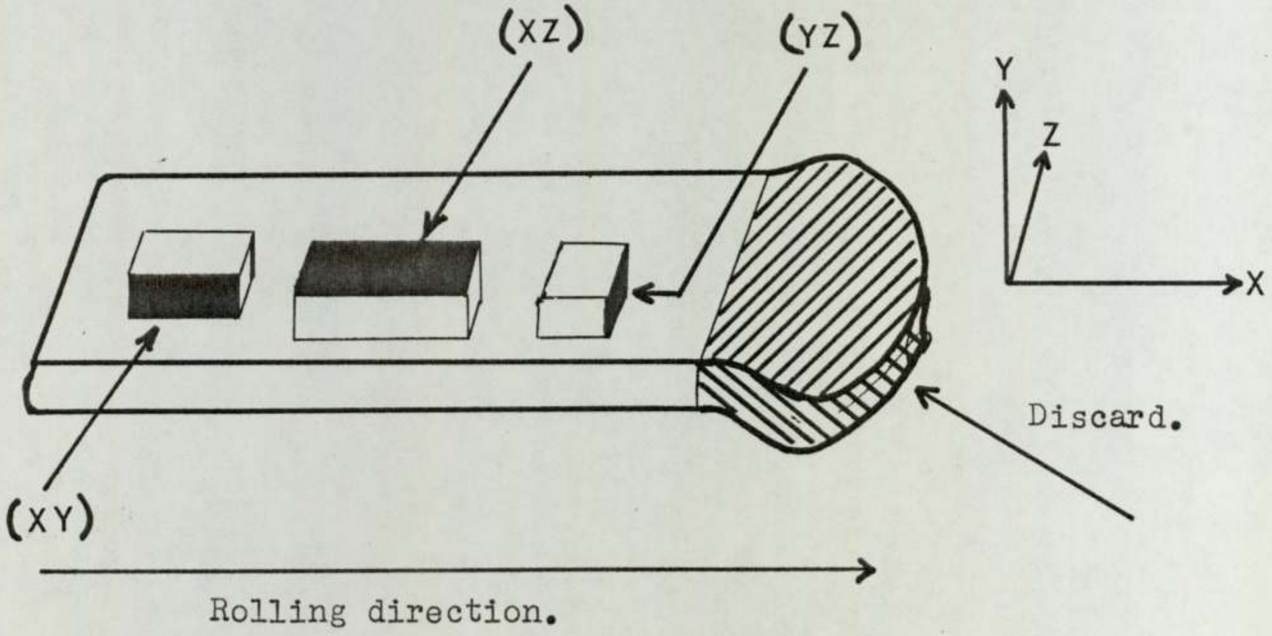

constant thickness in a 2 high mill, using paper to prevent sticking to the rolls. These strips were then lightly pressed together in alternate layers to form composite sandwiches. The composites were 25mm wide x 100mm long, their thicknesses being detailed in table 3.3(below)

Expt.	Initial thickness of strips	No. strips	Measured thickness of composite
1	1.90mm	13	24.7mm
2	1.90mm	7	13.3mm
3	1.40mm	17	23.8mm

These composite samples were rolled in the same 2 high mill as detailed in section 3.2.2.1., again using paper to prevent sticking. Samples of rolled material were taken at various height reductions. Sectioning of the samples in the (XY) and (YZ) planes was performed, and the thickness (height) of each ligament measured using a travelling microscope. The samples were cut using a fine copper wire or hair, coated with petroleum jelly to prevent smearing of the plasticine interfaces. Hair was found to give the clearest results.

3.3. Heat treatment.

3.3.1. Specimen size.

Samples of 'as cast' bars containing inclusions of various compositions within the MnO - SiO_2 - Al_2O_3 system were cut into specimens 10mm x 5mm x 2mm. A small size was chosen in order that they would reach temperature quickly. Because of their size it was important that there should be no oxidation of the samples, and for that reason a vacuum furnace was used.

3.3.2. Heat treatment temperatures.

Heat treatment temperatures were to cover the normal range encountered in hot working i.e. 900° - 1300°C. Three temperatures were chosen to cover this range i.e. 900°, 1100° and 1300°C.

3.3.3. Heat treatment times.

In order to observe the influence of soaking time upon the precipitation of phases within inclusions times ranging from ½ - 64 hours were employed. These times were those after the samples had reached their respective heat treatment temperatures. The time to reach temperature was approximately 30 minutes.

3.3.4. Heat treatment furnace.

The furnace used in this programme consisted of an alumina crucible (100 mm x 30mm) around which was a tungsten resistance element. The furnace unit was surrounded by molybdenum shields and covers, and the unit operated under a vacuum greater than 10^{-4} Torr. A Pt/Pt - 13%Rh thermocouple was placed in situ with the samples and continually monitored the furnace temperature.

3.4. Quantitive analysis.

3.4.1. Compositional analysis.

3.4.1.1. Chemical analysis.

Analysis of total oxygen content was carried out using a vacuum fusion technique. The instrument used was a 'Balzer Exhalograph EAl' which is described by Ramsey et al (207). Samples of steel weighing about 0.2gm were abraded, degreased and dried. The samples were then dissolved in a molten nickel bath contained within a graphite crucible held at 1750°C under a vacuum of 10^{-4}Torr. Under these conditions any oxygen present in the sample (even the stable oxides such as alumina) are reduced by carbon.

The oxygen in the form of carbon monoxide was measured by an infa-red absorption cell. Standardisation and calibration of the instrument was made by metering quantities of pure carbon monoxide into the analytical system.

Analysis of the other elements present in the steel and deoxidation alloys was by standard gravimetric techniques.

3.4.1.2. Inclusion analysis.

Inclusion compositions were determined 'in situ' by the use of a 'Cambridge Microscan 5' electron probe microanalyser The instrument was equipped with two spectrometers, and under normal operation in detecting for manganese, iron, aluminium and silicon, only two crystals were used in the measurement of radiations , i.e. LiF was used for detecting Mn and Fe.

R.A.P. was used for detecting Al and Si.

The detection of nickel, chromium and vanadium also required the use of the LiF crystal. However the detection of sulphur required the use of a P.E.T. crystal. This meant when measuring sulphur in inclusions a crystal change operation was required.

The specimens to be analysed had previously been polished for micro-examination. However, it was essential to ensure that the samples were degreased and ultrasonically cleaned prior to coating with a thin layer of carbon ($\sim$ 200 Å) in a vacuum coating unit. Failure to do this resulted in the contamination of the electron gun and specimen systems. Contamination caused a drastic loss in resolution of absorbed and backscattered electron images, important when looking for/at precipitates in inclusions.

The standards used in the comparison of count rates were pure metals, except when measuring sulphur counts, in which case and FeS standard was used. Using metal rather than metalic oxide standards had previously been shown to give consistently acceptable results. (182. 183.)

In all cases of inclusion analysis reported, an accelerating voltage of 15kV was used. The use of 15kV was however a compromise. Using a higher value of 20kV gave a greater number of counts, at the expense of excitation of a larger volume of material. This effectively increased the minimum size of inclusion which could be analysed with confidence. A lower voltage (e.g. 12kV) although it excited less volume of material, it was approaching the threshold potentials of the lighter elements, thus impairing sensitivity and accuracy of measurement. The minimum size of inclusion which could be measured with some confidence at 15kV was approximately 5 µm, although measurements on inclusions greater than 10 µm was preferred.

Absorption, atomic number and fluorescence corrections were applied to the apparent elemental analysis by the use of a suitable computer programme. (208.) The output of this programme was in terms of wt% oxides. These results were normalised to 100% total oxides where necessary in order to facilitate the plotting of results on ternary graph paper.

The presence of a thin film of carbon, to prevent the electrostatic charging up of the inclusions under the influence of the electron beam, did have the disadvantage of impairing optical viewing. This meant that the direct observation of inclusion hetrogeneity could not be done. It was therefore necessary to produce either an absorbed or reflected electron image to check for hetrogeneity. In addition X-ray images and line scans were used to detect variation in elemental concentration.

If the inclusions were of a glassy nature and with no visible hetrogenity, spot analysis at the centre of the inclusions was used. If however the inclusions were hetrogeneous, line or area scans were used in order to obtain an approximate mean composition.

3.4.2. Metallography.

3.4.2.1. Preparation of microstructures.

Conventional polishing techniques using silicon carbide papers were employed, followed by polishing on 6 μm, 1 μm and ¼ μm diamond impregnated pads. Care was needed to prevent inclusions falling out of the polished surface. It was therefore essential to keep the polishing time to a minimum. Although some inclusions inevitably fell out and scratched the polished surface, this technique was preferred to electrolytic polishing. Electrolytic polishing has the disadvantage of preferentially attacking the inclusion/matrix interface, and thus making it ill defined, which interferes with the measurement of inclusion axes. It may even lead to the smaller inclusions falling out.

Etching the polished structure was not employed because of inclusion/matrix preferential attack. The only time etching was used was in the observation of conical voids around inclusions, and matrix flow. In this case a repeated polish etch technique was used. In almost all cases samples were mounted in conducting bakelite, since they would later be used in the microprobe analyser.

3.4.2.2. Inclusion size and area distributions.

All the as cast bars were subject to quantitative size and area distributuions, samples being taken from the positions indicated in figure 3.3. . The quantitative examination was performed using a 'Metals Research Quantimet - series B' image analysing computer, with a manual stage operation. Inclusion size distribution was measured by counting the number of particles exceeding given diameters, and area distributions were in % area.

Quantitative measurements were made using the X5(0.15N.A.) and X20 (0.5 N.A.) objectives, and the monitor magnification was calibrated using a stage micrometer. The resolution of the system was in the range ½ - 2 µm dependent upon the objective used, and measurements were made for up to 600 fields, again dependent upon the magnification.

3.4.2.3. Aspect ratio analysis.

Sections from the rolled samples at various temperatures and reductions were taken for aspect ratio determinations. The sections and areas limited to inclusion measurement are illustrated in figure 3.5. . Aspect ratios were measured on a'Vickers projection microscope' at x1000 magnification, and the major and minor axes were measured to the nearest 0.5 µm using millimetre lined graph paper. The major axis of inclusions greater than 150 µm in length were however measured to the nearest 5 µm, since these inclusions had to be moved in order that their length could be measured. It must be added that not every deformed inclusion was measured.. Two or more inclusions in very close proximity influence each others behaviour, and were avoided. Also the aspect ratios of inclusions showing bending and folding are difficult to determine and unless the variations in inclusions showing bending were slight they were avoided. Inclusions showing folding were not measured. A note was also made of non deformable inclusions and the frequency of brittle behaviour was noted in some instances.

Inclusion strain was measured on the assumption that the inclusions were initially spherical and that the mode of deformation was 'idealised' plane strain leading to triaxial ellipsoides.

Using these assumptions, the estimated values of inclusion strain in the Y direction on the various planes were measured as:

$$\varepsilon'_{y}(XY) = \tfrac{1}{2}\, \mathrm{In}\, \lambda(XY)$$
$$\varepsilon'_{y}(XZ) = \mathrm{In}\, \lambda(XZ)$$
$$\varepsilon'_{y}(YZ) = \mathrm{In}\, \lambda(YZ)$$

The measurement of the major and minor axes (a , b) also provided an approximation to the size of the inclusion prior to deformation (D_o).

i.e. $D_o = \sqrt{a \times b}$

when measurement was on the (XY) plane.

Plasticity index determinations have been based upon the formula,

$$\nu = \frac{\varepsilon_y \text{ (inclusion)}}{\varepsilon_{my} \text{ (matrix)}}$$

where ε_y is the inclusion strain above, and ε_{my} is the matrix strain in the y direction given by the expression

$$\varepsilon_{my} = \mathrm{In}\, {}^{h_o}/hf$$

where ho and hf are the initial and final heights of the sample respectively.

On this basis the aspect ratios for between 10 and 200 deformed inclusions per sample were measured for inclusion sizes of 1 µm upwards. The mean plasticity index of all the deformed inclusions on the (XY) plane was given by the formula.

$$\bar{\nu} = \frac{\overline{\ln\lambda}}{2\ln(^{ho}/_{hf})} = \frac{\sum^{n}(\ln\lambda)}{2n\ln(^{ho}/_{hf})}$$

3.5. Electron metallography.

Although the majority of this work was concerned with optical examination, electron metallography was performed in order to obtain a three-dimensional picture of deformed inclusions. The unit used for this purpose was a stereoscan fitted with a 'Kevex' energy dispersion analyser which allowed a qualitative appraisal of the elements present within an inclusion or precipitate. In all the work reported here an accelerating voltage of 20kV was used.

3.5.1. Preparation of samples.

The maximum size of sample which would fit into the specimen stage of the stereoscan was 10mm x 10mm, if the specimen was to be rotated. The height of the specimen was also restricted to less than 10mm, and the samples approximately 5mm in height were used throughout.

Deformed inclusions were viewed either 'in situ' in a deeply etched matrix, or as extracted particles adhered to a stereoscan stub. In both cases the sample preparations were similar. The required specimen sections were taken from polished samples and submerged in a boiling mixture of 10% bromine in methanol. In the case of the deeply etched specimens they were left in the solution for 20 minutes, whereas the samples requiring extraction were left for approximately 1½ hours.

After removal from the solution the deeply etched specimens were repeatedly washed in methanol prior to drying. In the case of the 'extraction' samples, the solution was removed from the hot plate and allowed to cool. Subsequently the majority of the liquid was removed by pippette and the residue washed with methanol and allowed to stand. This procedure was repeated several times until there was no discolo~~u~~ration of the added methanol. By this method only the large inclusions remained in the residue. This residue was then washed, filtered and allowed to dry on the filter paper.

These fine residual inclusions were made to adhere to the stereoscan stub by lightly smearing the stub with facially secreted grease (A technique sucessfully used for metal powders (209.)) and pressing the stub lightly onto the residue on the filter paper. The deeply etched samples were stuck to the stub with non stringing clear adhesive and cured for 20 minutes at 40°C. Electrical contact (in this instance) between stub and sample was made by the application of 'silver dag' (a suspension of silver in a volatile solution).

As with microprobe analysis the samples were required to be coated with a conducting medium. This was accomplished by a gold sputtering technique, which gave better results than carbon coated specimens. However, even with the gold sputtering technique several inclusions charged up to some degree, presumably due to the failure of complete contact between the base of the inclusion and matrix of the stereoscan stub.

EXPERIMENTAL RESULTS.

4.1. Analysis of starting material.

The Japanese elctrolytic iron used as the basis of all melts was of the composition shown in table 4.1.below.

Table 4.1. Electrolytic iron composition.

C	S	P	Si	Mn	Al	O
0.01	0.01	0.01	0.01	0.01	0.005	0.055/0.075

Balance Iron

4.2 Oxygen analysis.

Table 4.2. shows the total oxygen contents of the electrolytic iron, including the melt prior to any Fe_2O_3 or deoxidant addition (M.O.), the melt after the addition of the Fe_2O_3 charge (M.O. + Fe_2O_3) and that of the 'as cast' bar after deoxidation.

Figure 4.1. shows the change in total oxygen of the system from 'charge' to 'as cast' bar, and also indicates the mean total oxygen contents at each stage indicated above.

From the analyses it would appear that the melting of the Japanese electrolytic iron resulted in the pick up of approximately 0.017% oxygen. This was probably the result of removing the susceptor lid and argon cover, in order to

Table 4.2

Total oxygen analysis

Melt	M.O. O_T%	M.O.+Fe_2O_3 O_T%	BAR O_T%
A 3	0.090	0.128	-
A 4	0.097	0.104	0.111
A 5 *	0.081	0.109	-
A 6	0.071	0.104	0.086
A 6(2)	-	0.091	-
A 7	-	0.109	0.076
A 8	-	0.127	0.084
A 9	-	0.156	0.149
A10	-	0.113	0.095
A11	-	0,111	0.072
A12	-	0.109	0.088
A13	-	0.102	0.083
A14	-	0.093	0.056
A15	-	0.115	0.046
A16	-	0.106	-
A17	-	0.102	-
A18	-	0.118	-
CRA12	-	0.105	-
VA12	-	0.094	-

* Melt not used in subsequent experiments.

Table 4.2 (cont.)

Analysis of Electrolytic iron samples

J.E.I.	i).	0.078%
	ii).	0.056%
	iii).	0.069%

Mean total oxygen contents

Electrolytic iron n=3	M.O. n=4	M.O.+Fe_2O_3 n=19	BAR n=11
0.068	0.085	0.110	0.086

Fig. 4·1

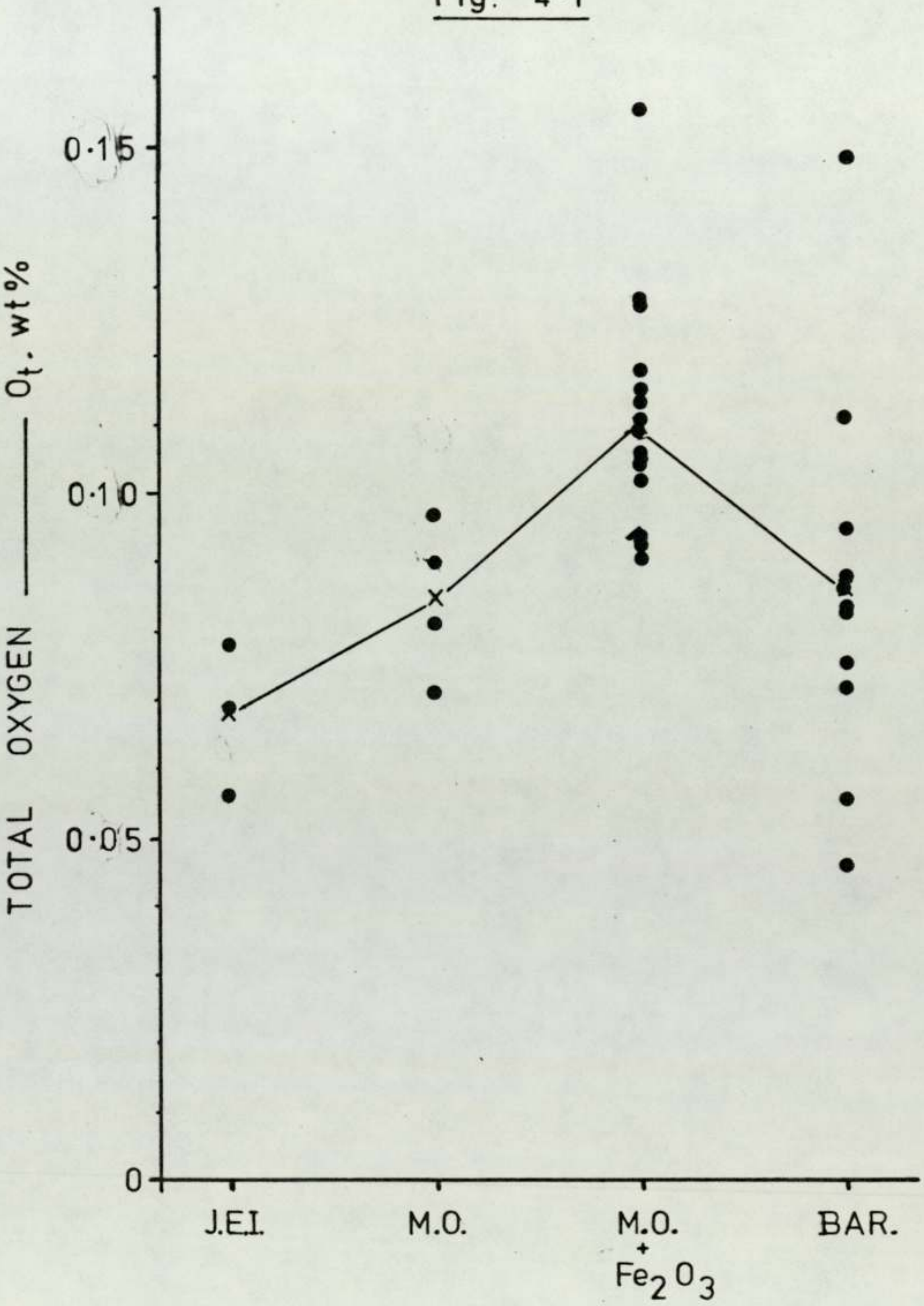

add the balance of the charge. In this period the melt surface was exposed for between 15 and 30 seconds.

The results indicate that the oxygen content as measured in the bar was lower than the melt prior to deoxidation (M.O. + Fe_2O_3). This indicated that the 'as cast' bar analysis was not a very useful guide to the oxygen present, attributable to the flotation of oxide products to the top of the bar.

.4.3
Deoxidant alloys.

Deoxidant alloy compositions and the weight percentage addition made to each melt are given in table 4.3. Calculations of alloy compositions are given in appendix 3.1. & 3.2.

4.4
Melt and inclusion analyses.

Chemical analysis of the 'as cast' bars are given in table 4.4. Microprobe analysis of inclusions are summarised as 'mean as cast' compositions for inclusions greater than 10 µm diameter (table 4.5.). Individual inclusion analysis for all inclusion sizes in both the 'as cast' and rolled specimens are tabulated in appendices 4.1. and 4.2. respectively.

Figures 4.2. & 4.3. show the mean as cast compositions plotted on the binary MnO - SiO_2 and ternary

ALLOY	DEOXIDATION ALLOY COMPOSITION						MELT ADDn wt%
	AIMED FOR			ANALYSED			
	Mn%	Si%	Al%	Mn%	Si%	Al%	
DA3	100	-	-	99.9	-	-	2.00
DA4	-	100	-	-	99.9	-	1.02
DA6	73.31	26.69	-	72.05	28.37	-	2.63
DA7	85.92	14.08	-	84.70	16.82	-	3.32
DA8	90.80	9.20	-	89.21	10.72	-	4.84
DA9	76.67	22.62	0.71	75.90	21.78	0.72	1.69
DA10	83.67	15.67	0.64	83.27	14.69	0.59	1.81
DA11	91.24	8.17	0.58	84.30	7.78	0.52	2.23
DA12	58.45	39.27	2.28	58.85	37.62	2.09	0.96
DA13	71.94	25.93	2.13	71.06	27.02	2.16	1.08
DA14	85.41	12.87	1.72	84.37	11.85	1.83	1.40
DA15	81.46	16.87	1.66	81.26*	17.04	1.70	1.92
DA16	51.30	46.40	2.28	58.45*	39.05	2.50	1.13

* By Difference

Table 4.3

Table 4.4

Chemical analysis of 'as cast' bars

Melt	%Mn	%Si	%Al	%C	%S	%other
A 3	1.37	0.03	Trace	<0.01	Trace	-
A 4	<0.01	0.99	<0.005	<0.01	N/D	-
A 6	1.57	0.57	"	"	Trace	-
A 6(2)	1.31	0.50	"	"	"	-
A 7	2.39	0.37	"	N/D	N/D	-
A 8	3.67	0.34	0.015	"	"	-
A 9	0.84	0.10	"	"	"	-
A10	0.79	0.03	<0.005	"	"	-
A11	1.67	0.08	<0.010	"	"	-
A12	0.36	0.21	"	"	"	-
A13	0.45	0.17	"	"	"	-
A13X	0.36	0.09	0.012	"	"	-
A14	0.88	0.02	"	<0.01	Trace	-
A14(2)	0.77	0.11	<0.005	"	0.001	-
A14C	1.05	0.09	<0.010	0.03	Trace	-
A15	1.11	0.29	0.12	<0.01	"	-
A16	0.41	0.23	0.013	"	"	-
A17	0.78	0.20	<0.005	"	0.002	-
A18	0.79	0.20	"	0.015	"	-
NIA12	0.54	0.29	"	<0.010	0.001	0.98Ni
CRA12	0.37	0.32	"	"	"	0.60Cr
VA12	0.48	0.32	"	0.015	"	0.91V
NI50A12	0.36	0.27	"	<0.010	"	49.16Ni

Mean 'as cast' inclusion compositions. Table 4.5

Melt	Oxide	$\overline{XO}\%$	Range	S.D.	S.E.	N_i
A3	FeO'	3.7	3.4 - 4.1	0.25	0.09	7
	MnO'	96.3	95.9 - 96.6	0.23	0.09	
A4	FeO'	2.2	1.8 - 2.5	0.25	0.08	11
	Al_2O_3'	2.1	1.3 - 3.2	0.59	0.18	
	SiO_2'	95.7	94.8 - 96.5	0.52	0.16	
A6	FeO'	1.4	0.1 - 3.0	0.85	0.19	19
	MnO'	55.7	51.9 - 64.3	2.81	0.65	
	Al_2O_3'	0.2	0.1 - 0.5	0.11	0.03	
	SiO_2'	42.7	35.0 - 46.1	3.10	0.71	
A6(2)	FeO'	3.0	0.0 - 11.1	3.42	1.08	10
	MnO'	53.5	48.7 - 57.6	3.61	1.14	
	Al_2O_3'	0.6	0.0 - 2.7	0.78	0.25	
	SiO_2'	42.9	39.6 - 44.5	3.22	1.02	
A7	FeO'	3.5	0.1 - 16.7	4.56	1.16	15
	MnO'	60.9	52.4 - 67.7	3.46	0.89	
	Al_2O_3'	0.3	0.1 - 0.6	0.13	0.03	
	SiO_2'	35.2	30.6 - 37.8	2.34	0.60	
A8	FeO'	1.1	0.4 - 1.7	0.41	0.12	12
	MnO'	60.6	55.6 - 64.6	2.47	0.71	
	Al_2O_3'	1.2	0.2 - 1.9	0.48	0.14	
	SiO_2'	37.1	34.0 - 42.9	2.31	0.67	

Table 4.5 (cont.)

Melt	Oxide	$\overline{XO}$%	Range	S.D.	S.E.	N;
A9	FeO'	1.2	0.3 - 3.2	0.88	0.17	27
	MnO'	48.3	39.0 - 55.6	4.32	0.83	
	Al_2O_3'	9.0	2.1 - 19.0	4.74	0.91	
	SiO_2'	41.5	38.9 - 45.4	1.95	0.38	
A10	FeO'	2.3	1.3 - 4.1	0.73	0.17	18
	MnO'	56.8	46.9 - 63.8	4.58	1.08	
	Al_2O_3'	5.2	1.4 - 16.5	3.65	0.86	
	SiO_2'	35.7	27.3 - 41.2	3.97	0.93	
A11	FeO'	1.8	0.6 - 4.1	1.02	0.22	22
	MnO'	58.2	53.2 - 66.1	3.85	0.82	
	Al_2O_3'	6.2	1.2 - 18.2	4.04	0.86	
	SiO_2'	33.8	29.7 - 42.1	4.36	0.93	
A12	FeO'	2.5	0.8 - 8.6	1.74	0.28	39
	MnO'	32.1	25.3 - 42.1	4.55	0.73	
	Al_2O_3'	14.3	8.1 - 21.1	2.70	0.43	
	SiO_2'	51.1	43.3 -63.0	4.58	0.73	
A13	FeO'	2.0	0.6 - 4.3	1.15	0.25	22
	MnO'	40.6	30.2 - 56.0	4.48	0.95	
	Al_2O_3'	9.5	3.2 - 15.9	2.94	0.63	
	SiO_2'	47.9	44.3 - 56.0	3.14	0.67	

Table 4.5 (cont.)

Melt	Oxide	$\overline{XO}$%	Range	S.D.	S.E.	N_i
Al3X	FeO'	7.7	6.5 - 8.5	0.77	0.31	6
	MnO'	41.0	35.3 - 45.0	3.75	1.53	
	Al_2O_3'	3.2	2.1 - 4.2	0.89	0.36	
	SiO_2'	48.1	44.6 - 52.0	2.57	1.05	
Al4	FeO'	1.8	0.7 - 3.1	0.67	0.13	16
	MnO'	47.1	41.9 - 54.8	2.72	0.53	
	Al_2O_3'	15.2	6.1 - 23.7	3.74	0.73	
	SiO_2'	39.9	27.8 - 41.4	2.63	0.52	
Al4(2)	FeO'	2.5	1.9 - 4.2	0.71	0.22	10
	MnO'	53.2	37.4 - 58.4	5.95	1.88	
	Al_2O_3'	8.0	2.1 - 35.3	9.69	3.06	
	SiO_2'	36.3	25.0 - 39.5	4.07	1.29	
Al4C	FeO'	0.8	0.3 - 1.2	0.27	0.07	15
	MnO'	49.1	42.8 - 52.1	2.71	0.20	
	Al_2O_3'	10.8	8.1 - 15.3	2.54	0.65	
	SiO_2'	39.3	36.4 - 41.2	1.59	0.41	
Al5	FeO'	1.6	0.9 - 2.1	0.39	0.12	10
	MnO'	45.3	42.1 - 52.0	3.02	0.95	
(sect)	Al_2O_3'	17.3	14.3 - 22.2	2.94	0.93	
(1)	SiO_2'	35.8	31.9 - 41.5	3.31	1.05	

Table 4.5 (cont.)

Melt	Oxide	$\overline{XO}$%	Range	S.D.	S.E.	N_i
A15 (sect) (2)	FeO'	0.9	0.2 - 2.2	0.43	0.07	40
	MnO'	49.4	41.9 - 53.5	2.09	0.33	
	Al_2O_3'	12.1	6.2 - 25.6	3.35	0.32	
	SiO_2'	37.6	31.7 - 40.6	2.18	0.34	
A15 (sect) (3)	FeO'	1.1	0.6 - 1.7	0.42	0.13	10
	MnO'	48.7	47.0 - 50.7	1.39	0.44	
	Al_2O_3'	12.5	7.9 - 15.0	2.77	0.87	
	SiO_2'	37.7	36.4 - 40.3	1.61	0.51	
A15 (sect) (5)	FeO'	1.4	0.5 - 1.8	0.45	0.14	10
	MnO'	49.2	48.0 -50.6	0.81	0.26	
	Al_2O_3'	10.7	9.0 - 14.2	1.74	0.55	
	SiO_2'	38.7	35.7 - 40.1	1.50	0.47	
A16	FeO'	2.4	1.8 - 4.5	0.55	0.11	26
	MnO'	33.1	32.5 - 34.3	0.49	0.10	
	Al_2O_3'	15.0	10.9 - 19.3	2.16	2.16	
	SiO_2'	49.5	45.5 - 52.3	1.81	1.81	
A17	FeO'	3.7	1.5 - 22.5	4.08	0.82	24
	MnO'	40.3	31.4 - 53.4	4.21	0.86	
	Al_2O_3'	24.0	7.7 - 39.8	7.12	1.45	
	SiO_2'	32.0	19.2 - 38.1	5.11	1.04	

Table 4.5 (cont.)

Melt	Oxide	$\overline{XO}$%	Range	S.D.	S.E.	N;
A18	FeO'	1.7	1.1 - 2.6	0.56	0.11	
	MnO'	36.5	30.6 - 42.2	7.81	1.48	
	Al_2O_3'	35.6	23.8 -100.0	14.17	2.68	
	SiO_2'	26.2	21.3 - 38.9	6.47	1.22	
NIA12	FeO'	2.2	1.6 - 8.8	1.22	0.20	39
	MnO'	30.8	28.4 - 32.3	0.68	0.11	
	Al_2O_3'	18.4	9.3 - 26.7	4.98	0.80	
	SiO_2'	48.6	41.8 - 54.7	3.21	0.51	
NI(50) A12	FeO'	1.5	1.2 - 2.0	0.19	0.03	50
	MnO'	23.2	20.5 - 25.8	1.54	0.22	
	Al_2O_3'	14.7	11.0 - 17.8	1.70	0.24	
	SiO_2'	60.1	53.2 - 65.5	3.00	0.42	
	NiO'	0.5	0.3 - 0.9	0.09	0.01	
CRA12	FeO'	0.6	0.2 - 1.1	0.21	0.04	25
	MnO'	32.7	31.3 - 35.5	1.15	0.23	
	Al_2O_3'	15.7	8.7 - 22.6	3.11	0.62	
	SiO_2'	50.3	41.2 - 56.5	2.97	0.59	
	Cr_2O_3'	0.7	0.4 - 1.4	0.30	0.06	
VA12	FeO'	0.6	0.3 - 0.8	0.15	0.05	9
	MnO'	31.5	29.7 - 33.3	1.13	0.38	
	Al_2O_3'	20.7	14.3 - 31.4	6.00	2.00	
	SiO_2'	46.4	37.7 - 51.6	5.22	1.74	
	V_2O_5'	0.8	0.5 - 1.5	0.30	0.10	

Fig. 4·2

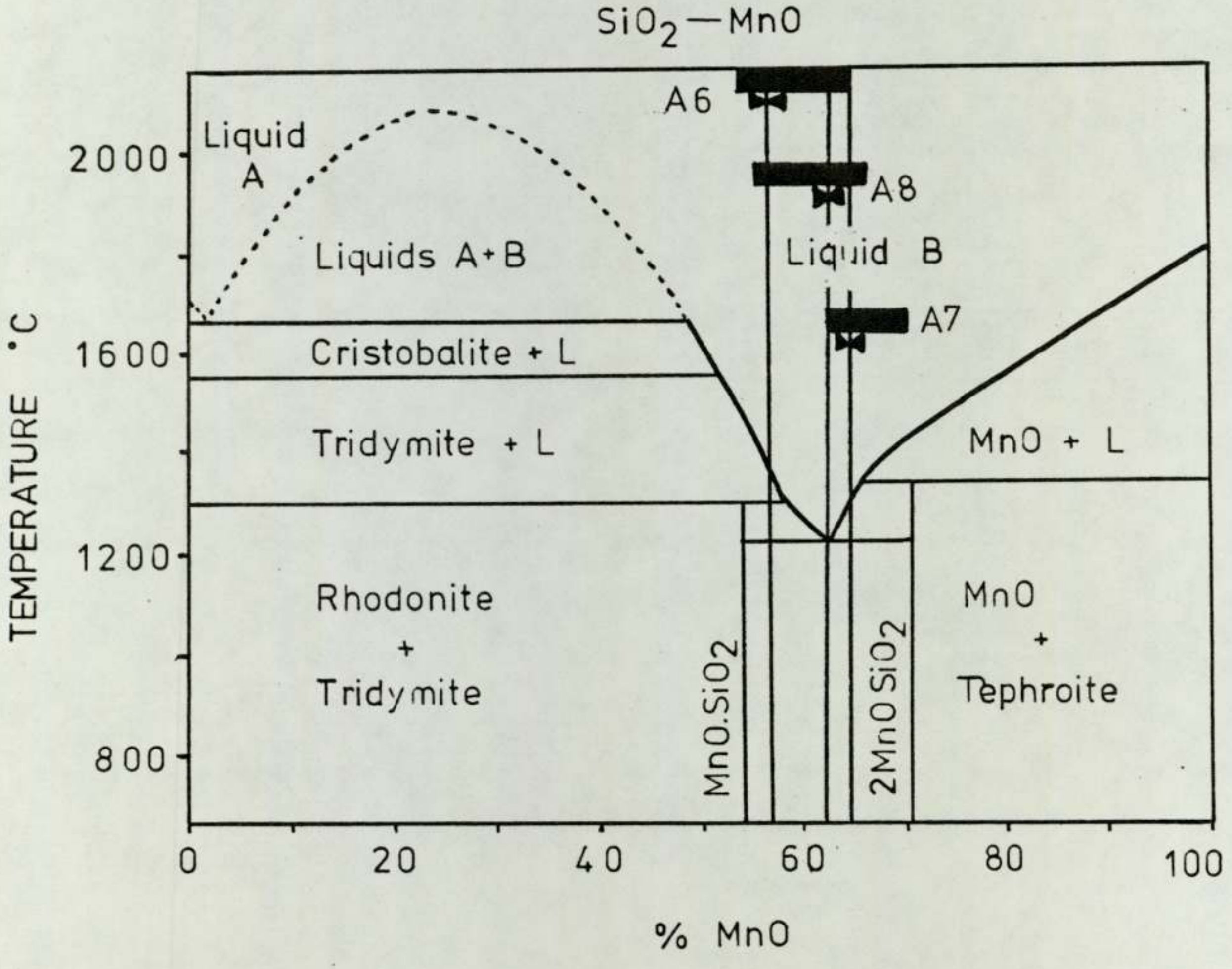
SiO2—MnO
Liquid A
Liquids A+B
Liquid B
A6
A8
A7
Cristobalite + L
Tridymite + L
MnO + L
Rhodonite + Tridymite
MnO + Tephroite
MnO.SiO2
2MnO SiO2
TEMPERATURE °C
2000
1600
1200
800
0
20
40
60
80
100
% MnO

Fig. 4·3 MEAN AS CAST INCLUSION COMPOSITIONS.

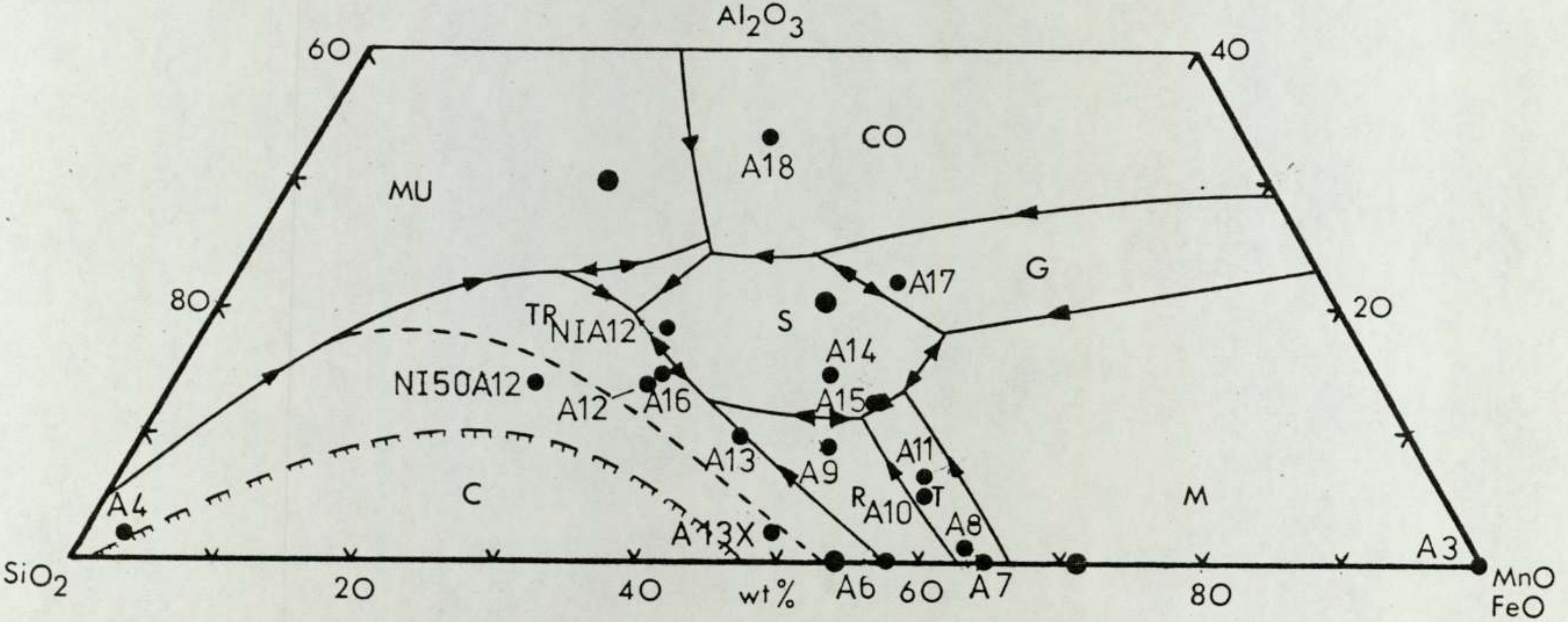

$MnO - SiO_2 - Al_2O_3$ systems. FeO contents are incorporated in the MnO content. Individual 'as cast' inclusion analysis ($\geqslant 10\ \mu m$ diameter) are shown in figures 4.4. to 4.6. indicating the ranges in 'as cast' compositon.

Inclusion size distribution and area content.

The results obtained from quantitative metallography of the 'as cast' samples are shown in tables 4.6. to 4.8. . The symbols used are:-

N_f = No. of fields examined
A_F = Field size (mm^2)
A_T = Total area of specimen examined (mm^2)
$N_i\%$ = Mean area percentage of inclusions
σ_a = Standard deviation of results.

The standard deviation quoted must only be regarded as a rough guide to the dispersion of results since the majority of the results do not show a true Gaussian distribution.

It had been hoped that the suction casting technique would lead to a uniform dispersion of inclusions in the 'as cast' bar. However, figure 4.7. shows that there is a concentration of inclusions in the top section of the bar and also a random distribution of groups of inclusions throughout the length of the bar. This indicated that the top section of the bar was not a good guide to inclusion distribution throughout the bar.

With regard to suction cast bars, there were a few latent features which are not shown in figure 4. 7.

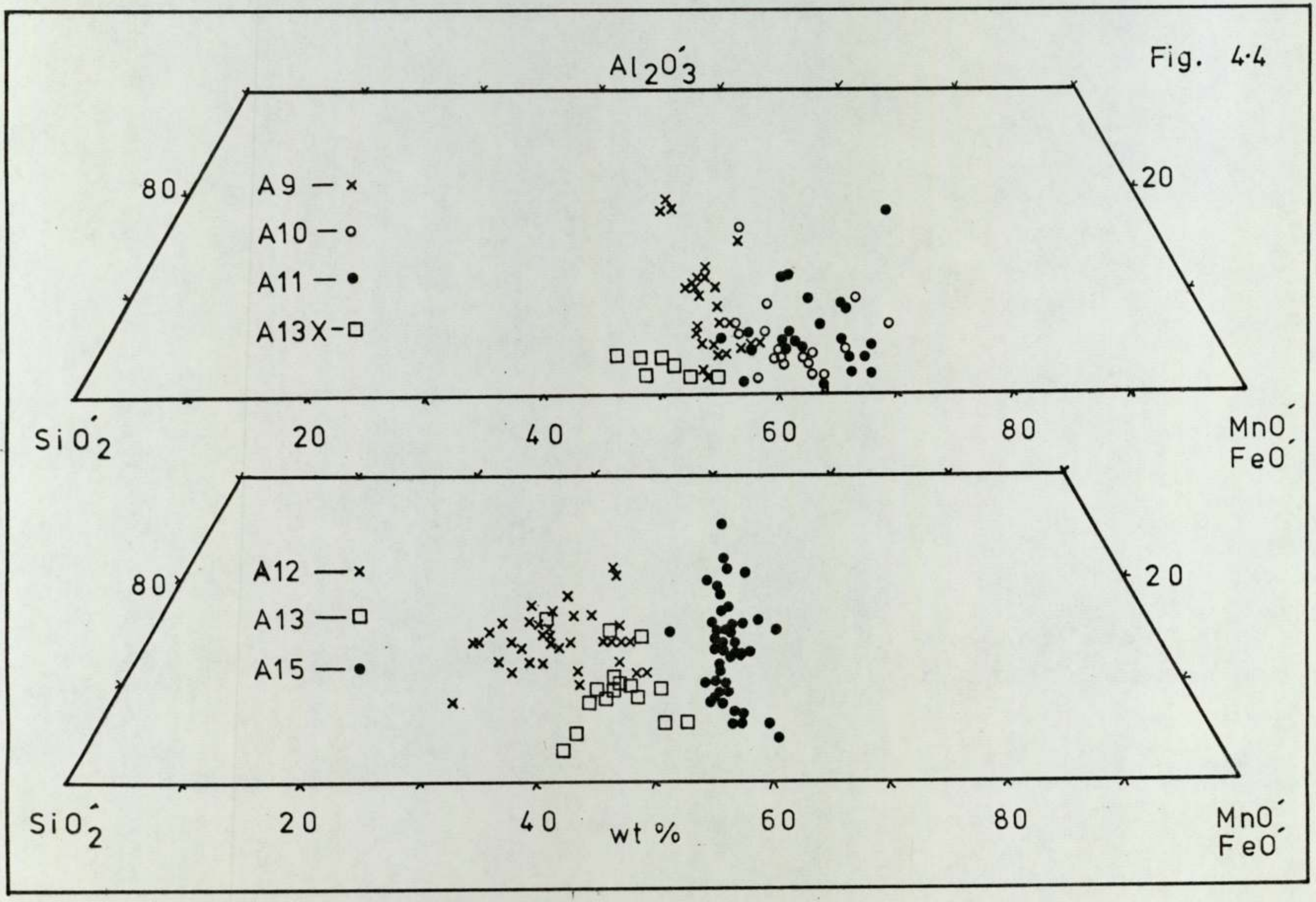
Al$_2$O$_3'$
80
20
A9 — ×
A10 — ○
A11 — ●
A13X — □
SiO$_2'$
20
40
60
80
MnO'
FeO'
80
20
A12 — ×
A13 — □
A15 — ●
SiO$_2'$
20
40
wt %
60
80
MnO'
FeO'

Fig. 4·4

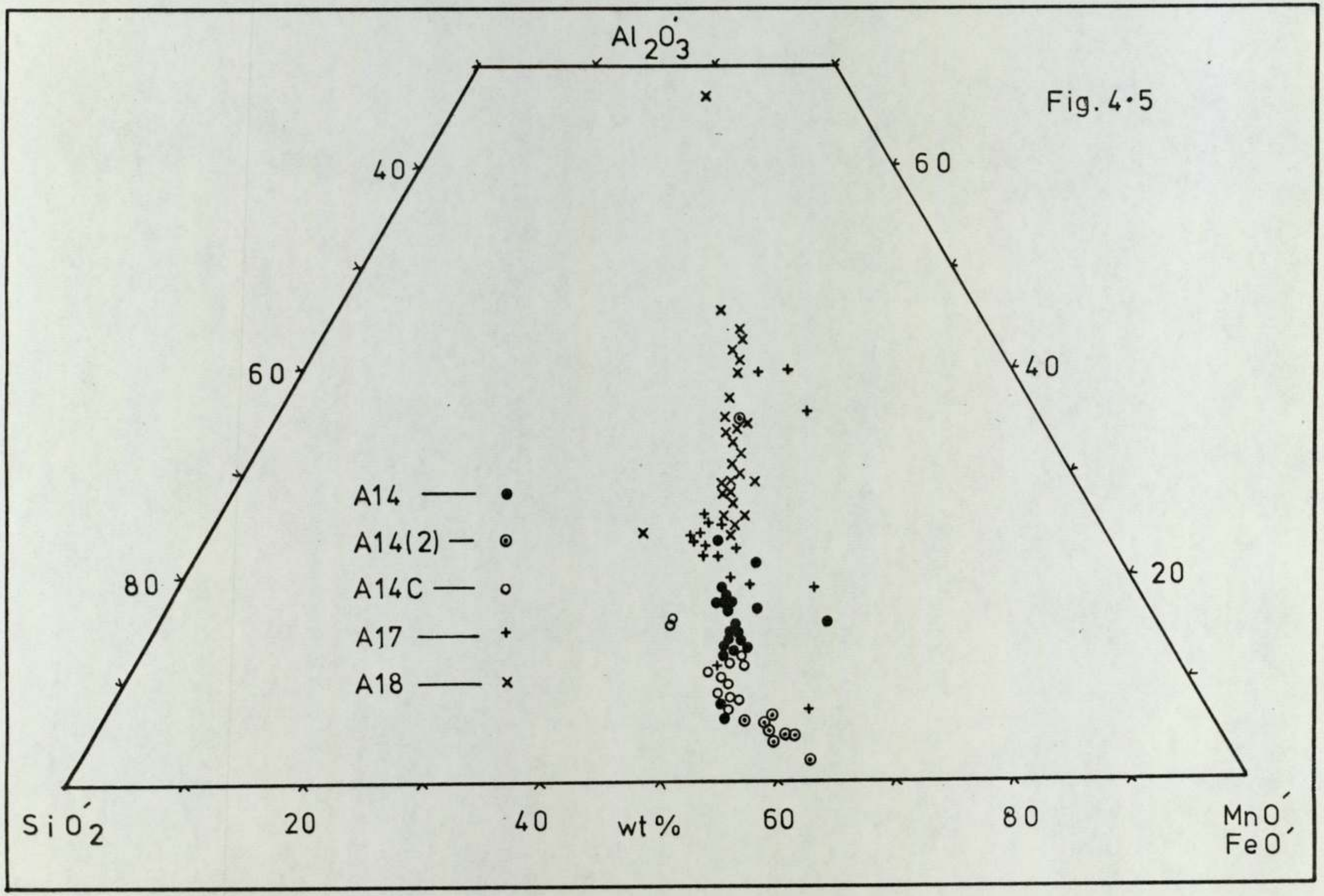
Al₂O₃
40
60
80
60
40
20
SiO₂
20
40
wt %
60
80
MnO
FeO
A14 — ●
A14(2) — ⊙
A14C — ○
A17 — +
A18 — ×

Fig. 4·5

Fig. 4·6

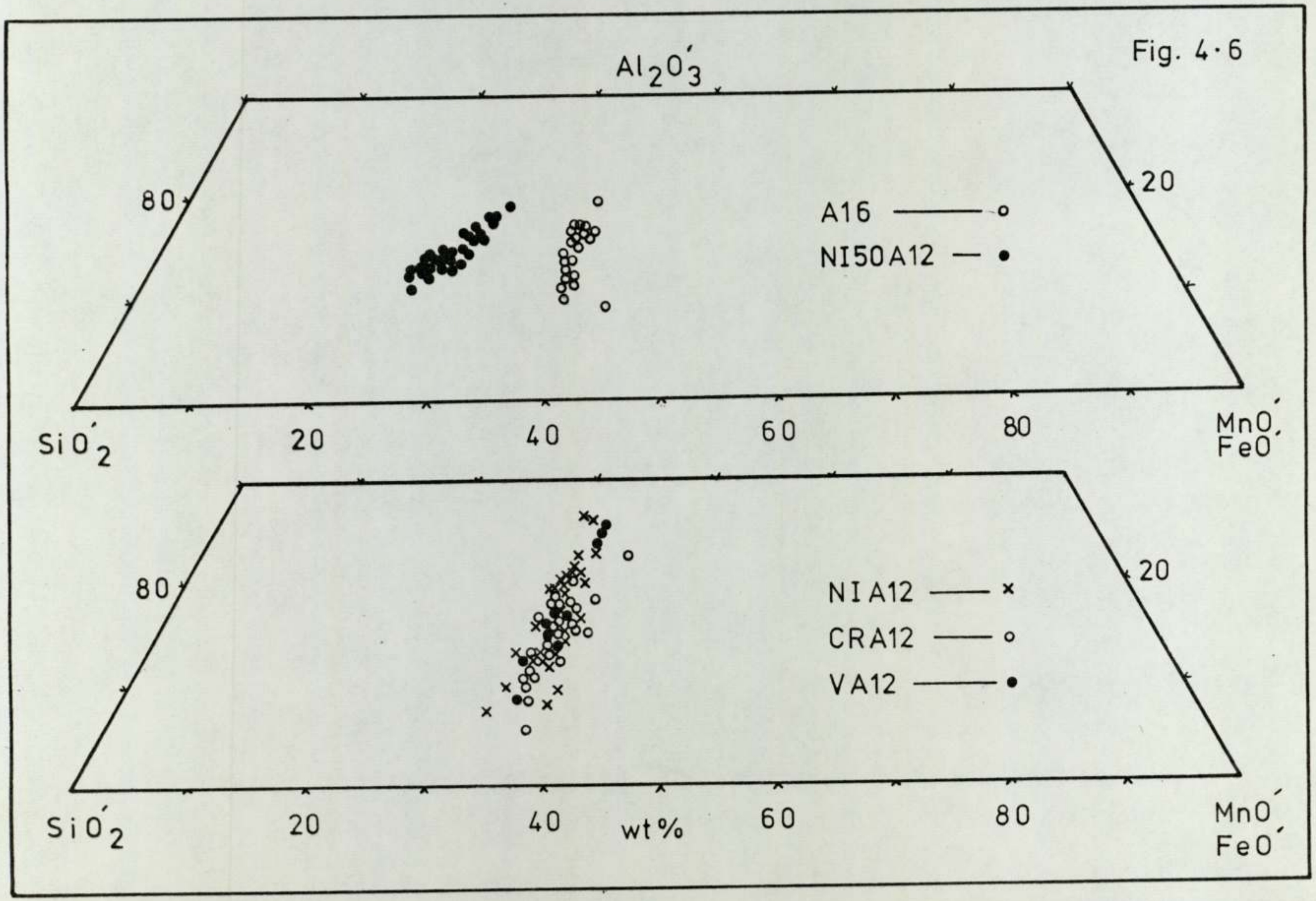
Al₂O₃'
80
20
A16
NI50A12
SiO₂'
20
40
60
80
MnO', FeO'
80
20
NIA12
CRA12
VA12
SiO₂'
20
40
wt%
60
80
MnO', FeO'

Table 4.6 **Inclusion size distribution (X20 (0.50 NA) Objective)**

Sample	N_F	No. inclusions $>$ Do (μm)							
		0 act(0.5u Res)	5	10	15	20	25	30	35
A 3	150	616	5.9	2.1	0.9	0.4	0.2		
A 4	140	1198	72.7	3.5					
A 6	140	531	17.6	5.6	3.5	2.8	2.8	2.8	2.1
A 6(2)	268	462	4.0	1.2	0.7	0.5	0.4	0.4	0.2
A 7	140	377	37.4	8.5	6.3	6.3	6.3	6.3	6.3
A 8	140	468	76.9	2.1	0.7	0.7	0.7	0.7	0.7
A 9	140	537	33.2	4.9	2.1	1.4	0.7	0.7	0.7
A10	140	670	27.5	8.5	6.3	6.3	5.6	3.5	3.5
A11	140	669	18.3	7.1	6.3	5.6	5.6	5.6	4.2
A12	140	706	58.6	9.2	7.1	5.6	4.9	2.8	2.8
A13	140	629	38.1	14.1	8.5	6.3	6.3	4.9	4.9
A13X		1034	9.0	2.8	1.2	1.0	0.6	0.6	0.2
A14	140	422	49.4	14.8	9.2	7.8	7.8	7.1	6.3

Table 4.6 (cont.)

		No. inclusions >Do (μm)							
Sample	N_F	0	5	10	15	20	25	30	35
A14(2)		593	17.3	2.9	1.7	1.4	1.2	1.0	0.6
A14C	150	610	7.6	2.5	1.7	1.1	0.6	0.4	0.2
A15		273	16.7	5.1	3.8	2.8	2.1	1.5	1.3
A16	180	731	21.0	4.2	2.5	1.8	1.1	0.7	0.5
A17		354	17.5	5.4	3.6	2.3	1.8	1.3	0.9
A18	154	559	28.4	7.9	3.9	3.5	3.0	3.0	3.0
NIA12	170	798	42.8	10.5	5.1	3.9	3.1	2.8	2.4
NI50A12	161	471	25.6	4.9	2.0	1.4	1.0	0.8	0.8
CRA12	150	898	14.8	5.1	2.5	2.1	1.5	1.5	1.3
VA12	224	1046	35.9	8.5	5.2	3.7	2.8	2.0	2.0

Table 4.7 Inclusion size distribution (X5 (0.15NA) objective)

Sample	N_F	No. Inclusions >Do .mm^{-2}										
		40	60	80	100	120	140	160	180	200	220	240
A 3	400	0.02	-	-	-	-	-	-	-	-	-	-
A 4	100	0.01	-	-	-	-	-	-	-	-	-	-
A 6	100	0.18	-	-	-	-	-	-	-	-	-	-
A 6(2)	400	0.25	0.05	0.01	-	-	-	-	-	-	-	-
A 7	400	0.43	0.25	0.18	0.14	0.12	0.08	0.05	0.05	0.05	0.01	-
A 8	400	0.43	0.25	0.08	0.06	0.03	0.03	0.02	0.01	-	-	-
A 9	400	0.39	0.10	0.03	0.03	0.01	0.01	0.01	-	-	-	-
A10	300	0.36	0.19	0.12	0.09	0.08	0.08	0.05	0.05	0.04	0.03	0.03
A11	350	0.42	+	0.07	0.05	0.01	-	-	-	-	-	-
A12	350	0.76	+	0.19	0.02	0.01	0.01	-	-	-	-	-
A13	400	0.78	0.45	0.21	0.18	0.13	0.08	0.05	0.03	0.02	0.01	0.01
A13X	160	0.64	0.39	0.19	0.07	0.05	0.03	0.03	0.03	-	-	-
A14	350	2.28	1.44	0.76	0.20	0.19	0.14	0.11	0.11	0.07	0.05	0.04

Table 4.7 (cont.)

Sample	N_F	No. inclusions Do $.mm^{-2}$ 40	60	80	100	120	140	160	180	200	220	240
A14C	400	0.61	0.25	0.14	0.08	0.05	0.04	0.03	0.02	0.01	0.01	0.01
A14(2)	400	0.51	0.23	0.18	0.14	0.09	0.08	0.08	0.08	0.06	0.05	0.03
A15	350	0.47	0.29	0.29	0.18	0.08	0.04	0.03	0.03	0.02	0.01	0.01
A16	350	0.52	0.52	0.18	0.02	0.02	0.02	0.02	-	-	-	-
A17	300	0.55	0.29	0.15	0.10	0.10	0.09	0.08	0.07	0.05	0.04	0.04
A18	168	1.20	0.46	0.28	0.24	0.22	0.21	0.21	0.21	0.19	0.19	0.18
NIA12	184	1.15	0.43	0.18	0.12	0.10	0.06	0.06	0.02	0.02	0.02	0.01
NI50A12	400	0.83	0.15	0.10	0.05	0.04	0.01	-	-	-	-	-
CRA12	400	1.16	0.39	0.20	0.10	0.07	0.07	0.05	0.04	0.04	0.03	0.01
VA12	400	0.71	0.21	0.09	0.03	0.02	0.01	0.01	-	-	-	-

Table 4.8

Sample	$\overline{A\%}$	σ_A
A 3	0.29	0.16
A 4	0.52	0.27
A 6	0.48	0.56
A 6(2)	0.19	0.25
A 7	0.52	0.76
A 8	0.39	0.39
A 9	0.32	0.25
A10	0.66	1.51
A11	0.38	0.69
A12	0.66	0.57
A13	0.42	0.59
A13X	0.31	0.48
A14	0.73	1.20
A14(2)	0.37	0.49
A14(C)	0.36	0.25
A15	0.55	0.67
A16	0.39	0.27
A17	0.45	0.65
A18	0.57	1.91
NIA12	0.67	1.05
NI50A12	0.57	0.38
CRA12	0.55	0.69
VA12	0.38	0.34

N_F = 200 (0.15 OBJ) A_{EXAM} =

CAST A15

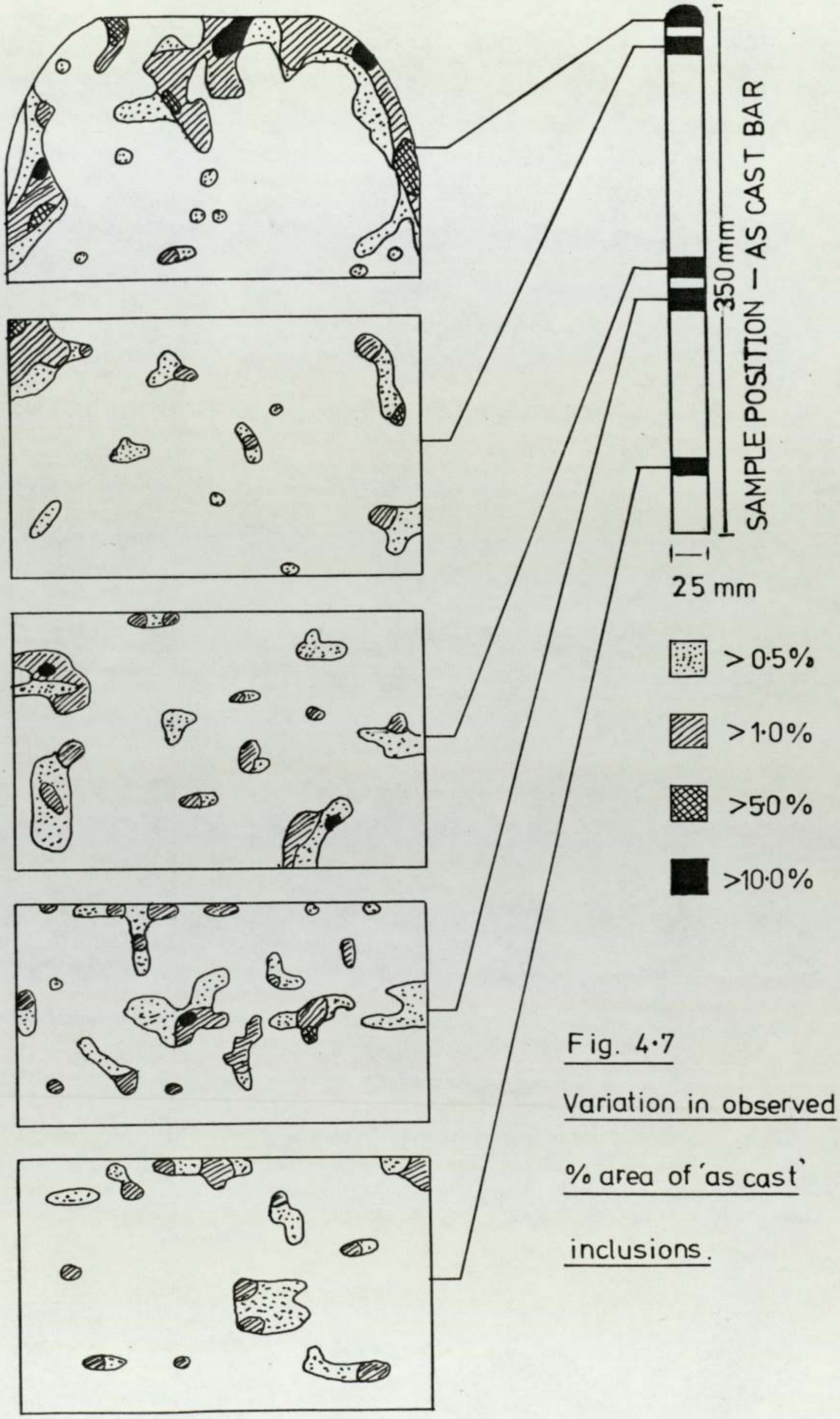

Fig. 4·7

Variation in observed % area of 'as cast' inclusions.

There was some evidence to suggest that some of the large inclusions are broken up during the casting process (Plate 4.1. probably due to turbulent conditions), with the possibility of forming stringer like inclusions with their major axis parallel to the bar axis. A number of small inclusions have also been observed in the peripheral regions of the bar.

4.6
Plasticity index analyses.

Plasticity index analyses have been calculated for the various melts at different rolling temperatures at a nominally similar reduction (i.e. a matrix height true strain of 1.12) table 4.9.

The symbols used:-

ε_m = Matrix height true strain

Nf = No. of fields examined

Ni = No. of measured deformed inclusions

$\bar{\varepsilon}_i$ = Mean inclusion strain

$\bar{\nu}$ = Mean plasticity index

σ_{ν} = Standard deviation

$\sigma_{\bar{\nu}}$ = Standard error

Plasticity indices refer to the (XY) section plane and values of ν have been measured for inclusions with $\sqrt{ab}$ (i.e. $\sqrt{\text{Major x Minor axes}}$) greater than 1 µm, 10 µm and 20 µm (given by 1+, 10+ and 20+) respectively. Although σ_{ν} and $\sigma_{\bar{\nu}}$ have been quoted for most data it may only be regarded as a rough guide when applied to $\bar{\nu}$ 1+, due to the skew distribution of results associated with $\sqrt{ab} > 1$ µm.

PLATE 4.1

INCLUSION TAKEN FROM MELT A15
SHOWING BREAK UP DUE TO
TURBULENCE DURING THE SUCTION
CASTING PROCESS

X200

4.1.

Table 4.9 Melt A3

Rolling Temp °C	Matrix Strain ε_m	No. of Fields n_f	Size Range (μm)	No. Incs. in Range	Mean Inc. Strain $\bar{\varepsilon}_i$	Mean Plas. Index $\bar{\nu}$	Std. Devn. σ_ν	Std. Error $\sigma_{\bar{\nu}}$
800	1.16	200	-	-	-	-	-	-
900	1.14	200	-	-	-	-	-	-
1100	1.19	200	-	-	-	-	-	-
1300	1.12	200	-	-	-	-	-	-
Melt A4								
900	1.19	200	-	-	-	-	-	-
1100	1.18	200	-	-	-	-	-	-
1300	1.12	200	-	-	-	-	-	-

Table 4.9 (cont.) Melt A6

Rolling Temp oC	Matrix Strain	No. of Fields	Size Range	No. Incs. in Range	Mean Inc. Strain	Mean Plas. Index	Std. Devn.	Std. Error
900	1.14	400	-	-	-	-	-	-
1000	1.13	400	-	-	-	-	-	-
1300	1.12	100	1+	8	1.03	0.92	0.38	0.13
			10+	8	1.03	0.92	0.38	0.13
			20+	7	1.18	1.05	0.13	0.05
Melt A6 (2)								
800	1.15	500	-	-	-	-	-	-
900	1.13	500	-	-	-	-	-	-
1100	1.16	500	1+	22	0.41	0.47	0.19	0.01
			10+	9	0.63	0.54	0.16	0.05
			20+	7	0.65	0.56	0.18	0.07

Table 4.9 (cont.) Melt A6 (2) (cont.)

Rolling Temp °C	Matrix Strain	No. of Fields	Size Range	No. Incs. in Range	Mean Inc. Strain	Mean Plas. Index	Std. Devn.	Std. Error
1200	1.16	150	1+	52	0.72	0.62	0.37	0.01
			10+	16	1.14	0.98	-	-
			20+	15	1.13	098	0.31	0.02
1300	1.13	150	1+	128	0.62	0.62	0.29	0.01
			10+	11	1.44	1.27	0.22	0.06
			20+	7	1.44	1.28	0.26	0.10
Melt A7								
900	1.13	400	-	-	-	-	-	-
1000	1.10	400	1+	4	-	0.41	0.25	0.13
			10+	2	-	0.30	0.38	0.27
			20+	1	-	0.04	-	-

Table 4.9 (cont.)   Melt A7 (cont.)

Rolling Temp °C	Matrix Strain	No. of Fields	Size Range	No. Incs. in Range	Mean Inc. Strain	Mean Plas. Index	Std. Devn.	Std. Error
1100	1.19	200	1+	19	0.71	0.60	0.29	0.07
			10+	6	1.07	0.90	0.06	0.03
			20+	5	1.08	0.91	0.06	0.03
1300	1.12	100	1+	32	0.72	0.64	0.31	0.31
			10+	4	1.18	1.05	0.32	0.16
			20+	3	1.32	1.18	0.19	0.11
				Melt A8				
900	1.13	400	-	-	-	-	-	-
1000	1.10	100	1+	71	0.69	0.63	0.41	0.05
			10+	14	1.01	0.92	0.53	0.14
			20+	2	0.03	0.03	0.02	0.02
1300	1.13	100	1+	32	0.72	0.64	-	-
			10+	4	1.24	1.10	0.07	0.03
			20+	2	1.30	1.15	0.02	0.01

Table 4.9 (cont.)   Melt A9

Rolling Temp °C	Matrix Strain	No. of Fields	Size Range	No. Incs. in Range	Mean Inc. Strain	Mean Plas. Index	Std, Devn.	Std. Error
900	1.16	400	-	-	-	-	-	-
1000	1.11	400	1+	56	0.34	0.34	0.32	0.04
			10+	9	0.53	0.48	0.45	0.15
			20+	6	0.43	0.39	0.41	0.17
1300	1.16	150	1+	50	0.67	0.69	0.41	0.06
			10+	17	1.33	1.15	0.26	0.06
			20+	13	1.36	1.17	0.20	0.06
					Melt A10			
900	1.16	400	-	-	-	-	-	-
1000	1.14	200	1+	12	0.14	0.12	0.34	0.03
			10+	6	0.04	0.04	0.03	0.01
			20+	2	0.03	0.03	0.01	0.01

Table 4.9 (cont.) Melt A10 (cont.)

Rolling Temp °C	Matrix Strain	No. of Fields	Size Range	No. Incs. in Range	Mean Inc. Strain	Mean Plas. Index	Std. Devn.	Std. Error
1300	1.16	150	1+	32	0.67	0.58	0.33	0.01
			10+	9	1.31	1.13	0.33	0.11
			20+	6	1.48	1.28	0.24	0.10
Melt A11								
900	1.16	400	-	-	-	-	-	-
1000	1.12	150	1+	14	1.26	1.13	0.28	0.02
			10+	7	0.83	0.74	0.48	0.18
			20+	-	-	-	-	-
1300	1.16	150	1+	32	0.59	0.51	0.32	0.01
			10+	8	1.16	1.00	0.19	0.07
			20+	6	1.28	1.10	0.10	0.04

Table 4.9(cont.) Melt A12

Rolling Temp °C	Matrix Strain	No. of Fields	Size Range	No. Incs. in Range	Mean Inc. Strain	Mean Plas. Index	Std. Devn.	Std. Error
800	1.26	100	1+	45	0.59	0.46	0.25	0.01
			10+	14	-	-	-	-
			20+	7	-	-	-	-
900	1.20	180	1+	52	1.03	0.86	0.23	0.01
			10+	16	-	-	-	-
			20+	7	-	-	-	-
1000	1.14	100	1+	116	1.12	0.99	0.19	0.02
			10+	11	-	-	-	-
			20+	7	-	-	-	-
Melt A13								
800	1.24	100	1+	88	0.27	0.22	0.14	0.01
			10+	12	0.37	0.30	0.13	0.04
			20+	5	0.30	0.24	0.13	0.06

Table 4.9(cont.) Melt A13 (cont.)

Rolling Temp °C	Matrix Strain	No. of Fields	Size Range	No. Incs. in Range	Mean Inc. Strain	Mean Plas. Index	Std. Devn.	Std. Error
850	1.19	250	1+	84	0.56	0.47	0.20	0.02
			10+	13	0.70	0.59	0.11	0.03
			20+	2	0.66	0.55	0.02	0.01
900	1.19	75	1+	29	0.89	0.74	0.27	0.05
			10+	17	0.51	0.43	0.23	0.06
			20+	11	0.37	0.31	0.14	0.04
1000	1.16	150	1+	115	1.06	0.92	0.16	0.01
			10+	15	1.15	0.99	0.21	0.06
			20+	10	1.12	0.97	0.25	0.08
				Melt A13X				
600	1.12	400	1+	5	0.16	0.14	0.12	0.05
			10+	1	0.01	0.01	-	-
			20+	1	0.01	0.01	-	-

Table 4.9 (cont.) Melt Al3X (cont.)

Rolling Temp °C	Matrix Strain	No. of Fields	Size Range	No. Incs. in Range	Mean Inc. Strain	Mean Plas. Index	Std. Devn.	Std. Error
700	1.12	380	1+	31	0.68	0.61	0.20	0.03
			10+	20	0.70	0.63	0.13	0.03
			20+	11	0.68	0.61	0.07	0.02
800	1.13	240	1+	39	0.66	0.58	0.11	0.05
			10+	5	0.75	0.66	0.56	0.25
			20+	5	0.86	0.76	0.56	0.25
900	1.13	220	1+	13	0.72	0.64	0.19	0.05
			10+	9	0.98	0.87	0.26	0.09
			20+	7	0.97	0.86	0.25	0.10
1000	1.13	150	1+	84	0.86	0.76	-	-
			10+	23	1.17	1.04	0.41	0.09
			20+	16	1.34	1.21	0.22	0.06
1100	1.13	30	1+	110	0.58	0.51	0.29	0.03
			10+	9	1.08	0.96	0.17	0.06
			20+	5	1.15	1.02	0.14	0.06

Table 4.9 (cont.)   Melt Al4

Rolling Temp °C	Matrix Strain	No. of Fields	Size Range	No. Incs. in Range	Mean Inc. Strain	Mean Plas. Index	Std. Devn.	Std. Error
900	1.78	100	1+	16	0.18	0.11	0.18	0.01
			10+	13	0.48	0.27	0.13	0.04
			20+	8	0.45	0.25	0.11	0.05
950	1.22	100	1+	11	1.29	1.07	0.51	0.15
			10+	8	1.45	1.19	0.50	0.18
			20+	6	1.78	1.46	0.09	0.04
1000	1.09	150	1+	115	1.56	0.92	0.21	0.02
			10+	32	1.03	0.95	0.16	0.03
			20+	14	1.13	1.04	0.13	0.03
				Melt Al4C				
600	1.12	400	1+	3	0.09	0.08	0.09	0.05
			10+	2	0.02	0.03	0.01	0.01
			20+	2	0.02	0.03	0.01	0.01

Table 4.9(cont.) Melt Al4 C (cont.)

Rolling Temp °C	Matrix Strain	No. of Fields	Size Range	No. Incs. in Range	Mean Inc. Strain	Mean Plas. Index	Std. Devn.	Std. Error
700	1.12	400	1+	36	1.12	1.00	0.36	0.06
			10+	26	1.28	1.14	0.24	0.05
			20+	14	1.45	1.22	0.10	0.03
800	1.13	400	1+	16	0.59	0.52	0.44	0.11
			10+	7	0.27	0.24	0.19	0.17
			20+	5	0.08	0.07	0.06	0.03
900	1.13	350	1+	11	0.63	0.56	0.45	0.14
			10+	3	1.24	1.10	0.27	0.16
			20+	-	-	-	-	-
1000	1.13	230	1+	22	1.06	0.94	0.40	0.09
			10+	9	1.36	1.20	0.33	0.11
			20+	5	1.50	1.33	0.24	0.11

Table 4.9(cont.) Melt A15

Rolling Temp °C	Matrix Strain	No. of Fields	Size Range	No. Incs. in Range	Mean Inc. Strain	Mean Plas. Index	Std. Devn.	Std. Error
900	1.20	600	1+	14	1.43	1.19	0.41	0.11
			10+	14	1.43	1.19	0.41	0.11
			20+	13	1.43	1.19	0.43	0.12
1100	1.16	60	1+	107	0.85	0.73	0.32	0.03
			10+	12	1.44	1.24	0.17	0.05
			20+	6	1.58	1.36	0.07	0.05
1300	1.11	50	1+	105	0.81	0.73	0.38	0.04
			10+	76	1.42	1.28	0.16	0.02
			20+	34	1.49	1.34	0.14	0.02
Melt A16								
800	1.16	600	1+	98	0.32	0.28	0.12	0.01
			10+	51	0.36	0.31	0.13	0.02
			20+	19	0.24	0.21	0.09	0.02

Table 4.9(cont.)   Melt A16 (cont.)

Rolling Temp °C	Matrix Strain	No. of Fields	Size Range	No. Incs. in Range	Mean Inc. Strain	Mean Plas. Index	Std. Devn.	Std. Error
850	1.16	200	1+	180	1.17	1.01	0.35	0.03
			10+	38	1.43	1.23	0.14	0.02
			20+	21	1.40	1.21	0.15	0.03
900	1.13	500	1+	37	1.09	0.97	0.37	0.06
			10+	10	1.44	1.27	-	-
			20+	7	1.51	1.34	-	-
1100	1.17	380	1+	98	0.63	0.54	0.32	0.03
			10+	11	1.37	1.17	-	-
			20+	6	1.52	1.35	-	-
1300	1.13	100	1+	155	0.63	0.56	0.33	0.03
			10+	42	1.21	1.07	-	-
			20+	25	1.31	1.16	-	-

Table 4.9(cont.) Melt A17

Rolling Temp oC	Matrix Strain	No. of Fields	Size Range	No. Inc. in Range	Mean Inc. Strain	Mean Plas. Index	Std. Devn.	Std. Error
750	1.15	200	1+	69	0.44	0.38	0.15	0.02
			10+	22	0.32	0.28	0.15	0.03
			20+	9	0.26	0.23	0.10	0.03
800	1.13	400	1+	7	1.31	1.16	0.12	0.05
			10+	7	1.31	1.16	0.12	0.05
			20+	7	1.31	1.16	0.12	0.05
850	1.12	250	1+	7	1.23	1.10	0.14	0.05
			10+	7	1.23	1.10	0.14	0.05
			20+	6	1.21	1.08	0.15	0.06
900	1.13	200	1+	12	1.20	1.06	0.17	0.05
			10+	12	1.20	1.06	0.17	0.05
			20+	12	1.20	1.06	0.17	0.05

Table 4.9(cont.) Melt A17(Cont.)

Rolling Temp °C	Matrix Strain	No. of Fields	Size Range	No. Incs. in Range	Mean Inc. Strain	Mean Plas. Index	Std. Devn.	Std. Error
1000	1.13		1+	4	1.25	1.11	0.04	0.02
			10+	4	1.25	1.11	0.04	0.02
			20+	4	1.25	1.11	0.04	0.02
				Melt A18				
750	1.16	400	1+	44	0.23	0.20	0.25	0.04
			10+	9	0.16	0.14	0.20	0.07
			20+	2	0.42	0.36	0.42	0.30
800	1.14	410	1+	5	1.38	1.21	0.10	0.04
			10+	5	1.38	1.21	0.10	0.04
			20+	5	1.38	1.21	0.10	0.04

Table 4.9 (cont.)   Melt A18 (cont.)

Rolling Temp °C	Matrix Strain	No. of Fields	Size Range	No. Incs. in Range	Mean Inc. Strain	Mean Plas. Index	Std. Devn.	Std. Error
850	1.13	600	1+	10	0.69	0.61	0.54	0.17
			10+	10	0.69	0.61	0.54	0.17
			20+	9	0.76	0.67	0.54	0.18
900	1.13	630	1+	4	1.41	1.25	0.14	0.07
			10+	4	1.41	1.25	0.14	0.07
			20+	4	1.41	1.25	0.14	0.07
1000	1.13	350	1+	5	1.32	1.17	0.23	0.10
			10+	5	1.32	1.17	0.23	0.10
			20+	5	1.32	1.17	0.23	0.10

Table 4.9(cont.)   Melt NIAl2

Rolling Temp °C	Matrix Strain	No. of Fields	Size Range	No. Incs. in Range	Mean Inc. Strain	Mean Plas. Index	Std. Devn.	Std. Error
800	1.14	220	1+	242	0.54	0.47	0.23	0.02
			10+	65	0.38	0.33	0.20	0.02
			20+	33	0.22	0.19	0.13	0.02
850	1.12	500	1+	176	1.10	0.98	0.29	0.02
			10+	82	1.20	1.07	0.21	0.02
			20+	43	1.15	1.03	0.19	0.03
900	1.12	500	1+	47	1.37	1.22	0.24	0.04
			10+	36	1.42	1.27	0.15	0.03
			20+	22	1.46	1.30	0.09	0.02
1000	1.13	100	1+	184	1.17	1.04	0.35	0.03
			10+	82	1.48	1.31	0.20	0.02
			20+	43	1.51	1.34	0.20	0.03

Table 4.9(cont.) Melt NI50A12

Rolling Temp °C	Matrix Strain	No. of Fields	Size Range	No. Incs. in Range	Mean Inc. Strain	Mean Plas. Index	Std. Devn.	Std. Error
750	1.11	200	1+	31	0.04	0.04	0.02	-
			10+	22	0.04	0.04	0.02	-
			20+	10	0.03	0.03	0.01	-
800	1.12	200	1+	51	0.08	0.07	0.06	0.01
			10+	38	0.08	0.07	0.04	0.01
			20+	14	0.07	0.06	0.02	0.01
850	1.12	100	1+	115	0.33	0.30	0.15	0.02
			10+	46	0.33	0.30	0.11	0.02
			20+	16	0.36	0.32	0.09	0.02
900	1.14	100	1+	152	0.34	0.30	0.21	0.02
			10+	69	0.32	0.28	0.17	0.02
			20+	36	0.35	0.31	0.20	0.03
1000	1.13	70	1+	175	0.96	0.85	0.36	0.03
			10+	93	1.12	0.99	0.31	0.03
			20+	29	1.34	1.19	0.15	0.03

Table 4.9(cont.) Melt NI50A12 (cont.)

Rolling Temp °C	Matrix Strain	No. of Fields	Size Range	No. Incs. in Range	Mean Inc. Strain	Mean Plas. Index	Std. Devn.	Std. Error
1100	1.09	117	1+	261	0.93	0.85	0.37	0.02
			10+	51	1.33	1.22	0.21	0.03
			20+	16	1.40	1.28	0.18	0.04
Melt CRA12								
750	1.17	100	1+	37	0.42	0.36	0.17	0.03
			10+	11	0.36	0.31	0.12	0.04
			20+	5	0.22	0.19	0.04	0.02
800	1.15	50	1+	145	0.78	0.68	0.28	0.02
			10+	33	0.71	0.62	0.15	0.03
			20+	19	0.44	0.38	0.20	0.02
850	1.15	500	1+	51	1.39	1.21	0.21	0.03
			10+	37	1.45	1.26	0.12	0.02
			20+	15	1.46	1.27	0.15	0.03

Table 4.9(cont.) Melt CRA12 (cont.)

Rolling Temp °C	Matrix Strain	No. of Fields	Size Range	No. Incs. in Range	Mean Inc. Strain	Mean Plas. Index	Std. Devn.	Std. Error
900	1.16	370	1+	116	0.76	0.66	0.47	0.04
			10+	35	1.25	1.08	0.39	0.07
			20+	11	1.60	1.39	0.14	0.04
1000	1.16	70	1+	125	0.97	0.84	0.38	0.03
			10+	26	1.47	1.27	0.18	0.04
			20+	10	1.52	1.31	0.17	0.03
				Melt VA12				
800	1.14	120	1+	133	0.40	0.35	0.16	0.01
			10+	39	0.22	0.19	0.12	0.02
			20+	15	0.08	0.07	0.03	0.01
850	1.15	170	1+	135	0.91	0.79	0.37	0.03
			10+	58	1.21	1.05	0.23	0.03
			20+	19	1.39	1.21	0.10	0.03

Table 4.9(cont.)   Melt VAl2 (cont.)

Rolling Temp °C	Matrix Strain	No. of Fields	Size Range	No. Incs. in Range	Mean Inc. Strain	Mean Plas. Index	Std. Devn.	Std. Error
900	1.16	250	1+	116	1.03	0.89	0.39	0.04
			10+	47	1.37	1.18	0.11	0.02
			20+	17	1.43	1.23	0.09	0.04
1000	1.14	40	1+	130	1.15	1.01	0.32	0.03
			10+	21	1.56	1.37	0.18	0.04
			20+	14	1.65	1.45	0.17	0.03
1100	1.10	52	1+	259	0.73	0.66	0.40	0.02
			10+	36	1.29	1.17	0.13	0.02
			20+	12	1.24	1.13	0.10	0.03

Individual values of plasticity index have also been plotted against inclusion size (given by $\sqrt{ab}$)

4.7
Metallographic examination (As cast).

Typical examples of inclusions found in the as cast bars resulting from the deoxidation treatments are shown in plates 4.2 to 4.12. The majority of inclusions observed were of a glassy nature

Manganese deoxidation (Melt A3).

Products of deoxidation resulting from a 2% manganese addition were greyish blue in appearance. The small inclusions were often idiomorphic in appearance and often found grouped together. The analysis of the inclusions showed that they were almost pure MnO (96%) although some FeO (~4%) was detected (Appendix 4.1.)

Silicon deoxidation (Melt A4).

Deoxidation by silicon resulted in the formation of almost pure glassy silica (Appendix 4.1.) products. These tended to be spherical in nature, although necking and joining is evident in plates 4.2. and 4.3.

Manganese + Silicon deoxidation.

Melts A6, A6(2), A7 and A8 were all deoxidised by Mn - Si alloys. Although the majority of inclusions were glassy some hetrogeneous inclusions were observed. Melt A6(2) appeared to contain a higher proportion of

PLATES 4.2 & 4.3

COALESCING GLASSY SILICATES FROM
MELT A4. DEOXIDISED BY A 1%
(MELT WEIGHT ADDITION) OF SILICON.

X400

4.2.

4.3.

hetrogeneous inclusions containing pure silica precipitates observed as silica rosettes or spots in section, similar to those observed for melt A13X (plates 4.4.&.5.)

The higher manganese inclusions sometimes contained a light precipitate phase within a darker grey matrix (plate 4.6.) and opaque inclusions with no resolvable precipitate infrequently occurred.

Manganese + silicon + aluminium deoxidation.

Melts A9 to A16 contained a very high proportion of glassy inclusions, melts A14(C), A15 and A16 appeared to contain glassy inclusions only. Hetrogeneous inclusions from the higher silicon melts A12, A13 and A13(X) had precipitates of silica and/or rhodonite inclusions, although opaque inclusions were also found (plates 4.7. to 4.9.).

The melts of higher manganese contents i.e. A10, A11 and A14 if not glassy contained inclusions which precipitated rhodonite (plate 4.10.).

Melts A17 to A18 which were deoxidised with the same deoxidant as in A14, but in the presence of additional aluminium gave rise to either glassy inclusions or hetrogeneous inclusions of alumina with a glassy matrix (plate 4.11.). It was mainly the small inclusions which were of a glassy nature, and the large inclusions often appeared to contain white regions (plate 4.12.) which were found to be areas of iron and or iron oxide.

As an oversimplified generalisation it appeared that it was usually the larger inclusions which contained the precipitates.

PLATES 4.4 & 4.5

ABSORBED ELECTRON IMAGE PHOTOGRAPHS SHOWING TWO PHASE INCLUSIONS TAKEN FROM MELT (A13X)

PHOTOGRAPHS SHOW LIGHT PRECIPITATES OF SILICA WITHIN GLASSY MATRICES

X1000

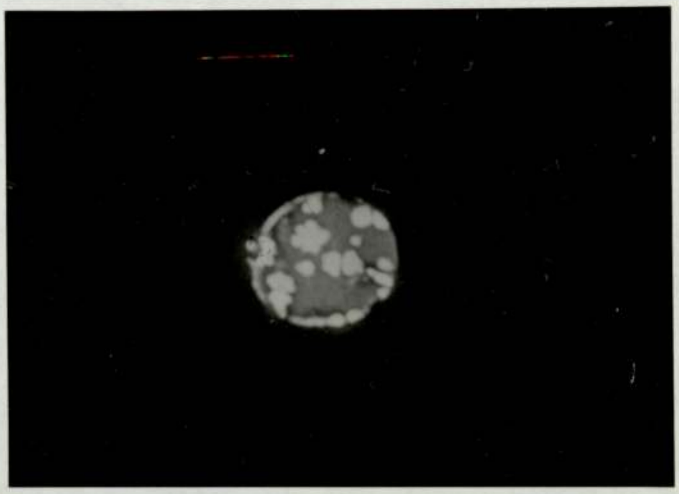

4.4.

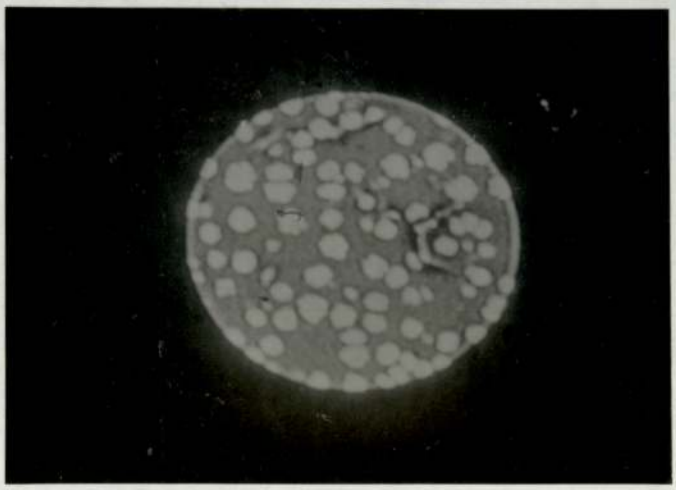

4.5.

PLATE 4.6

TWO PHASE SILICATE INCLUSION
TAKEN FROM MELT (A7)

X750

PLATE 4.7

GLASSY INCLUSIONS TAKEN FROM
MELT (A12) DEOXIDISED BY
Mn - AL - Si DEOXIDANT.
THERE APPEARS TO BE A SECOND
PHASE PRECIPITATION WITHIN
THE LARGEST INCLUSION.

X750

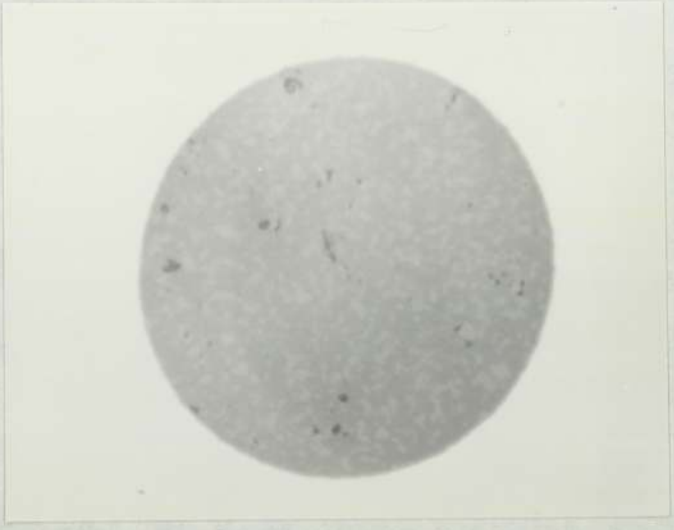

4.6.

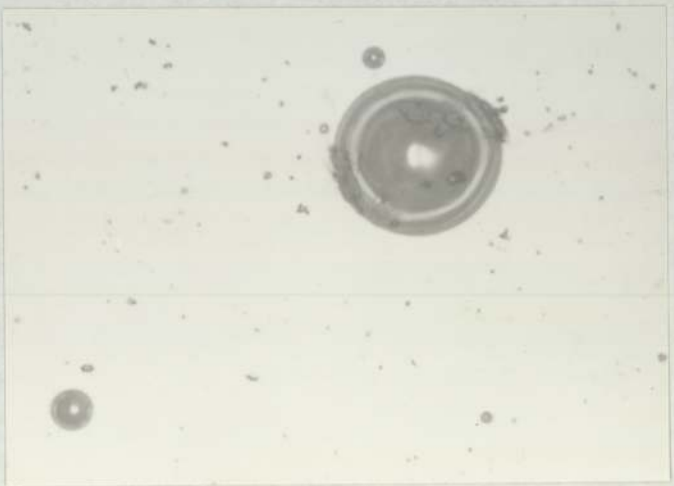

4.7.

PLATE 4.8

INCLUSION FROM MELT (A12) SHOWING
NON-GLASSY CHARACTER.

X800

PLATE 4.9

OPAQUE INCLUSIONS FROM MELT (A12)
WHICH APPEARS TO CONTAIN VERY
FINE PRECIPITATES

X750

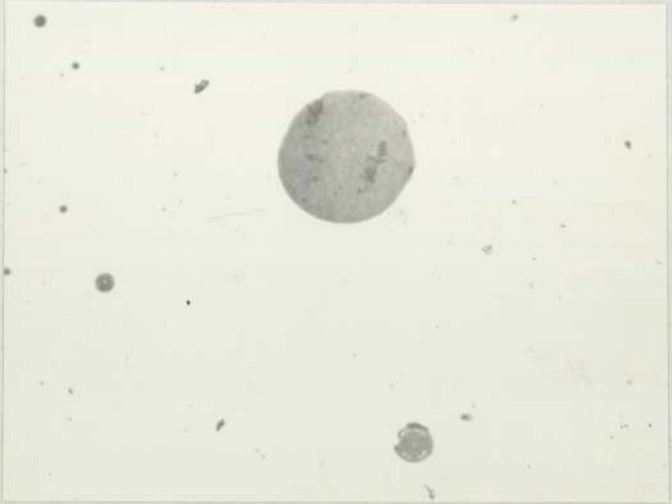

4.8.

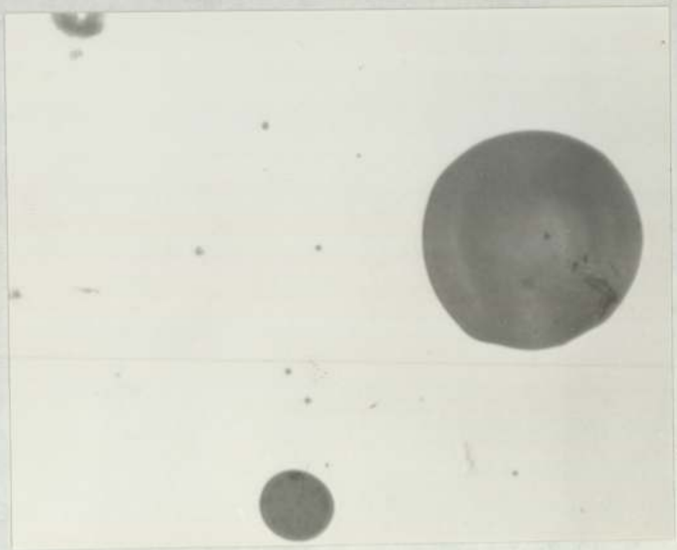

4.9.

PLATE 4.10

GLASSY AND PRECIPITATED INCLUSIONS
TAKEN FROM MELT (A14)
X570

PLATE 4.11

TWO PHASE AL_2O_3 - SILICATE
INCLUSIONS TAKEN FROM MELT
(A18)

X105

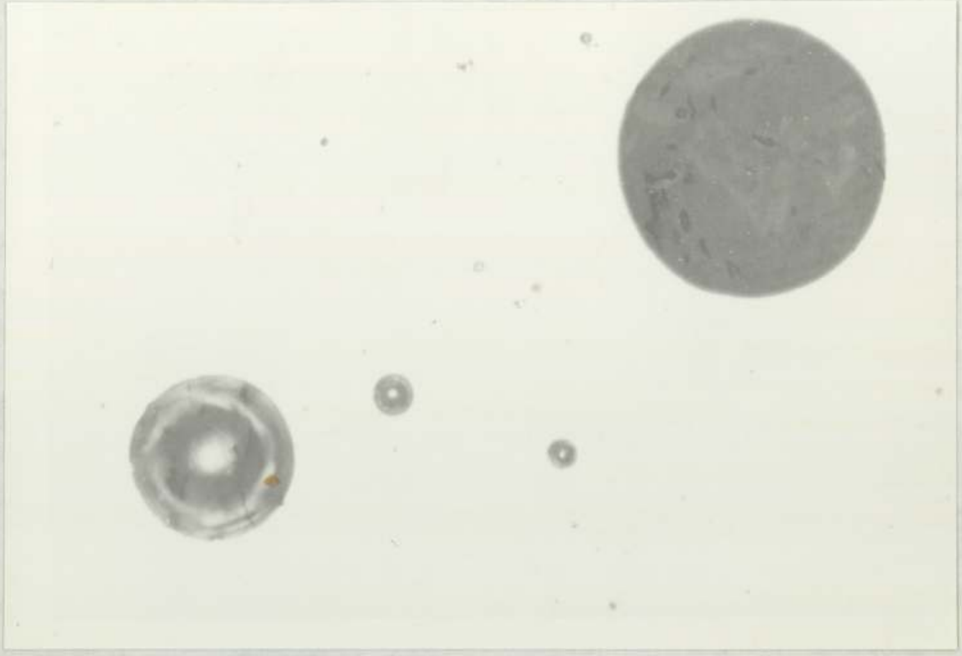

4.10.

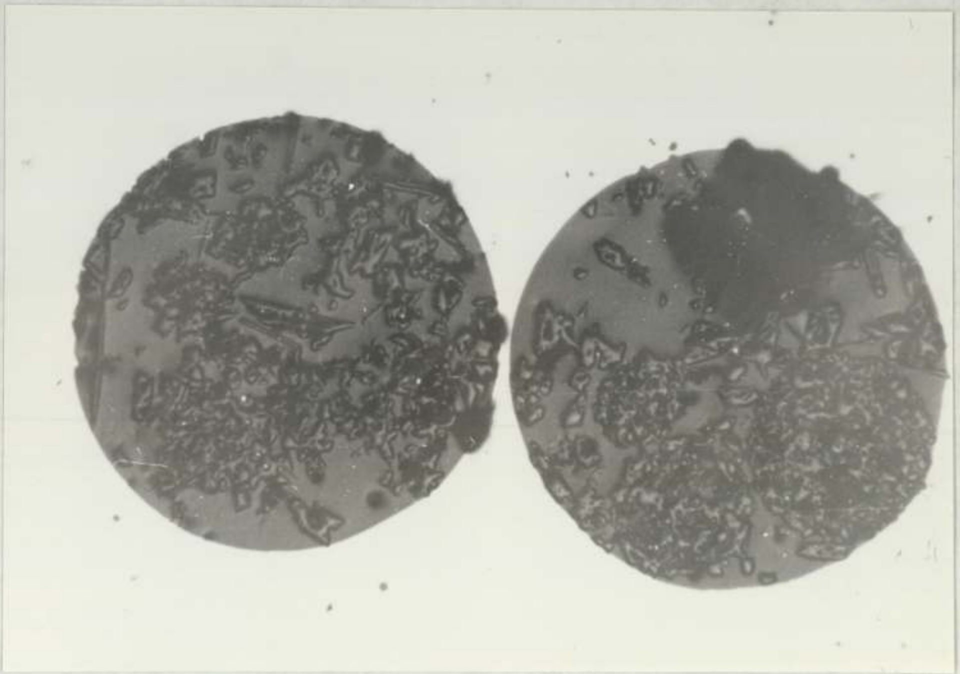

4.11.

PLATE 4.12

LARGE TWO PHASE Al_2O_3 - SILICATE INCLUSION, CONTAINING WHITE AREAS WHICH ARE Fe/(FeO)RICH

X210

4.12.

The melts deoxidised with the same deoxidant as in melt A12, but which had alloying additions present (i.e. melts NIA12, NI50A12, CRA12 and VA12) all the inclusions were glassy. Plate 4.13. shows the typical glassy nature of such inclusions, which are analogous with the glassy inclusions found in melts A4 - A18.

4·8
Metallographic examination (Hot rolled samples).

The behaviour of inclusion phases when rolled at various temperatures have been compiled into tabular form (table 4.10.) rather than expressing repetitive statements. This table relates the general characteristics of the larger inclusions found within the mid plane (XY) section at a matrix height true strain of approximately 1.2 (70% reduction). Their behaviour has been coded viz: and characterised in figures.

G refers to glassy inclusions

O refers to opaque inclusions

P refers to inclusions containing resolvable precipitate

Non deformable inclusions (N.D.)

X indicates that the inclusions were observed to be non deformable

Brittle inclusions (B) (figure 4.8.)

Deformed inclusions (D) (figure 4.9.)

With regard to the smaller inclusions it was usual to observe that they had either deformed or not. There was no directly observable evidence that inclusions less than 5 µm

PLATE 4.13

TYPICAL DISTRIBUTION OF GLASSY INCLUSIONS

MELT NIA12

X 140

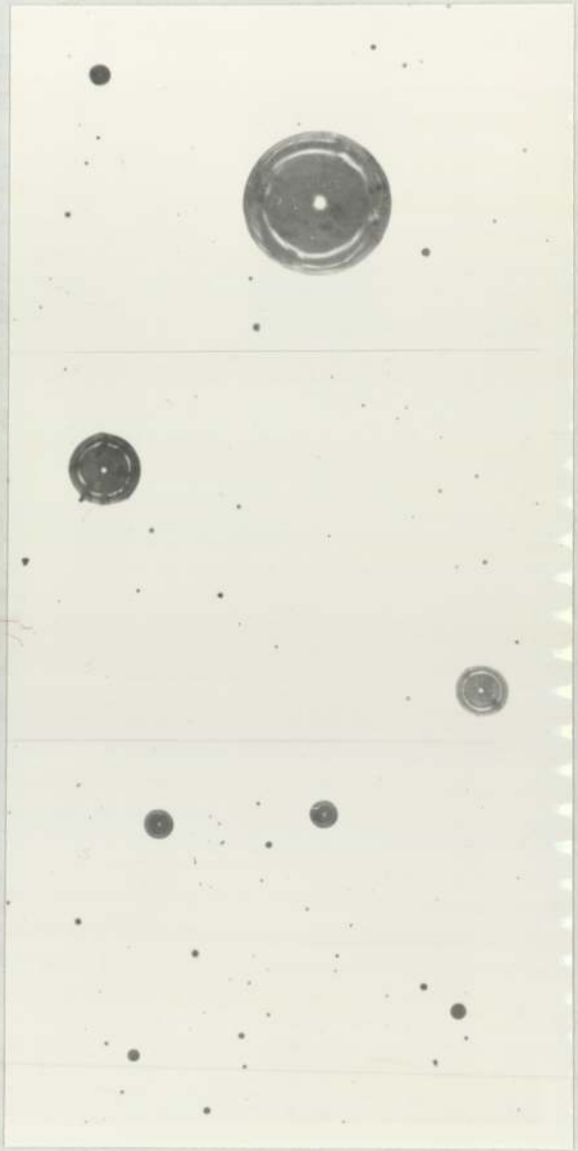

4·13

Behaviour of inclusions upon rolling. Table 4.10

(General characteristics - larger inclusions).

Melt	Rolling Temp °C	Incl^{n} Type	Inclusion Behaviour		
			ND	B	D
A3	800	O	X	-	-
	900	O	X	-	-
	1100	O	X	-	-
	1300	O	X	-	-
A4	900	G	X	-	-
	1000	G	X	-	-
	1300	G	X	-	-
A6	900	G	X	-	-
		O	X	-	-
		P	X	1.2.3	-
	1000	G	X	-	-
		O	X	-	-
		P	X	1.2.3	-
	1300	G		-	1.2.4
		P		-	1.2.4
A6(2)	800	G	X	-	-
	900	G	X	-	-
		P	X	-	-
	1100	G		-	1.2
		P		-	1.2
	1200	G		-	1.2.4
	1300	G		-	2.4
A7	900	G	X	-	-
		O	X	-	-
		P	X	1.2.3	-
	1000	G	X	-	1
		O	X	-	-
		P	X	1.2.3	-
	1100	G		-	1.2
		P		4	1
	1300	G		-	1.2.4
		P		-	1.2.4
A8	900	G	X	-	-
		O	X	-	-
		P	X	-	-
	1000	G		-	1
		O	X	-	-
		P	X	3.4	-
	1300	G		-	1.2.4
		P		4	1.2.4

Table 4.10

Melt	Rolling Temp °C	Incl^{n} Type	Inclusion Behaviour		
			ND	B	D
A9	900	G	X	-	-
		O	X	-	-
		P	X	-	-
	1000	G		-	1
		O	X	-	-
		P	X	2.3.4	1
	1300	G		-	1.2.3.4
		P		2.4	1.2.4
A10	900	G	X	-	-
		O	X	-	-
		P	X	-	-
	1000	G	X	1	1
		O	X	-	-
		P	X	1.2.3.4	1
	1300	G		-	1.2.4
		P		4	1.2.4
A11	900	G	X	-	-
		O	X	-	-
		P	X	-	-
	1000	G	X	1	1.2
		O	X	-	-
		P	X	4	1.2
	1300	G		-	1.2.4
		P		-	1.2.4
A12	800	G		-	1.2
		O	X	-	-
		P	X	1.2.3.4	1.2
	900	G		-	-
		O	X	-	-
		P	X	1.2.3.4	1
	1000	G		-	1.4
		O	X	-	-
		P	X	1.2.3.4	1.4
A13	800	G		-	1
		O	X	-	-
		P	X	-	1
	850	G		-	1.2
		O	X	-	-
		P	X	3.4	1
	900	G		-	1.2
		O	X	-	-
		P	X	3.4	1
	1000	G		-	1.2
		O	X	-	-
		P		2.3.4	1

Table 4.10

Melt	Rolling Temp °C	Incl^n Type	Inclusion Behaviour		
			ND	B	D
A13X	600	G	X	-	1
		P	X	-	1
	700	G	X	-	1.2
		P	X	-	1.2
	800	G		-	1.2
		P	X	3.4	1
	900	G		3.4	1.2
		P		3.4	1.2
	1000	G		-	1.2
		P		-	1.2
	1100	G		-	1.2.4
		P		-	1.2.4
A14	900	G	X	-	1
		O	X	-	-
		P	X	1.2.3.4	1
	950	G	X	-	1.2.3.4
		O	X	-	-
		P	X	3.4	1.2.3.4
	1000	G		-	1.2.3
		P		-	1.2
A14(2)	1000	G		-	2.4
		O		-	-
		P		-	1.2.4
A14C	600	G	X	-	1
	700	G		-	1.2
	800	G	X	-	-
		O	X	-	-
		P	X	1.2.3.4	1
	900	O	X	-	-
		P	X	1.2.3.4	-
	1000	G		-	2.4
		P		-	2.4
A15	900	G		-	1.2
		P	X	4	1.2.4
	1100	G		-	1.2.3
		P		-	1.2
	1300	G		-	2.3.4
		P		-	2.3.4
A16	800	G	X	-	1
	850	G		-	1.2
	900	G		-	-
	1100	G		-	2.3
	1300	G		-	2.3.4

Table 4.10

Melt	Rolling Temp°C	Incl^{n} Type	Inclusion Behaviour		
			ND	B	D
A17	750	G	X	-	1
		P	X	1.2.3.4	1
	800	G		-	2
		P	X	1.2.3.4	2.4.5
	850	G		-	2
		P	X	1.2.3.4	2.4.5
	900	G		-	2
		P		1.2.3.4	2.4.5
	1000	G		-	1
		P		2.3.4	2.5
A18	750	P	X	1.2.3.4	2
	800	P		1.2.3.4	2
	850	P		1.2.3.4	2
	900	P		1.2.3.4	2.5
	1000	P		1.2.3.4	2.4.5
NIA12	800	G	X	1	1
	850	G		-	2.4
	900	G		-	2.3.4
	1000	G		-	2.3.4
CRA12	750	G	X	-	1
	800	G		1	1.2
	850	G		-	1.2
	900	G		-	2.4
	1000	G		-	2.3.4
VA12	800	G	X	-	1
	850	G	X	1	1.2
	900	G		-	2.4
		P		-	2.4
	1000	G		-	2.3.4
	1100	G		-	2.3.4
N150A12	750	G	X	-	1
	800	G		-	1
	850	G		-	1
	900	G		-	1.2
	1000	G		-	1.2.4
	1100	G		6	2.3.4

Fig. 4.8

Brittle inclusions.

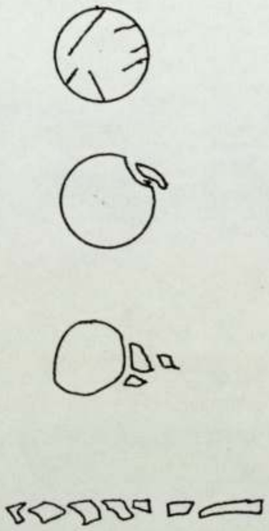

1. cracked/shattered.
2. chipped.
3. fractured.
4. disseminated.

Fig. 4.9

Deformed inclusions.

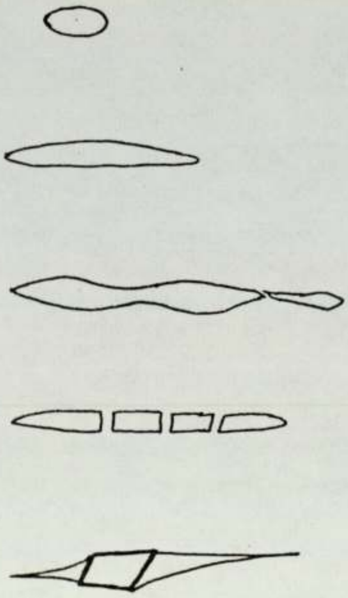

1. slightly deformed.
2. well deformed.
3. neck and/or fracture.
4. deformed + fracture .
5. tailing of plastic phase from precipitate.

had undergone brittle fracture, even when their larger counterparts had done so.

Occasionally with small well deformed inclusions there was some evidence of type (4) deformable behaviour.

The behaviour of small inclusions for various inclusion compositions and rolling temperatures has been examined for several melts (table 4.11.) on a deformable/non deformable basis. This behaviour may also be obtained from the data presented on inclusion plasticity. (table 4.9.).

Plates 4.14. to 4.23. show examples of non deformable and brittle behaviour of inclusions, when rolled at 900°C (a temperature where this behaviour seems prevalent for the inclusion compositions under investigation).

From these figures it is observed that when an inclusion does not deform there may be a tendency to form conical voids in the direction of matrix flow (plates 4.14 & 15) If the inclusions behave in a brittle manner they may crack, shear or disseminate into the rolling direction, plates 4.16.–.23. illustrate these characteristics.

Unfortunately it is not always true that for a given temperature inclusions within a given section will behave in a similar manner. Plate 4.23. shows an example of a deformed inclusion in the proximity of an inclusion which has sheared (An observation which is discussed later).

A similar situation is shown in Plate 4.24 . Three inclusions in proximity are seen to exhibit totally different behaviour, whilst also showing that inclusions within the same melt may have different compositions. Inclusions which were observed to be plastically deformed

Table 4.11

Relationship between number of deformable inclusions (1-20 μm) and rolling temperature.

Melt	Rolling Temp. °C	N_{DI} (1-20 μm)	N_f^*	$\frac{N_{DI}}{N_f}$	N_{DI} (1-20) mm^{-2}
A12	800	38	100	0.38	32
	900	45	180	0.25	21
	1000	109	100	1.09	90
NIA12	800	209	220	0.95	79
	850	143	500	0.29	24
	900	25	500	0.05	4
	1000	141	100	1.41	117
NI50A12	750	21	200	0.11	9
	800	37	200	0.19	15
	850	99	100	0.99	82
	900	116	100	1.16	96
	1000	146	70	2.08	173
	1100	245	117	2.09	174
CRA12	800	126	50	2.52	209
	850	36	500	0.07	6
	900	105	370	0.28	24
	1000	115	70	1.64	136

* 1 Field = 0·012 mm^2

Table 4.11

Melt	Rolling Temp. °C	N_{DI} (1-20μm)	N_f	$\frac{N_{DI}}{N_f}$	N_{DI} (1-20) mm^{-2}
VA12	800	118	120	0.98	82
	850	116	170	0.68	57
	900	99	250	0.39	33
	1000	116	40	2.90	241
	1100	247	52	4.75	394
A13X	600	4	400	0.01	1
	700	20	380	0.05	4
	800	34	240	0.14	12
	900	6	220	0.03	2
	1000	68	150	0.45	38
	1100	105	30	3.50	291
A14C	600	1	400	0.01	0
	700	22	400	0.06	5
	800	11	400	0.03	2
	900	11	350	0.03	3
	1000	17	230	0.07	6
A16	800	79	600	0.13	11
	850	159	200	0.80	66
	900	30	500	0.06	5
	1100	92	380	0.24	20
	1300	130	100	1.30	108

PLATE 4.14

NON DEFORMABLE INCLUSIONS, SHOWING CONICAL VOIDS IN THE ROLLING DIRECTION. TAKEN FROM MELT A6. ROLLED AT 900°C TO A HEIGHT TRUE STRAIN OF $\varepsilon_m = 1.14$

X400

PLATE 4.15

CONICAL VOID PRODUCED IN THE ROLLING DIRECTION.

TAKEN FROM MELT A7. ROLLED AT 900°C

$\varepsilon_m = 0.69$ (50%).

X200

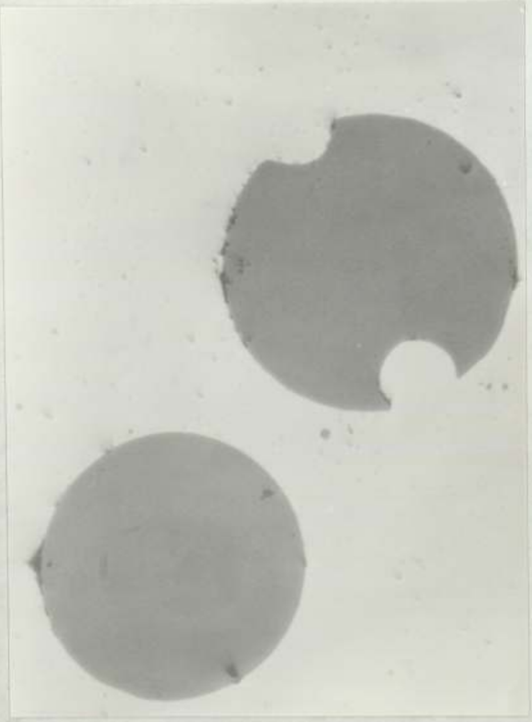

4.14.

4.15.

PLATES 4.16 & 4.17

BRITTLE INCLUSIONS WHICH HAVE CRACKED AND SHOW MATRIX PENETRATION INTO THE CRACKS.

4.16

FROM MELT A7 ROLLED AT 900°C. TO A MATRIX TRUE STRAIN OF 1.2 (70%)

X200

4.17

FROM MELT A8 ROLLED AT 900°C. TO A MATRIX TRUE STRAIN OF 1.2 (70%)

X400

4.16.

4.17.

PLATES 4.18 & 4.19

INCLUSIONS WHICH HAVE BEHAVED IN A BRITTLE MANNER WHEN ROLLED AT 900°C.

4.18

FROM MELT A7 ROLLED TO A MATRIX HEIGHT TRUE STRAIN OF 0.69 (50%)
X200

4.19

FROM MELT A9 ROLLED TO A MATRIX HEIGHT TRUE STRAIN OF 1.2 (70%)
X400

4 . 18 .

4.19.

PLATES 4.20 & 4.21

INCLUSIONS ROLLED AT 900°C. TO A
MATRIX HEIGHT TRUE STRAIN OF 2.23(90%)

4.20

FROM MELT A6

X400

4.21

FROM MELT A7

X200

4.20.

21

4.21.

PLATE 4.22

BRITTLE INCLUSION FROM MELT A9
ROLLED AT 900°C. TO A MATRIX
HEIGHT TRUE STRAIN OF 2.23(90%)

X400

PLATE 4.23

TWO INCLUSIONS FROM MELT A14
SHOWING DISTINCTLY DIFFERENT
BEHVIOUR. THE SMALLER INCLUSION
HAS DEFORMED, WHEREAS THE LARGER
HAS SHEARED AT APPROXIMATELY 45°
TO THE ROLLING DIRECTION.
ROLLED AT 900°C TO A MATRIX HEIGHT
TRUE STRAIN OF 1.2(70%)

X400

4.22.

4.23.

PLATE 4.24

THREE INCLUSIONS WITH CLOSE PROXIMITY SHOWING DIFFERENT BEHAVIOUR WHEN ROLLED AT 850°C. THESE INCLUSIONS ALSO EXHIBIT DIFFERENT COMPOSITIONS AS INDICATED BY X-RAY SCANS FROM THE MICROPROBE ANALYSER.

4.24 (a) FE - X RAY
(b) MN - X RAY
(c) SI - X RAY
(d) AL - X RAY
X 500

INCLUSIONS TAKEN FROM MELT A17 ROLLED TO 70% TOTAL REDUCTION

24

4.24.

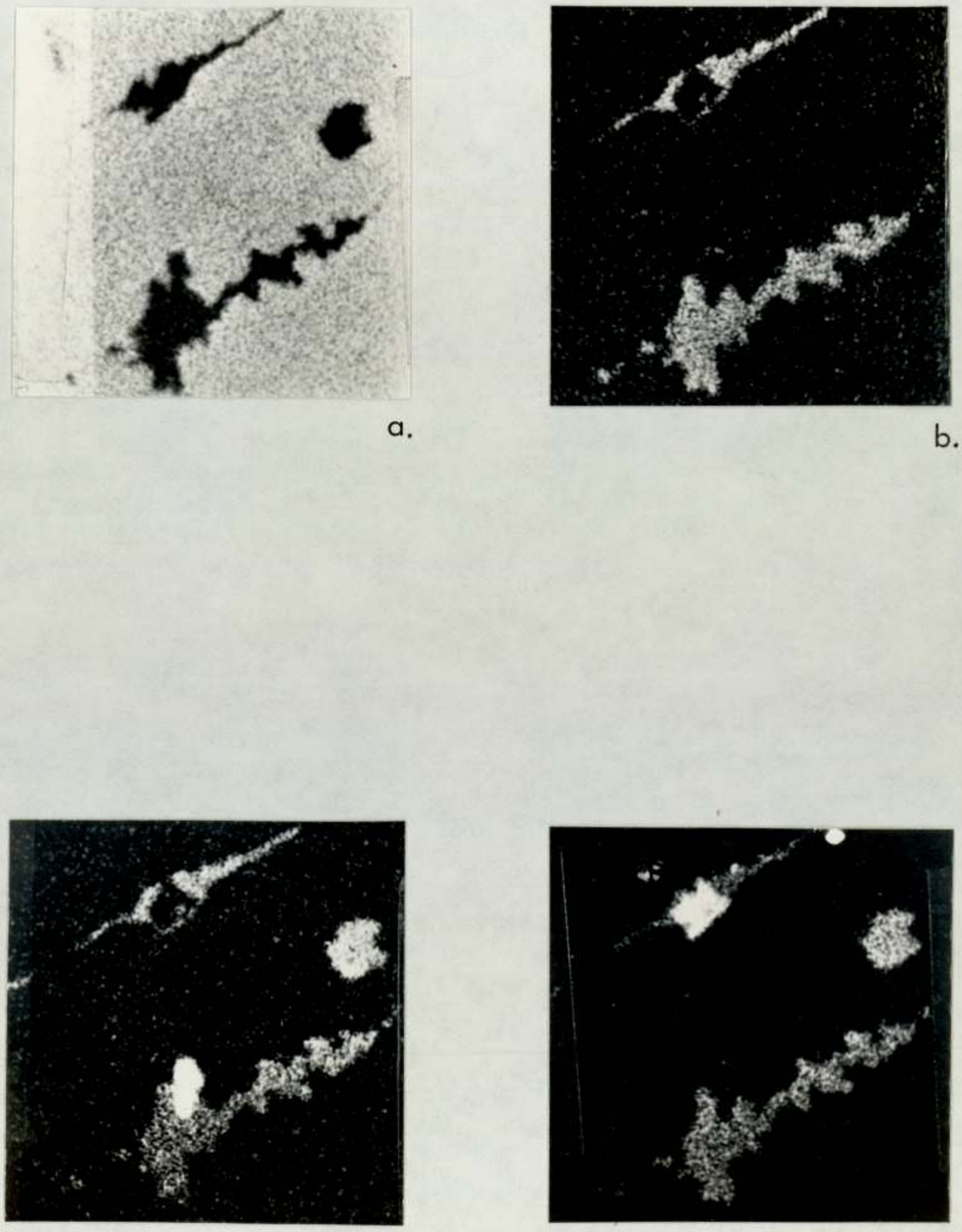

a. b. c. d.

at rolling temperatures below 900°C sometimes showed signs of inclusion fracture when rolled at 900°C

Plates 4.25. to 4.34. show the general characteristics of inclusion behaviour at various rolling temperatures Although the figures shown are those for melt A13X (where a large number of inclusions contain silica precipitates) they appeared to show the similar characteristics observed for other glassy type inclusions.

At low rolling temperatures the inclusions had not deformed (plates 4.25. to 4.26.). An increase in rolling temperature led to the presence of both plastically deformed inclusions, and inclusions which show both plastic and brittle characteristics (plates 4.27. to.28.

An increase in temperature caused the inclusions to deform in a plastic manner, to some degree, although the presence of precipitates within the glassy phase was observed to retard plastic deformation (plates 4. .29. to 4.32.). At temperatures above the plastic/ fluid transition temperature inclusions may exhibit undulating matrix/inclusion interfaces. (plates 4.34.&.35.)

Plates 4.36. to 4.37. show examples of initially glassy inclusions which were rolled in the 'plastic' temperature ranges, where it may be observed that there is non uniformity of inclusion strain with respect to inclusion size (plate 4.37.) also that precipitation within an inclusion will inhibit its deformation (plate 4.36) even at 90% reduction.

At temperatures well in excess of the plastic fluid

PLATES 4.25 & 4.26

INCLUSIONS FROM MELT A13X
ROLLED AT 600°C. TO A
MATRIX HEIGHT TRUE STRAIN
OF 1.2(70%)

X210

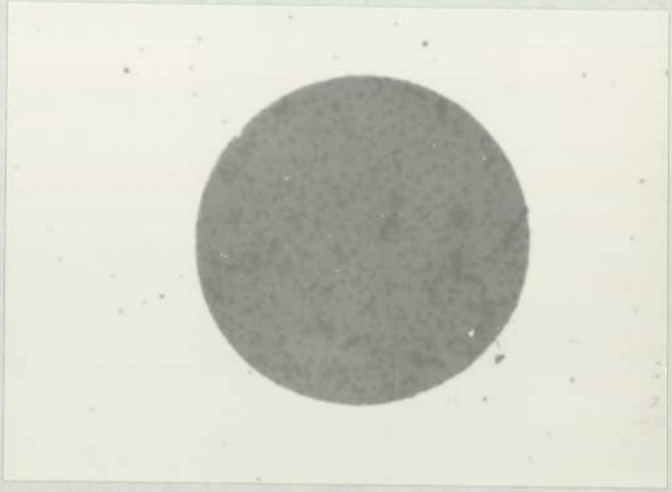

4.25.

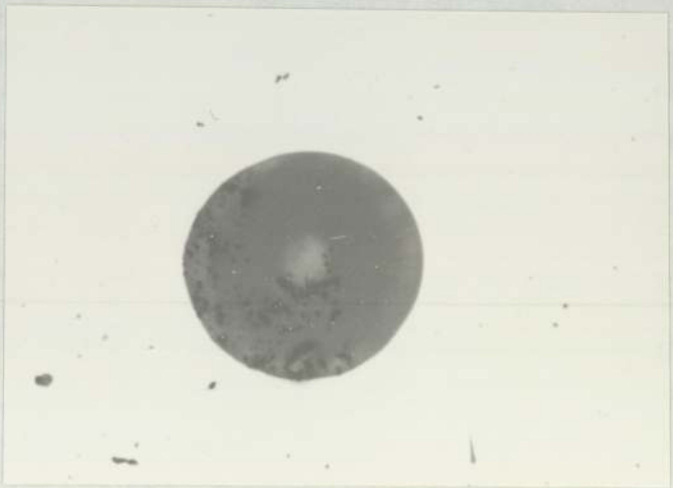

4.26.

PLATES 4.27 & 4.28

MELT A 13X

$\varepsilon_m = 1.2$ (70%)

ROLLED AT 700°C

X210

4.27.

4.28.

PLATE 4.29 → 4.32

MELT A13X

ε_m = 1.2(70%)

ROLLED AT 800°C.

X210

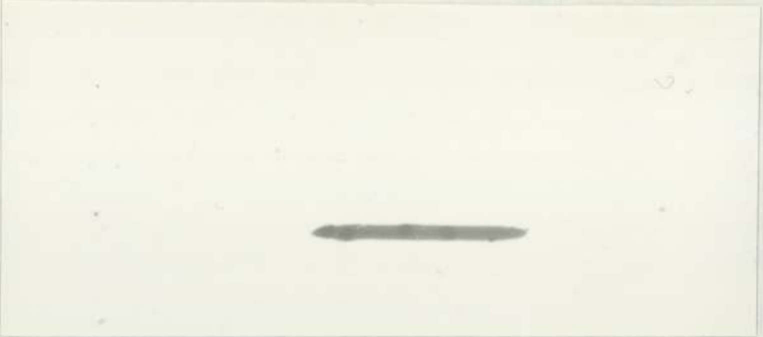

4.29.

.30.

.31.

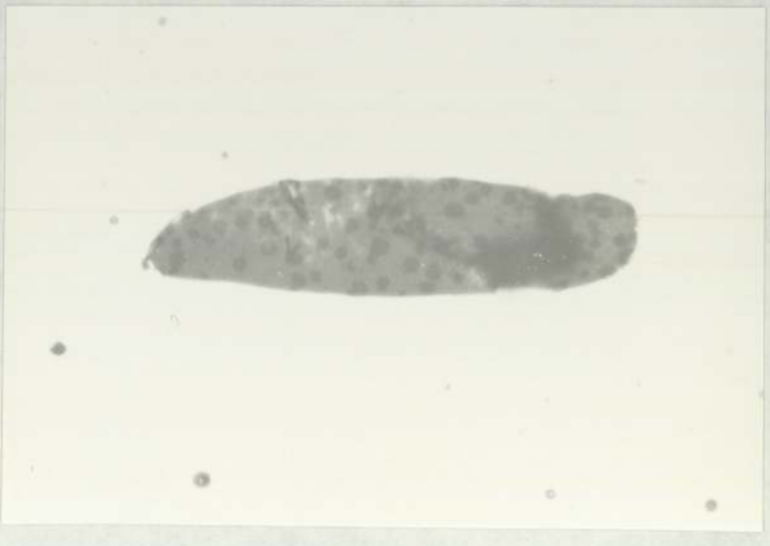

.32.

PLATES 4.33 & 4.34

MELT A13X

ε_m = 1.2 (70%)

ROLLED AT 1000°C.

X210

4.33.

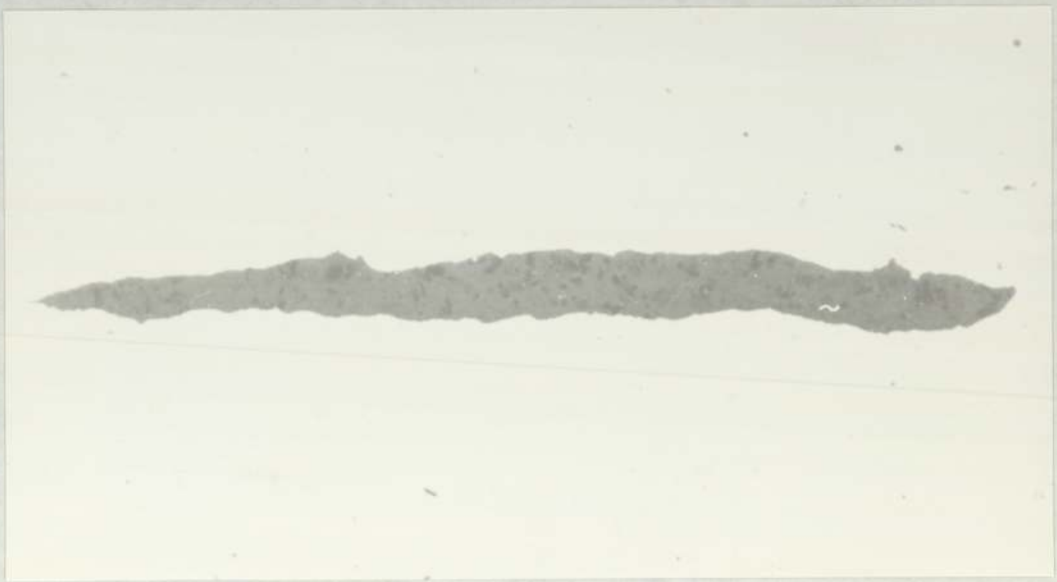

4.34.

PLATE 4.35

MELT NIA12

ε_m = 1.2 (70%)

ROLLED AT 1000°C.

X100

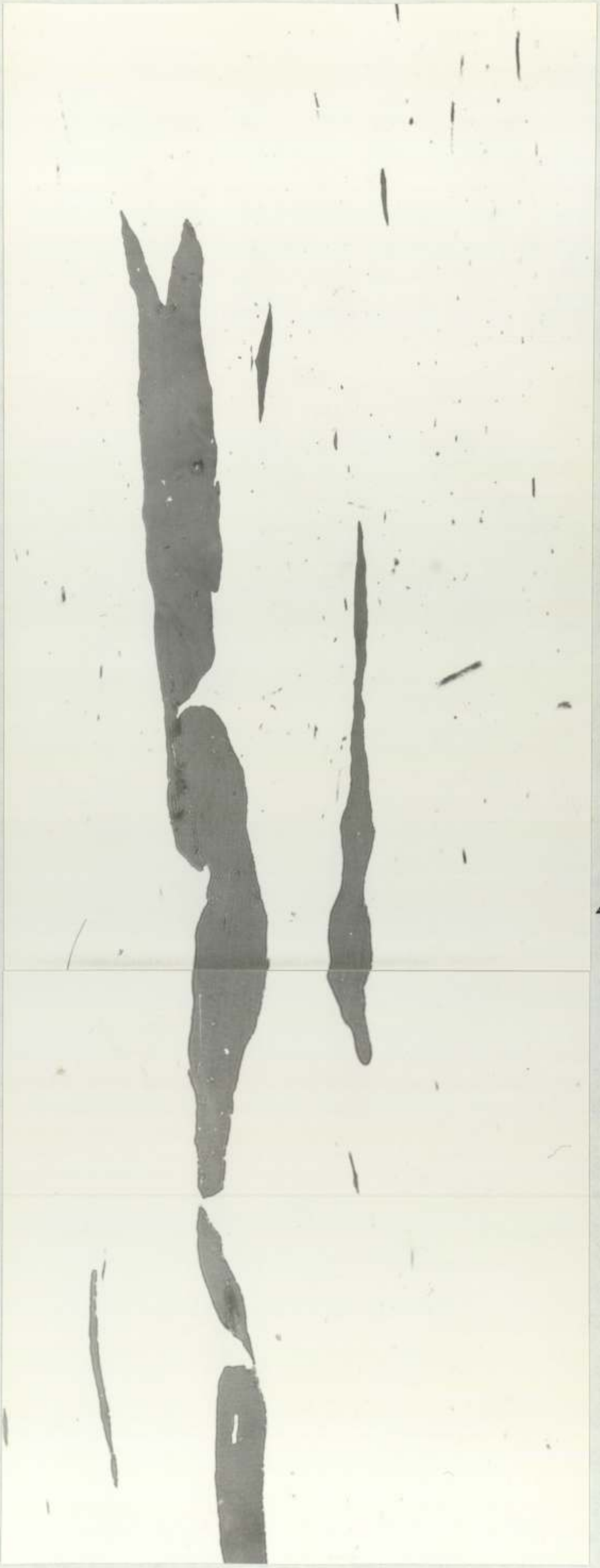

4.35.

PLATE 4.36

MELT A12

ε_m = 2.3 (90%)

ROLLED AT 800°C.

X 400

PLATE 4.37

MELT A12

ε_m = 1.2 (70%)

ROLLED AT 800°C

X400

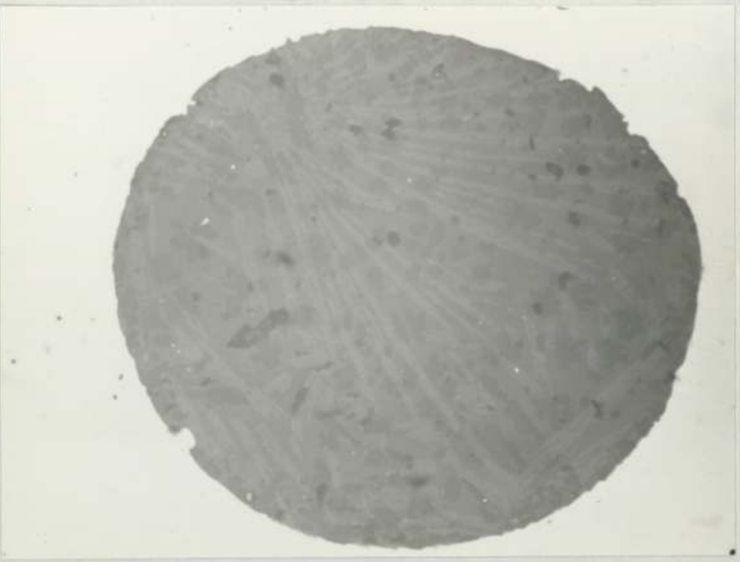

4.36.

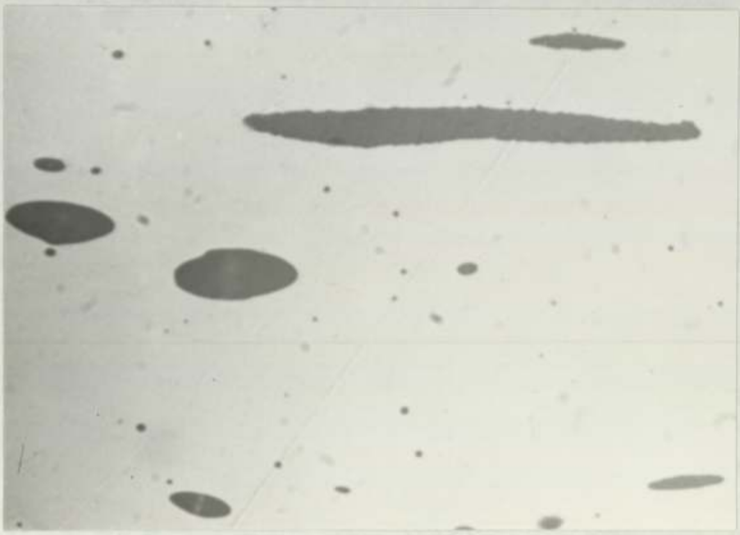

4.37.

transition temperatures some fluid inclusions appeared to neck and break up. (plate 4.35.)

4.9

Stereoscopic examination of rolled structures.

Plates 4.38. to 4.40. show examples of deformed inclusions, extracted from the central region of the strip formed on rolling melt A13X at 1100°C to a height strain of (1.2), and show the general shapes of inclusions after deformation at temperatures above the plastic/fluid transition temperature.

Plate 4.41. shows the a and b axis of a deformed inclusion from melt Al4 rolled to a strain of 1.2 at 900°C. This figure shows the presence of large precipitates protruding from out of the surface of the matrix of the inclusion. Smaller cuboid shaped holes can be seen in the surface regions of the inclusion. These are presumed to show the regions where smaller precipitates have been extracted from the inclusion matrix, due to the action of the brominol solution. However, the shape of these holes should be compared to the electron image photographs of melt Al4 plate 4.41a . These cuboid holes can again be seen in plate 4.42. which is the a - D section of the inclusion. It is also clear that the surface of the inclusion phases cannot be regarded as totally smooth, but contain undulations.

Plate 4.41b shows a inclusion from melt Al8 which had been deeply etched. In this plate it can be seen that the deformed inclusion is highly jagged due to the presence of angular alumina precipitates. This figure does contrast

PLATES 4.38, 4.39 & 4.40

STEREOSCAN PHOTOGRAPHS SHOWING EXAMPLES OF DEFORMED INCLUSIONS FROM THE CENTRAL REGION OF A DEFORMED BAR.

MELT A13X
$\varepsilon_m = 1.2$ (70%)
ROLLED AT 1100°C

INCLUSIONS WERE EXTRACTED FROM SAMPLES DEEP ETCHED USING A 10% BROMINOL (BROMINE IN METHANOL) SOLUTION.

4.38 X230
4.39 X550
4.40 X600

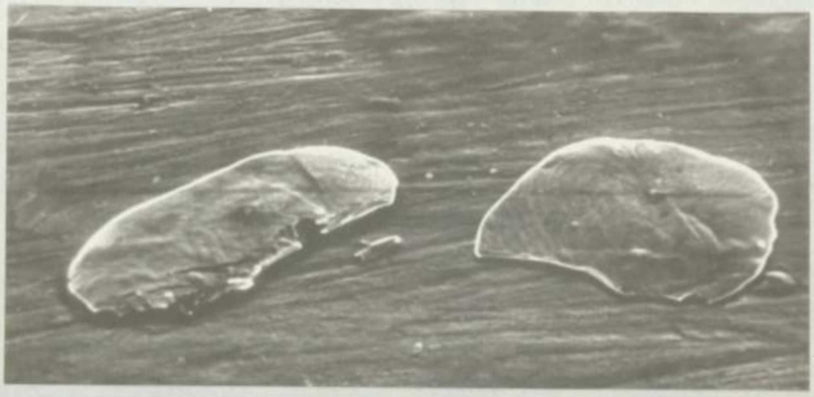

4.38.

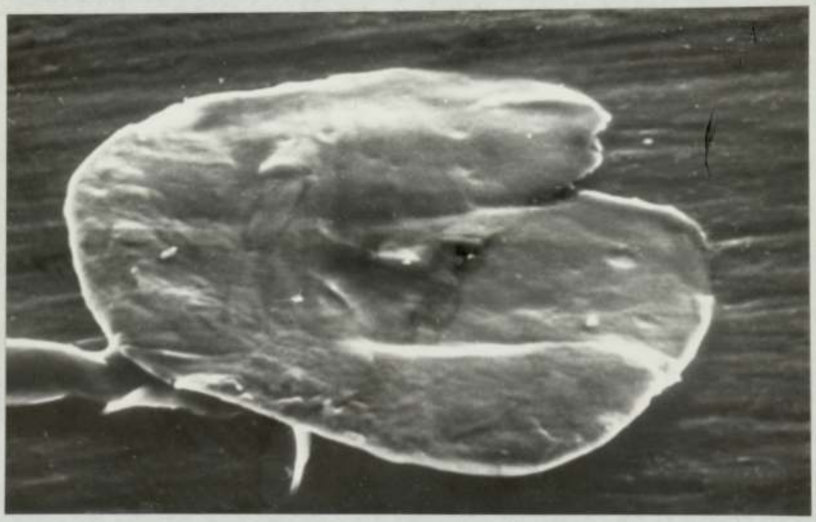

.39.

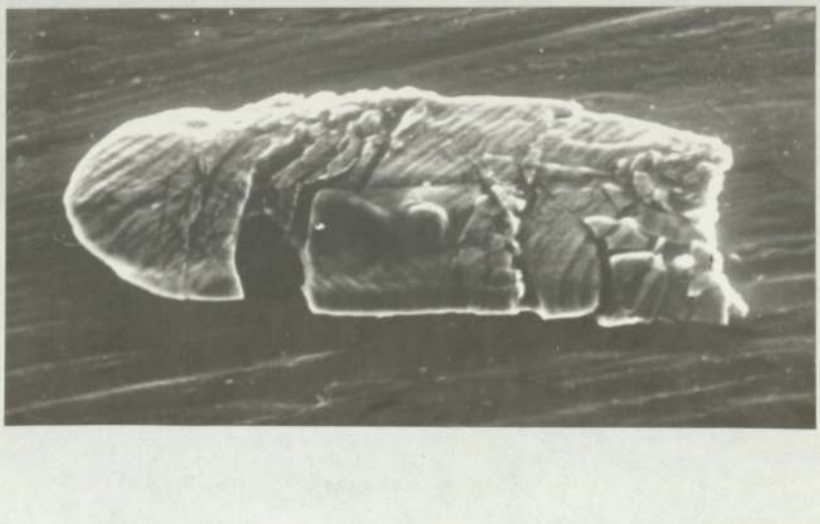

.40.

PLATE 4.41 (a)

STEREOSCAN PHOTOGRAPH OF A DEFORMED INCLUSION FROM THE CENTRAL REGION OF A DEFORMED BAR.

MELT A14
ROLLED AT 900°C.
$\varepsilon_m = 1.78$

X 830

(ETCHED IN 10% BROMINOL)

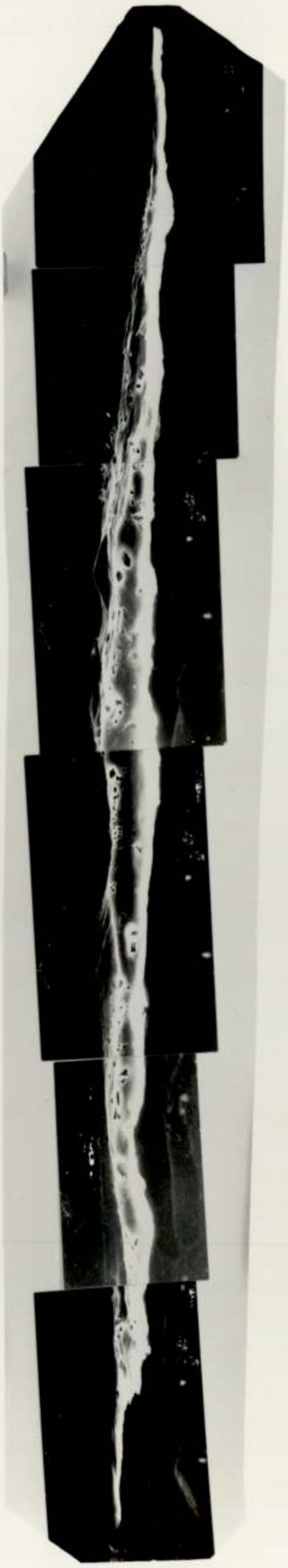

PLATE 4.41 (b)

STEREOSCAN PHOTOGRAPH OF A
DEFORMED INCLUSION FROM
MELT A18

ROLLED AT 900°C
$\mathcal{E}_m = 1.12$

X400

(ETCHED IN 10% BROMINOL)

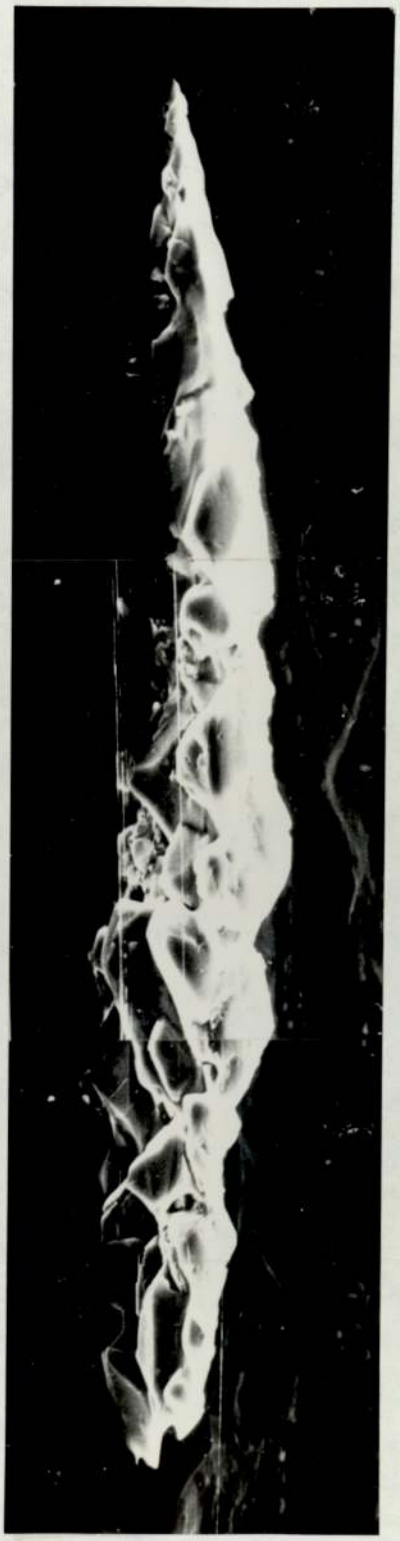

PLATE 4.41 (c)

STEREOSCAN PHOTOGRAPH OF A
DEFORMED INCLUSION FROM
MELT A17

ROLLED AT 900°C.
$\varepsilon_m = 1.2$

X 800

(ETCHED IN 10% BROMINOL)

PLATE 4.42

STEREOSCAN PHOTOGRAPH OF AN INCLUSION FROM A DEEP ETCHED (10% BROMINAL) MATRIX

MELT A14

ε_m = 1.2 (70%)

ROLLED AT 950°C.

PLATE (b) IS AN ENLARGEMENT OF THE TOP L.H.S. OF THE INCLUSION IN (a)

(a) X0.6K

(b) X2.4K

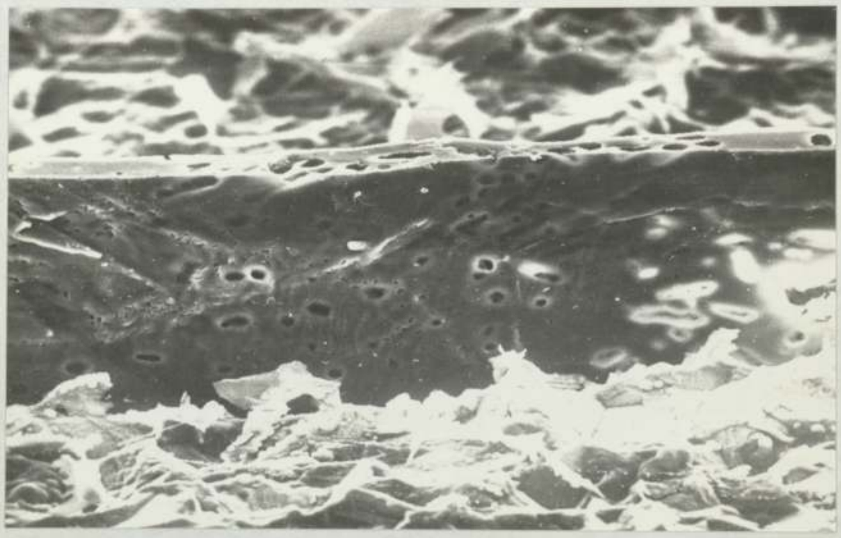

a.

4 . 42.

b.

with the much smoother appearance of the inclusions encountered in melts where less aluminium and hence fewer particles were present.

4.10

Heat treatment.

Optical examination of samples from melts A7, A11, A12, A13, A14, A15, heat treated at temperatures of 900, 1100, and 1300°C for various times showed that in most instances some change in the initial glassy structure had taken place. However the effect observed for a given sample varied, some inclusions showing signs of precipitation, and others remaining glassy. It must however be added that in the 'as cast' state a few inclusions with precipitated phases were observed, and as a result would mask the effect of heat treatment to some degree.

The times employed i.e. 1, 3, 8 and 16 hours at temperature showed only slight differences in inclusion structure, the observations again being impaired by the variability of the precipitation phenomenon. In general it appeared, subjectively, that as time at temperature increased fewer glassy inclusions were observed. For a given time at temperature it appeared that precipitates were larger at 1100°C than at 900°C. However at 1300°C it was evident that the majority of inclusions were of a glassy nature when compared to the inclusions at 900 and 1100°C. In table 4.12. the influence of heat treatment upon inclusion microstructure is shown albeit after 3hrs and 16hrs, the 1 and 3 hr samples appear indistinguishable, as did the 8 and 16hr samples.

Plates 4.43. —.56. are fairly representative examples of inclusions after heat treatment, from which it is evident that a variation in behaviour with regard to precipitation occurs within any given sample.
Plates 4.57. & .58. are X-ray photographs of precipitated inclusions found in melt Al4 after heat treatment at 1100°C for 2 hours. These plates illustrate the presence of sulphur at the periphery of inclusions adjacent to manganese rich precipitate area.

Plates 4.59. — .65. are electron images of heat treated inclusions showing precipitate phases. Analysis of these inclusion phases (Appendix 4.3) and phases present within inclusions resulting from Mn - Si and Mn - Si - Al deoxidation in this investigation have indicated that the only phases apparently present are: Silica, Alumina or Rhodonite. However, the size of precipitate is highly variable, as indicated in plate 4.63.

TABLE 4.12

Melt.	Temp. °C	Soaking Time 3 hrs.	 16 hrs.
A7	1300	Small inclusions 10 μm glassy Large inclusions often opaque and contain precipitates. Some show the presence of reaction rims.	Comparable with 3 hrs. However, precipitate size appears slightly larger.
	1100	As 1300, reaction rim less evident. Some inclusions appear to contain small white areas, possibly iron globules.	As 3 hrs.
	900	As 1100 and 1300°C. Presence of white areas less evident.	As 3 hrs.

TABLE 4.12 (cont.)

Melt	Temp. °C	Soaking Time.	
		3 hrs.	16 hrs.
All	1300	Small inclusions 10 µm glassy 10 - 20 µm inclusions appear opaque. Above 20 µm some inclusions appear to contain globules of Fe.	As 3 hrs.
	1100	As 1300°C, although there appears to be the presence of MnS cusps at the inclusion steel matrix interface.	As 3 hrs.
	900	As 1300°C.	As 3 hrs.

TABLE 4.12 (cont.)

Melt	Temp. °C	Soaking Time	
		3 hrs.	16 hrs.
A12	1300	With the exception of a few large inclusions > 50 µm, all appear glassy. The large inclusions appear to contain fine precipitates.	As 3 hrs. However all inclusions appear glassy with few exceptions.
	1100	Larger number of small inclusions appear to contain a precipitate phase, and some MnS cusps are evident. A large number of inclusions have appeared to remain glassy. Less evidence of reaction rim than encountered in melts A7 and A14.	Fewer glassy inclusions Inclusions 10 um appear opaque, often containing precipitates.

TABLE 4.12 (cont.)

Melt	Temp °C.	Soaking time.	
		3 hrs.	16 hrs.
A12	900	Essentially very little difference to 1100°C.	As 3 hrs.
A13	1100 (only)	2 hrs. (only) Smaller inclusions 20 µm in the main appear to be glassy However, the larger inclusions frequently observed to contain precipitated phases.	

TABLE 4.12 (cont.)

Melt	Temp. °C	Soaking time.	
		3 hrs.	16 hrs.
A14	1300	Small inclusions appear glassy (i.e. 10 µm). 10 - 20 µm inclusions appear opaque. 20 µm precipitation observed, (some large precipitates). However a large number of inclusions appear glassy.	As 3 hrs.
	1100	As 1300°C, although the presence of MnS cusps observed. Reaction rims also evident.	As 3 hrs. except that fewer glassy inclusions are evident.
	900	As 1300°C, however fewer glassy inclusions observed.	As 3 hrs.

TABLE 4.12 (cont.)

Melt.	Temp. °C	Soaking time.	
		3 hrs.	16 hrs.
A15	1300	All inclusions appear glassy with the exception of a few large inclusions which appear opaque.	As 3 hrs.
	1100	Small inclusions glassy. Larger inclusions often appear opaque, signs of very fine precipitate. Some small white areas evident as in A7 and A11.	As 3 hrs. Reaction rim only evident at 1100°C.
	900	Small inclusions glassy. Majority of large inclusions are opaque and/or contain small precipitation.	As 3 hrs.

PLATES 4.43 - 4.45

OPTICAL MICROGRAPHS OF HEAT
TREATED INCLUSIONS

MELT A7
HEAT TREATED AT 1100°C. FOR
3HOURS.

X570

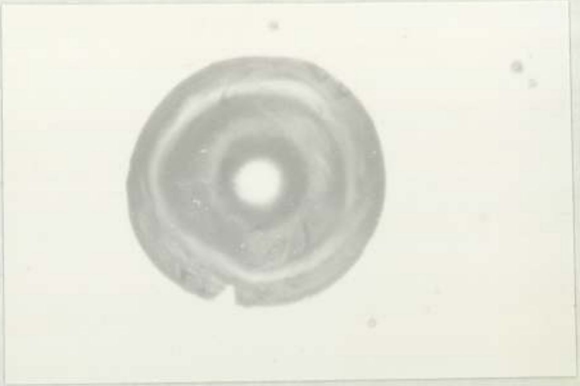

4.43.

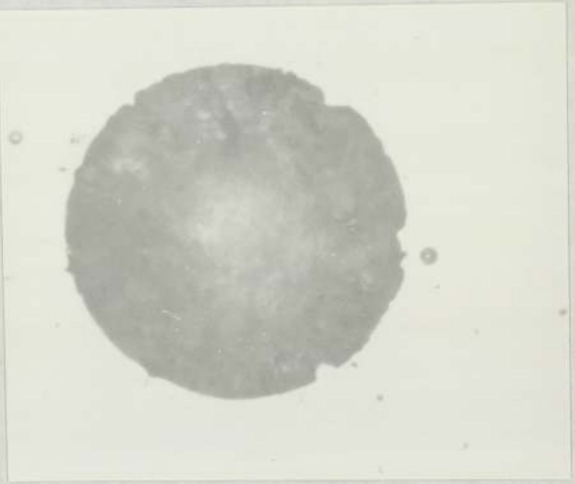

.44.

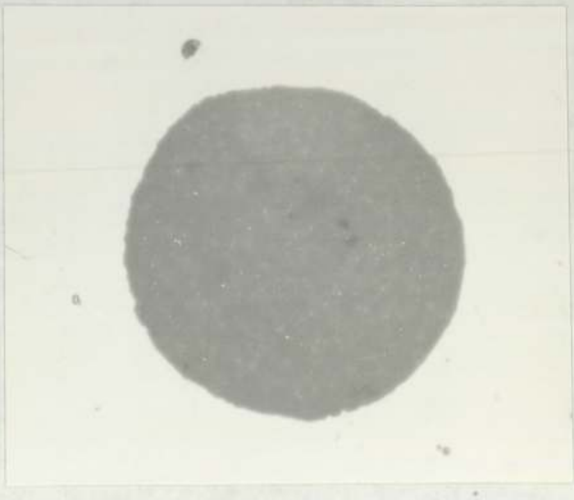

.45.

PLATES 4.46 & 4.47

HEAT TREATED INCLUSIONS SHOWING
MNS CUSPS

MELT A11

HEAT TREATED AT 1100°C FOR
3 HOURS

X570

4 . 46.

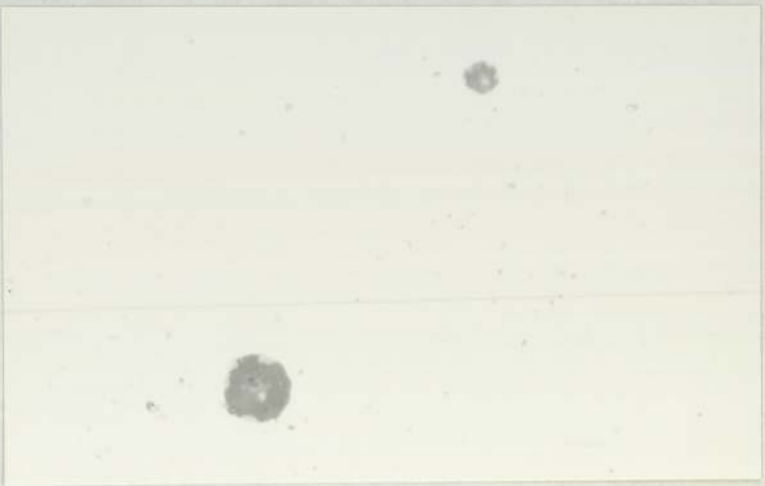

.47.

PLATES 4.48 - 4.50

MELT A12

HEAT TREATED AT 1100°C. FOR

3 HOURS

X570

4. 48.

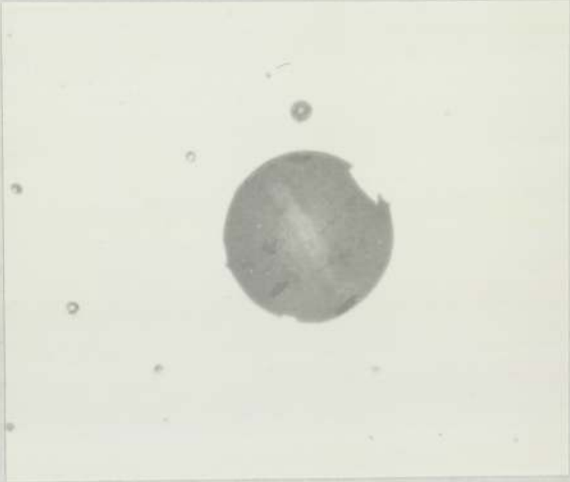

.49.

.50.

PLATES 4.51 - 4.53

MELT A14

HEAT TREATED AT 1100°C. FOR

3 HOURS

X570

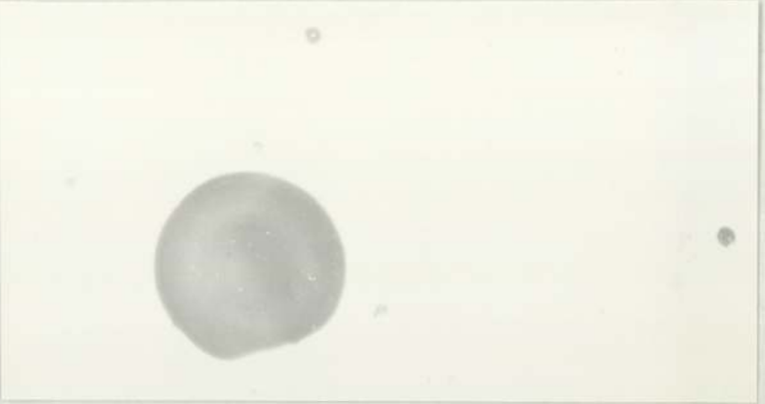

4.51.

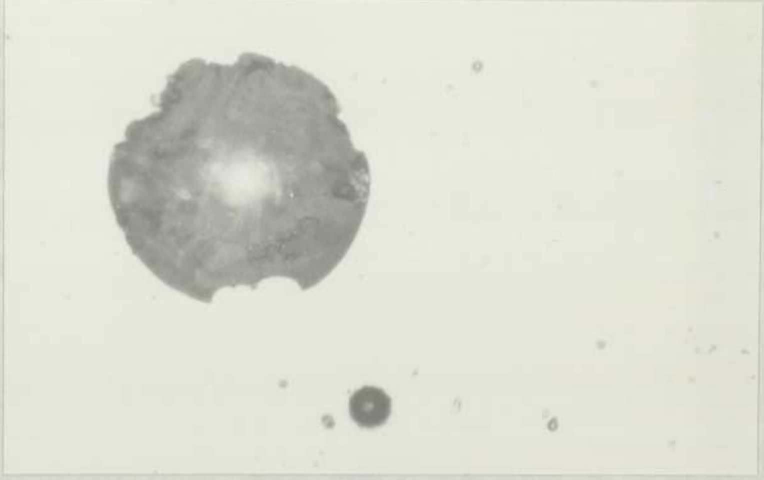

.52.

.53.

PLATE 4.54

MELT A15

HEAT TREATED AT 1100°C. FOR

3 HOURS

X570

PLATE 4.55

MELT A13

HEAT TREATED AT 1100°C FOR

2 HOURS

X400

PLATE 4.56

MELT A14C

QUENCHED FROM 820°, AFTER

BEING HELD AT TEMPERATURE

FOR 1 HOUR

X570

4 . 54.

.5 5.

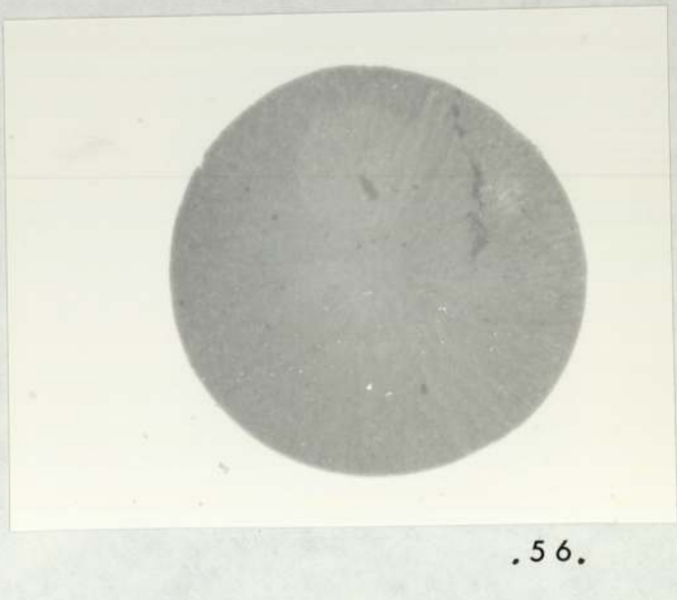

.5 6.

PLATE 4.57

MICROPROBE ANALYSER X-RAY MICROGRAPHS

MELT A14

HEAT TREATED AT 1100°C. FOR

2 HOURS

(a) SI - XRAY

(b) S - XRAY

(c) MN - XRAY

(d) AL - XRAY

X800

4 . 57.

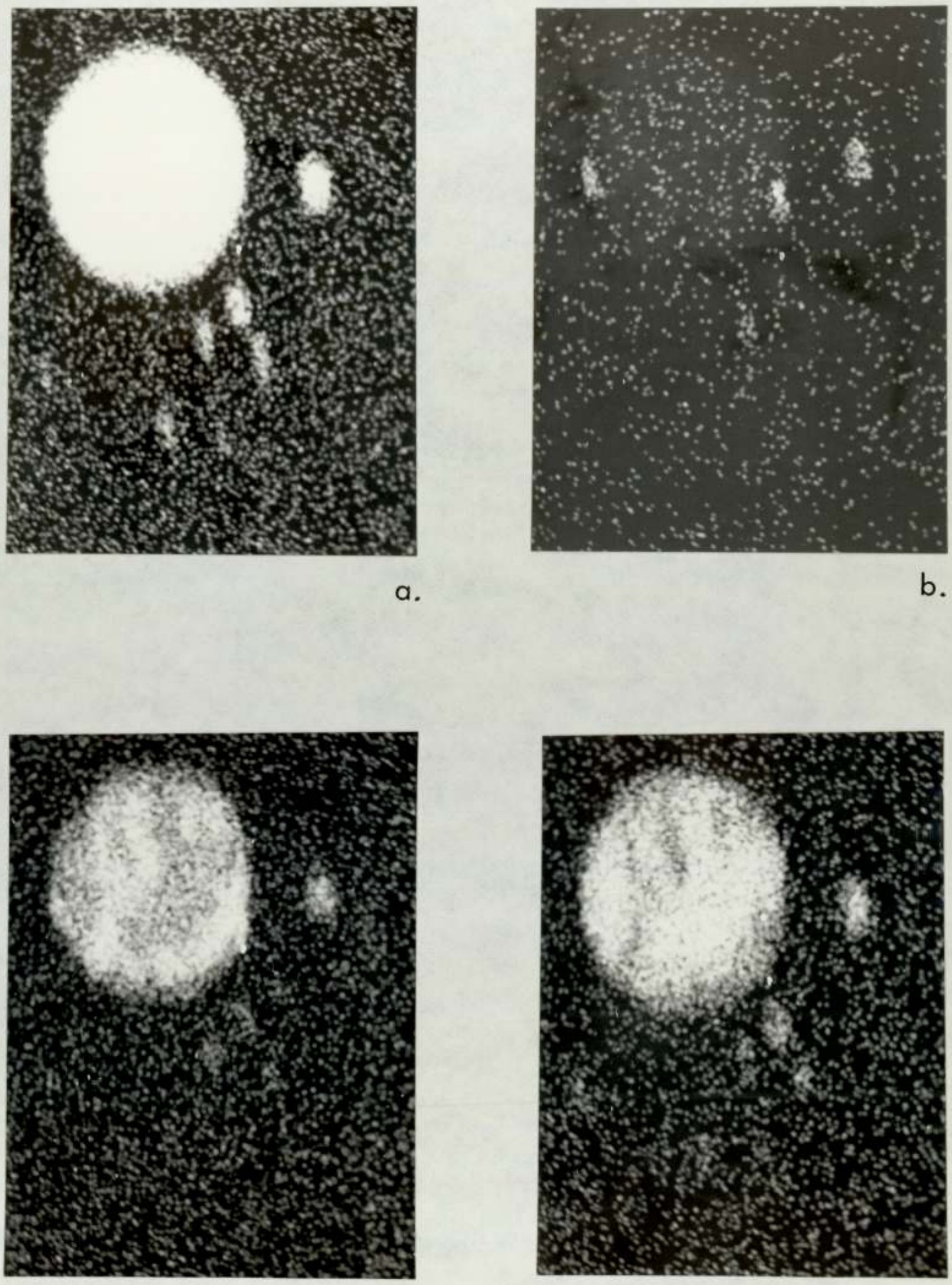

a.

b.

c.

d.

PLATE 4.58

MICROPROBE ANALYSER X- RAY
MICROGRAPHS

MELT A14
HEAT TREATED AT 1100°C. FOR
2 HOURS.

(a) SI - XRAY
(b) MN - XRAY
(c) AL - XRAY
(d) S - XRAY

X800

4.58.

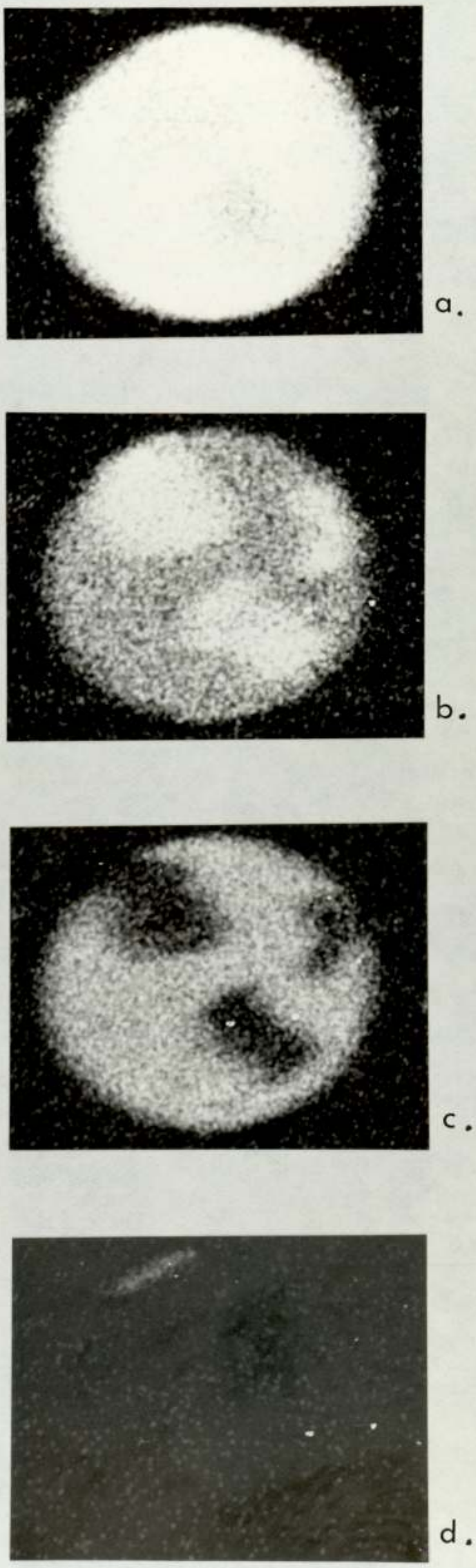

MELT A13
HEAT TREATED AT 1100°C FOR
2 HOURS

PLATE 4.59

TRIDYMITE PRECIPITATES
(93%SiO_2, 4%Al_2O_3, 2%MnO, 1%FeO)
WITHIN A MATRIX
(55%SiO_2, 11%Al_2O_3, 32%MnO, 1%FeO)
ABSORBED ELECTRON IMAGE
X800

PLATE 4.60

BACKSCATTERED ELECTRON IMAGE OF
THREE PHASE INCLUSION
X800

PLATE 4.61

BACKSCATTERED ELECTRON IMAGE SHOWING
RHODONITE APPROX 52%SiO_2, 42%MnO, 4%Al_2O_3
2%FeO, and SiO_2
WITHIN A MATRIX OF COMPOSITION APPROX
48%SiO_2, 37%MnO, 14%Al_2O_3 1%FeO
X1600

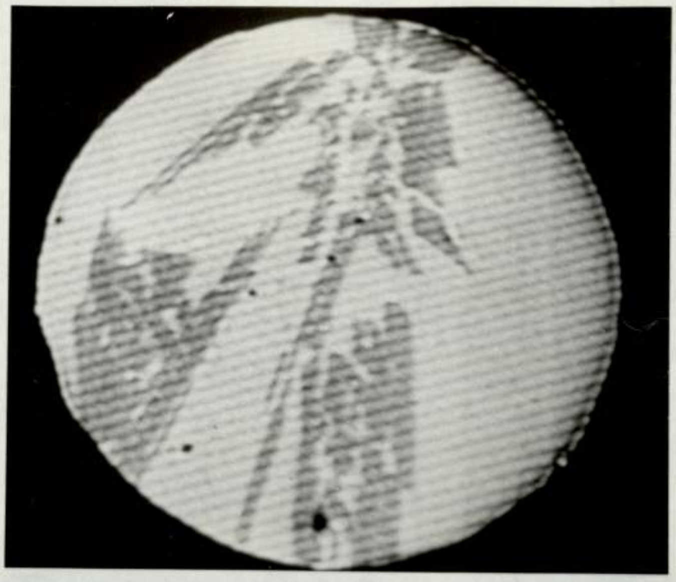

4 .59.

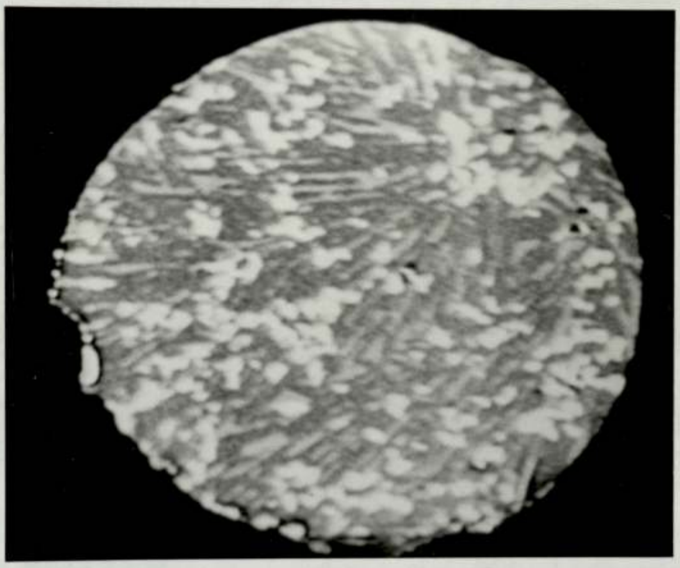

.60.

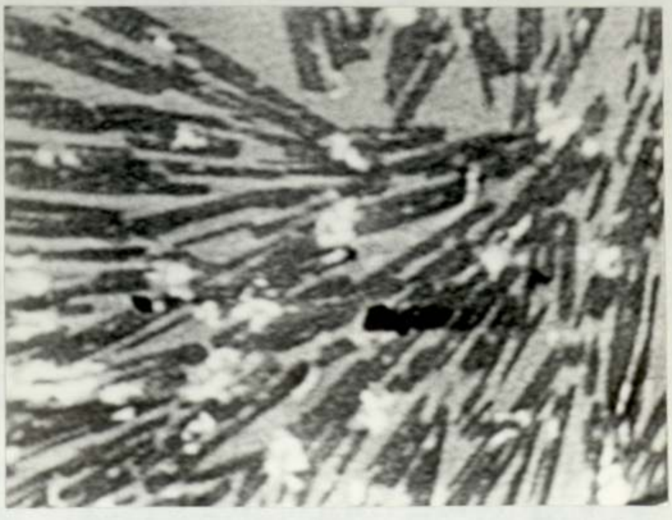

.61.

PLATES 4.62 - 4.65

MELT A14

HEAT TREATED AT 1100°C FOR

2 HOURS

PRECIPITATES OF RHODONITE COMPOSITION

PLATE 4.62 X800

PLATE 4.63 X800

TYPICAL ANALYSIS OF BOTH SMALL AND

LARGE PRECIPITATES

46%SiO_2, 50%MnO, 1%Al_2O_3, 2%FeO

PLATES 4.64 and 4.65 X800

PRECIPITATES TYPICALLY

47%SiO_2, 50%MnO, 2%Al_2O_3, 1%FeO

MATRIX

58%SiO_2, 24%MnO, 17%Al_2O_3, 1%FeO

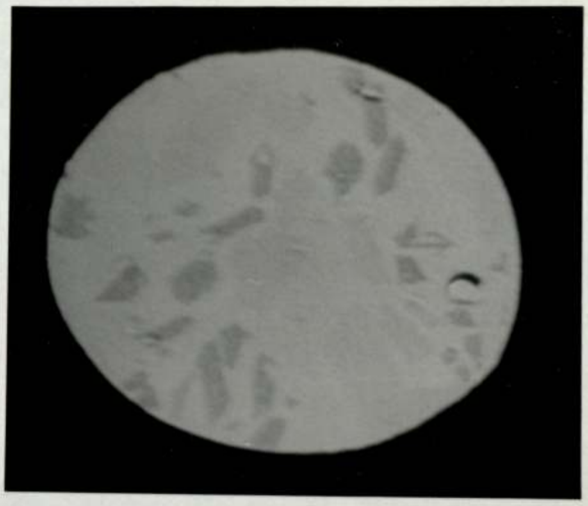

4.62.

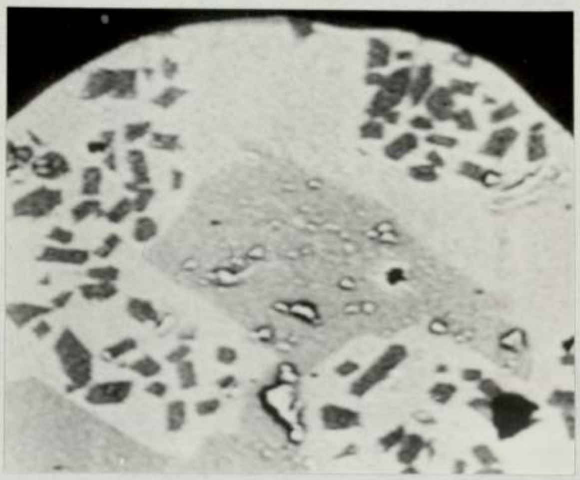

.63.

.64.

.65.